

11-2020

## EVALUATION OF THE GENETIC AND STRUCTURAL VARIATIONS OF CAMEL HEMOGLOBIN

Amanat Ali

Follow this and additional works at: [https://scholarworks.uaeu.ac.ae/all\\_dissertations](https://scholarworks.uaeu.ac.ae/all_dissertations)



Part of the [Molecular Biology Commons](#)

---

### Recommended Citation

Ali, Amanat, "EVALUATION OF THE GENETIC AND STRUCTURAL VARIATIONS OF CAMEL HEMOGLOBIN" (2020). *Dissertations*. 119.

[https://scholarworks.uaeu.ac.ae/all\\_dissertations/119](https://scholarworks.uaeu.ac.ae/all_dissertations/119)

This Dissertation is brought to you for free and open access by the Electronic Theses and Dissertations at Scholarworks@UAEU. It has been accepted for inclusion in Dissertations by an authorized administrator of Scholarworks@UAEU. For more information, please contact [mariam\\_aljaberi@uaeu.ac.ae](mailto:mariam_aljaberi@uaeu.ac.ae).



United Arab Emirates University

College of Science

EVALUATION OF THE GENETIC AND STRUCTURAL  
VARIATIONS OF CAMEL HEMOGLOBIN

Amanat Ali

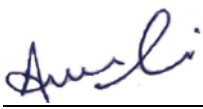
This dissertation is submitted in partial fulfilment of the requirements for the degree  
of Doctor of Philosophy

Under the Supervision of Dr Ranjit Vijayan

November 2020

### **Declaration of Original Work**

I, Amanat Ali, the undersigned, a graduate student at the United Arab Emirates University (UAEU), and the author of this dissertation entitled “*Evaluation of the Genetic and Structural Variations of Camel Hemoglobin*”, hereby, solemnly declare that this dissertation is my own original research work that has been done and prepared by me under the supervision of Dr Ranjit Vijayan, in the College of Science at UAEU. This work has not previously been presented or published, or formed the basis for the award of any academic degree, diploma or a similar title at this or any other university. Any materials borrowed from other sources (whether published or unpublished) and relied upon or included in my dissertation have been properly cited and acknowledged in accordance with appropriate academic conventions. I further declare that there is no potential conflict of interest with respect to the research, data collection, authorship, presentation and/or publication of this dissertation.

Student's Signature: 

Date: 08-12-2020

Copyright © 2020 Amanat Ali  
All Rights Reserved



## **Advisory Committee**

1) Advisor: Dr Ranjit Vijayan

Title: Associate Professor

Department of Biology

College of Science

2) Member: Dr Mohammed Akli Ayoub

Title: Associate Professor

Department of Biology

College of Science

3) Member: Dr Asma Al Menhali

Title: Associate Professor

Department of Biology

College of Science

## Approval of the Doctorate Dissertation

This Doctorate Dissertation is approved by the following Examining Committee Members:

- 1) Advisor (Committee Chair): Dr Ranjit Vijayan

Title: Associate Professor

Department of Biology

College of Science

Signature \_\_\_\_\_ 


Date 22/11/2020

- 2) Member: Dr Sajid Maqsood

Title: Associate Professor

Department of Food Science

College of Food and Agriculture

Signature \_\_\_\_\_ 

Date 22/11/2020

- 3) Member: Dr Khalid Muhammad

Title: Assistant Professor

Department of Biology

College of Science

Signature \_\_\_\_\_ 

Date 23/11/2020

- 4) Member (External Examiner): Professor Syed M. Shozeb Haider

Title: Professor

School of Pharmacy

Institution: University College London, United Kingdom

Signature \_\_\_\_\_ 

Date 22/11/2020

This Doctorate Dissertation is accepted by:

Dean of the College of Science: Professor Maamar Benkraouda

Signature Maamar Benkraouda Date December 16, 2020

Dean of the College of Graduate Studies: Professor Ali Al-Marzouqi

Signature Ali Hassan Date December 17, 2020

Copy \_\_\_\_ of \_\_\_\_

## Abstract

The single-humped Arabian camel (*Camelus dromedarius*) thrives in the hot arid Arabian desert. Many unique adaptations permit it to accomplish this. Camel erythrocytes or red blood cells (RBCs) have a peculiar elliptical shape and are amenable to large variations in physical conditions resulting from dehydration and rehydration cycles. The oxygen transport protein hemoglobin is found abundantly in RBCs and is also believed to behave differently in camels. While several physiological and biochemical studies have been performed on camel hemoglobin, very little is known about genetic and structural adaptations in this protein. The camel genome harbors several unique variations which are being investigated for the treatment of several disorders such as diabetes, cancer, and hepatitis. In this study, several aspects of camel hemoglobin were investigated from genetic, pharmacological and molecular modeling perspectives. Genetic analysis of camel hemoglobin revealed that camels harbor a unique variation in the region of hemoglobin that harbors a peptide called hemorphin. Hemorphins are endogenous bioactive peptides produced during proteolytic cleavage of hemoglobin and are highly conserved among mammals. Several therapeutic properties of mammalian hemorphins have been reported. However, their precise molecular binding behavior remain elusive. This study extensively investigated the binding behavior and pharmacologic effects of human and camel hemorphins, with angiotensin-converting enzyme (ACE), mu-opioid receptor (MOR), and insulin-regulated aminopeptidase (IRAP) receptor using *in silico* and *in vitro* approaches. Camel hemorphins produced more potent activity, better binding affinity, and more stable interactions with critical residues of ACE, MOR and IRAP receptors when compared to human hemorphins. This study also identified, for the first time, a G protein-coupled receptor angiotensin II type 1 receptor (AT1R) that is a target of hemorphins. *In silico* and *in vitro* data demonstrated that LVV-hemorphin-7 binds to the intracellular side of AT1R and allosterically potentiated the potency of AngII as well as its downstream signaling. Lastly, 1000 nanosecond (ns) comparative molecular dynamics (MD) simulations were performed using camel and human hemoglobin protein structures to see how these molecules differ in varying conditions of osmolarity and temperature. Camel

hemoglobin demonstrated limited fluctuations, especially near the heme binding regions at higher salt and temperature conditions, compared to human hemoglobin. Additionally, the binding pose, energetics and interaction stability of oxygen-affinity determining energy molecules, adenosine triphosphate (ATP) and 2,3-bisphosphoglycerate (2,3-BPG) were determined *in silico*. 2,3-BPG is abundantly present in erythrocytes and plays a significant role in the unloading of oxygen molecules in peripheral tissues, compared to ATP. In simulations, 2,3-BPG formed more stable interactions with camel hemoglobin at severe dehydrated conditions compared to human hemoglobin. In summary, this study provides insights into the overall stability of camel hemoglobin as well as the binding behavior of ATP and 2,3-BPG at different dehydrated conditions, along with pharmacological and therapeutic activity of the hemoglobin derived hemorphin peptides.

**Keywords:** Camel, Hemoglobin, Hemorphins, Molecular docking, Molecular dynamics, Molecular biological techniques.

## Title and Abstract (in Arabic)

### تقييم الإختلافات الجينية والبنائية في بروتين الهيموجلوبين المستخلص من الجمال

#### الملخص

ينمو الجمل العربي وحيد السنام (*Camelus dromedarius*) في الصحراء العربية القاحلة الحارة حيث يتميز بالعديد من الخصائص الفريدة التي تسمح لهم بالعيش في ظل هذه الظروف المناخية القاهرة. خلايا الدم الحمراء لهذا الجمل أو كريات الدم الحمراء لها شكل بيضاوي فريد وهي قابلة للتغيرات الكبيرة في ظل الظروف الفيزيائية الناتجة عن دورات الجفاف ودورات معالجة الجفاف. وتم العثور على بروتين الهيموجلوبين الناقل الأساسي للأكسجين في كريات الدم الحمراء ويعتقد أيضًا أنه يعمل بطريقة مختلفة في الإبل. في حين أنه تم إجراء العديد من الدراسات الفسيولوجية والكيميائية الحيوية على بروتين الهيموجلوبين في الإبل، إلى الآن لا يُعرف سوى القليل جدًا عن التغيرات الوراثية والهيكلية في هذا البروتين. تحتوي المعلومات الجينية في الإبل على العديد من الاختلافات المميزة التي يتم دراستها لعلاج العديد من الأمراض.

في هذه الدراسة، تم دراسة الهيموجلوبين في الإبل من جوانب مختلفة كالنمذجة الوراثية والدوائية والجزئية. أظهر التحليل الجيني للهيموجلوبين في الإبل أنه يحتوي على اختلاف فريد في منطقة الهيموجلوبين وبالتحديد في بيتيد يسمى الهيمورفين. الهيمورفين هو عبارة عن بيتيدات نشطة بيولوجيًا يتم إنتاجها أثناء الانقسام البروتيني للهيموجلوبين وهي موجودة بشكل متشابه في جميع الثدييات كما تم التأكد من العديد من الخصائص العلاجية للهيمورفين في الثدييات. ومع ذلك، فإن ترابط بيتيد الهيمورفين الجزئي مبهما إلى الآن.

توصلت هذه الدراسة إلى نتائج تخص التأثيرات العلاجية و سلوك الترابط الجزئي لبيتيد الهيمورفين في الأبل والبشر، وارتباطه مع إنزيم المحول للأنجيوتنسين (ACE)، ومستقبلات ميو أفيونيد (MOR)، ومستقبلات أمينوبيتيداز (IRAP) التي ينظمها الأنسولين (IRAP) باستخدام تقنيات مخبرية (*in vitro*) و تقنيات معلوماتيه حيوية (*in silico*). ومن المثير للاهتمام أن الهيمورفين في الإبل أظهر نشاطًا أكثر فاعلية، وارتباط أفضل تماسكًا، وتفاعلات أكثر ثباتًا مع مستقبلات ACE و MOR و IRAP عند مقارنتها بالهيمورفين البشري. كما حددت هذه الدراسة أيضًا، ولأول مرة، مستقبلات الأنجيوتنسين 2 من النوع الأول (AT1R)

المقترنة ببروتين G والتي تستهدف الهيومورفين. أظهرت البيانات باستخدام تقنيات مختبرية (*in vitro*) و تقنيات معلوماتيه حيوية (*in silico*) أن LVV-hemorphin-7 يرتبط بالجانب الداخلي من AT1R ويقوي فاعلية الإشارات الحيوية ل AngII. أخيراً، تم إجراء محاكاة 1000 نانوثانية للحركة الجزيئية (MD) باستخدام هياكل بروتين الهيموجلوبين البشري والإبل لمعرفة كيفية إختلاف هذه الجزيئات في ظروف مختلفة من الأسموزية ودرجة الحرارة.

ومن المثير للاهتمام، أن الهيموجلوبين في الإبل أظهر تقلبات محدودة، خاصة بالقرب من مناطق ارتباط الحديد في ظروف ارتفاع الملح ودرجة الحرارة، مقارنة بالهيموجلوبين البشري. علاوة على ذلك ، تم تحديد شكل الارتباط ، وتقارب الارتباط، واستقرار تفاعل جزيئات الطاقة التي تحدد تقارب الأكسجين ، وثلاثي فوسفات الأدينوزين (ATP) و 2،3-بيسفسوجليسيرات (BPG-3،2) باستخدام التقنيات المعلوماتيه الحيوية. وفي نموذج المحاكاة، أظهر BPG-3،2 تفاعلات مستقرة مع هيموجلوبين الأبل في ظل الظروف الجافة مقارنة بالهيموجلوبين البشري. وفي الختام ، هذا البحث تحقق من استقرار بروتين الهيموجلوبين في الأبل، إضافة الى سلوك ارتباطه مع ال ATP و BPG-3،2 في حالات الجفاف المختلفة، إلى جانب النشاط الدوائي والعلاجي لبيبتيدات الهيومورفين المشتقة من الهيموجلوبين.

**مفاهيم البحث الرئيسية:** الأبل، الهيموجلوبين، الإرتباط الجزئي، الحركة الجزيئية، الدراسات الجزيئية الحيوية.

## **Acknowledgements**

I would like to extend thanks to the many people, who so generously contributed to the work presented in this dissertation.

Special mention goes to my enthusiastic supervisor Dr Ranjit Vijayan for the useful comments, detailed discussions, remarks and engagement through the learning process of this doctoral dissertation. You have been a tremendous mentor for me. I would like to thank you for introducing me to the exciting field of computational biology and drug design.

I would like to thank my committee for their guidance, support, and assistance throughout my preparation of this dissertation, especially Dr Mohamed Akli Ayoub. I would like to thank the chair and members of the Department of Biology at the United Arab Emirates University for assisting me during my studies and research.

Special thanks go to my parents, wife, brothers, and sisters who helped me along the way. I am sure they suspected it was endless. In addition, special thanks are extended to Bincy Baby, Amna Harib and my PhD batch mates for their assistance and friendship.



## **Dedication**

*To my beloved parents and family*

## Table of Contents

Title.....	i
Declaration of Original Work .....	ii
Copyright.....	iii
Advisory Committee .....	iv
Approval of the Doctorate Dissertation .....	v
Abstract.....	vii
Title and Abstract (in Arabic) .....	ix
Acknowledgements .....	xi
Dedication. ...	xii
Table of Contents .....	xiii
List of Tables.....	xvii
List of Figures .....	xviii
List of Abbreviations.....	xxiii
Chapter 1: Introduction .....	1
1.1 Overview .....	1
1.1.1 Unique physiological characteristics of camels.....	2
1.1.2 Unique genetic characteristics of camels.....	3
1.1.3 The model protein, camel hemoglobin .....	5
1.2 Relevant literature .....	7
1.2.1 Camel hemoglobin.....	9
1.2.2 Hemorphins .....	11
1.2.3 Therapeutic properties of hemorphins .....	13
1.2.4 Molecular mechanism of the interaction of hemorphins and their targets .....	18
1.3 Statement of the problem .....	20
1.4 Hypothesis and objectives.....	22
Chapter 2: Methods .....	24
2.1 Ethical approval .....	24
2.2 Sample collection and storage condition .....	24
2.3 DNA extraction .....	24
2.4 Primers .....	25
2.5 PCR amplification and purification .....	26
2.6 DNA sequencing and analysis .....	27
2.7 Multiple sequence alignment of hemoglobin $\beta$ protein .....	28

2.8	Generation of homology model .....	28
2.9	Protein structure pre-processing.....	29
2.10	Ligand preparation .....	29
2.11	Active site identification and grid generation .....	30
2.12	Peptide and ligand docking .....	30
2.13	Analysis of docking results and binding free energy calculation .....	31
2.14	Molecular dynamics (MD) simulations .....	31
2.14.1	Simulation of membrane bound proteins.....	32
2.14.2	Simulation of non-membrane bound proteins .....	33
2.15	<i>In vitro</i> ACE inhibition assay.....	34
2.16	cDNA constructs and ligands.....	35
2.17	Cell culture and transfection .....	35
2.18	Dose–response BRET assay.....	36
2.19	Real-time BRET kinetic assay .....	36
2.20	IP1 accumulation assay .....	37
2.21	Data presentation and statistical analysis.....	38
Chapter 3: Insights into the Interaction of Hemorphin and its Targets.....		39
3.1	Results .....	39
3.1.1	Multiple sequence alignment of hemoglobin $\beta$ protein sequences .....	39
3.1.2	Structure-based homology modeling of $\mu$ -type opioid receptor .....	41
3.1.3	Molecular docking.....	42
3.1.4	$\mu$ -opioid receptor .....	42
3.1.5	Insulin-regulated aminopeptidase.....	51
3.1.6	Molecular dynamics simulations .....	56
3.1.7	Simulations of camel and non-camel LVV-hemorphin-7 bound to MOR.....	57
3.1.8	Simulations of camel and non-camel LVV-hemorphin-7 bound to IRAP .....	62
3.2	Discussion .....	69
Chapter 4: <i>In silico</i> and <i>In vitro</i> Comparison of the Angiotensin-I Converting Enzyme Inhibitory Activity of Camel and other Mammalian Hemorphins .....		73
4.1	Results .....	73
4.1.1	Molecular docking.....	73
4.1.2	Docking of non-camel and camel LVV-hemorphin-7 to ACE.....	73
4.1.3	Docking of non-camel and camel hemorphin-7 to ACE .....	83
4.1.4	Molecular dynamics simulations .....	89
4.1.5	Simulations of different peptides of non-camel and camel hemorphins bound to ACE .....	89
4.1.6	<i>In vitro</i> ACE inhibition assay .....	98

4.1.7 Determination of ACE inhibitory potential of non-camel and camel hemorphin peptides .....	98
4.1.8 Comparison of the ACE inhibitory activity of different hemorphin peptides.....	101
4.2 Discussion .....	103
Chapter 5: Pharmacological Action of LVV-Hemorphin-7 on Angiotensin II Type 1 Receptor .....	109
5.1 Results .....	109
5.1.1 Weak agonistic effect of LVV–Hemorphin-7 on AT1R .....	109
5.1.2 Positive allosteric effects of LVV–hemorphin-7 on AT1R.....	113
5.1.3 Confirmation of the positive allosteric effects of LVV–hemorphin-7 on AT1R .....	116
5.1.4 Activation of AT1R by LVV-hemorphin-7 .....	121
5.1.5 Effects of LVV–hemorphin-7 on AT1R-mediated downstream signaling .....	122
5.1.6 Molecular docking and molecular dynamics studies.....	125
5.1.7 LVV-hemorphin-7 binds to an intracellular site of AT1R .....	126
5.1.8 Binding of LVV-H7 to AT1R potentiated the binding of AngII.....	131
5.2 Discussion .....	142
Chapter 6: Structural and Genetic Changes of Camel Hemoglobin .....	151
6.1 Results .....	151
6.1.1 Hemoglobin $\alpha$ and $\beta$ genes sequences .....	151
6.1.2 Molecular dynamics (MD) simulation of camel and human hemoglobin .....	155
6.1.3 Molecular docking of 2,3-BPG and ATP with camel hemoglobin .....	165
6.1.4 Molecular docking of 2,3-BPG and ATP with human hemoglobin .....	166
6.1.5 Molecular dynamics (MD) simulations of 2,3-BPG and ATP bound to camel and human hemoglobin .....	169
6.1.6 MD simulations of camel and human hemoglobin bound to 2,3-BPG at different salt concentrations.....	170
6.1.7 MD simulations of camel and human hemoglobin bound to 2,3-BPG at different temperature conditions.....	176
6.1.8 MD simulations of ATP bound to camel and human hemoglobin at different salt conditions .....	181
6.1.9 MD simulations of ATP bound to camel and human hemoglobin at different temperature conditions.....	186
6.2 Discussion .....	191
Chapter 7: Conclusion.....	198

Chapter 8: Future Prospects ..... 199  
References.....200  
List of Publications .....216

## List of Tables

Table 1: Sequence of hemorphin peptides. ....	13
Table 2: Primer sets used in PCR to amplify hemoglobin $\alpha$ and $\beta$ genes. ....	26
Table 3: Interacting residues of the best pose of non-camel (LVVYPWTQRF) and camel (LVVYPWTRRF) hemorphin with MOR, and IRAP. ....	44
Table 4: List of interactions formed by the top binding pose of LVVYPWTQRF, LVVYPWTRRF, YPWTQRF, and YPWTRRF hemorphin peptides with ACE. ....	75
Table 5: Log EC <sub>50</sub> values of LVV-hemorphin-7 and AngII. ....	112
Table 6: Percentage E <sub>max</sub> values of AngII in the various BRET assays. ....	120
Table 7: AT1R residues that interacted with the best docked pose of LVV-H7 and AngII. ....	128
Table 8: List of coding and non-coding variations observed in hemoglobin genes of different breeds of camel. ....	153
Table 9: MD simulation conditions used for simulating complex systems of camel and human hemoglobin. ....	156
Table 10: Interacting residues of camel and human hemoglobin with 2,3-BPG and ATP. ....	168
Table 11: MD simulation conditions used for simulating complex systems of 2,3-BPG and ATP with camel and human hemoglobin. ....	169

## List of Figures

Figure 1: Three dimensional structure of camel hemoglobin .....	7
Figure 2: Classification of camels.....	8
Figure 3: Proposed pharmacological action of hemorphin on different opioid receptors and its regulation of signaling pathways leading to analgesia.....	15
Figure 4: Therapeutic targets of hemorphins and the molecular mechanism of action.....	20
Figure 5: Sequence alignment of hemoglobin $\beta$ protein sequences of closely related mammals.....	40
Figure 6: Ramachandran plot of the human mu opioid receptor model. ....	41
Figure 7: 3D structure of modeled active human MOR. ....	47
Figure 8: Interactions of hemorphin peptides with MOR. ....	48
Figure 9: Interactions of non-camel LVV-hemorphin-7 residues with mu-opioid receptor.....	49
Figure 10: Interactions of camel LVV-hemorphin-7 residues with mu-opioid receptor.....	50
Figure 11: 3D structure of IRAP.....	53
Figure 12: Interactions of hemorphin peptide with IRAP.....	54
Figure 13: Interactions of non-camel LVV-hemorphin-7 residues with IRAP.....	55
Figure 14: Interactions of camel LVV-hemorphin-7 residues with IRAP.....	56
Figure 15: RMSD and RMSF plots of triplicate 100 ns simulations of MOR.....	59
Figure 16: The average percentage of equilibrium simulation time during which residues of MOR maintained contact with LVVYPWTQRF peptide in triplicate 100 ns simulations. ....	60
Figure 17: The average percentage of equilibrium simulation time during which residues of MOR maintained contact with LVVYPWTRRF peptide in triplicate 100 ns simulations.....	61
Figure 18: Histograms of the percentage of simulation time where a MOR residue maintains contact with the hemorphin peptide in triplicate simulations. ....	62
Figure 19: RMSD and RMSF plots of triplicate 100 ns simulations of IRAP.....	65
Figure 20: The average percentage of equilibrium simulation time during which residues of IRAP maintain contact with LVVYPWTQRF peptide from triplicate 100 ns simulations. ....	66

Figure 21: The average percentage of equilibrium simulation time during which residues of IRAP maintain contact with LVVYPWTRRF peptide from triplicate 100 ns simulations. ....	67
Figure 22: Histograms of the percentage of simulation time where an IRAP residue maintains contact with the hemorphin peptide in triplicate simulations. ....	68
Figure 23: The active site of Angiotensin-I converting enzyme (ACE) shown in red circle and a closer look at the interaction of LVV-hemorphin-7 in the active site of ACE. ....	77
Figure 24: Closer view of the docked pose of LVVYPWTQRF peptide and the hydrogen bond interactions it forms with ACE shown as black dashed lines. ....	78
Figure 25: Closer view of the docked pose of LVVYPWTRRF peptide and the hydrogen bond interactions it forms with ACE shown as black dashed lines ....	79
Figure 26: Interactions of human hemorphin (LVVYPWTQRF) with ACE. ....	80
Figure 27: Interactions of camel hemorphin (LVVYPWTRRF) with ACE. ....	81
Figure 28: Closer view of the docked pose of YPWTQRF peptide and the hydrogen bond interactions it forms with ACE shown as black dashed lines. ....	85
Figure 29: Closer view of the docked pose of YPWTRRF peptide and the hydrogen bond interactions it forms with ACE shown as black dashed lines. ....	86
Figure 30: Interactions of human hemorphin (YPWTQRF) with ACE. ....	87
Figure 31: Interactions of camel hemorphin (YPWTRRF) with ACE. ....	88
Figure 32: RMSD plots of C $\alpha$ atoms of ACE protein extracted from triplicate 200 ns simulations of hemorphin-ACE complex. ....	91
Figure 33: RMSF plots of C $\alpha$ atoms of ACE protein extracted from triplicate 200 ns simulations of hemorphin-ACE complex. ....	92
Figure 34: The average percentage of equilibrium simulation time during which ACE residues retain interaction with human hemorphin (LVVYPWTQRF) peptides from triplicate 200 ns simulations. ....	93
Figure 35: The average percentage of equilibrium simulation time during which ACE residues retain interaction with camel hemorphin (LVVYPWTRRF) peptides from triplicate 200 ns simulations. ....	94
Figure 36: The average percentage of equilibrium simulation time during which ACE residues retain interaction with human hemorphin (YPWTQRF) peptides from triplicate 200 ns	



simulations. ....	96
Figure 37: The average percentage of equilibrium simulation time during which ACE residues retain interaction with camel hemorphin (YPWTRRF) peptides from triplicate 200 ns simulations. ....	97
Figure 38: Dose-response curves of different hemorphin peptides. ....	100
Figure 39: IC50 of different hemorphin peptides. ....	102
Figure 40: LVV-hemorphin-7's action on AT1R. ....	111
Figure 41: Positive allosteric modulation of LVV-hemorphin-7 on AT1R activation demonstrated by dose-response BRET technique. ....	115
Figure 42: Positive allosteric modulation of LVV-hemorphin-7 on AT1R activation demonstrated by dose-response BRET technique. ....	116
Figure 43: Positive allosteric modulation of LVV-hemorphin-7 on AT1R activation demonstrated by real-time BRET kinetic analysis. ....	119
Figure 44: AT1R-selective antagonist (irbesartan) inhibited both AngII- and LVV-hemorphin-7-mediated BRET potentiation. ....	122
Figure 45: Positive allosteric modulation of LVV-hemorphin-7 on AT1R-mediated IP1 production. ....	124
Figure 46: Structure of AT1R with the docked peptide. ....	129
Figure 47: 2D ligand interaction diagram of LVV-hemorphin-7 with AT1R. ....	130
Figure 48: Plots of RMSD and RMSF of protein C $\alpha$ atoms extracted from three independent 500 ns simulations of AT1R complexes. ....	131
Figure 49: Binding pose of AngII with AT1R in the presence and absence of LVV-H7. ....	133
Figure 50: 2D ligand interaction diagram of AngII with AT1R. ....	134
Figure 51: 2D ligand interaction diagram of AngII with AT1R-LVV-hemorphin-7. ....	135
Figure 52: Average percentage of simulation time from three 500 ns runs during which AT1R residues maintain contact with LVV-H7. ....	137
Figure 53: Average percentage of simulation time from three 500 ns runs during which AT1R residues maintain contact with AngII in the absence of LVV-H7. ....	138
Figure 54: Average percentage of simulation time from three 500 ns	

runs during which AT1R residues maintain contact with AngII in the presence of LVV-H7. ....	139
Figure 55: Histograms of the percentage of simulation time where an AT1R residue maintained contact with a peptide. ....	140
Figure 56: Chromatograms of camel samples.....	152
Figure 57: Root mean square standard deviation (RMSD) and root mean square fluctuation (RMSF) of protein C $\alpha$ atoms obtained from a 1000 ns run of camel and human hemoglobin simulation at different salt conditions. ....	160
Figure 58: Root mean square standard deviation (RMSD) and root mean square fluctuation (RMSF) of protein C $\alpha$ atoms obtained from a 1000 ns run of camel and human hemoglobin simulation at different temperature conditions.. ....	164
Figure 59: Docked pose of 2,3-BPG and ATP with camel and human hemoglobin.....	167
Figure 60: Root mean square standard deviation (RMSD) and root mean square fluctuation (RMSF) of protein C $\alpha$ atoms obtained from a 200 ns run of 2,3-BPG bound camel and human hemoglobin simulations at different salt conditions. ....	173
Figure 61: The percentage of simulation time during which different residues of camel hemoglobin interacted with 2,3-BPG.....	175
Figure 62: The percentage of simulation time during which different residues of human hemoglobin interacted with 2,3-BPG. ....	176
Figure 63: Root mean square standard deviation (RMSD) and root mean square fluctuation (RMSF) of protein C $\alpha$ atoms obtained from a 200 ns run of 2,3-BPG bound camel and human hemoglobin simulations at different temperature conditions.....	178
Figure 64: The percentage of simulation time during which different residues of camel hemoglobin interacted with 2,3-BPG.....	180
Figure 65: The percentage of simulation time during which different residues of human hemoglobin interacted with 2,3-BPG. ....	181
Figure 66: Root mean square standard deviation (RMSD) and root mean square fluctuation (RMSF) of protein C $\alpha$ atoms obtained from a 200 ns run of ATP bound camel and human hemoglobin simulations at salt conditions. ....	183
Figure 67: The percentage of simulation time during which different residues of camel hemoglobin interacted with ATP.. ....	185
Figure 68: The percentage of simulation time during which different	

residues of human hemoglobin interacted with ATP.....	186
Figure 69: Root mean square standard deviation (RMSD) and root mean square fluctuation (RMSF) of protein C $\alpha$ atoms obtained from a 200 ns run of ATP bound camel and human hemoglobin simulations at different temperature conditions.....	188
Figure 70: The percentage of simulation time during which different residues of camel hemoglobin interacted with ATP..	190
Figure 71: The percentage of simulation time during which different residues of human hemoglobin interacted with ATP.....	191

## List of Abbreviations

ACE	Angiotensin Converting Enzyme
AKT/PKB	Protein Kinase B
AngII	Angiotensin II
ANOVA	Analysis of Variance
AT1R	Angiotensin II Type 1 Receptor
ATP	Adenosine Triphosphate
AT4R	Angiotensin Type 4 Receptor
AVP	Arginine Vasopressin
BBB	Blood Brain Barrier
BLAST	Basic Local Alignment Search Tool
BPG	Bisphosphoglycerol
BRET	Bioluminescence Resonance Energy Transfer
CYP450	Cytochrome P450
CNS	Central Nervous System
DAG	Diacylglycerol
DOR	Delta Opioid Receptor
DMEM	Dulbecco Modified Eagle Medium
DMSO	Dimethyl Sulfoxide
dNTPs	Deoxynucleoside triphosphates
DPP4	Dipeptidyl Peptidase

DPPC	Dipalmitoylphosphatidylcholine
DNA	Deoxyribonucleic acid
ECL	Extracellular Loop
EDTA	Ethylene Diamine Acetate
ERK	Extracellular Signal-Regulated Kinase
FDA	Food and Drug Administration
GC	Guanine Cytocine
GLP	Glucagon Like Peptidase
GLUT4	Glucose Transporter Type 4
GPCR	G-Protein Coupled Receptor
GPI	Glucose Phosphate Isomerase
Hb	Hemoglobin
HBB	Hemoglobin Beta
HCAbs	Heavy Chain Antibodies
H7	Hemorphin-7
HEK293	Human Embryonic Kidney 293 Cells
IC <sub>50</sub>	The Half Maximal Inhibitory Concentration
ICL	Intracellular Loop
IP1	Inositol Phosphate
IR	Immune Response
IRAP	Insulin Regulated Aminopeptidase
KOR	Kappa Opioid Receptor

KKS	Kallikrein Kinnin System
MD	Molecular Dynamics
MHC	Major Histocompatibility Complex
MM-GBSA	Molecular Mechanics-Generalized Born Surface Area
mM	Millimolar
MOR	Mu Opioid Receptor
NCBI	National Center for Biotechnology Information
NFAT	Nuclear Factor of Activation T Cell
nM	Nanomolar
NPT	Number of particles, Pressure and Temperature
OPLS	Optimized Potentials for Liquid Simulations
PAR1	Protease Activated Receptor 1
PBS	Phosphate Buffer Saline
PBST	Phosphate Buffer Saline Tween
PCR	Polymerase Chain Reaction
PDB	Protein Data Base
PI3K	Phosphoinositide 3-kinases
PLC	Phospholipase-C
RAS	Renin Angiotensin System
RAAS	Renin Angiotensin Aldosterone System
RBCs	Red Blood Cells

RESPA	Reference System Propagator Algorithm
RMSD	Root Mean Square Deviation
RMSF	Root Mean Square Fluctuation
SNPs	Single Nucleotide Polymorphisms
SP	Standard Precision
SPC	Single Point Charge
SDS-PAGE	Sodium Dodecyl Phosphate Polyacrylamide Gel Electrophoresis
SEM	Standard Error of the Mean
SPSS	Statistical Package for the Social Sciences
TCR	T-Cell Receptor
TK	Tyrosine Kinase
TM	Transmembrane
XP	Extra Precision
YPET	Yellow Fluorescent Protein

## **Chapter 1: Introduction**

### **1.1 Overview**

Camels play a vital role in the survival of mankind, particularly those living in arid regions, due to their versatile role and unique capability to acclimatize to these extreme environmental conditions (Beuzen, Stear, & Chang, 2000; Burger, 2016; Soman & Tinson, 2016). Despite the huge economic, cultural, and biological significance, the genetic architecture of camels has not been extensively studied to gain a deeper understanding of the molecular biology that underlies these unique adaptations. The camel genome contains approximately 20,000 genes and is roughly 2.38 gigabases in size (Jirimutu et al., 2012). The genetic architecture of camels has a profound impact that enables them to survive under extreme conditions (Andersson & Georges, 2004; Wu et al., 2014). Variations in the genome and proteome of the camel are also being explored for the treatment of a number of disorders (Agrawal, Jain, Shah, Chopra, & Agarwal, 2011; Jirimutu et al., 2012; Muyldermans et al., 2009).

Camels harbor numerous unique traits that permit them to live and thrive in distant areas, scorched lands, and high mountains (Jirimutu et al., 2012). They have an inherent ability to endure thirst and hunger for longer period of times in extremely harsh environmental conditions. Studies focused on the camel genome have demonstrated the contribution of numerous genes that permit them to acclimatize to severe ecological conditions (Elmahdi, Sallmann, Fuhrmann, von Engelhardt, & Kaske, 1997; Jirimutu et al., 2012; Kasahara et al., 2007; Muyldermans, 2001). Additionally, multiple studies have assessed the therapeutic potential of camel products in the management of several human ailments (Agrawal et al., 2011; Fitak,



Mohandesan, Corander, & Burger, 2016; Jirimutu et al., 2012; Muyldermans et al., 2009).

### **1.1.1 Unique physiological characteristics of camels**

Camels harbor unique attributes that permit them to survive in extreme desert conditions. Previous studies have shown that camels store energy in their humps in the form of fat which permits them to survive without food and water for a longer period of time when compared to other closely related mammals (Emmanuel & Nahapetian, 1980). The body temperature of camels fluctuate between 34 to 41°C within the day (Schmidt-Nielsen, Schmidt-Nielsen, Jarnum, & Houpt, 1956). Camels have the ability to lose water up to 25% of its body weight (Macfarlane, Morris, & Howard, 1963). Another study revealed that camels could lose water up to 30% of its body weight in severe dehydrated conditions. Compared to this, other closely related mammals will not be able to withstand such drastic changes and will probably die because of circulatory failure when the water loss surpasses 12% of their body weight (McKinley, McBurnie, & Mathai, 2001). Several factors are involved in regulating the body water balance including tissue osmolality and particularly blood osmolality (Andersson, Olsson, & Rundgren, 1980).

Camel kidneys are primarily involved in the conservation of water by raising the osmolarity of urine. The camel kidney has the ability to reabsorb more water and produce highly concentrated urine compared to other mammals. Furthermore, unlike other mammals, a camel's intestine has the unique capability to reabsorb water and water loss via feces is extremely low (Davidson, 2014). Surprisingly, camels can withstand high blood glucose level (twofold than other ruminants) without exhibiting

any signs of diabetes. Camels can also ingest approximately eight times more salt compared to other mammals without demonstrating any signs of hypertension (Al-Ali, Husayni, & Power, 1988; Jirimutu et al., 2012).

### **1.1.2 Unique genetic characteristics of camels**

Although camels have huge economic, cultural, and biological significance, very little is reported about the camel genome and the evolutionary preferences it confers. Camels along with other domestic animals and livestock, possess unique attributes and genetic variations (Andersson & Georges, 2004). The camel genome is nearly 2.38 gigabases and encodes around 20,821 genes (Jirimutu et al., 2012).

Recent genomic and transcriptomic studies have unlocked the characteristics of the unique adaptations in camels (Jirimutu et al., 2012; Wu et al., 2014). Researchers have explored the importance of ‘rapidly evolving genes’ in species differentiation and adaptation in camels (Kasahara et al., 2007; Ming et al., 2017; Muyltermans et al., 2009). Fast divergence of protein-coding genes are typically estimated by a high ratio of non-synonymous-to-synonymous substitutions (dN/dS) (Jirimutu et al., 2012). Jirimutu et al. (2012) reported approximately 2,730 notably faster evolving genes in camels compared its adjacent cattle orthologs. Importantly, these genes were augmented in metabolic pathways such as lipid and carbohydrate metabolism, adipocytokine signaling pathways, and insulin signaling pathways. They suggested that these genes might have assisted the camel to enhance their energy storage and production in the desert.

Camels are ruminant herbivores with a large forestomach. Nevertheless, they have significantly higher blood glucose levels (6–8 mmol/l) compared to other

mammals. Cytochrome 2E (CYP2E) and cytochrome 2J (CYP2J) genes, which belong to a set rapidly evolving genes, could be associated with type II diabetes mellitus (Jirimutu et al., 2012). Phosphoinositide 3-kinases (PI3K) and protein kinase (PKB) are two crucial genes in the insulin signaling pathway that has seen rapid divergence in camels and could have altered their sensitivity to insulin (Ming et al., 2017). This reinforces earlier findings that a higher glucose blood level in camels is primarily due to their high insulin resistance (Kaske, Elmahdi, Engelhardt, & Sallmann, 2001). Additionally, cytochrome P450 (CYP450) genes distribution has also be reported to be different in camels compared to other mammals. CYP genes are principally involved in arachidonic acid metabolism. Interestingly, an analysis of the Bactrian camel genome revealed more copies of CYP450 genes. For instance, camels have eleven copies of CYP2J gene and two copies of CYP2E gene compared to other mammals including humans. However, copies of CYP4A and CYP4F genes were found to be lower in camels in comparison to other mammals (Jirimutu et al., 2012). CYP2E and CYP2J support to convert arachidonic acid into 19(S)-hydroxy-eicosatetraenoic acid [19(S)-HETE], while CYP4F and CYP4A convert it into 20-HETE (Wu et al., 2014). 19(S)-HETE is a strong vasodilator of renal preglomerular vessels that potentiate water reabsorption and is particularly important for its survival in deserts (Carroll et al., 1996). Several copies of CYP2J genes enable them to withstand high amount of salt without exhibiting hypertension (Wu et al., 2014). The prime activity of CYP2J2 gene is controlled by high-salt diet and the inhibition of this gene can lead to high blood pressure (Zhao, Pollock, Inscho, Zeldin, & Imig, 2003). The impact of extreme desert conditions results in substantial increase in sodium levels of serum, urea, creatinine, and plasma arginine vasopressin (AVP) levels while plasma aldosterone level was not significantly changed (Al-Ali et al.,

1988). These findings support earlier studies that demonstrated that renin-angiotensin system is vital for the regulation of water balance during dehydration. Additionally, studies have also shown an upsurge of serum creatinine and serum urea levels in dehydration (Finberg, Yagil, & Berlyne, 1978; Siebert & Macfarlane, 1971). Camels also have the inherent ability to survive starvation while maintaining a consistent nitrogen level via urea-nitrogen recycling (Mousa, Ali, & Hume, 1983).

Camels are comparatively more resistant to many infectious diseases, compared to other mammals residing in the same terrestrial area. However, the immunogenome of camel remains elusive (Burger, 2016; Muyldermans et al., 2009; Wernery & Kaaden, 2004). The camel's immune system comprises of a unique heavy chain antibody homodimer. More importantly, camels are the only mammals that possess heavy-chain antibodies (HCAbs) that is devoid of the light chain (Hamers-Casterman et al., 1993; Tillib, Vyatchanin, & Muyldermans, 2014). However, very little is known about the major histocompatibility complex (MHC) region of the camel genome (Antczak, 2013). The immune response (IR) genes that demonstrate a critical role in host–pathogen interactions are present in the genomic MHC region (Janeway, Travers, Walport, & Shlomchik, 2001).

### **1.1.3 The model protein, camel hemoglobin**

The protein hemoglobin is abundantly present in red blood cells (RBCs) or erythrocytes. Hemoglobin is the oxygen carrying protein that gives the typical red color to blood. Adult vertebrate hemoglobin is composed of four protein chains, two  $\alpha$  chains and two  $\beta$  chains. These chains were produced as a result of gene duplication (Storz, 2016). A ferrous ion ( $\text{Fe}^{2+}$ ) contained in the heme group present

in each chain acts as a cofactor for this tetrameric protein. Oxygen is transported in blood by reversibly binding to these  $\text{Fe}^{2+}$  ions. Structurally, hemoglobin chains retain the classic globin fold, which is shared by several proteins. Myoglobin, for example, a monomer, retains the same fold albeit with just around 25% sequence identity to hemoglobin.

Camel hemoglobin contains more charged amino acid residues and are more hydrophilic than hemoglobins of other mammalian species (Bogner, Csutora, Cameron, Wheatley, & Miseta, 1998). The availability of a three dimensional X-ray crystal structure of the camel hemoglobin molecule now permits structural comparisons of this molecule with that of several other well-studied species including humans, rats and mice (Balasubramanian, Moorthy, Neelagandan, & Ponnuswamy, 2009) (Figure 1).

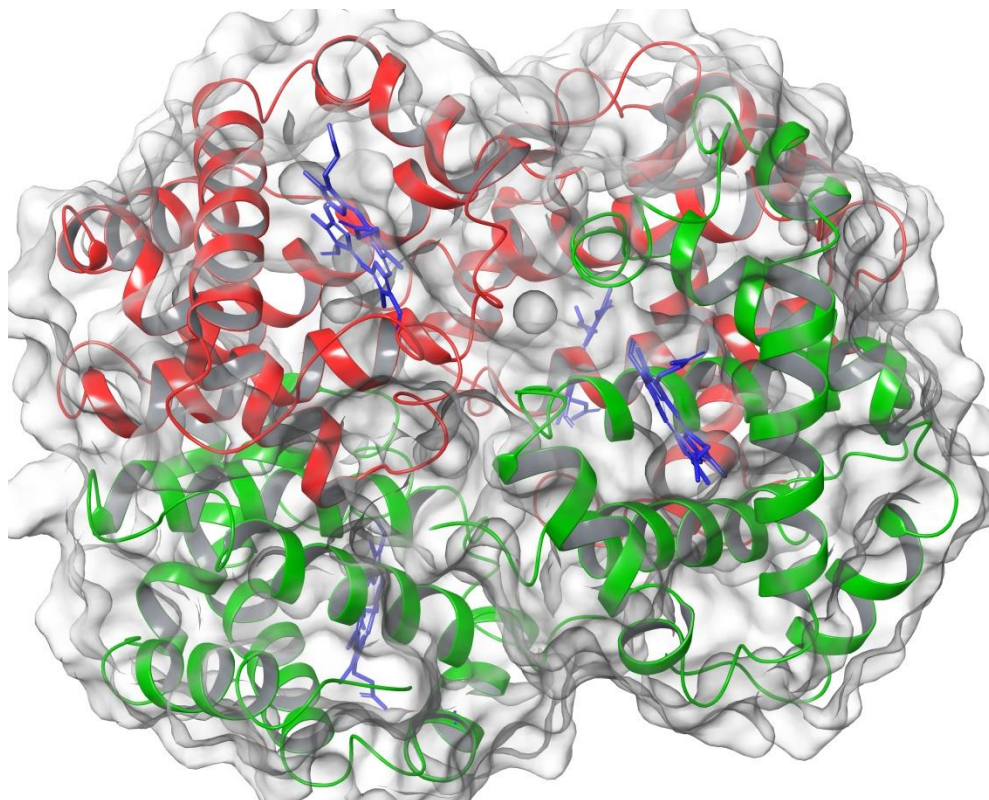


Figure 1: Three dimensional structure of camel hemoglobin (PDB ID: 3GDJ) with  $\alpha$  chains shown in red and  $\beta$  chains shown in green. The heme group is shown in blue stick representation.

## 1.2 Relevant literature

Camels play an important role in less economically compromised parts of Asian, Arabian, and African deserts. Camels have been used as a source food, for transportation, and for protection for a very long time. Currently, they are enormously vital in various parts of the scorched world as sustainable livestock species (Burger, 2016). Camels belong to Camelidae family. The Camelidae family could be traced back to North America approximately 35 million years ago during the Eocene period (Reed, 1972). Camels are broadly classified into two major types – small and large camels – which are further subdivided into *Camelus*, *Lama*, and *Vicugna* genera. A distinct collective classification of camels is not present so far.

Nevertheless, the most frequently used and known classification is given in Figure 2 (Wu et al., 2014). Irrespective of their classification, camels are usually differentiated based on habitat, function, and color. Camels has roughly the same shape but deviate in body size, color, and conformation (Al-Swailem et al., 2010). The large camelids comprise of two domestic species: the single-humped dromedary camel *Camelus dromedarius*, and the two-humped Bactrian camel *Camelus bactrianus*. Dromedary camels are also referred to as Arabian camels and are predominantly found in the hot and barren region between the northern part of Africa and east of Asia. The domestication of dromedary camel first started around five thousand or six thousand years ago in the Arabian peninsula (Almathen et al., 2016; Trinks, Burger, Beneke, & Burger, 2012). Bactrian camels are primarily found in deserted areas of central Asia and colder regions. The llama and the alpaca are the two members of small camelids which are limited to South America.

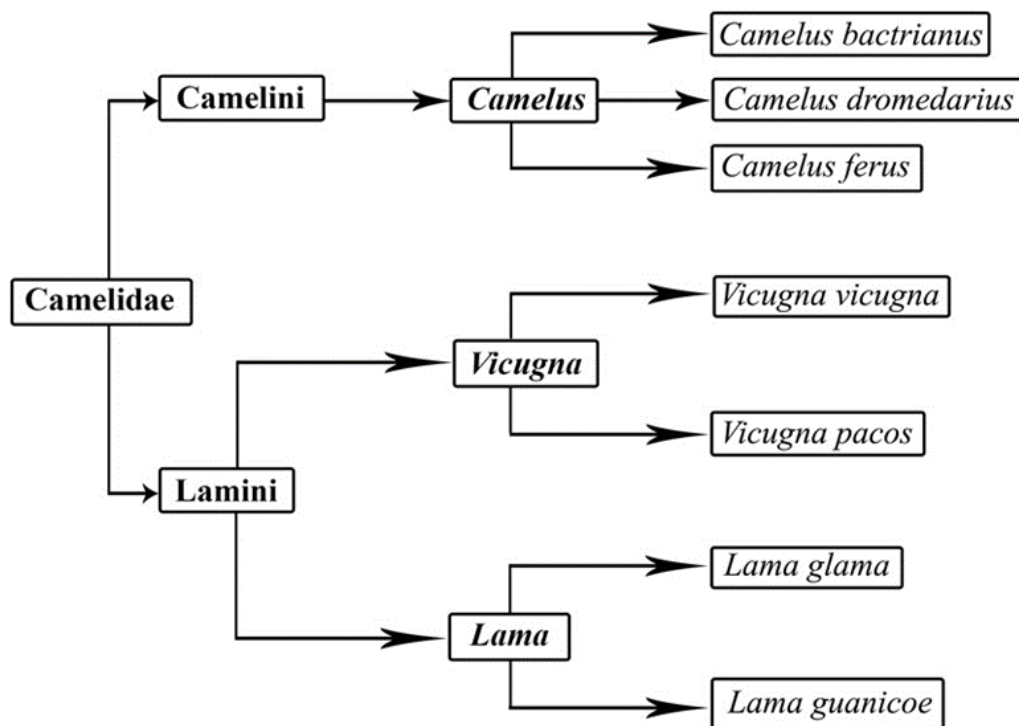


Figure 2: Classification of camels.

### 1.2.1 Camel hemoglobin

Camel red blood cell (RBC) is a fascinating case study of adaptation to severe environmental conditions (Oyewale et al., 2011). It has been well established that the shape of the erythrocytes in all mammals is spherical or concave. However, camels erythrocytes are extremely enucleated, ovaloid, small, flat, and circulates in large numbers (Azwai, Abdousslam, Al-Bassam, Al Dawek, & Al-Izzi, 2007; Goniakowska-Witalinska & Witalinski, 1976). This unique elliptical shape of camel erythrocytes enables their flow in dehydrated conditions and permit them to cross small capillaries (Eitan, Aloni, & Livne, 1976). Moreover, camel RBCs are extremely resistant to osmotic hemolysis and has the ability to swell up to 240% of their normal volume without rupturing (Oyewale et al., 2011). It is believed that this could be because of different arrangement of membrane phospholipids in its erythrocytes (Wardeh, 2004). There are several possible hypotheses on how the cells could survive severe osmotic shock. This includes: (1) erythrocyte membrane plasticity and its composition (Eitan et al., 1976); (2) variations in the cytoskeleton molecules of camel erythrocyte including erythrocytic spectrin (Ralston, 1975); (3) the water holding capacity of camel hemoglobin and its packaging inside the erythrocyte (Bogner et al., 2005); (4) the concentration of energy rich compounds in the erythrocyte cytosol, including adenosine triphosphate (ATP), 2,3-bisphosphoglycerate (2,3-BPG) and cofactors such as chloride ions and its binding affinity to hemoglobin in different stages of osmotic stress (Garby, Gerber, & De Verdier, 1969).

Camels have inherent ability to survive without drinking water for longer period of time. Camels can lose 30% of their body weight during dehydrated



conditions. Studies have shown that a dehydrated camel can regain the lost water (approximately 30 gallons) within 10 minutes. Notwithstanding, the high flow of water into the bloodstream, camel's erythrocytes remained intact (Perk, 1963). However, in humans entry of only 600 ml of water into the blood circulation cause hemoglobinuria (Perk, 1963). It has been suggested that the ability of camel erythrocytes to resist high dilutions are due to higher binding capacity of camel erythrocytes with water (Perk, 1963).

Studies have shown that 2,3-bisphosphoglycerate (2,3-BPG) and ATP interact with hemoglobin and substantially decreases its affinity for oxygen (Chu, Breite, Ciraolo, Franco, & Low, 2008; Macdonald, 1977). The hemoglobin oxygenation is critically controlled by the 2,3-BPG levels in the RBCs (Berg, Tymoczko, & Stryer, 2002). 2,3-BPG is the most abundant phosphate compound present in red blood cells and is generally formed from the rearrangement of 1,3 bisphosphoglycerate during glycolysis (Chen, Yu, Zulfajri, Lin, & Wang, 2017). The presence of 2,3-BPG and ATP in erythrocytes promote the unloading of oxygen in tissue capillaries and subtle changes in their levels could substantially affects the release of oxygen. The molecular binding of 2,3-BPG and ATP with human hemoglobin has been explored using *in vitro* and *in silico* studies (Gerber, Berger, Jänig, & Rapoport, 1973; Lennon, Scott, Chapman, & Kuchel, 1994). However, the stability of binding residues, especially critically important residues of human and other mammalian hemoglobin, with these abundantly present co-factors under different stresses have not been explored.

### 1.2.2 Hemorphins

The cryptome is a part of the proteome that forms cryptic peptides with important biological activities (Pimenta & Lebrun, 2007). The cryptome is naturally incorporated in protein sequences and has the ability to form multiple biologically active peptides called cryptides when exposed to proteolytic cleavage (Ivanov, Karelin, Philippova, Nazimov, & Pletnev, 1997; Pimenta & Lebrun, 2007). Cryptides produce similar or, entirely different biological activities, compared to the protein from which it was excised. Lately, numerous cryptides have been reported and their putative pharmacological activities in several diseases have been described (Fesenko et al., 2019; Gaglione et al., 2019; Haines et al., 2019). Hemorphins are known endogenous cryptides. They belong to the family of atypical opioid peptides and are released during the serial degradation of hemoglobin proteins (Blishchenko et al., 2005; Jinsmaa & Yoshikawa, 2002). Generally, opioid peptides are roughly divided into typical and atypical opioid peptides. Typical opioid peptides include enkephalins, betaendorphins and dynorphins. These bioactive peptides are formed by the degradation of proenkephalin, proopiomelanocortin and prodynorphin, respectively, and possessed the same N-terminal amino acid sequence tyrosine-glycine-glycine-phenylalanine (Goldstein, Tachibana, Lowney, Hunkapiller, & Hood, 1979; Hughes et al., 1975). Sequential lysis of some proteins releases another group of peptides known as atypical opioid peptides. Casomorphins, cytochromins, and hemorphins, produced from casein, cytochrome b, and hemoglobin, respectively, belong to this group (Brantl et al., 1985). All atypical opioid peptides possess a single common factor, which is an N-terminal tyrosine residue. Compared to typical opioid peptides, further extension of the amino acid sequence beyond the tyrosine

residue at the N terminal is possible in atypical opioid peptides (Teschemacher, 1993).

Hemorphins are 4–10 amino acid long bioactive peptides formed by the sequential degradation of hemoglobin proteins (Brantl et al., 1985). The initial well-characterized hemoglobin-derived peptide was hemorphin-4 obtained from bovine blood (Brantl et al., 1986). Afterwards, Glamsta and colleagues described longer isoforms of hemorphins in the human pituitary (Glamsta et al., 1991). Serial cleavage of hemoglobin generates a chain of biologically active peptides with overlapping sequences. These endogenous peptides have been identified and produced from several biological fluids such as brain, plasma, hypothalamic tissues, cerebrospinal fluids, pituitary glands, peripheral and central nervous systems, and adrenal tissues (Glamsta, Meyerson, Silberring, Terenius, & Nyberg, 1992). Studies have reported the association of hemorphins to several physiological and pathological conditions such as long distance running, inflammation, cancer, and cerebrovascular bleeding (Glamsta et al., 1992; Sanderson, Andren, Caprioli, & Nyberg, 1996). These peptides are also produced during alteration from usual behavior and the action of certain enzymes in particular tissues (Ivanov et al., 1997). These bioactive short peptides contain an essential tetrapeptide core - tyrosine-proline-tryptophan-threonine (YPWT) (Nyberg, Sanderson, & Glamsta, 1997). Extended hemorphin peptides have been produced in human and bovine tissues due to N- and C- terminal extensions of this core sequence (Glamsta *et al.*, 1992). Known hemorphin peptides of different lengths are given in Table 1. Amongst all known hemorphins, LVV-hemorphin-7 and VV-hemorphin-7 are considered to be the longest and most stable form of hemorphins (Moeller et al., 1997). The relatively small size of hemorphins also

enable them to cross the blood-brain barrier (BBB) (Glamsta et al., 1992). The sequence of hemorphin is highly conserved among mammals. Several studies have reported promising therapeutic potential of hemorphins in various disorders (Ali, Baby, Soman, & Vijayan, 2019; Cheng, Tao, Cheng, & Huang, 2012). Nevertheless, the detailed cellular and molecular mechanisms that trigger the interaction of hemorphins and their targets remain elusive.

Table 1: Sequence of hemorphin peptides.

<b>Name</b>	<b>Amino acid sequence</b>
Hemorphin-4	Tyr-Pro-Trp-Thr (YPWT)
Hemorphin-5	Tyr-Pro-Trp-Thr-Gln (YPWTQ)
Hemorphin-6	Tyr-Pro-Trp-Thr-Gln-Arg (YPWTQR)
Hemorphin-7	Tyr-Pro-Trp-Thr-Gln-Arg-Phe (YPWTQRF)
LVV-hemorphin-4	Leu-Val-Val-Tyr-Pro-Trp-Thr (LVVYPWT)
LVV-hemorphin-5	Leu-Val-Val-Tyr-Pro-Trp-Thr-Gln (LVVYPWTQ)
LVV-hemorphin-6	Leu-Val-Val-Tyr-Pro-Trp-Thr-Gln-Arg (LVVYPWTQR)
VV-hemorphin-7	Val-Val-Tyr-Pro-Trp-Thr-Gln-Arg-Phe(VVYPWTQRF)
LVV-hemorphin-7	Leu-Val-Val-Tyr-Pro-Trp-Thr-Gln-Arg-Phe(LVVYPWTQRF)

### 1.2.3 Therapeutic properties of hemorphins

Hemorphin-4 (YPWT) was the first short hemorphin peptide obtained from hemoglobin. This peptide was extracted from bovine blood that was subjected to a mixture of gastrointestinal enzymes (Lau & Dunn, 2018). After that, a number of other peptides, such as hemorphin-4 to -7 and LVV-hemorphin-4, -6, and -7, were identified that also have the YPWT sequence (Dagouassat, Garreau, Sannier, Zhao, & Piot, 1996; Moisan et al., 1998). These peptide are generally formed in the cerebrospinal fluid, brain, plasma and spinal cord (Glamsta et al., 1992; Karelina,

Philippova, Karelina, & Ivanov, 1994). Different lengths of hemorphins have been associated with several biological activities such as pharmacological actions on spatial learning, inflammation, analgesia and transient hypotension (Cheng et al., 2012; Lee et al., 2004). Out of all hemorphins, LVV-hemorphin-7 (LVV-H7 or LVVYPWTQRF) is the longest with 10 amino acids. Several reports have indicated that LVV-hemorphin-7 is the most hydrophobic peptide and is abundantly present in mammalian central nervous system (CNS) (Karelina et al., 1994; Moeller et al., 1997).

The existence and discovery of different opioid binding sites in the mammalian brain started several studies to determine their precise natural ligands. Met- and Leu-enkephalin were the earliest endogenous opioid peptides to be reported (Hughes et al., 1975). After that, different bioactive peptides were reported that were released from controlled cleavage of protein precursors. Classical opioid peptides such as enkephalins, dynorphins, and  $\beta$ -endorphins are produced by the lysis of proenkephalin, prodynorphin and proopioidmelanocortin, respectively. These are mostly present in the CNS (Kakidani et al., 1982). Three opioid receptors namely  $\mu$ ,  $\delta$ , and  $\kappa$  have been investigated extensively. Several groups of peptides are produced as a result of partial proteolysis of proteins. For example, cytochromins are produced from mitochondrial cytochrome b, casomorphins released from the milk protein  $\beta$ -casein, and hemorphins derived from hemoglobin (Karelina et al., 1994). Investigating the agonistic activity of peptides to opioid receptors is of great importance as their binding produces profound analgesia in inflamed tissue (Stein, Schäfer, & Machelska, 2003). Studies have illustrated that hemorphins could also bind to opioid receptors (Glamsta et al., 1992). Moreover, a study conducted on electrically stimulated myenteric plexus/longitudinal muscle preparation of the guinea pig ileum,

demonstrated that hemorphin-5, -6, and -7 possessed opioid-like activity. Glucose phosphate isomerase (GPI) bioassay has shown agonistic opioid-like effects of different hemorphins (Zadina, Kastin, Kersh, & Wyatt, 1992). Furthermore, opioid receptor affinity of hemorphin was evaluated in membranes from rat brain and the findings indicated  $IC_{50}$  values in the micromolar range (Yukhananov, Glämsta, & Nyberg, 1994). Additionally, studies have also suggested that hemorphins mimic opioid peptides in terms of their analgesic activities. A dose-dependent antinociceptive response of hemorphins have also been reported in mice (Davis, Gillespie, & Porreca, 1989). Chow and colleagues have also reported that intrathecal doses of angiotensin IV (Ang IV) and LVV-hemorphin-7 causes anti-hyperalgesia in rats (Chow et al., 2018). The proposed binding of hemorphins and canonical opioid receptor signaling is given in Figure 3.

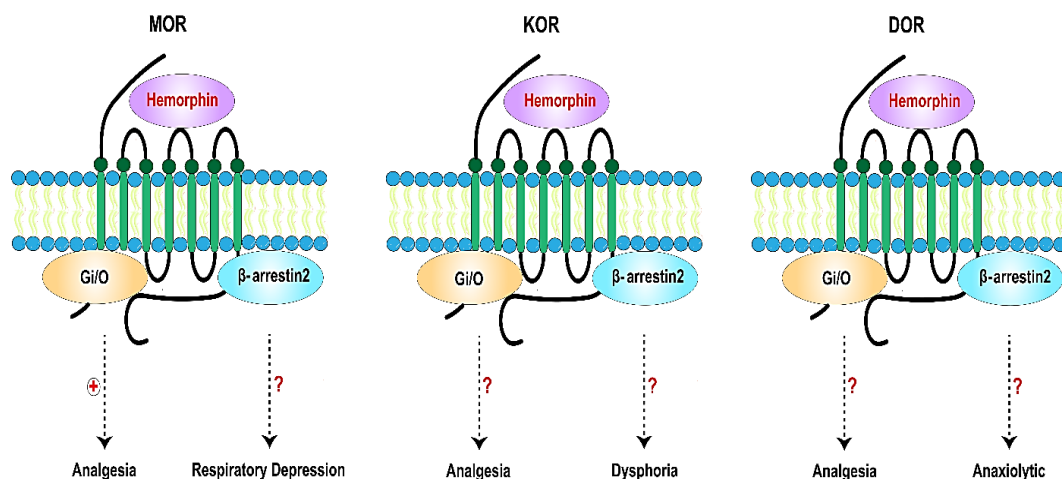


Figure 3: Proposed pharmacological action of hemorphin on different opioid receptors and its regulation of signaling pathways leading to analgesia. Analgesic effects of  $\mu$  opioid receptor (MOR),  $\kappa$  opioid receptor (KOR), and  $\delta$  opioid receptor (DOR) are mainly correlated with Gi-protein signaling. Hemorphins exhibit its pain killing effects by activating the MOR induced Gi-dependent signaling pathway. The pharmacological action of hemorphin on DOR and KOR are remain elusive. + represents activation and ? indicates that the mechanism is currently not known.

Hypertension is considered to be one of the most significant health problems that prevail globally. The mortality rate is highly dependent on its timely discovery and management. Worldwide, approximately 13.5% of total deaths are associated with hypertension (Lawes, Vander Hoorn, & Rodgers, 2008). Recent studies also suggest that hypertension affects approximately 972 million adults and this number is expected to further increase up to 1.56 billion by the year 2025 (Kearney et al., 2005). Hypertension is also considered to be one of the major risk factors for disorders related to the heart and contributes to over nine million deaths every year (Sawicka et al., 2011). The pathophysiology of hypertension is extremely complicated, and it involves various risk factors such as stress, smoking, and consumption of alcohol, elevated sodium, genetics, obesity and some environmental factors. Apart from these factors the activity of the renin-angiotensin system (RAS) has also been observed to play a well-known role in the pathogenesis of hypertension (Schütten, Houben, de Leeuw, & Stehouwer, 2017).

The zinc metallopeptidase angiotensin-I converting enzyme (ACE) is found in many tissues and biological fluids and is one of an important player in regulating RAS and kallikrein-kinin system (KKS). ACE causes hypertension by two mechanisms. Firstly, two amino acids are cleaved by ACE from the decapeptide angiotensin I for producing the octapeptide angiotensin II which is a relatively stronger vasoconstrictor. Secondly, ACE is associated with the degradation of bradykinin which is considered a potent vasodilator (Ondetti, Rubin, & Cushman, 1977; Priyanto et al., 2015). ACE is linked closely to hypertension and is an important target for discovering the anti-hypertensive drugs as a result of these effects. Captopril and lisinopril are widely prescribed ACE inhibitors, and currently,

these drugs are limited in their use because of well-documented side effects such as angioedema, kidney problems, cough and allergic reactions (Yu et al., 2018). In addition to that, increase in the incidence of cardiovascular diseases has led the search for safer and novel alternatives. Endogenous or biologically active peptides are a few of the alternatives that are being considered and explored due to their long-term regulation of tissue homeostasis, high bioavailability, and better safety profile (Iwaniak, Minkiewicz, & Darewicz, 2014; Wang, Chen, Fu, Li, & Wei, 2017).

It has been demonstrated that hemorphins have beneficial effects in the control of blood pressure. The observations also revealed that hemorphins can significantly reduce blood pressure in hypertensive rats (Cejka, Zelezna, Velek, Zicha, & Kunes, 2004). Additionally, it has been reported in various studies that anti-hypertensive effects are produced by hemorphins while inhibiting ACE, the key component of RAAS (Fruitier-Arnaudin, Cohen, Bordenave, Sannier, & Piot, 2002; Lantz, Glämsta, Talbäck, & Nyberg, 1991).

RAS in the brain is believed to be involved in processes other than homeostatic control. It has been associated with neuronal differentiation, nerve regeneration, learning and memory (Lee et al., 2004). Ang IV has been associated with various physiological functions, including the facilitation of memory (Albiston et al., 2004; Moeller et al., 1997). LVV-hemorphin-7 was recognized as an endogenous high-affinity ligand of the presumed angiotensin IV receptor (AT4R) (Moeller et al., 1997). Further studies characterize this putative receptor and indicated that this protein was analogous to IRAP, a type II integral membrane protein whose catalytic activity is inhibited by LVV-hemorphin-7 and Ang IV (Lee et al., 2004; Ye, Chai, Lew, & Albiston, 2007). *In vivo* and *in vitro* studies revealed



that LVV-hemorphin-7 could play a pivotal role in learning and memory. When an intracerebral administration of LVV-hemorphin-7 was carried out, it enhanced the spatial learning in rats and lessened the effects of scopolamine-induced learning deficits in spatial learning tests and fear conditioning (Albiston et al., 2004). LVV-hemorphin-7 has also been shown to modify the behavior of rats. Additionally, LVV-hemorphin-7, reduced depression and increased locomotion in rats. However, this depended on the activation of oxytocin receptors most likely due to changes in the oxytocinase activity of AT4R (Da Cruz et al., 2017). It was presumed that by inhibiting IRAP activity, LVV-hemorphin-7 protects the substrates of IRAP such as oxytocin and vasopressin. These substrates play a key role in memory and learning (Engelmann, Wotjak, Neumann, Ludwig, & Landgraf, 1996). *In vivo* microdialysis showed that LVV-hemorphin-7 improved spatial working memory without a significant increase in blood flow or hippocampal glucose uptake (De Bundel et al., 2009).

#### **1.2.4 Molecular mechanism of the interaction of hemorphins and their targets**

Several *in vitro* studies have shown the high stability of hemorphins, specifically LVV-hemorphin-7 in human plasma and tissue (Lantz et al., 1991; Sanderson, Nyberg, & Khalil, 1998). Furthermore, *in vivo* studies have demonstrated that peptidase enzyme present in extracellular fluid, especially amastatin-sensitive amino peptidase, cleaves hemorphin peptide (Nydahl, Pierson, Nyberg, Caprioli, & Andren, 2003). Nevertheless, LVV-hemorphin-7 has shown high stability in the blood for longer periods of time when incubated with numerous proteolytic enzymes. Notably, resistance of LVV-hemorphin-7 to proteolytic cleavage could be of major importance to its pharmacological and biological activities (John, Schulz, &

Forssmann, 2007; Sanderson et al., 1998). Hemorphins exist not only in blood, but also in numerous organs and brain regions, such as adrenal, hypothalamus and pituitary glands. Hemorphins have been reported to be involved in several cellular and molecular mechanisms and determining the complex molecular interactions is a challenging task. Based on previous reports, hemorphins have been revealed to interact with opioid, RAS, immune and neuroendocrine and immune systems (Figure 4).

Ligand-dependent biased signaling is an interesting concept in the field of GPCRs pharmacology where the same receptor could exhibit either Gi-dependent signaling pathway or  $\beta$ -arrestin-dependent signaling pathway based on the bound ligand.  $\mu$  opioid receptor (MOR) induced analgesia is correlated with Gi-dependent signaling whereas  $\beta$ -arrestin-dependent signaling is linked with different side effects such as constipation and respiratory. Hemorphins demonstrate their activities by activating the Gi-dependent signaling of MOR. Nevertheless, MOR  $\beta$ -arrestin-2 associated activity of hemorphins are still unknown. The putative action of hemorphins on KOR and DOR, however, remain elusive. Hemorphins may also produce selective agonism through the recruitment of  $\beta$ -arrestin-2 and internalization of receptors, and may produce anxiolytic and dysphoric activities via DOR and KOR, respectively.

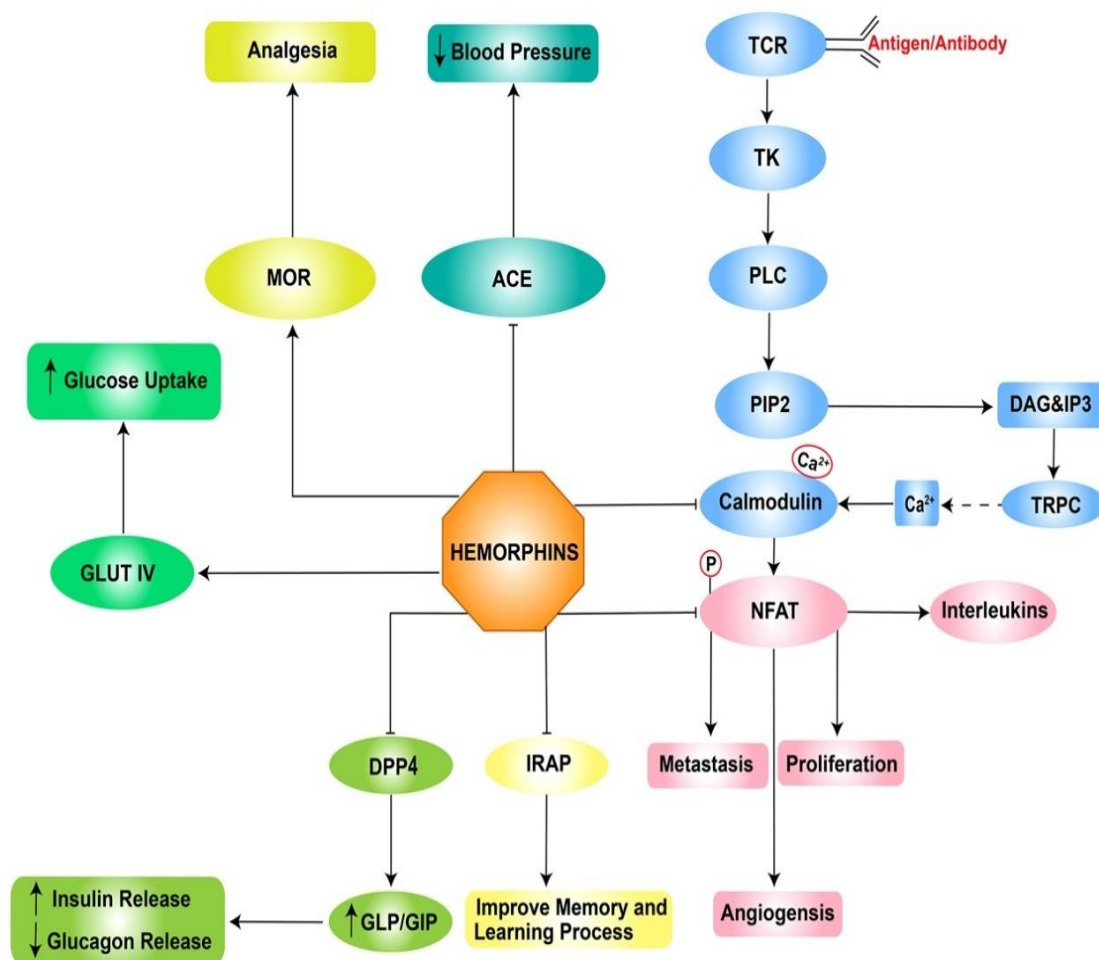


Figure 4: Therapeutic targets of hemorphins and the molecular mechanism of action. Blocked, dashed, and pointed, represent inhibition, release of ions, and activation of target, respectively.

### 1.3 Statement of the problem

Hemoglobin is one of the well-characterized and widely studied protein genetically, biochemically, and structurally. Studies have elucidated the structural and genetic variations amongst the mammalian hemoglobin. However, camel hemoglobin has not been greatly explored. Some physiological and biochemical studies have been performed on camel hemoglobin. However, very little is known from a structural perspective. Therefore, a comparative study principally focused on structural and genetics aspects of camel hemoglobin will provide insights into how

the camel hemoglobin behaves in varying conditions of osmolarity and temperature that it is normally susceptible to in contrast to human hemoglobin.

The co-factors ATP and 2,3-BPG are abundantly present in RBCs and are involved in the release of oxygen molecule during hypoxic and dehydrated conditions. Several studies on different mammals including humans have shown that ATP, and 2,3-BPG preferentially bind to  $\beta$  subunits of hemoglobin and helps in the unloading of oxygen molecules into tissues. Despite the inherent ability of camel to survive severe dehydrated conditions, the role of these energy molecules in camel hemoglobin have not been studied yet. Hence, it would benefit from a comparative investigation aimed at elucidating the molecular interactions of these molecules with camel and human hemoglobin under different stress conditions such as different conditions of temperature and salt concentrations in greater depth.

Several bioactive peptides are generally produced from proteolytic degradation of precursors proteins including hemoglobin. Numerous studies have identified the existence of several hemoglobin derived peptides such as hemorphins from different mammals including humans and these have been shown to diverse biological activities. However, functional and biological activities of camel hemoglobin derived peptides remain elusive. Thus, it is important to identify the genetic variations among these bioactive peptides in closely related mammals and determine the impact of small variation on the overall functioning of the therapeutic drug targets.

#### 1.4 Hypothesis and objectives

The physiological function of camel hemoglobin is not affected by sudden changes in osmolarity and temperature. This is an evolutionary advantage for dromedaries to endure the dehydration. The main hypothesis is that the extreme adaptive features of camel hemoglobin could be attributed to its primary as well as quaternary structures and its interaction with co-factors. The overarching aim of this study was to determine the structural and genetic variations of camel hemoglobin and to identify the activity of hemoglobin-derived biologically active peptides. This project adopted computational modeling and molecular approaches to investigate several aspects of camel hemoglobin to address these issues.

The objectives of this study are to:

- 1) Study the behavior of camel hemoglobin protein under a range of osmolarity and temperature variations using long time scale molecular dynamics (MD) simulations under different salt and temperature conditions.
- 2) Compare the binding of ATP and 2,3-BPG in camel and other mammalian hemoglobin structures using binding site analysis, molecular docking and MD simulations to identify any mechanistic differences in the action of these molecules.
- 3) Sequence and analyze  $\alpha$  and  $\beta$  hemoglobin genes to identify SNPs in camels belong to different breeds to identify SNPs that could potentially be correlated with oxygen affinity.

- 4) Identify the most likely binding pose of human or other mammals and camel LVV-hemorphin-7 with ACE, MOR and IRAP and to calculate the binding affinity using molecular docking and MD simulations.
  
- 5) Investigate the binding and activation of AT1R by human and camel LVV-hemorphin-7 by *in silico* approaches and in transfected human embryonic kidney (HEK293) cells using bioluminescence resonance energy transfer technology (BRET).

## **Chapter 2: Methods**

### **2.1 Ethical approval**

Ethical approval was obtained from United Arab Emirates University to collect blood samples. Ethical approval no: ERA\_2017\_5655, was granted on 24 January 2018.

### **2.2 Sample collection and storage condition**

10 ml of whole blood was taken from three different breeds of camels (50 Sudani, 50 Omani, 50 Mixed breeds, and 20 dairy) into vacuum collection tubes containing dipotassium EDTA (Ethylene Diamine Acetate) and transferred to the Department of Biology, United Arab Emirates University, for further analysis. In order to store them for longer period of time, all blood samples obtained in EDTA tubes were stored at  $-50^{\circ}\text{C}$  in the Molecular Biology Lab of the Department of Biology.

### **2.3 DNA extraction**

DNA was isolated from camel blood using Norgen blood DNA isolation kit (Norgen Biotek, Canada) following manufacturer's guidelines. Briefly, 20  $\mu\text{l}$  of proteinase K was added to the microcentrifuge tube and 200  $\mu\text{l}$  of camel blood was then added to the same tube. After that, 300  $\mu\text{l}$  of lysis buffer B was added to the tube containing blood and proteinase K, and was vortexed for 10 seconds. After mixing the reaction mixture, the centrifuge tubes were incubated for 10 minutes at  $55^{\circ}\text{C}$ . After incubation, tubes were briefly spun and 110  $\mu\text{l}$  of 96% ethanol was added to each tube containing the samples and mixed well by vortexing for 10 seconds. Next, binding columns were assembled on the collection tubes provided

with the kit. Reaction mixture from each tube was transferred to the column and centrifuged for 1 minute at approximately 8,000 rpm. Flowthrough was discarded and columns were reassembled again with the collection tube. After that, the column was washed with washing buffer provided with the kit in two steps by adding 500  $\mu$ l of washing buffer in each step and centrifuged for 1 minute at 8000 rpm. After each step of washing, the flowthrough was discarded and columns were assembled with new collection tubes. In order to dry the columns, the columns were centrifuged for 2 minutes at 14000 rpm and collection tubes were discarded. Next, the columns were placed into the elution tubes provided with the kit and approximately 200  $\mu$ l of elution buffer was added to each column. The elution tubes containing elution buffer and column were incubated at room temperature for 1 minute. After incubation, the elution tubes were centrifuged at 8000 rpm for 1 minute. After eluting the DNA, the quality and quantity of DNA was measured by loading 1  $\mu$ l of extracted DNA in NanoDrop 2000/c (Thermo Fisher Scientific, USA) which is a microvolume spectrophotometers. After that, the extracted DNA samples were stored at -20°C.

## **2.4 Primers**

The sequence of camel hemoglobin  $\alpha$  and  $\beta$  genes were retrieved from National Center for Biotechnology Information (NCBI) browser. Several overlapping primers were designed using Primer-Basic Local Alignment Search Tool (BLAST) to amplify the full genes of hemoglobin  $\alpha$  and  $\beta$ . Melting temperature and Guanine Cytocine (GC) content of each primer were also determined. Designed primers were purchased from Macrogen (Korea). The optimum conditions for the primers were then determined experimentally. The list of primers and their optimal conditions are given in Table 2.



Table 2: Primer sets used in PCR to amplify hemoglobin  $\alpha$  and  $\beta$  genes.

Forward (F) / Reverse (R)	Sequence (5' - 3')	Annealing Time (sec)	Annealing Temperature (°C)
F	GCACACTTCCGATCCTGACCTA	45	59
R	GCTTAACGGTATTTGGAGGTC		
F	CCCATCATGGTGCTGTCTTCC	37	57
R	CGGTATTTGGAGGTCAGCACG		
F	CTGGGCATAAAAGGAAGAGCAG	31	54
R	GCATAGGTGCCCTTGAGGTT		
F	GGTGCTAAACTCCTTTGGTG	38	59
R	GACAGAGGCCAGATGCTCAA		
F	CTCACATCAAGAGCAACCTC	36	54
R	GAGGTTGCTCTTGATGTGAG		
F	ACCTTCTTGCCATGGGCCTTG	38	59
R	CAAGGCCCATGGCAAGAAGGT		

## 2.5 PCR amplification and purification

In this study a premixed ready-to-use solution called the Go Taq® Green Master Mix (Promega, USA), was used. Go Taq® Green Master Mix comprises an optimal concentration of dNTPs, Taq DNA polymerase, MgCl<sub>2</sub> and reaction buffers. A total reaction volume of 50  $\mu$ l was prepared and used for each PCR run. For amplification of hemoglobin genes, 2  $\mu$ l of extracted DNA from each sample, 1.5  $\mu$ l of forward and reverse primers, 25  $\mu$ l of green master mix, and 20  $\mu$ l of deionize water were added to each PCR tube. The following reaction conditions were used in the Thermal Cycler: 1 cycle of pre-denaturation for 3 minutes at 95°C for 3 minutes, followed by 34 cycles of denaturation at 95°C for 30 seconds, annealing at specific temperature and time demonstrated in Table 3, and lastly final extension at 72°C for

one minute. After the amplification, amplified PCR products were visualized on 1.5% (w/v) agarose gel using electrophoresis. After visualization of PCR products, the amplified PCR products were purified using the Norgen PCR purification kit (Norgen Biotek, Canada) following the manufacturer's guidelines. For this purpose, the binding buffer provided in the kit was added in each PCR tube in 5:1 ratio to the PCR product. After the addition of binding buffer, the PCR tubes were briefly vortexed and pulse-spun. The mixture was then added into a column placed on the tube provided in the kit and centrifugation was performed for 1 minute at 8000 rpm. The flow-through was discarded and 500  $\mu$ l of washing buffer (96-100% ethanol) was added to the column and again centrifugated for 1 minute at 10,000 rpm. The flow-through was discarded again and the spun for 2 minutes at 14,000 rpm in order to dry the column. After that, the column was assembled with the 1.7 ml elution tube. In order to obtain high concentration of DNA, 10  $\mu$ l of elution buffer was added to the center of the column bed and kept standing at room temperature for 1 minute. After that, the column was centrifuged at 14, 000 rpm for 2 minutes. The last step of purification was repeated one more time. Finally, the quantity and quality of the purified amplified DNA was measured by loading 1  $\mu$ l of purified DNA in NanoDrop 2000/c (Thermo Fisher Scientific, USA) which is a microvolume spectrophotometer.

## **2.6 DNA sequencing and analysis**

Samples that fulfilled the quality and quantity required were sent for sequencing to Macrogen, (Korea). The sequences and chromatograms were provided by Macrogen which were then analyzed further. FinchTV chromatogram viewer version 1.4.0 (Geospiza) was used to visualize the chromatograms. BioEdit Sequence

Alignment Editor Version v7.0.5 (Tom Hall Ibis Therapeutics) as used to carry out sequence alignment. Reference sequences for hemoglobin  $\alpha$  (NCBI Accession: 105098415) and hemoglobin  $\beta$  genes (NCBI Accession: 105097953) were obtained from NCBI RefSeq database.

## **2.7 Multiple sequence alignment of hemoglobin $\beta$ protein**

NCBI protein database was used to obtain the hemoglobin  $\beta$  protein sequences of *Homo sapiens* (NP\_000509), *Camelus dromedarius* (XP\_010988890), *Equus caballus* (XP\_001504239), *Bos taurus* (NP\_776342), *Sus scrofa* (NP\_001138313), *Ovis aries* (NP\_001091117), *Pan troglodytes* (NC\_036890) and *Oryctolagus cuniculus* (NP\_001075729). Multiple sequence alignment of these sequences was carried out using ClustalW (Thompson, Higgins, & Gibson, 1994).

## **2.8 Generation of homology model**

In order to dock the hemorphin peptides to the human MOR, a homology model was developed using Schrödinger Prime. Briefly, a BLAST search of Protein Data Bank (PDB) was carried out to determine homologous protein structures. The X-ray crystallographic structure of the active MOR from *Mus musculus* (PDB ID: 5C1M) was used as the template, with an overall sequence identity of 72%, to produce three-dimensional homology model of the active human MOR (UniProt accession: P35372). Protein refinement modules of Schrödinger Prime were used to refine the loops and the structure was minimized and optimized.

## 2.9 Protein structure pre-processing

PDB was used to retrieve three dimensional structures of MOR (PDB ID: 5C1M), IRAP (PDB ID: 5MJ6), ACE (PDB ID: 2XY9), AT1R (PDB ID: 4ZUD), and hemoglobin (PDB ID: 3GDJ, 2HHB) (Akif et al., 2011; Fermi et al., 1984; H. Zhang et al., 2015a; H. Zhang et al., 2015b). Protein Preparation Wizard of Schrödinger Suite 2016-4 was used to pre-process the protein structure retrieved from PDB (Schrödinger, LLC, New York, NY). The preparation of protein involved a number of steps including the proper assignment of bond orders, adjustment of ionization states, orientation of disorientated groups, creation of disulphide bonds, removal of water molecules, metal and co-factors, capping of terminus amide, assignment of partial charges, and the addition of missing atoms and side chains. Hydrogen atoms were integrated and protonation state at pH 7 was used. In order to acquire a geometrically stable structure, optimization and minimization steps were carried out (Sastry, Adzhigirey, Day, Annabhimoju, & Sherman, 2013).

## 2.10 Ligand preparation

Two dimensional structures of 2,3 BPG and ATP were retrieved from PubChem. These two ligands were prepared and conformers were produced using Schrödinger Ligprep (Schrödinger, LLC, New York, NY). Briefly, preparation of ligands included conversion of 2D structures to 3D format, addition of hydrogen atoms, generation of tautomer and ionization states, neutralization of charged groups, structure filtration and finally geometry optimization of the molecule.

### **2.11 Active site identification and grid generation**

A receptor grid was created, by using default parameters, around the active site of the prepared protein. Van der Waal's scaling factor of 1 and a charge cutoff of 0.25 were used for this purpose. Lastly, a cubic search space was made which focused specifically on the centroid of the active site residues of the studied drug targets.

### **2.12 Peptide and ligand docking**

In order to predict the binding pose of hemorphins in MOR, IRAP, ACE and AT1R, as well as to measure the binding free energy, peptide docking was used. The Schrödinger Peptide Docking version 2016-4 was used to perform peptide docking with penalties for cis amide bonds (Schrödinger, LLC, New York, NY). All peptides were docked into active sites of the MOR, IRAP, ACE, and hemoglobin by using default parameters. Additionally, flexible ligand sampling was used to produce diverse ligand conformations by the ConfGen algorithm (Watts et al., 2010). The OPLS 2005 force field was used to describe the protein and peptide and post docking minimization was also executed in the gridded protein field. The GlideScore (GScore) scoring function was used to rank different poses (Friesner et al., 2006). Finally, the lowest GScore value of the top docked pose was reported for each peptide small ligands.

For predicting the binding pose, activity and affinity of 2,3-BPG and ATP molecules with camel and human hemoglobin, ligand docking was carried out. Grid based docking was performed using Schrödinger Glide version 2016-4 (Schrödinger, LLC, New York, NY). Standard precision (SP) docking was carried out first

followed by extra precision (XP) docking. To soften the potential of nonpolar parts of ligands, the scaling factor for the ligand van der Waals radii was set in 0.80 with a partial atomic charge of 0.15. In both SP and XP docking procedures, flexible ligand sampling was used to generate various ligand conformations. No constraints were used in the entire docking studies. Optimized Potentials for Liquid Simulations (OPLS) 2005 force field was used and post docking minimization was also carried out. Both 2,3-BPG and ATP were docked flexibly to camel and human hemoglobin structures.

### **2.13 Analysis of docking results and binding free energy calculation**

Schrödinger Maestro was used to visualize and interpret interactions such as hydrogen bond interactions,  $\pi$  interactions and hydrophobic interactions involving the top pose (Schrödinger, LLC, New York, NY). Binding free energy calculations were performed using molecular mechanics-generalized born surface area (MM-GBSA), in an implicit solvent model. These MM-GBSA based binding energies were estimated using the OPLS 2005 force field and Schrödinger Prime employing the VSGB 2.0 implicit solvent model (Li et al., 2011). For the purpose of MM-GBSA binding energy estimations, the receptor was treated rigidly and the peptide was minimized.

### **2.14 Molecular dynamics (MD) simulations**

MD simulations were carried out to determine the protein dynamics and interaction stability of the top binding pose of the LVVYPWTQRF, LVVYPWTRRF, YPWTQRF, YPWTRRF, 2,3-BPG, and ATP in the active site of appropriate target receptor as explicitly detailed in the results section of each chapter.

MD simulations of these ligand-protein complexes were carried out using Desmond employing the OPLS 2005 force field (Bowers et al., 2006).

#### **2.14.1 Simulation of membrane bound proteins**

Different systems of human and camel hemorphin peptides docked to MOR, and AT1R were prepared. Each of the peptide bound simulations were carried out with different initial velocities in triplicates for 100 ns and 500 ns, respectively. The complex structures of MOR and AT1R with hemorphin peptides were embedded into a pre-equilibrated DPPC membrane in an orthorhombic box. Each prepared system of hemorphin bound to MOR and AT1R were solvated using the single point charge (SPC) water model with a water box, and a buffer distance of 10 Å was maintained. In order to maintain a salt concentration of 0.15 mM NaCl, counterions and appropriate number of ions were incorporated. Prior to conducting MD simulations, each system was subjected to steepest descent minimization with Desmond's default protocol.

The default relaxation protocol for membrane proteins was used to initially relax the prepared systems. Eight stages of relaxation procedure encompassed minimization with constraint on solute heavy atoms, constraint free minimization, simulation with heating from 0 K to 300 K heating, H<sub>2</sub>O barrier and gradual constraining, simulation under constant number of particles, pressure and temperature NPT equilibration with H<sub>2</sub>O barrier with heavy atoms restrained, NPT equilibration of solvent and lipids, simulation in the presence of NPT ensemble with protein heavy atoms constraint decreased from 10.0 to 2.0 kcal/mol, NPT equilibration with C $\alpha$  atoms constrained at 2 kcal/mol, and simulation with no

constrains for 1.5 ns under the NPT ensemble. Finally, production simulation runs were carried out for 100 ns or 500 ns each system of MOR and AT1R, respectively.

The simulation runs were carried out under NPT ensemble using the Nose-Hoover thermostat to maintain a temperature of 300 K and isotropic Martyna-Tobias-Klein barostat to maintain the pressure at 1 atm (Martyna, Klein, & Tuckerman, 1992; Martyna, Tobias, & Klein, 1994). The short-range Coulombic interactions were investigated with a cut-off value of 9.0 Å using the short-range approach (Essmann et al., 1995). A time-reversible reference system propagator algorithm (RESPA) integrator was used with a time step of 2.0 fs (Tuckerman, Berne, & Martyna, 1992). For the purpose of analysis, the trajectories were saved at an interval of 100 ps. When simulation runs were finished, RMSD, RMSF, and protein-ligand contacts were evaluated.

#### **2.14.2 Simulation of non-membrane bound proteins**

Different systems of human and camel hemorphin peptides bound to ACE, and IRAP were prepared and each of the peptide bound simulations were carried out with different initial velocities in triplicates for 200 ns or 100 ns, respectively. Additionally, complex systems of 2,3-BPG and ATP with human and camel hemoglobin were prepared and simulated for 200 ns. Briefly, each complex system was solvated in an orthorhombic box by using the SPC water model, and a buffer distance of 10 Å was maintained (Schrödinger, LLC, New York, NY). In order to maintain a salt concentration of 0.15 mM NaCl, counterions and appropriate number of ions were incorporated. Prior to conducting MD simulations, each system was subjected to steepest descent minimization with Desmond's default protocol. The



simulation runs were carried out under NPT ensemble using the Nose-Hoover thermostat to maintain a steady temperature of 300 K and isotropic Martyna-Tobias-Klein barostat to sustain the pressure at 1 atm (Martyna et al., 1992; Martyna et al., 1994). The short-range Coulombic interactions were investigated with a cut-off value of 9.0 Å using the short-range approach (Essmann et al., 1995). A time-reversible reference system propagator algorithm (RESPA) integrator was used with a time step of 2.0 fs (Tuckerman et al., 1992). For the purpose of analysis, the trajectories were saved at an interval of 100 ps. Lastly, root mean square deviation (RMSD), root mean square fluctuation (RMSF), and protein-ligand contacts of each complex system was determined from the trajectories.

### **2.15 *In vitro* ACE inhibition assay**

The inhibition of ACE was assessed using the ACE Kit WST (Dojindo Laboratories, Mashiki-machi, Japan). Custom synthesized hemorphin peptides (LVVYPWTQRF, LVVYPWTRRF, YPWTQRF, and YPWTRRF) were purchased from New England Peptide (Gardner, MA, USA). Manufacturer's instructions were followed for preparing the indicator working solution and enzyme working solution. From each hemorphin peptide, 10 µl of each dose was added to the wells of a 96-well microplate. While, in blank 1 and blank 2, 20 µl and 40 µl of deionized water were added, respectively. A volume of 20 µl of the substrate buffer was added to each well. Next, 20 µl of enzyme working solution was added in all of the sample wells and blank 1. The plate was then immediately incubated at 37°C for 1 h. After 1 h of incubation, 200 µl of indicator working solution was added to each well and then incubated for 5 min at room temperature. After 5 min of room temperature incubation, plate absorbance was determined at 450 nm using Glomax Discover

Microplate Reader (Promega, Madison, WI, USA). Finally, the ACE inhibitory activity was computed using the following equation: Inhibition rate (%) =  $(A_{\text{blank1}} - A_{\text{sample}}) / (A_{\text{blank1}} - A_{\text{blank2}}) \times 100$ . From the obtained ACE inhibitory data,  $IC_{50}$  was measured using Prism 7 (GraphPad, San Diego, CA, USA) from a non-linear regression plot of ACE inhibition (%) against peptide concentration ( $\mu\text{M}$ ).

## 2.16 cDNA constructs and ligands

The human protein-coding plasmids, AT1R-RlucII, yPET- $\beta$ -arrestin 2, and Venus-G $\alpha$ q for the brief expression in HEK293 cells were generously provided by Dr Stéphane Laporte (McGill University, Montréal, QC, Canada), Dr Mark Scott (Cochin Institute, Paris, France), and Dr Nevin Lambert (Augusta University, GA, USA), respectively. Irbesartan and AngII (Sigma, St. Louis, MO, USA) and LVV-hemorphin-7 (LVVYPWTQRF) (New England Peptide, Gardner, MA, USA) were used as ligands in this study.

## 2.17 Cell culture and transfection

HEK293 cells were kept at 37°C, 5% CO<sub>2</sub> in complete medium (Dulbecco modified Eagle medium (DMEM) containing 100 IU/ml of penicillin, 100  $\mu\text{g/ml}$  of streptomycin, and 0.3 mg/ml of glutamine), complemented with 10% fetal calf serum (GIBCO BRL, Carlsbad, CA, USA). For bioluminescence resonance energy transfer (BRET) measurements, brief transfections were performed in 96-well plates. However, IP1 experiments were carried out in six-well plates using lipofectamine 2000 (Invitrogen). Precisely, for BRET experiments, in each 96-well plate, 50 ng of either Venus-G $\alpha$ q or yPET- $\beta$ -arrestin 2 was mixed with 25 ng of AT1R-Rluc in 25  $\mu\text{l}$  of serum-free DMEM and kept at room temperature for 5 min. Next, 25  $\mu\text{l}$  of

serum-free DMEM containing 0.5  $\mu$ l of Lipofectamine 2000 was added in the plasmid solution and kept at room temperature for 20 min. Finally, 96 well plates were seeded with cells ( $10^5$  in 150  $\mu$ l/well) resuspended in DMEM complemented with 10% fetal calf serum (FCS) were then kept with the final DNA-Lipofectamine 2000 mix (50  $\mu$ l/well). All experiments were performed after 48 h transfection.

### **2.18 Dose–response BRET assay**

For dose-response assays, BRET technology was used as mentioned earlier (Ayoub et al., 2015). Briefly, cells were initially washed with 50  $\mu$ l/well of phosphate-buffered saline (PBS) and challenged at 37°C for 30 min with 40  $\mu$ L of PBS containing or not (vehicle) the designated doses of either LVV-hemorphin-7, AngII (control), or AngII in the presence of the specified doses of LVV–hemorphin-7. Immediately after treatment, 10  $\mu$ l of coelenterazine h (Promega) in PBS was incorporated to a final concentration of 5  $\mu$ M, and BRET signals were measured using the Tristar 2 multilabel plate reader (Berthold, Germany), permitting sequential measurements of light emission at 480 and 540 nm. While, for the antagonist assays using irbesartan, cells were initially incubated with 30  $\mu$ l of irbesartan (10  $\mu$ M) at 37°C for 15 min before their stimulation with 10  $\mu$ l of LVV–hemorphin-7 (10  $\mu$ M) followed by the activation with 10  $\mu$ l of AngII (10 nM) at 37°C for 30 min, and BRET measurements were carried out as mentioned above.

### **2.19 Real-time BRET kinetic assay**

Several protocols were adopted for the real-time BRET kinetics. For this, cells were initially washed with 50  $\mu$ l/well of PBS and resuspended in 40  $\mu$ l/well of PBS having coelenterazine h (5  $\mu$ M), and BRET signals were determined in real time

for approximately 5 min to estimate the baseline. While, in the direct protocol, 10  $\mu$ l/well of PBS with or not (vehicle) either 10  $\mu$ M of LVV-hemorphin-7, 10 nM of AngII (control), or both, was added, after the baseline, and BRET reading were measured for 50 min. However, for sequential protocol, after the baseline, BRET readings were measured in real time upon two sequential treatments (T1 and then T2). This comprises of 10  $\mu$ l/well of PBS with or not (vehicle) 10  $\mu$ M of LVV-hemorphin-7 (T1) and BRET signals were measured for 10 min. Immediately after that, 10  $\mu$ l/well of PBS with or not (vehicle) 10 nM of AngII were added and BRET signal were again measured for 25 min. Finally, the BRET measurements were also performed in opposite order (10 nM of AngII followed by 10  $\mu$ M of LVV-hemorphin-7) as discussed in results section of Chapter 5.

## **2.20 IP1 accumulation assay**

Analysis of IP1 accumulation was carried out in HEK293 cells briefly co-expressing either AT1R-Rluc with Venus-G $\alpha$ q similar to previous BRET experiments or only untagged AT1R (AT1R-WT) with the help of IP-One Tb kit (Cisbio Bioassays, France) as per manufacturer's instructions. For this set of experiments, cells were initially incubated or not (control) with 10  $\mu$ M of LVV-hemorphin-7 at 37°C for 15 min before activated or not (vehicle) with the different doses of AngII at 37°C for 30 min. After that, cells were lysed by using the available assay reagents, and the assay was kept at room temperature for 1 h. Finally, fluorescence emission was determined after excitation at 340 nm, at 620 nm and 665 nm, for 50  $\mu$ s using the Tristar 2 multilabel plate reader (Berthold, Germany).

## 2.21 Data presentation and statistical analysis

The data obtained from BRET experiments are given as the ratio of light emission at 540 nm over 480 nm was initially transformed into “ligand-induced BRET” signals by deducting the ratio obtained from vehicle-treated cells from the same ratio obtained from AngII/LVV-hemorphin-7-treated cells. Next, for BRET and IP1 experiments, % responses were obtained by taking the maximal AngII-induced signal as 100% in the control condition in different assays. Additionally, the kinetic and the sigmoidal dose-response curves were adjusted to appropriate nonlinear regression equations using GraphPad Prism software (San Diego, CA, USA). The data being measured was demonstrated as mean  $\pm$  SEM (Standard Error of the Mean). As appropriate, one- way or two-way analysis of variance (ANOVA) was carried out and Tukey multiple-comparisons test or Sidak’s multiple-comparisons test was used to compare means for determining the degree of significance between the different treatments statistically.

## **Chapter 3: Insights into the Interaction of Hemorphin and its Targets**

### **3.1 Results**

Extensive computational approaches were employed to investigate the binding mode and binding stability of hemorphin peptides with MOR and IRAP.

#### **3.1.1 Multiple sequence alignment of hemoglobin $\beta$ protein sequences**

The reference sequence of  $\beta$  hemoglobin (HBB) proteins of closely related mammals were obtained from NCBI Protein database. Multiple sequence alignment was carried out using ClustalW to identify the similarities and differences in HBB protein sequences (Clustal, Thompson, Higgins, & Gibson, 1994). LVV-hemorphin-7 is a 10 amino acids long peptide, and its sequence is highly conserved among mammals. It ranges from amino acid positions 32 to 41 in the HBB protein sequence in human, chimpanzee, camel, pig, and rabbit. In the bovine and sheep protein, it lies between amino acids positions 30 to 39, and in the horse, the LVV-hemorphin-7 is positioned between amino acids 31 to 40. The multiple sequence alignment results indicated a single amino acid substitution in the camel HBB protein at position 40, where glutamine has been substituted with arginine (Q > R). The remaining residues in this region are identical (Figure 5).

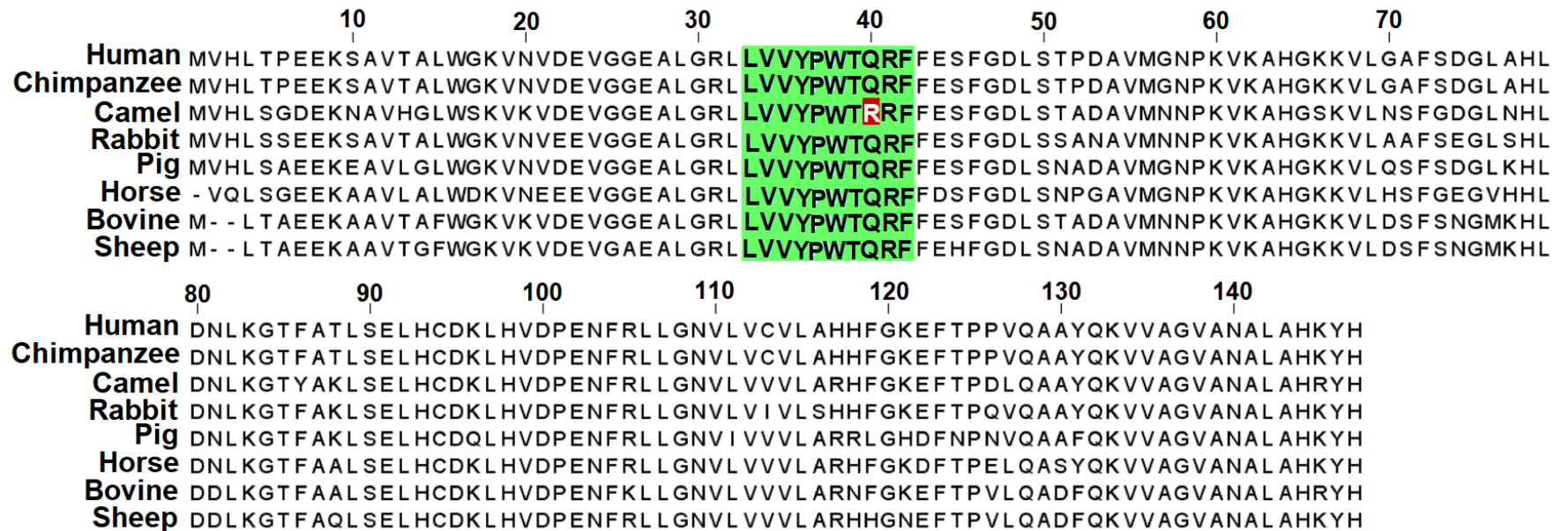


Figure 5: Sequence alignment of hemoglobin  $\beta$  protein sequences of closely related mammals - *Homo sapiens* (human), *Pan troglodytes* (chimpanzee), *Camelus dromedarius* (camel), *Oryctolagus cuniculus* (rabbit), *Sus scrofa* (wild pig), *Equus caballus* (horse), *Bos taurus* (bovine), and *Ovis aries* (sheep). Multiple sequence alignment showed a variation in camel hemoglobin at position 40, where glutamine was changed to arginine. The hemorphin region of hemoglobin  $\beta$  protein is shown in green color and substituted residue is represented with red color.

### 3.1.2 Structure-based homology modeling of $\mu$ -type opioid receptor

The X-ray crystallographic structure of MOR from *Mus musculus* (PDB ID: 5C1M) was used as a template to generate the three-dimensional (3D) homology model of the active state of the human  $\mu$ -type opioid receptor (MOR) (UniProt accession: P35372) (Figure 7). The generated structural model of the active MOR's active conformation is similar to the conserved seven-transmembrane topology of G protein-coupled receptors (GPCRs). Additionally, the Ramachandran plot indicated that the produced model's general stereochemical quality was good with nearly all the residues are in the permissible and favorable regions (Figure 6).

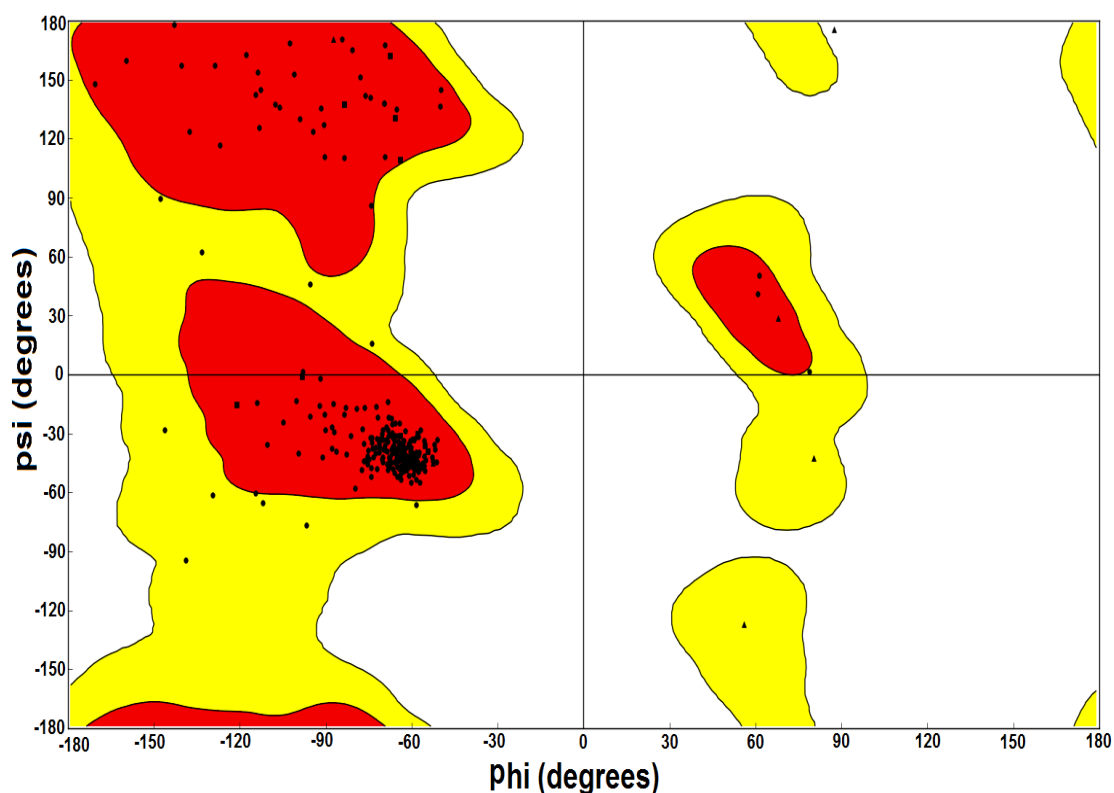


Figure 6: Ramachandran plot of the human mu opioid receptor model.



### 3.1.3 Molecular docking

The binding mode of both non-camel (LVVYPWTQRF) and camel (LVVYPWTRRF) LVV-hemorphin-7 peptides was determined through extensive docking and free energy calculations. For each binding mode the binding free energies were calculated with the help of molecular mechanics generalized Born and surface area (MM-GBSA) method.

### 3.1.4 $\mu$ -opioid receptor

The docking of both LVVYPWTRRF and LVVYPWTQRF peptides with MOR produced 10 models each. The top five docked poses of LVVYPWTQRF peptide produced the GScore of -10.88 kcal/mol, -10.61 kcal/mol, -10.23 kcal/mol, -9.83 kcal/mol, -9.35 kcal/mol and the calculated MM-GBSA binding free energies corresponding to these poses were -97.82 kcal/mol, -94.38 kcal/mol, -91.86 kcal/mol, -87.91 kcal/mol, and -84.79 kcal/mol, respectively. The top five docked poses of LVVYPWTRRF peptide produced the GScore of -10.65 kcal/mol, -10.53 kcal/mol, -10.35 kcal/mol, -10.23 kcal/mol, -9.96 kcal/mol and the calculated MM-GBSA binding free energies corresponding to these poses were -108.35 kcal/mol, -115.07 kcal/mol, -101.61 kcal/mol, -94.73 kcal/mol, and -91.89 kcal/mol, respectively. The list of interacting residues of the best pose of each peptide along with their respective Gscore and MM-GBSA binding free energy are provided in Table 3. The top-docked conformation of LVVYPWTQRF peptide demonstrated that the residues of the N-terminal of the peptide formed interactions with residues in transmembrane helices 5 and 6 (TM5 and TM6) present at the bottom of the binding site. The N-terminal residues (Leu1-Val2-Val3) of LVVYPWTQRF formed multiple hydrophobic

interactions with TM6 residues Ile298, Tyr301, Val302, Ala306, and Val308. A hydrogen bond was formed between Leu1 and the backbone amino group of the hydrophilic Asn232 located on TM5. Tyr4 of the peptide produced interactions with Asp149 via a hydrogen bond and, along with Pro5, it exhibited hydrophobic interactions with Ile146 and Tyr150 located on TM3. However, Pro5, Trp6, and Thr7 residues of LVVYPWTQRF formed interactions with Arg213, Ile217, Cys219, Thr220, and Leu221 on the  $\beta$  sheet. The C-terminal residues (Thr7-Gln8-Arg9-Phe10) of LVVYPWTQRF peptide formed hydrophobic interactions with Trp320, His321, Ile324, and Tyr328 on TM7. His321 located on TM7 formed a  $\pi$ - $\pi$  stacking with Trp6 and a hydrogen bond with Gln8. Additionally, Gln8 also produced hydrogen bonds with the side chain of the Glu312 situated on the third extracellular loop and with Lys305 on TM5 (Figure 8A and Figure 9).

Table 3: Interacting residues of the best pose of non-camel (LVVYPWTQRF) and camel (LVVYPWTRRF) hemorphin with MOR, and IRAP.

<b>Protein</b>	<b>Peptide</b>	<b>Glide docking score - GScore (kcal/mol)</b>	<b>MM-GBSA (kcal/mol)</b>	<b>Residues forming hydrogen bonds</b>	<b>Residues forming hydrophobic interactions</b>	<b>Residues forming <math>\pi</math>-<math>\pi</math> stacking</b>
MOR	LVVYPWTQRF	-10.88	-97.82	Gln126, Asn129, Leu131, Asp149, Asn232, Lys305, Glu312, His321	Leu58, Pro61, Pro65, Tyr77, Tyr130, Met132, Ile146, Tyr150, Ile217, Cys219, Leu221, Trp228, Ile298, Tyr301, Val302, Ala306, Val308, Trp320, Ile324, Tyr328	His321
MOR	LVVYPWTRRF	-10.53	-115.08	Asp149, Lys211, Tyr212, Glu231, Lys305, Ala306, Glu312	Ile146, Tyr150, Cys219, Leu221, Phe223, Trp228, Leu234, Ile236, Val238, Ile298, Val302, Ile303, Leu307, Val308, Trp320, Ile324, Tyr328	

Table 3: Interacting residues of the best pose of non-camel (LVVYPWTQRF) and camel (LVVYPWTRRF) hemorphin with MOR, and IRAP (Continued).

<b>Protein</b>	<b>Peptide</b>	<b>Glide docking score - GScore (kcal/mol)</b>	<b>MM-GBSA (kcal/mol)</b>	<b>Residues forming hydrogen bonds</b>	<b>Residues forming hydrophobic interactions</b>	<b>Residues forming <math>\pi</math>-<math>\pi</math> stacking</b>
IRAP	LVVYPWTQRF	-14.857	-148.038	Gly428, Glu441, Lys460, Glu509, Asp510, Glu541, Glu818, Glu825, Glu895	Tyr272, Pro296, Ala427, Ala429, Met430, Ala453, Leu457, Ile461, Tyr495, Ala514, Phe544, Tyr549, Phe550, Ala763, Leu769, Ala822, Phe826, Tyr961	
IRAP	LVVYPWTRRF	-13.653	-163.028	Gly428, Glu441, Asp510, Glu541, Glu818, Glu825, Glu895	Tyr272, Pro296, Ala427, Ala429, Met430, Ala453, Leu457, Ile461, Leu469, Tyr495, Ala514, Phe544, Tyr549, Phe550, Ala822, Phe826, Pro957, Tyr961	

The top pose of LVVYPWTRRF peptide exhibited a GScore of  $-10.53$  kcal/mol and MM-GBSA binding energy of  $-115.08$  kcal/mol (Table 1). Leu1, Val2, and Val3 residues of LVVYPWTRRF formed interactions with residues located on TM5 (Glu231 and Ile236) and TM6 (Val302, Ile303, and Leu307). As compared to LVVYPWTQRF, the Pro5 and Trp6 residues produced hydrogen bonds with Tyr212 and Lys211, respectively, as well as showed hydrophobic interactions with the  $\beta$ -sheet residues. However, the C-terminal residues of LVVYPWTRRF peptide showed interactions with residues situated on TM3, TM5 and TM7. A hydrogen bond was formed between Arg9 and Asp149 on TM3, while the substituted arginine at position 8 exhibited a hydrogen bond with the side chain of Glu312 located on the third extracellular loop. Moreover, Val3, Tyr4 and Thr7 formed hydrogen bonds with Glu231 (Figure 8B). A list of hydrophobic interactions that were observed between LVVYPWTRRF and MOR are shown in Figure 10.

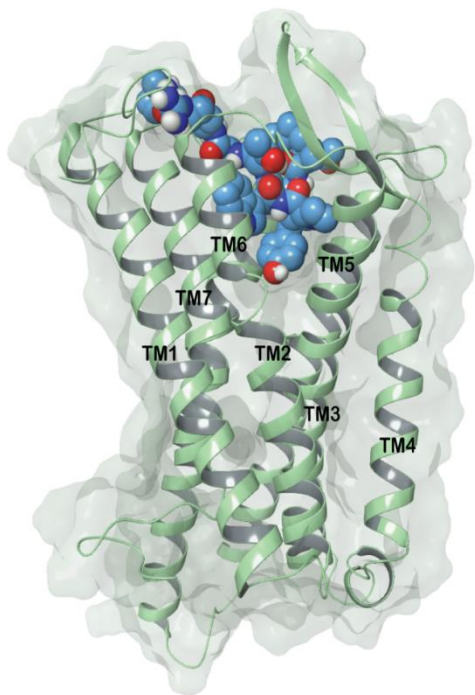
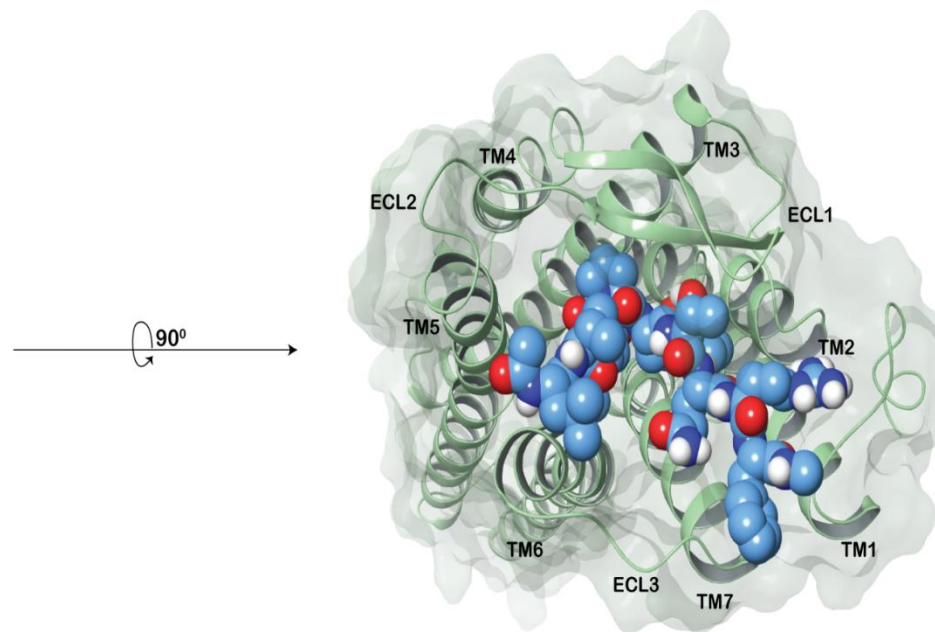
**A****B**

Figure 7: 3D structure of modeled active human MOR. (A) Side view of the binding pocket of MOR; (B) Top view of the binding pocket of MOR. The MOR protein is shown with a sea green cartoon representation.

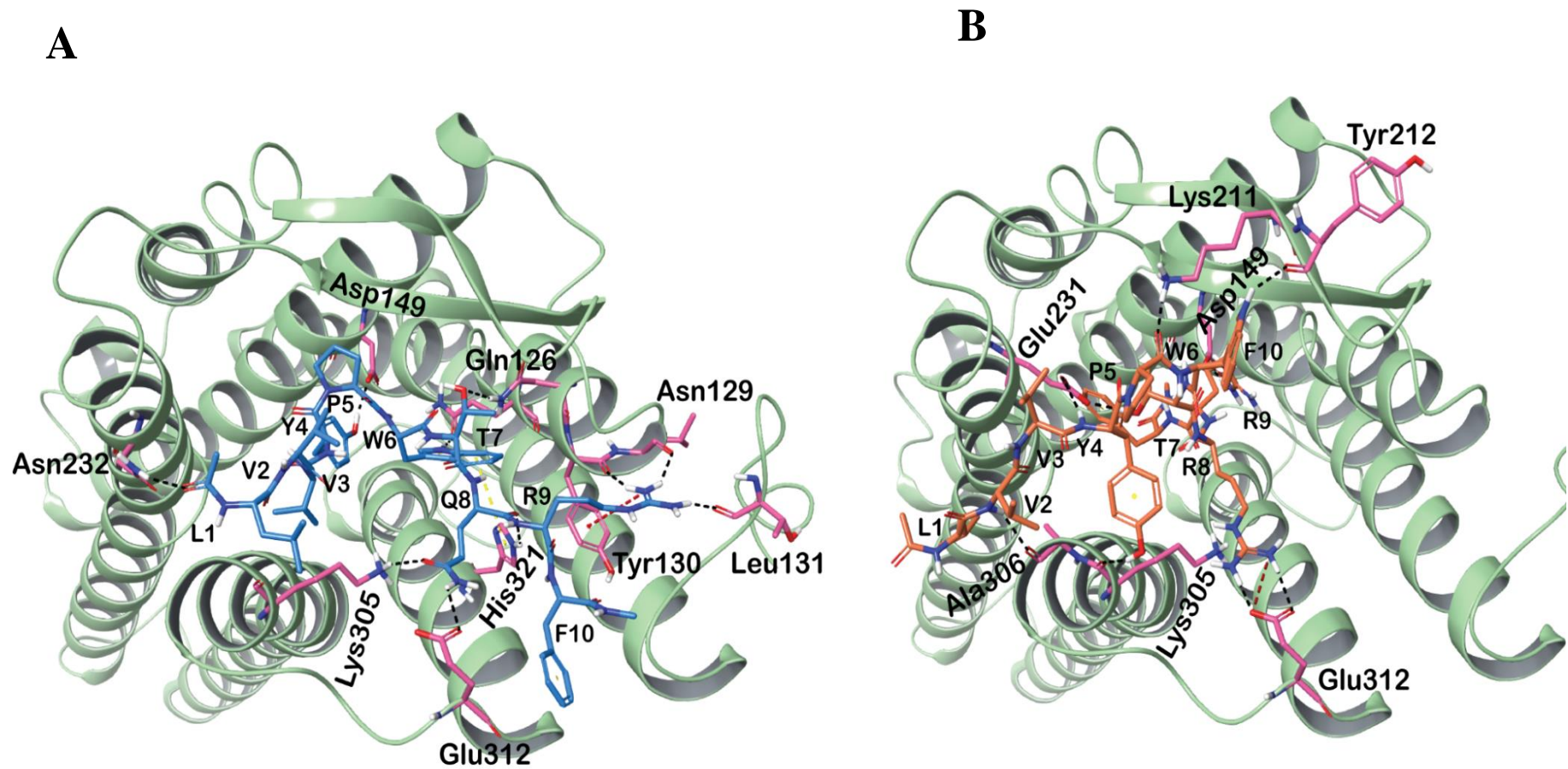


Figure 8: Interactions of hemorphin peptides with MOR. (A) LVVYPWTQRF (non-camel hemorphin) docked in the binding pocket of MOR. (B) LVVYPWTRRF (camel hemorphin) docked in the binding pocket of MOR. The MOR protein is shown with a sea green cartoon representation. Hydrogen bonds are represented by black dotted lines and cation- $\pi$  interactions are represented by red dotted lines.

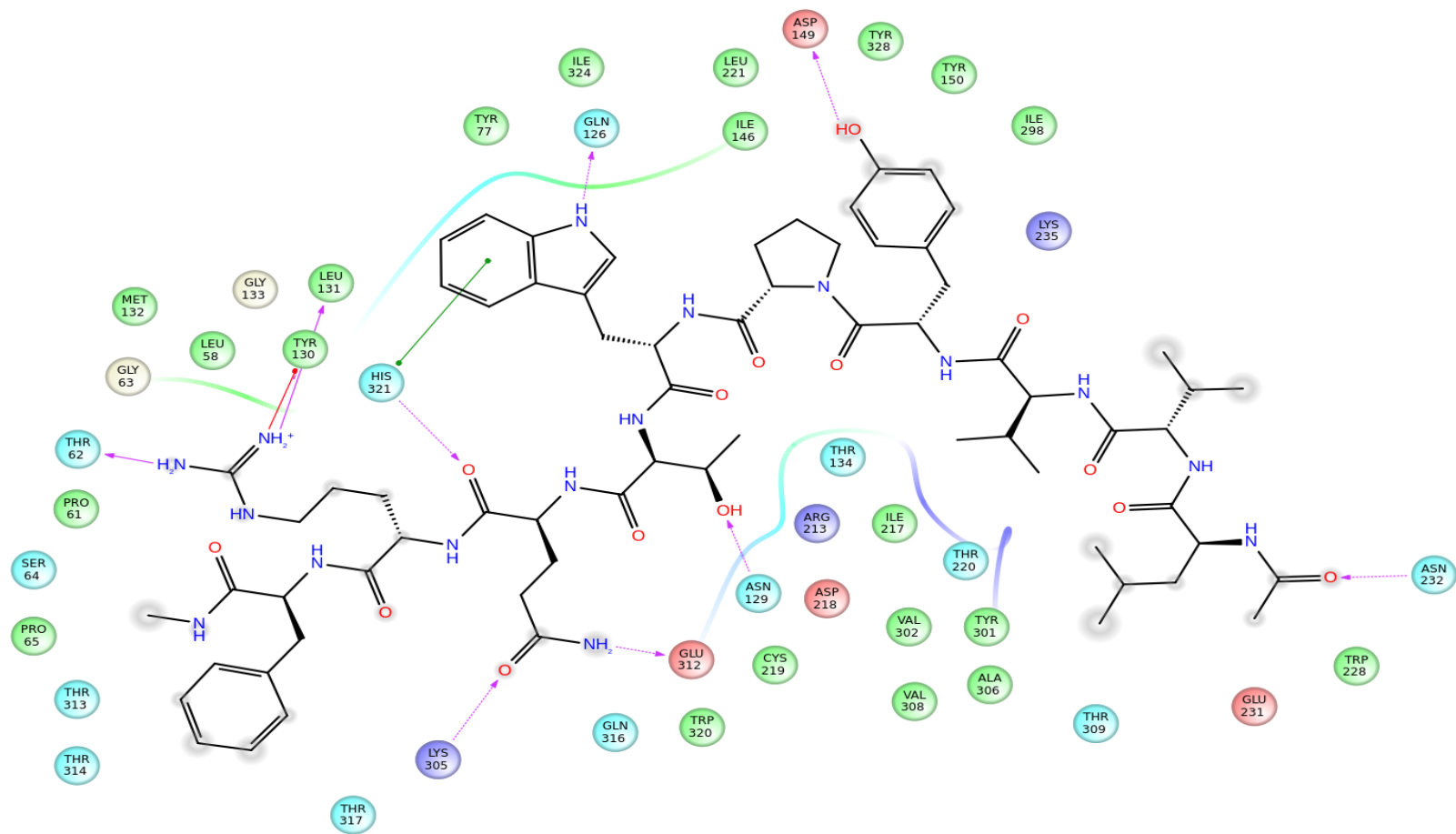


Figure 9: Interactions of non-camel LVV-hemorphin-7 residues with mu-opioid receptor.



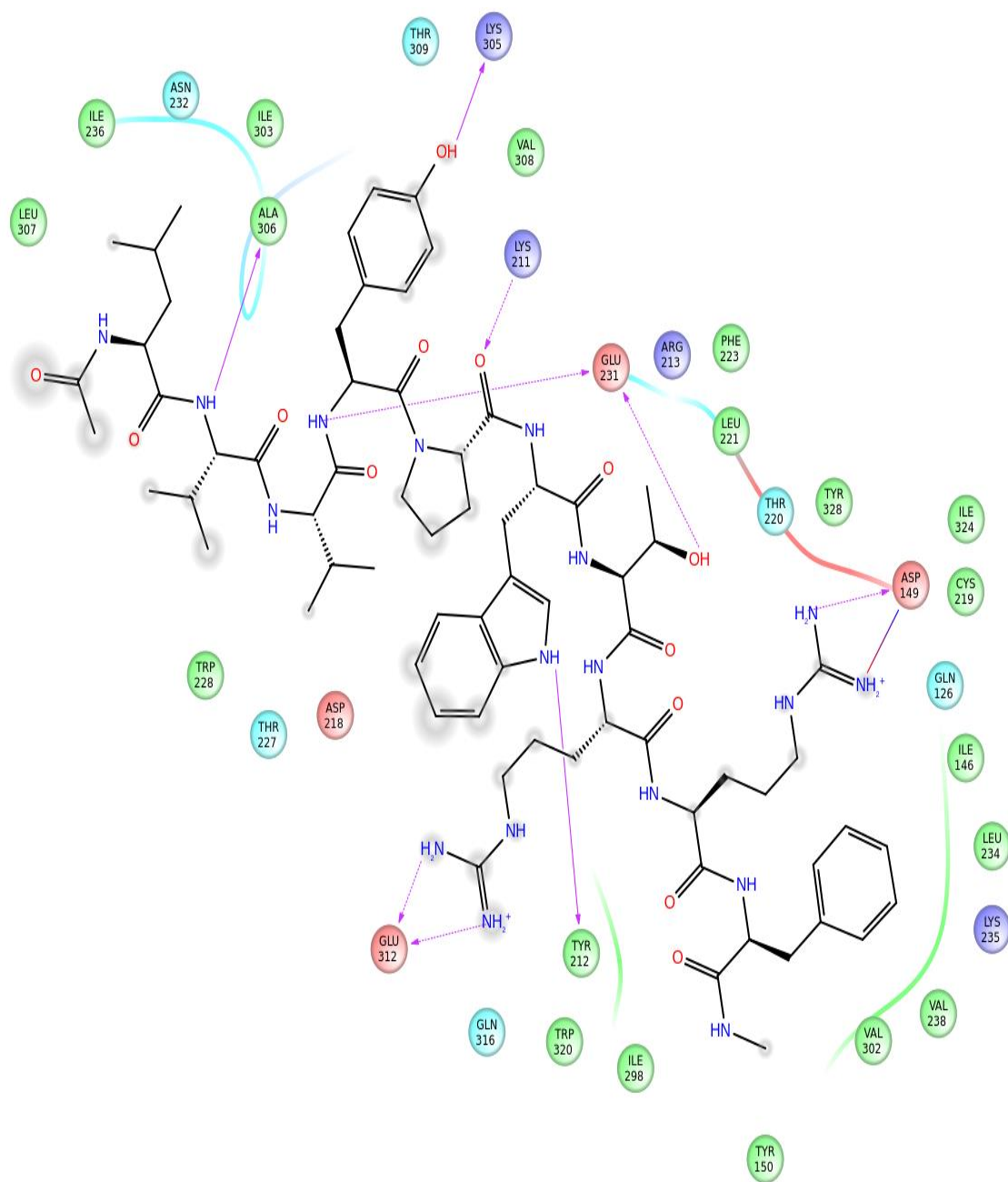


Figure 10: Interactions of camel LVV-hemorphin-7 residues with mu-opioid receptor.

### 3.1.5 Insulin-regulated aminopeptidase

Binding free energy calculations were performed for the different docking conformations of LVVYPWTQRF and LVVYPWTRRF peptides. The top five docked poses of LVVYPWTQRF peptide exhibited the GScore of -14.86 kcal/mol, -13.91 kcal/mol, -13.33 kcal/mol, -12.73 kcal/mol, and -12.45 kcal/mol and the calculated MM-GBSA binding free energies corresponding to these poses were -148.04 kcal/mol, -129.41 kcal/mol, -122.81 kcal/mol, -119.71 kcal/mol, and -114.88 kcal/mol, respectively. The top five docked poses of LVVYPWTRRF peptide generated the GScore of -13.65 kcal/mol, -13.41 kcal/mol, -13.19 kcal/mol, -12.81 kcal/mol, -12.53 kcal/mol and the calculated MM-GBSA binding free energies corresponding to these poses were -163.03 kcal/mol, -151.21 kcal/mol, -137.29 kcal/mol, -129.91 kcal/mol, and -119.44 kcal/mol, respectively. The list of interacting residues of the best pose of each peptide along with their respective Gscore and MM-GBSA binding free energy are provided in Table 3. The N-terminal of LVVYPWTQRF and LVVYPWTRRF peptides occupied the S1 pocket, which is adjacent to the binding pocket. Figure 12A displays the binding mode for LVVYPWTQRF. In the reported binding mode, the N-terminal residues (Leu1, Val2, and Val3) of LVVYPWTQRF occupied the S1 pocket and showed hydrogen bonds with Leu541, Tyr549, and Gly428. These three N-terminal residues produced hydrophobic interactions with residues in the S1 pocket - Tyr272, Pro296, Phe425, Ala427, Ala429, Met430, Phe544, and Tyr961. Hydrogen bonds were formed between aromatic residues Tyr4 and Trp6 of LVVYPWTQRF and Glu441 and Lys460, respectively. They also interacted hydrophobically with Ala453, Leu457, Ile461, Tyr495, Ala514, and Phe550. Gln8, Arg9, and Phe10 interacted

hydrophobically with Ala763, Leu769, Phe770, Ala822, and Phe826. Thr7 exhibited a hydrogen bond with Asp510, Gln8 showed hydrogen bonds with Glu509, and Glu818 and Arg9 formed hydrogen bonds with the side chain of residues Glu825 and Glu895 (Figures 12A, and 13). The interacting residues and binding scores are shown in Table 3.

LVVYPWTRRF demonstrated a similar binding mode with the N-terminal stabilized in the S1 pocket. The N-terminal residues (Leu1, Val2, and Val3) bound in the S1 pocket and formed interactions hydrophobically with Tyr272, Pro296, Ala427, Ala429, Met430, Phe544, Tyr549, Pro957, and Tyr961. Importantly, Val2 residue formed a hydrogen bond with the amino group of Gly428 of the GAMEN loop (Gly428-Ala429-Met430-Glu431-Asn432). Tyr4, Pro5, and Trp6 residues of LVVYPWTRRF peptide formed hydrophobic interactions with the active site residues Leu457, Ile461, Tyr495, Ala514, and Phe550 and Trp6 produced a hydrogen bond with Lys460. Arg8 formed hydrogen bonds with the side chain of Glu825 and Glu895. However, Arg9 produced hydrogen bonds with Asp510 and Glu818. The last three residues of C-terminal also formed hydrophobic interactions with Leu769, Ala822, and Phe826 (Figures 12B and 14).

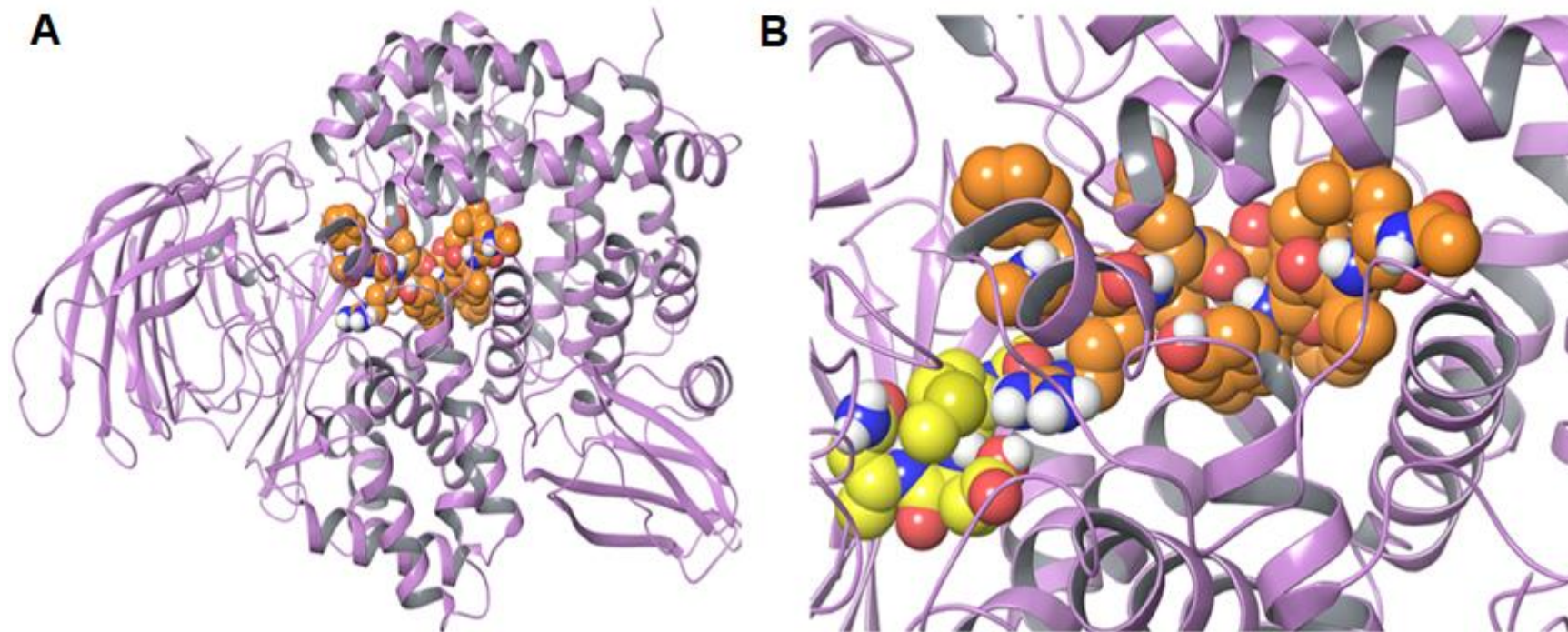


Figure 11: 3D structure of IRAP. (A) The active site of IRAP; (B) The enlarged view of the active site of IRAP in A. The hemorphin peptide bound in the active site is shown in orange CPK representation, while GAMEN motif is shown in yellow CPK representation. The IRAP protein is shown with a purple cartoon representation.

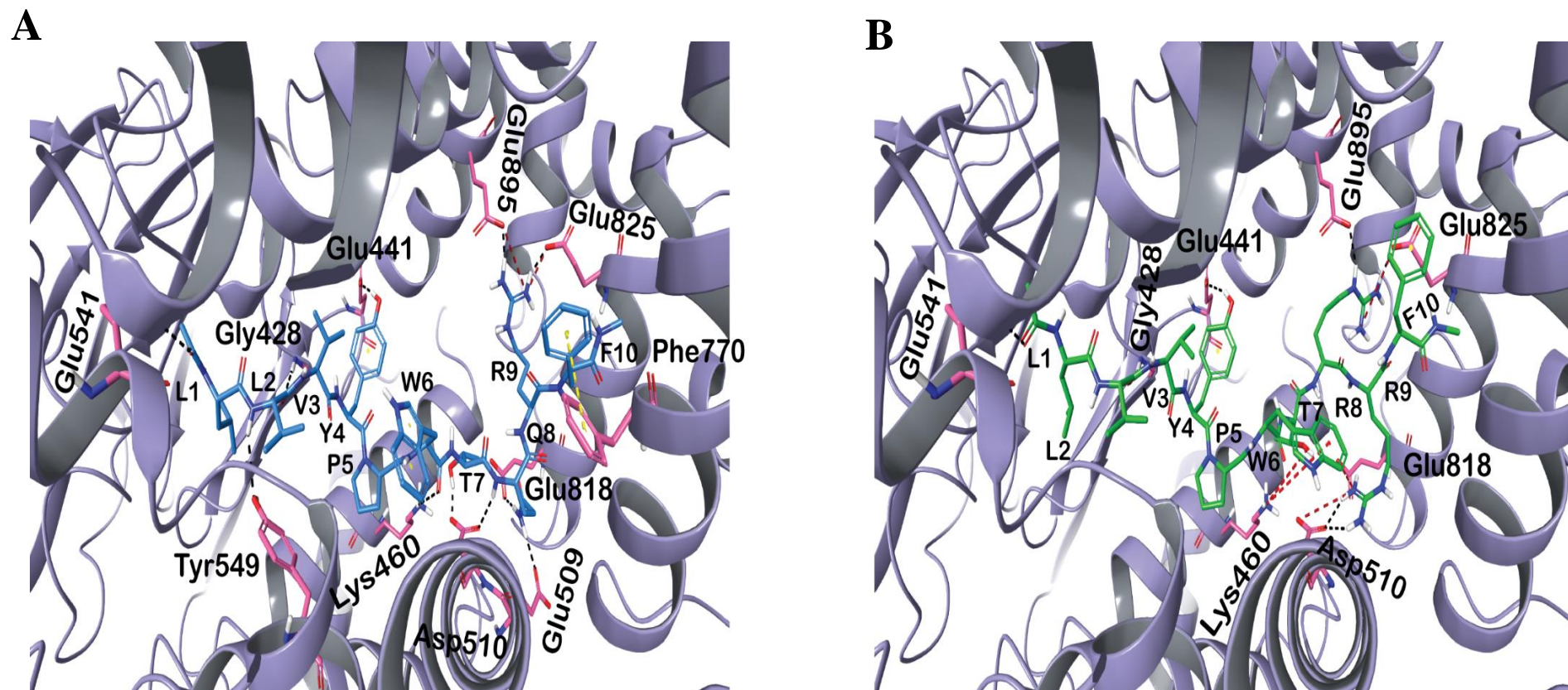


Figure 12: Interactions of hemorphin peptide with IRAP. (A) LVVYPWTQRF (non-camel hemorphin) docked in the binding pocket of IRAP. (B) LVVYPWTRRF (camel hemorphin) docked in the binding pocket of IRAP. The IRAP protein is shown with a purple cartoon representation. Hydrogen bonds are represented by black dotted lines and cation- $\pi$  interactions are represented by red dotted lines.



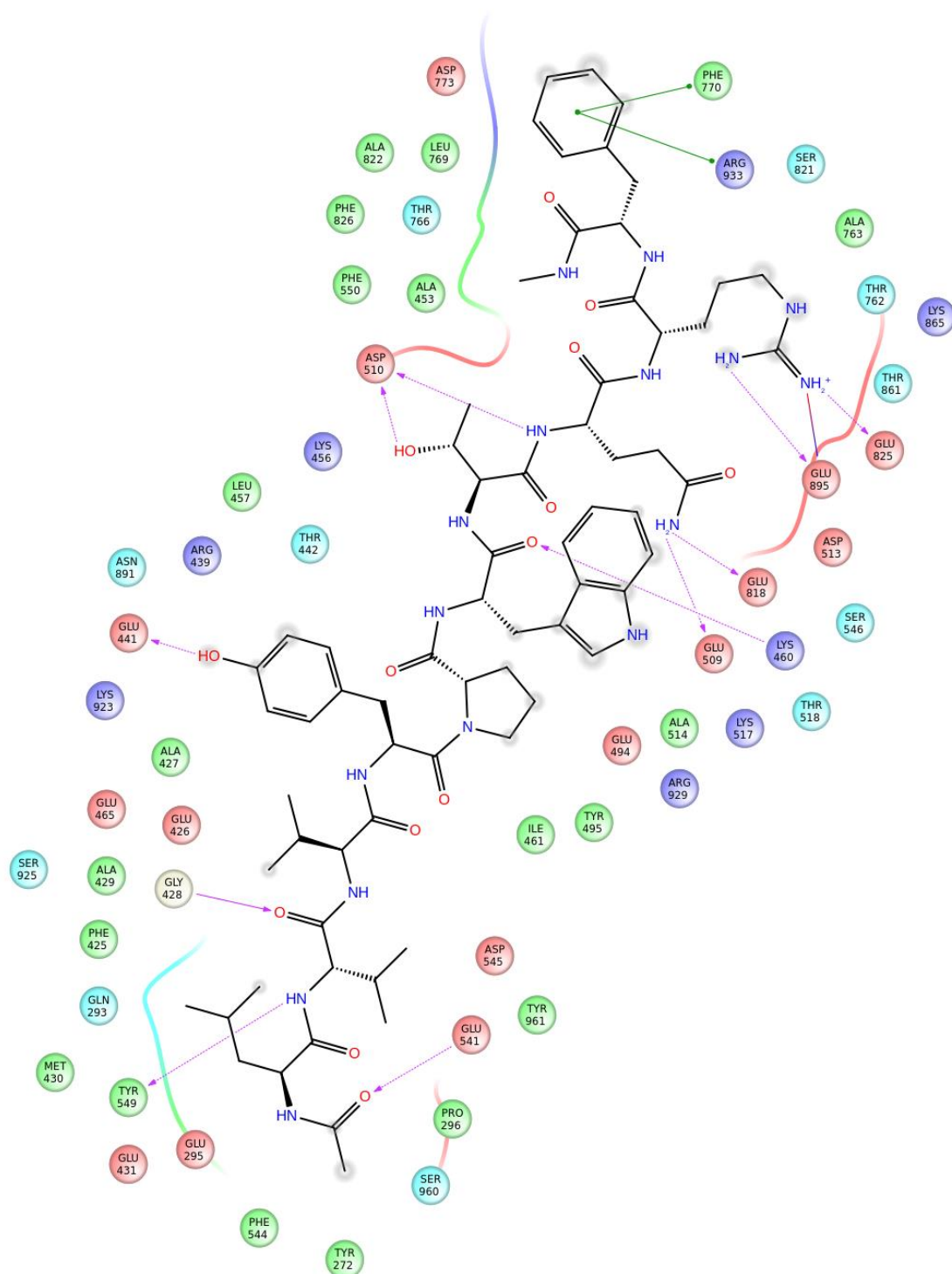


Figure 13: Interactions of non-camel LVV-hemorphin-7 residues with IRAP.

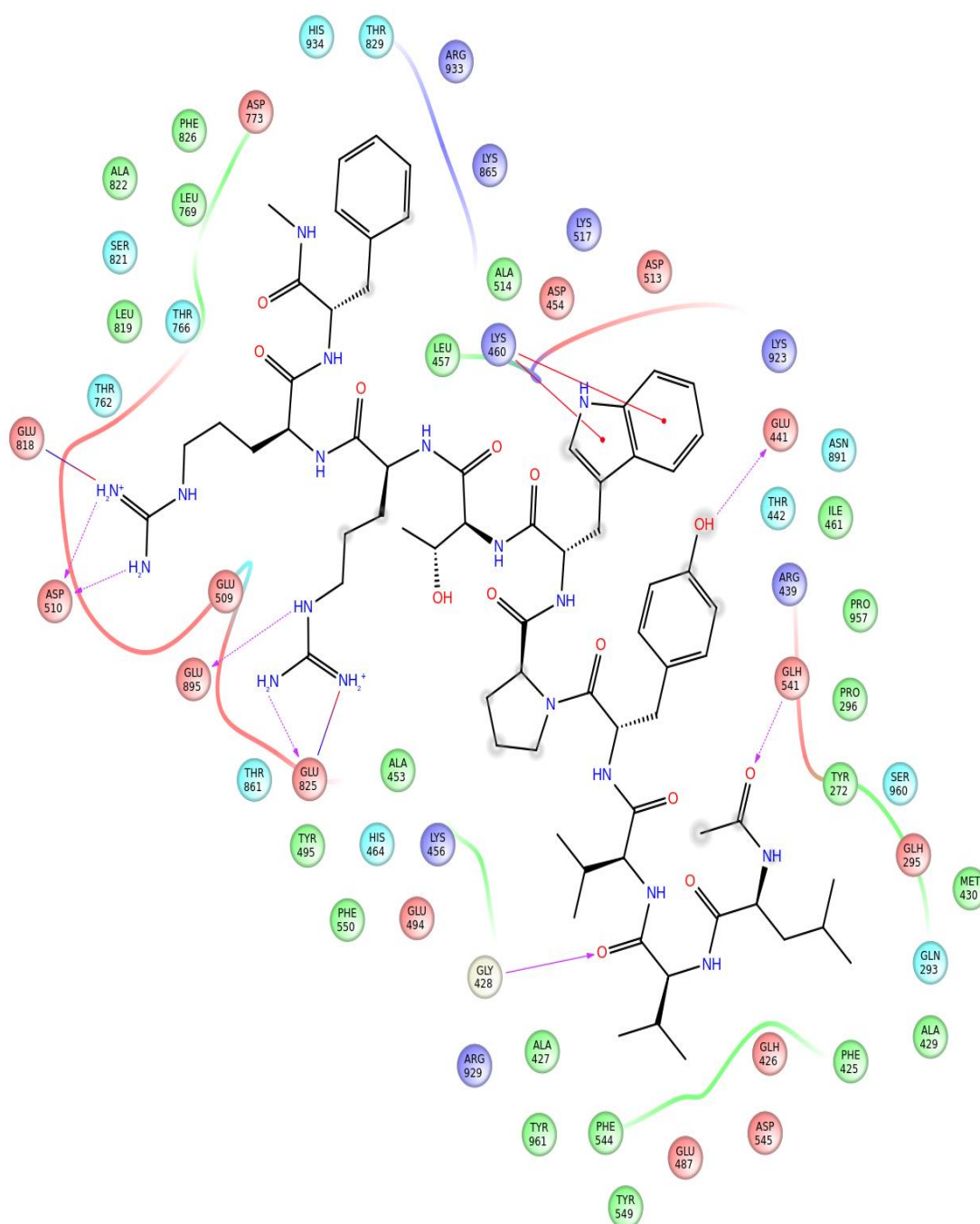


Figure 14: Interactions of camel LVV-hemorphin-7 residues with IRAP.

### 3.1.6 Molecular dynamics simulations

In order to investigate the stability and dynamics of the docked complexes, all-atom MD simulations were carried out in triplicates using Desmond (Bowers et al., 2006).

### 3.1.7 Simulations of camel and non-camel LVV-hemorphin-7 bound to MOR

Three independent 100 ns all atom MD simulations of the LVVYPWTQRF bound to modeled MOR structure embedded in a dipalmitoylphosphatidylcholine (DPPC) membrane resulted in stable simulations with a protein C $\alpha$  RMSD below 5 Å (Figure 15A). The per-residue RMSF demonstrated that the third intracellular (ICL-3) and extracellular loop (ECL-2) regions were the most flexible whereas the regions that were membrane-embedded were the least flexible (Figure 15B). LVVYPWTQRF formed interaction with residues located on TM3 and TM7 during MD simulations. Tyr4 and Trp6 produced sustained hydrogen bond and hydrophobic interactions with Tyr150 and Asp149, respectively on TM3. Leu1 formed interaction with the TM5 residue Glu231. Tyr4 residue showed interaction with Lys305 whereas Val3, Trp6, and Arg9 residues formed sustained interactions with Trp320, Ile324 and His321, respectively located on TM7 in the simulations. The average percentage of equilibrated simulation period during which LVVYPWTQRF formed interactions with MOR residues is shown in Figure 16. Contributions from each simulation are given in Figure 18A.

In the case of LVVYPWTRRF peptide bound simulations, the protein structure remained stable with RMSD below 4.5 Å in all three independent simulations (Figure 15C). Figure 15E shows the distribution of the RMSD values extracted from the LVVYPWTQRF and LVVYPWTRRF bound simulations. ECL-2 and ICL-3 regions demonstrated higher fluctuations. More importantly, ICL-3 produced higher fluctuations when compared to the MOR-LVVYPWTQRF complex (Figure 15D). LVVYPWTRRF exhibited interactions with residues from TM2, TM3, TM5, TM6, TM7 and the  $\beta$ -sheet. Arg9 showed interactions with Asp149 for the full



duration of all three simulations, whereas Phe10 formed interaction with Tyr150 during the simulations. Additionally, LVVYPWTRRF peptide also formed interaction with Glu231, Asn232, and Lys235 residues of TM5. Leu1 and Tyr4 residues formed consistent interactions with Ala306 and Lys305, respectively, located on TM6 and the C-terminal residues showed interactions with Trp320, and Tyr328 present on TM7. They also exhibited consistent interactions with Ile310 and Glu312 on the third extracellular loop. The average percentage of equilibrated simulation time during which the non-camel LVV-hemorphin-7 interacted with MOR residues is given in Figure 17. Contributions from each simulation are shown in Figure 18B.

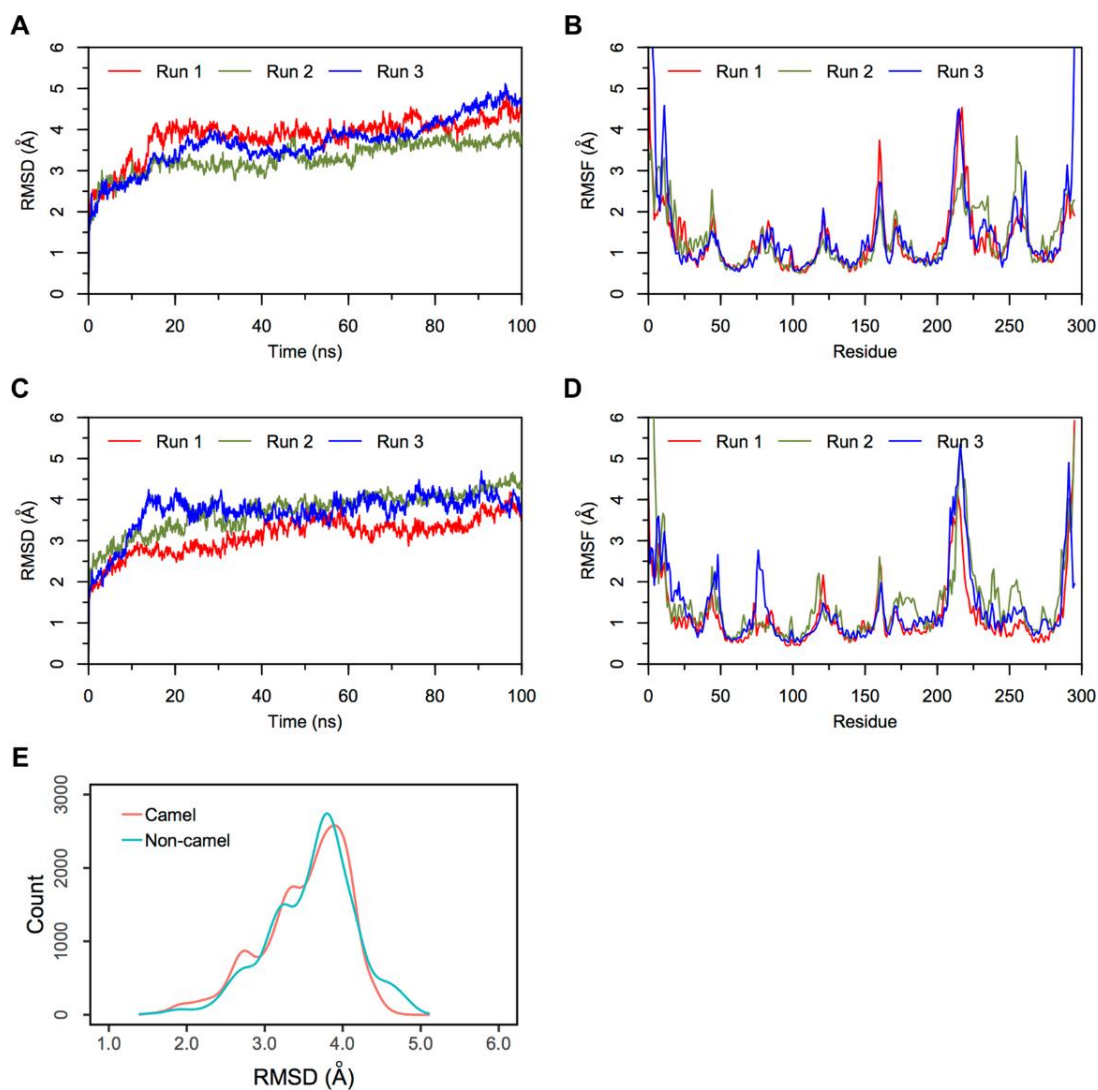


Figure 15: RMSD and RMSF plots of triplicate 100 ns simulations of MOR. Data from the three independent runs are represented with red, blue, and green lines. (A) RMSD of MOR-LVVYPWTQRF complex. (B) RMSF of MOR-LVVYPWTQRF complex. (C) RMSD of MOR-LVVYPWTRRF complex. (D) RMSF of MOR-LVVYPWTRRF complex. (E) Density functions corresponding to the distribution of RMSD values from three independent hemorphin-bound simulations.

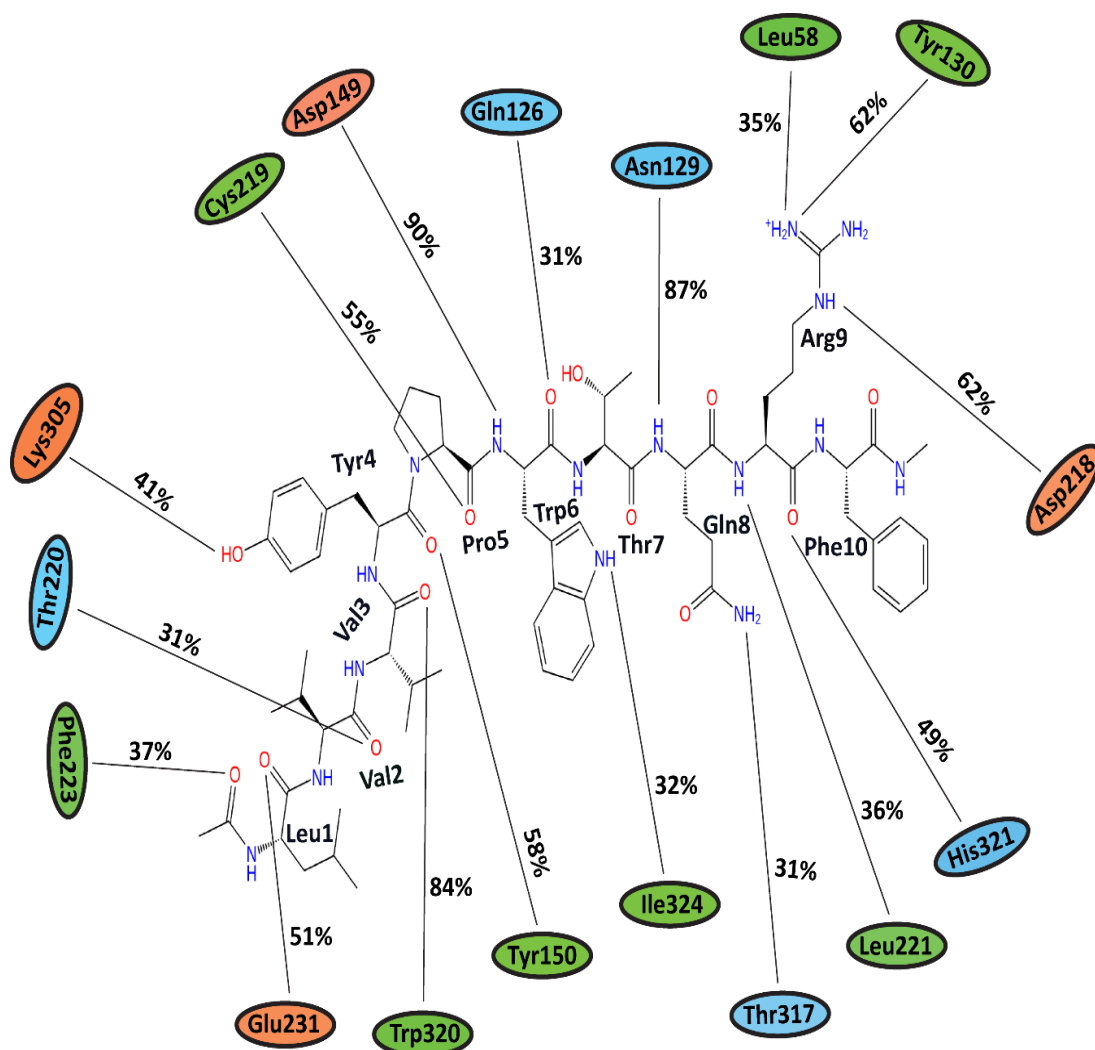


Figure 16: The average percentage of equilibrium simulation time during which residues of MOR maintained contact with LVVYPWTQRF peptide in triplicate 100 ns simulations. To extract the equilibrium simulation data, the initial 50 ns of run 1 was removed, whereas the initial 30 ns of runs 2 and 3 were removed. Charged, hydrophobic, and polar amino acids are shown with orange, green and blue color respectively.

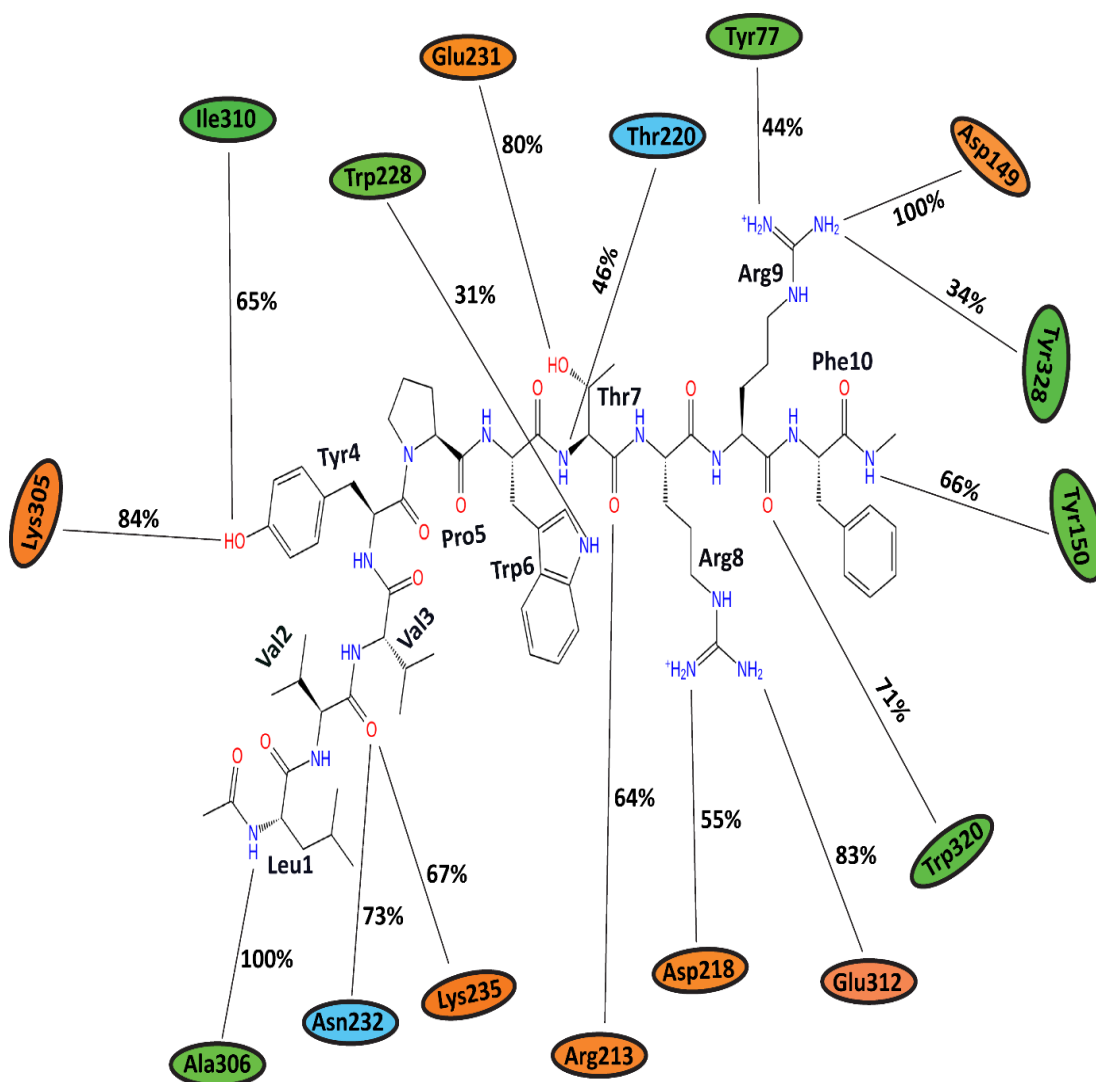


Figure 17: The average percentage of equilibrium simulation time during which residues of MOR maintained contact with LVVYPWTRRF peptide in triplicate 100 ns simulations. To extract the equilibrium simulation data, the initial 50 ns of run 1 was removed, whereas the initial 30 ns of runs 2 and 3 were removed. Charged, hydrophobic, and polar amino acids are shown with orange, green and blue color respectively.

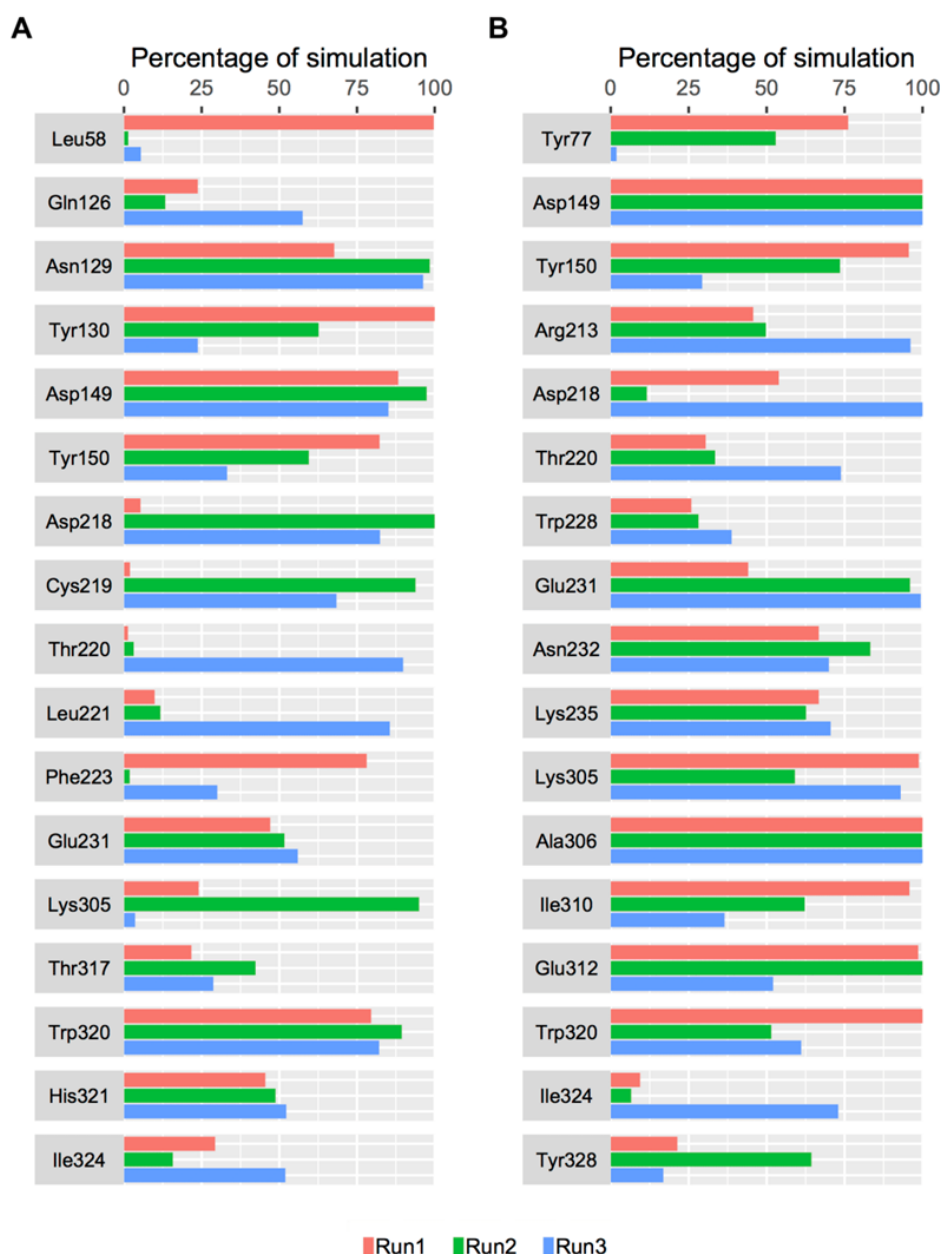


Figure 18: Histograms of the percentage of simulation time where a MOR residue maintains contact with the hemorphin peptide in triplicate simulations. For equilibrium simulation data, the first 50 ns of run 1 was discarded, while the first 30 ns of runs 2 and 3 were discarded. A) MOR-LVVYPWTQRF. B) MOR-LVVYPWTRRF.

### 3.1.8 Simulations of camel and non-camel LVV-hemorphin-7 bound to IRAP

100 ns molecular dynamics simulation runs in triplicates were used to determine the binding stability of the bound peptide. In the case of LVVYPWTQRF

bound simulations, the IRAP structure maintained stability with RMSD below 2.5 Å (Figure 19A). Overall, simulations showed lower fluctuations in the protein residues and the secondary structure was preserved during all simulations (Figure 19B). The first three residues of the N-terminal of LVVYPWTQRF peptide were stabilized in the S1 pocket by forming hydrogen bonds and hydrophobic interactions. Leu1, Val2, and Val3 showed sustained hydrogen bonds with Tyr549 and Gly428 throughout the simulations and also formed interactions with Phe544. Tyr4, Pro5, and Trp6 formed consistent interactions with Glu441, Phe550, and Asn965. However, the C-terminal residues sustained their interactions with Asp510, Asp513, Glu818, Glu825, and Glu895 residues. Moreover, during the course of simulations, new contacts were observed between the first three residues of LVVYPWTQRF and Trp6 with Arg929, and Asn965. The average percentage of equilibrated simulation period during which LVVYPWTQRF peptide formed interactions with IRAP residues is shown in Figure 20. Contributions from each simulation are shown in Figure 22A.

LVVYPWTRRF bound simulations showed stability with an RMSD below 2.75 Å (Figure 19C). Overall, LVVYPWTRRF bound simulations produced limited fluctuations in IRAP residues (Figure 19D). The secondary structure was also preserved during the simulations. Figure 19E shows the distribution of the RMSD values extracted from the LVVYPWTQRF and LVVYPWTRRF bound simulations. The first three residues of LVVYPWTRRF were stabilized in the S1 pocket of IRAP by forming hydrogen bonds and hydrophobic interactions. Val2 residue formed a sustained hydrogen bond with Gly428 in the GAMEN loop throughout the simulation runs. The N-terminal residues (Leu1, Val2, and Val3) also formed sustained hydrophobic interactions with Ala429, Phe544, Tyr549, and Tyr961. Pro5

showed consistent interactions with Lys460, whereas Trp6 formed interaction with Asp513. The mutated Arg8 demonstrated sustained hydrogen bonds with the negatively charged residues Glu509, Asp510 and Glu818. Lastly, Arg9 and Phe10 residues of LVVYPWTQRF also formed consistent interactions with Lys517, Phe770, Glu825 and Glu895. The average percentage of equilibrated simulation period during which LVVYPWTRRF interacted with IRAP residues is shown in Figure 21. Contributions from each simulation are given in Figure 22B.

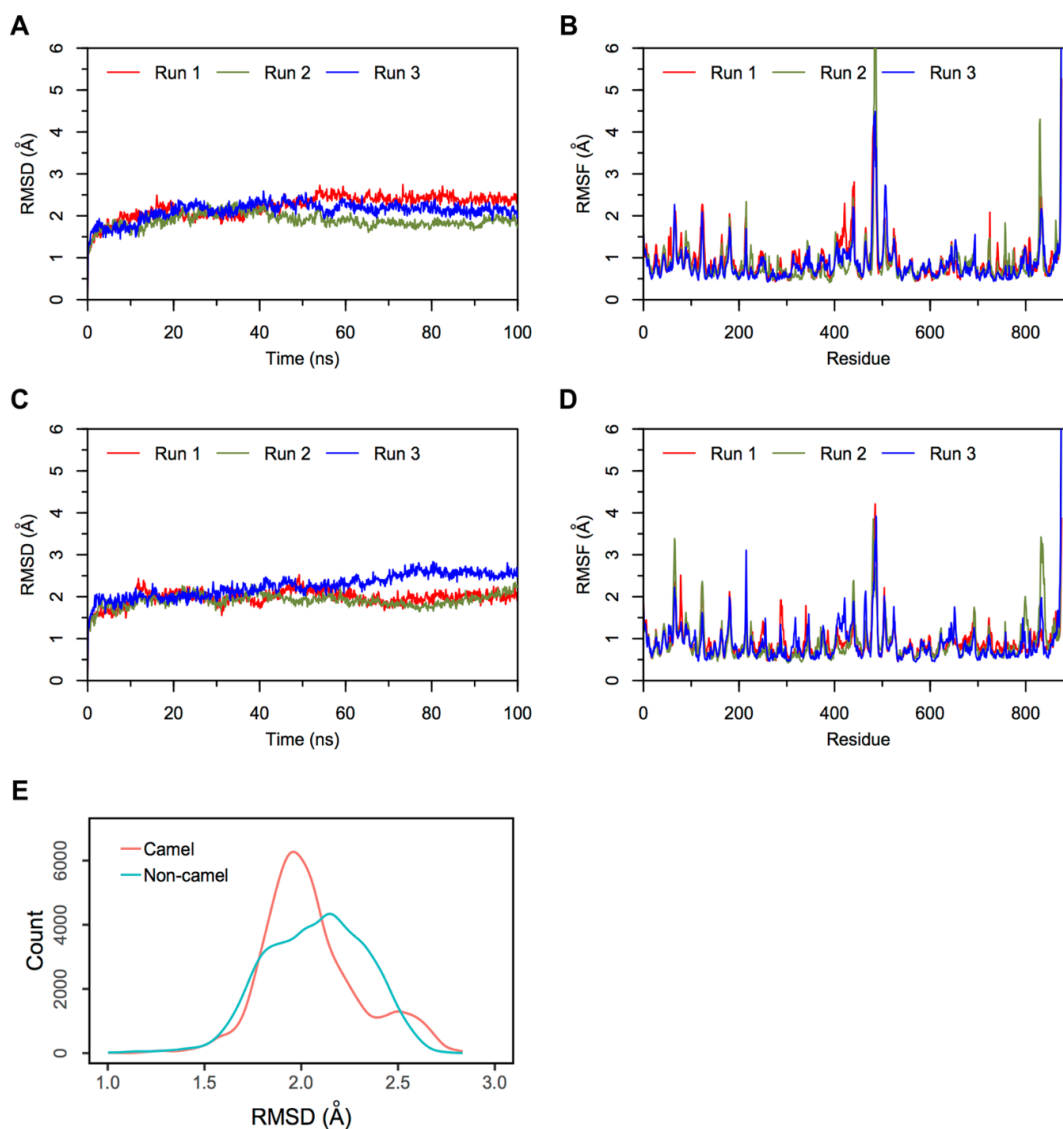


Figure 19: RMSD and RMSF plots of triplicate 100 ns simulations of IRAP. Data from the three independent runs are represented with red, blue, and green lines. (A) RMSD of IRAP-LVVYPWTQRF complex. (B) RMSF of IRAP-LVVYPWTQRF complex. (C) RMSD of IRAP-LVVYPWTRRF complex. (D) RMSF of IRAP-LVVYPWTRRF complex. (E) Density functions corresponding to the distribution of RMSD values from three independent hemorphin-bound simulations.



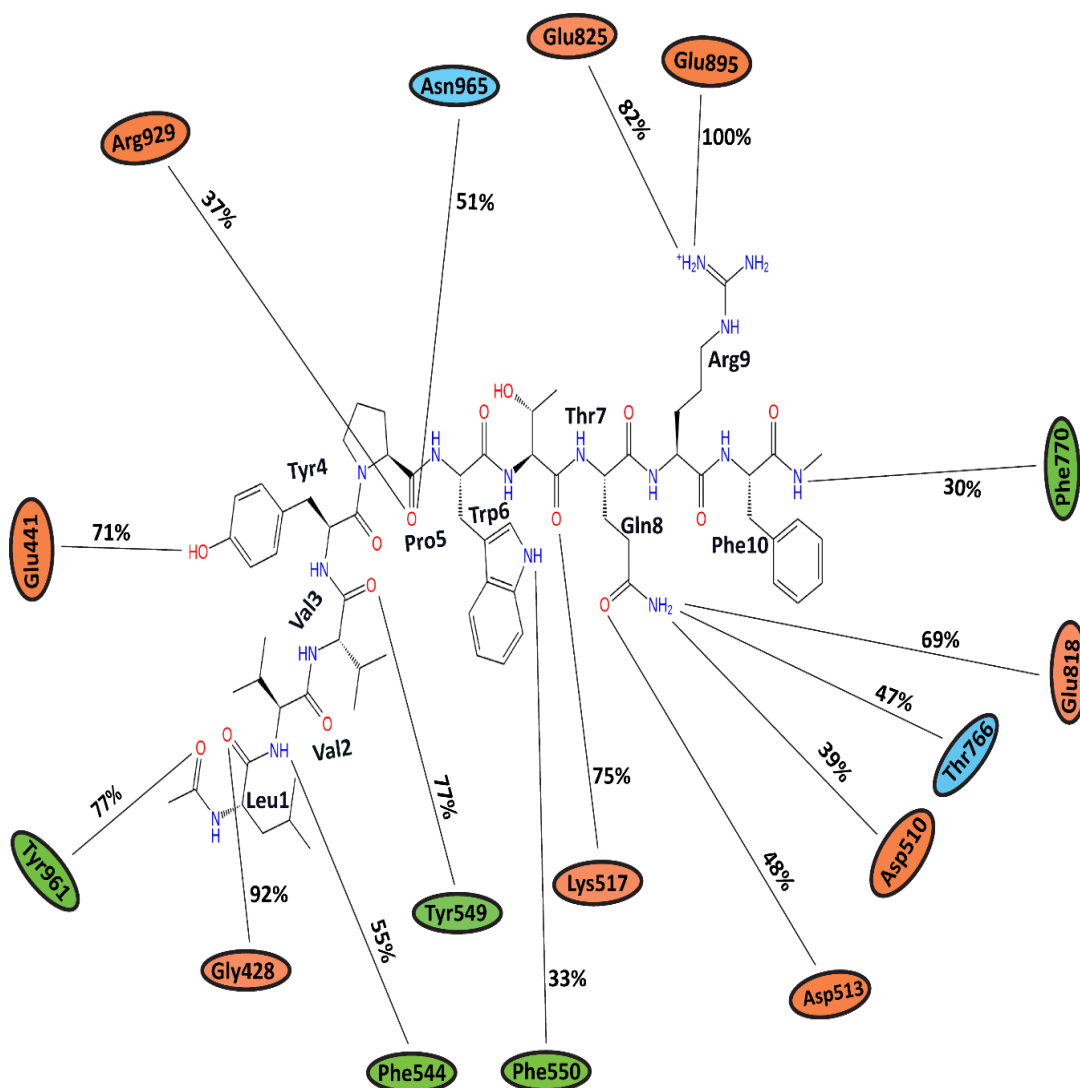


Figure 20: The average percentage of equilibrium simulation time during which residues of IRAP maintain contact with LVVYPWTQRF peptide from triplicate 100 ns simulations. The initial 30 ns of each of the 3 simulations were removed to extract the equilibrium simulation data. Charged, hydrophobic and polar amino acids are shown with orange, green and blue color respectively.

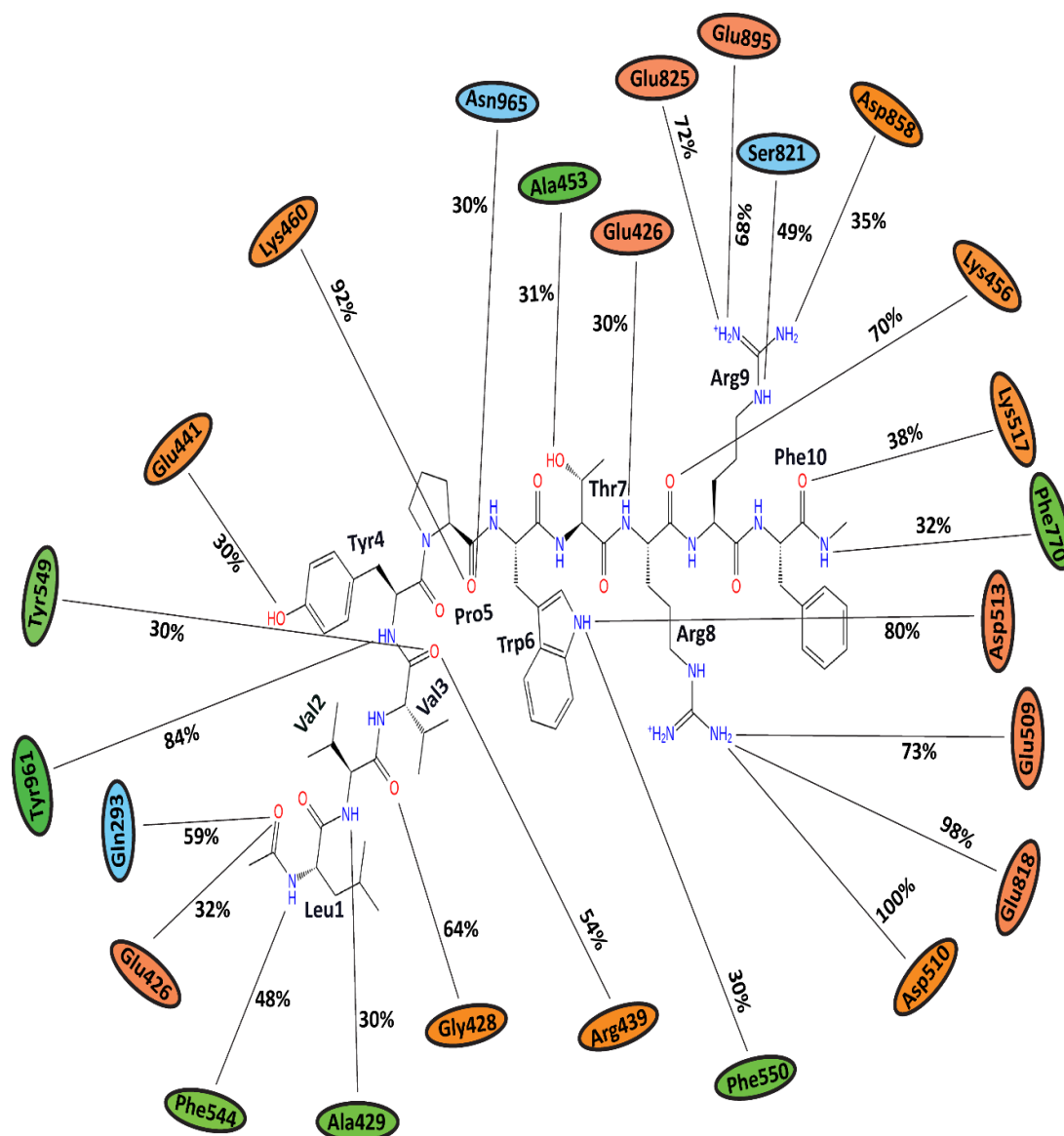


Figure 21: The average percentage of equilibrium simulation time during which residues of IRAP maintain contact with LVVYPWTRRF peptide from triplicate 100 ns simulations. The initial 30 ns of each of the 3 simulations were removed to extract the equilibrium simulation data. Charged, hydrophobic and polar amino acids are shown with orange, green and blue color respectively.

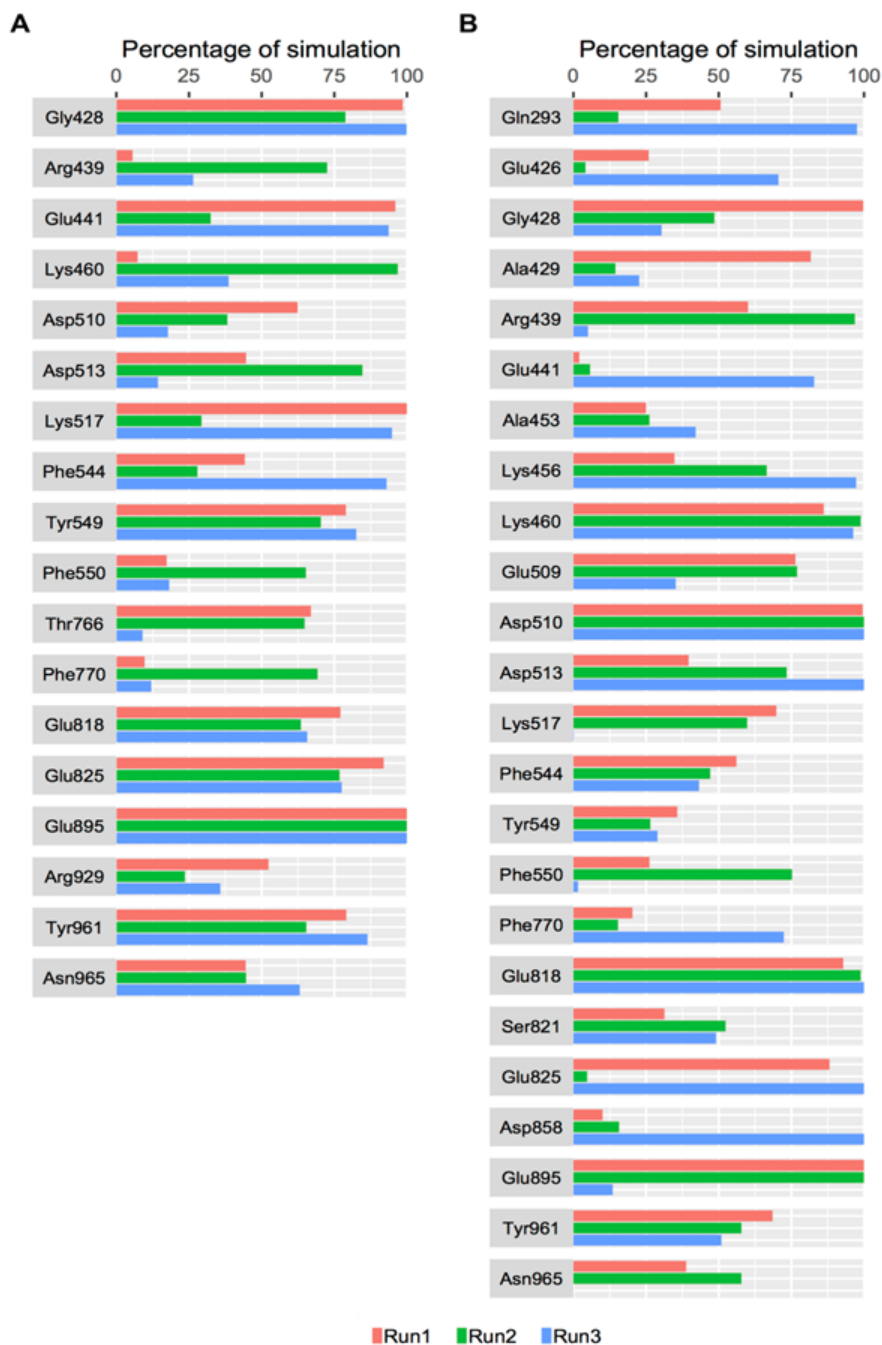


Figure 22: Histograms of the percentage of simulation time where an IRAP residue maintains contact with the hemorphin peptide in triplicate simulations. For equilibrium simulation data, the first 30 ns of each run were discarded. A) IRAP-LVVYPWTQRF. B) IRAP-LVVYPWTRRF.

### 3.2 Discussion

The therapeutic potential of hemorphins has already been demonstrated by multiple *in vivo* and *in vitro* studies (Cheng et al., 2012; Fruitier-Arnaudin et al., 2002; J. Lee et al., 2004). Understanding the binding mode and activity of these peptides at the molecular level is important as LVV-hemorphin-7 binds to several proteins with high affinity. Computational molecular modeling and simulation studies often supplements experimental studies. In this study, extensive computational methods were used to explore the precise binding mode of both camel and non-camel LVV-hemorphin-7 with MOR, and IRAP to elucidate how the peptide interacts with these structurally and functionally different.

In MOR, camel and non-camel LVV-hemorphin-7 adopted distinct poses. The critical residues involved in the binding are in agreement with prior theoretical and experimental data (Cui, Yeliseev, & Liu, 2013). Asp149, an acidic residue of MOR, was found to make a hydrogen bond with both camel and non-camel LVV-hemorphin-7 (Figures 8A, and 8B). Interestingly, camel LVV-hemorphin-7 showed sustained interaction for the full duration of the three simulations, whereas the same interaction was consistent for an average of 90% of the three non-camel LVV-hemorphin-7 simulations. These results complement several site directed mutagenesis studies and structural models that showed the vital role played by Asp149 (Asp147 in murine MOR) in opioid ligand recognition and the interaction with several opioid ligands (Li et al., 1999; Spivak et al., 1997; Xu et al., 1999). This critical interaction therefore should be given special consideration while designing future novel MOR ligands. Camel LVV-hemorphin-7 formed interactions hydrophobically with Tyr328, which is in agreement with a prior study that showed

that hemorphins interact with Tyr326 of mouse MOR49,( Li et al., 1999). Additionally, Trp320 residue of TM7 formed interactions with hemorphins and is also in agreement with earlier studies (Eguchi, 2004; Noori, Mucksch, & Urbassek, 2014). Interestingly, camel LVV-hemorphin-7 formed interactions with essential residues in the active site for a longer duration than non-camel hemorphin (Figure 18).

LVVYPWTRRF formed more stable interactions with Thr220, Glu231, and Tyr328 residues when compared to LVVYPWTQRF in the human MOR model. The equivalent residues in the murine MOR – Thr200, Glu299, and Tyr326 – have been shown to form interactions with agonists (Cui et al., 2013; Noori et al., 2014). Moreover, RMSF values were observed to be higher for ICL-3 residues when bound to camel LVVYPWTRRF. Camel LVV-hemorphin-7 mostly formed interactions with TM3, TM6, and TM7 of MOR, which has been proposed to contain the ionic lock important for GPCR activation (Huang et al., 2015). As observed, the peptide-bound simulations increased the ICL-3 region's flexibility, which is consistent with downstream protein complex interactions and signaling pathways stimulated by receptor agonists (Waldhoer, Bartlett, & Whistler, 2004). The simulations of MOR bound to camel LVV-hemorphin-7 demonstrated a lower RMSD than non-camel LVV-hemorphin-7 (Figure 15). ECL-2 exhibited limited fluctuations upon binding to both LVVYPWTRRF and LVVYPWTQRF peptides. This could support the binding and selectivity of peptides. This is also in agreement with several mutagenesis studies that established the role of ECL-2 in ligand orthosteric and allosteric activation (Huang et al., 2015; Venkatakrishnan et al., 2013; Wheatley et al., 2012). Furthermore, Trp320 and Tyr328 residues are essential in regulating biased MOR

signaling and are vital in effector coupling (Hothersall et al., 2017). Interestingly, LVVYPWTRRF formed interactions with both residues, whereas LVVYPWTQRF interacted with only Trp320. Therefore, due to ligand bias, it is conceivable that camel LVV-hemorphin-7 could produce its effect on MOR.

In the case of IRAP, both LVVYPWTRRF and LVVYPWTQRF demonstrated analogous binding interactions. The binding pose of both camel and non-camel hemorphin peptides showed that their N-terminal residues were stabilized in the S1 pocket by forming sustained hydrogen bonds with Gly428 and Tyr549 (Figure 12). Studies have shown that Tyr549 is an essential residue for binding and stabilizing the catalytic transition state and is extremely conserved in the M1 family of metalloproteases (Wong, Zhou, & Rini, 2012). Moreover, it also interacted with Phe544 and Tyr961 in the active site. Importantly, the interaction with Phe544 was earlier demonstrated as an essential interaction for substrate and ligand binding (Albiston et al., 2010). HEXXH Zn<sup>2+</sup> binding motif and the GXMEN exopeptidase motif are two conserved motifs present in the catalytic domain of IRAP. Mutagenesis studies of these motifs revealed that Gly428, Ala429, and Asn432 are critical for binding both inhibitors and peptide substrates, and also indicated that peptide inhibitors of IRAP competitively bind to its catalytic site (Ye et al., 2007). In the present study, the N-terminal residues of LVVYPWTRRF peptide formed interactions with the GAMEN loop residues Gly428 and Ala429, whereas LVVYPWTQRF interacted with only Gly428 (Figs. 21 and 22). Particularly, Val2 of LVVYPWTRRF exhibited interactions with Gly428 and Ala429 (Figure 10B). However, Val3 of both LVVYPWTRRF and LVVYPWTQRF peptides showed interactions with Tyr549. Val3 is critical for hemorphins binding to IRAP; exclusion

of Val3 residue results in the annihilation of binding to IRAP (Lee et al., 2003). Tyr4 and Trp6 residues formed interactions with Glu441 and Phe550. It has been suggested that monosubstitutions of Tyr4 and Trp6 with alanine leads to a 10-fold reduction in binding affinity (Lee et al., 2003). Additionally, the N-terminal residues of hemorphins are essential for the inhibition of IRAP by forming sustained interactions with key IRAP residues. It has been reported that the removal of C-terminal residues of LVV-hemorphin-7, such as Thr7, Gln8, Arg9, and Phe10 did not substantially alter their binding affinity for IRAP. However, a moderate reduction in affinity was demonstrated with the removal of Arg9 residue in cerebellar membranes. Interestingly, during MD simulations, LVVYPWTQRRF residues Arg8 and Arg9 were noticed to form consistent interactions with charged residues Lys456, Glu509, Asp510, Asp513, and Glu818 in relation to LVVYPWTQRF bound simulations (Figures 22A, and 22B). These sustained interactions could lead to a better affinity of LVVYPWTRRF peptide in the IRAP catalytic pocket.

## **Chapter 4: *In silico* and *In vitro* Comparison of the Angiotensin-I Converting Enzyme Inhibitory Activity of Camel and other Mammalian Hemorphins**

### **4.1 Results**

*In silico* and *in vitro* studies were performed to determine the ACE inhibitory activities of both camel and non-camel hemorphins.

#### **4.1.1 Molecular docking**

Molecular docking and binding free energy calculations methods were used to identify the binding pose of human hemorphins LVVYPWTQRF and YPWTQRF and camel hemorphins LVVYPWTRRF and YPWTRRF. The docked poses of each peptide obtained from peptide docking were examined using the GScore scoring function (Friesner et al., 2006).

#### **4.1.2 Docking of non-camel and camel LVV-hemorphin-7 to ACE**

The binding score and residues of ACE that formed interactions with LVVYPWTQRF, LVVYPWTRRF, YPWTQRF, and YPWTRRF peptides are listed in Table 4. The active site of ACE is comprised of three subsites, which are also essential for ACE inhibition, termed S1, S2, and S1'. These subsites contain residues that form interactions with potential inhibitors (Abdelhedi et al., 2018; Priyanto et al., 2015). Ala354, Glu384, and Tyr523 comprise the S1 subsite; Gln281, His353, Lys511, His513, and Tyr520 comprise the S2 subsite, and Glu162 constitutes the S1' subsite (Ma et al., 2018). These hemorphin peptides interacted with important residues in the active site of ACE. LVVYPWTQRF and LVVYPWTRRF peptides exhibited an extensive network of interactions including hydrogen bonds,



hydrophobic and electrostatic interactions with ACE as demonstrated by the two dimensional ligand in interaction diagram (Figures 24 and 25).

Table 4: List of interactions formed by the top binding pose of LVVYPWTQRF, LVVYPWTRRF, YPWTQRF, and YPWTRRF hemorphin peptides with ACE.

Peptide	Glide docking score-GScore (kcal/mol)	MM-GBSA (kcal/mol)	Residues forming hydrogen bonds	Residues forming hydrophobic interactions	Residues forming $\pi$ - $\pi$ stacking or cation- $\pi$ interaction
LVVYPWTQRF	-14.045	-134.860	Asn70, Glu123, Arg124, Glu162, Thr282, Ala354, Ala356, Glu384, Tyr523	Tyr51, Trp59, Tyr62, Ala63, Ile88, Ala89, Val119, Leu122, Ala125, Leu139, Leu140, Cys352, Trp357, Tyr360, Cys370, Val379, Val380, Phe391, Tyr394, Ala418, Phe457, Phe512, Val518, Tyr520, Phe527	His410
LVVYPWTRRF	-18.824	-147.566	Trp59, Glu123, Glu162, Thr166, Trp220, Ala354, Ala356, Glu384, Asp415, Tyr523	Tyr62, Ala63, Ile88, Leu139, Leu161, Ala204, Ala207, Ala216, Met223, Trp279, Val379, Val380, Phe391, Tyr394, Pro407, Phe457, Phe512, Val518, Pro519, Phe527	
YPWTQRF	-15.955	-112.525	Glu123, Glu162, Asn277, Ala354, Ala356, Asn377, Glu384	Tyr62, Ala63, Trp279, Cys352, Trp357, Phe359, Tyr360, Cys370, Val379, Val380, Phe391, Tyr394, Pro407, Phe457, Phe512, Tyr520, Phe527	Trp59, His410
YPWTRRF	-17.202	-130.392	Lys118, Glu162, Gln281, Ala354, Ala356, Tyr360, Asn377, Glu384, Arg402, Asp415, Tyr523	Tyr62, Ala63, Ile88, Trp279, Trp357, Cys370, Val379, Val380, Phe391, Tyr394, Pro407, Phe457, Phe512, Val518, Phe527	Trp59, His410

The top binding pose of LVVYPWTQRF peptide exhibited a GScore and an MM-GBSA binding energy of  $-14.045$  kcal/mol and  $-134.860$  kcal/mol, respectively (Table 4). The C-terminal residue Phe10 of LVVYPWTQRF formed a hydrogen bond and hydrophobic interactions with Thr282 and Phe527 of ACE. Phe10 also formed a polar interaction with the S2 subsite residue Gln281 and three electrostatic interactions with residues Glu376, His383, and Asp453. A hydrogen bond was formed between Glu162 residue of S1' subsite and the sidechain of Arg9. Moreover, it also exhibited an electrostatic interaction with Lys454, and three hydrophobic interactions with Cys352, Val379, and Val380. LVVYPWTQRF residues Thr7, and Gln8 were situated in the S1 and S2 subsites of ACE. A hydrogen bond was formed between the sidechain of Gln8 and Glu384, Thr7 formed hydrogen bonds with Ala354 and Tyr523 residues of ACE. Additionally, Gln8 residue of the peptide also exhibited electrostatic and polar interactions with Glu411, Lys511, and His513 and two hydrophobic interactions with Phe457, and Tyr520. A cation- $\pi$  interaction was observed between His410 and Trp6. A hydrogen bond was also formed between the backbone amino group of Trp6 and Ala356. LVVYPWTQRF peptide residues Tyr4, Pro5, and Trp6 formed interactions hydrophobically with Leu139, Leu140, Trp357, Phe391, Tyr394, and Pro407, and electrostatically with Glu143, Asp358, Lys368, Glu403, and Arg522. The N-terminus residues (Leu1, Val2, and Val3) of LVVYPWTQRF formed hydrophobic interactions with ACE residues Tyr51, Trp59, Tyr62, Ala63, Ile88, Ala89, Val119, and Leu122. Hydrogen bonds were formed between the sidechain amino group of Leu1 and sidechain carboxyl group of Val3 with Glu123 and Arg124, respectively (Figures 24, and 26).

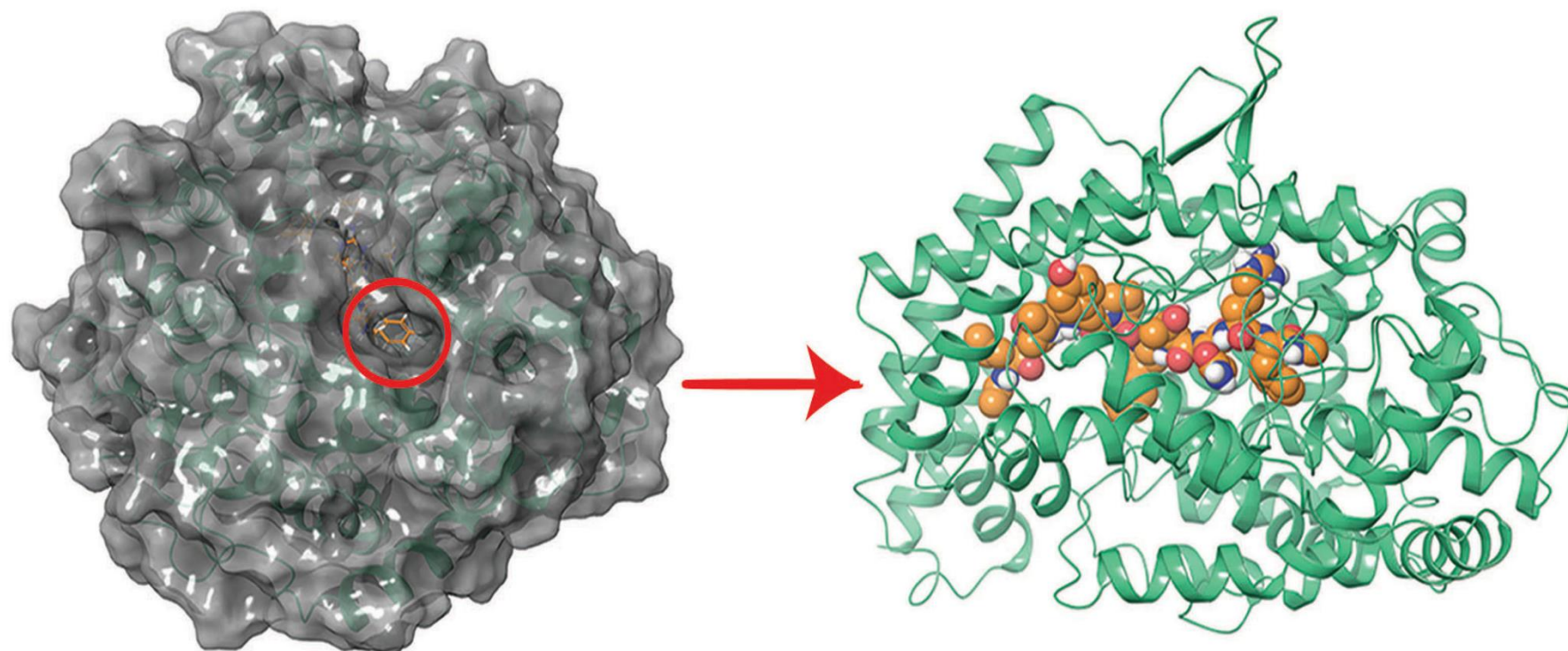


Figure 23: The active site of Angiotensin-I converting enzyme (ACE) shown in red circle and a closer look at the interaction of LVV-hemorphin-7 in the active site of ACE.

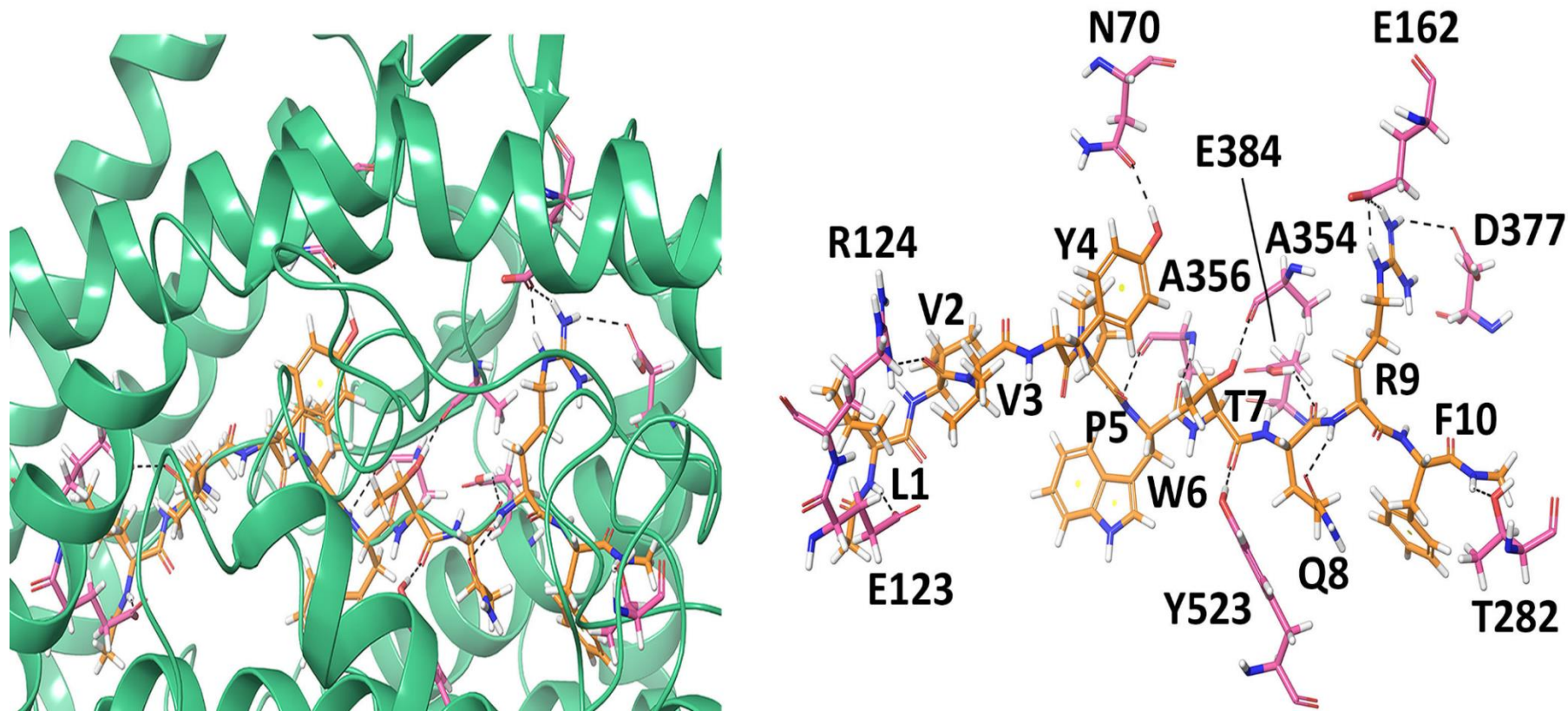


Figure 24: Closer view of the docked pose of LVVYPWTQRF peptide and the hydrogen bond interactions it forms with ACE shown as black dashed lines. The ACE protein is shown with a green cartoon representation and its interacting residues are highlighted in pink stick representation; the docked ligand is shown as orange sticks, and hydrogen bonds are represented as black dashed lines.



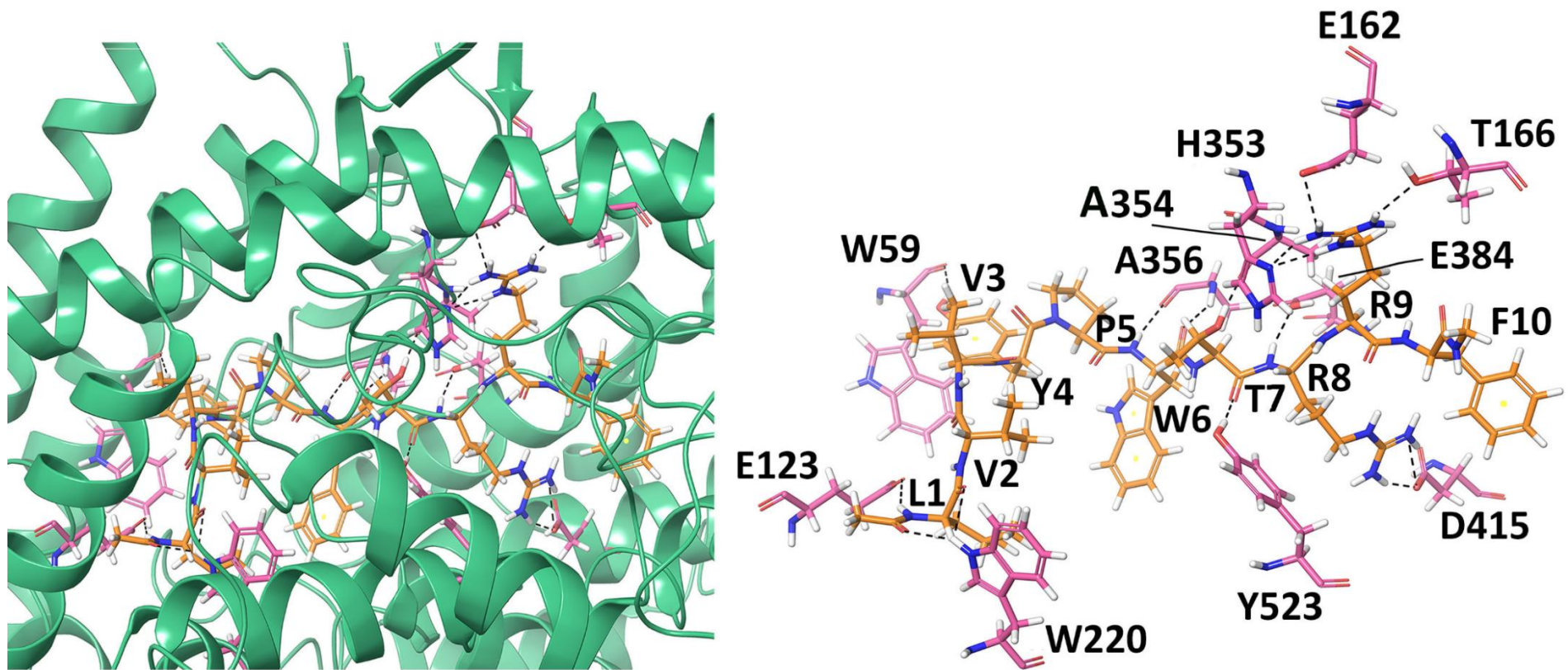


Figure 25: Closer view of the docked pose of LVVYPWTRRF peptide and the hydrogen bond interactions it forms with ACE shown as black dashed lines. The ACE protein is shown with a green cartoon representation and its interacting residues are highlighted in pink stick representation; the docked ligand is shown as orange sticks, and hydrogen bonds are represented as black dashed lines.

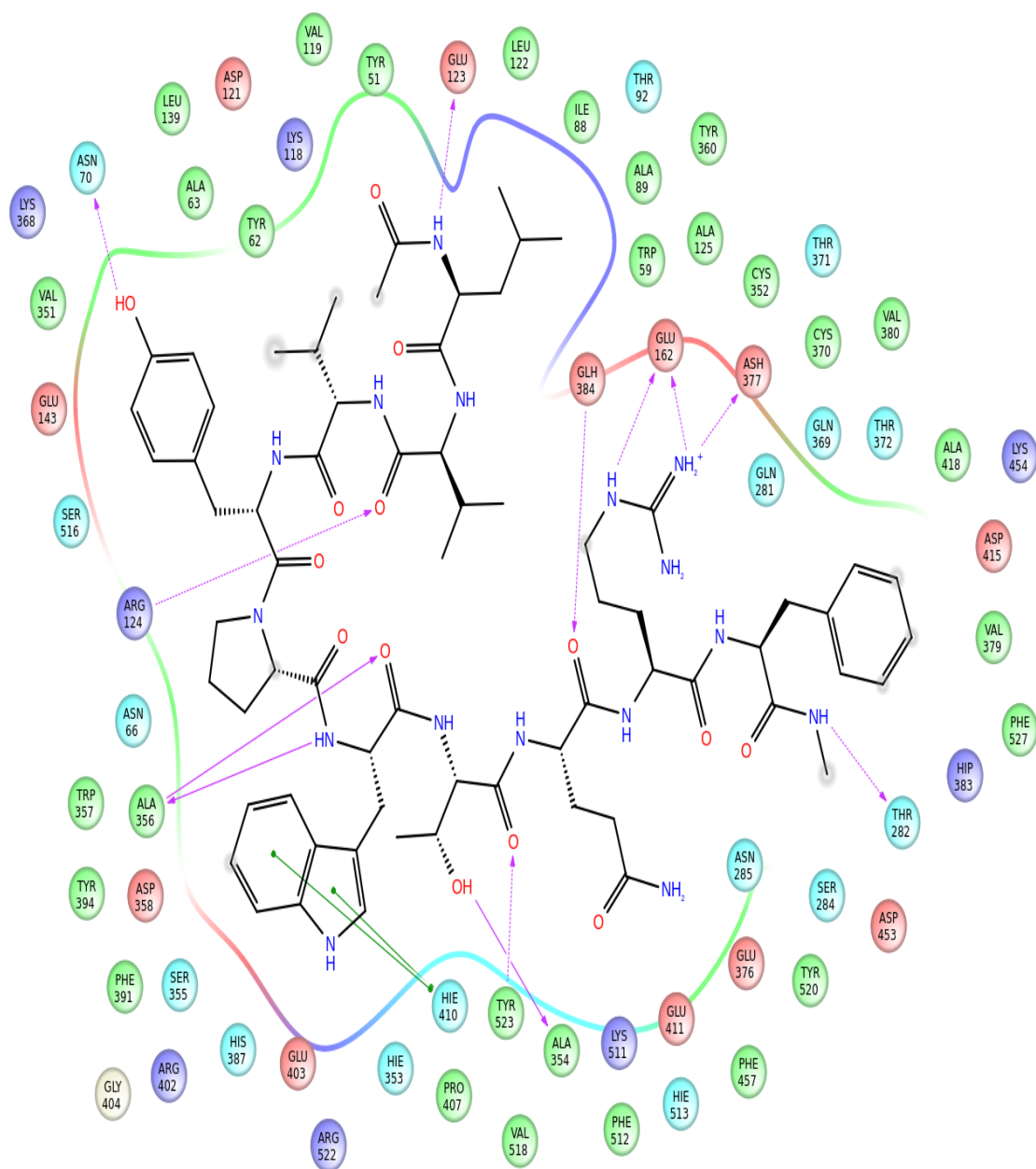


Figure 26: Interactions of human hemorphin (LVVYPWTQRF) with ACE. Colored circles represent amino acids that form interaction with bound ligand. Red circles indicate negatively charged amino acids, dark blue colors indicate positively charged amino acids, light blue circles indicate polar amino acids, and green circles indicate hydrophobic amino acids. Hydrogen bonds are shown with purple arrows – dashed arrows for hydrogen bonds involving amino acid side chain and regular arrows for hydrogen bonds involving amino acid backbone.  $\pi$ - $\pi$  interactions are represented with green lines.

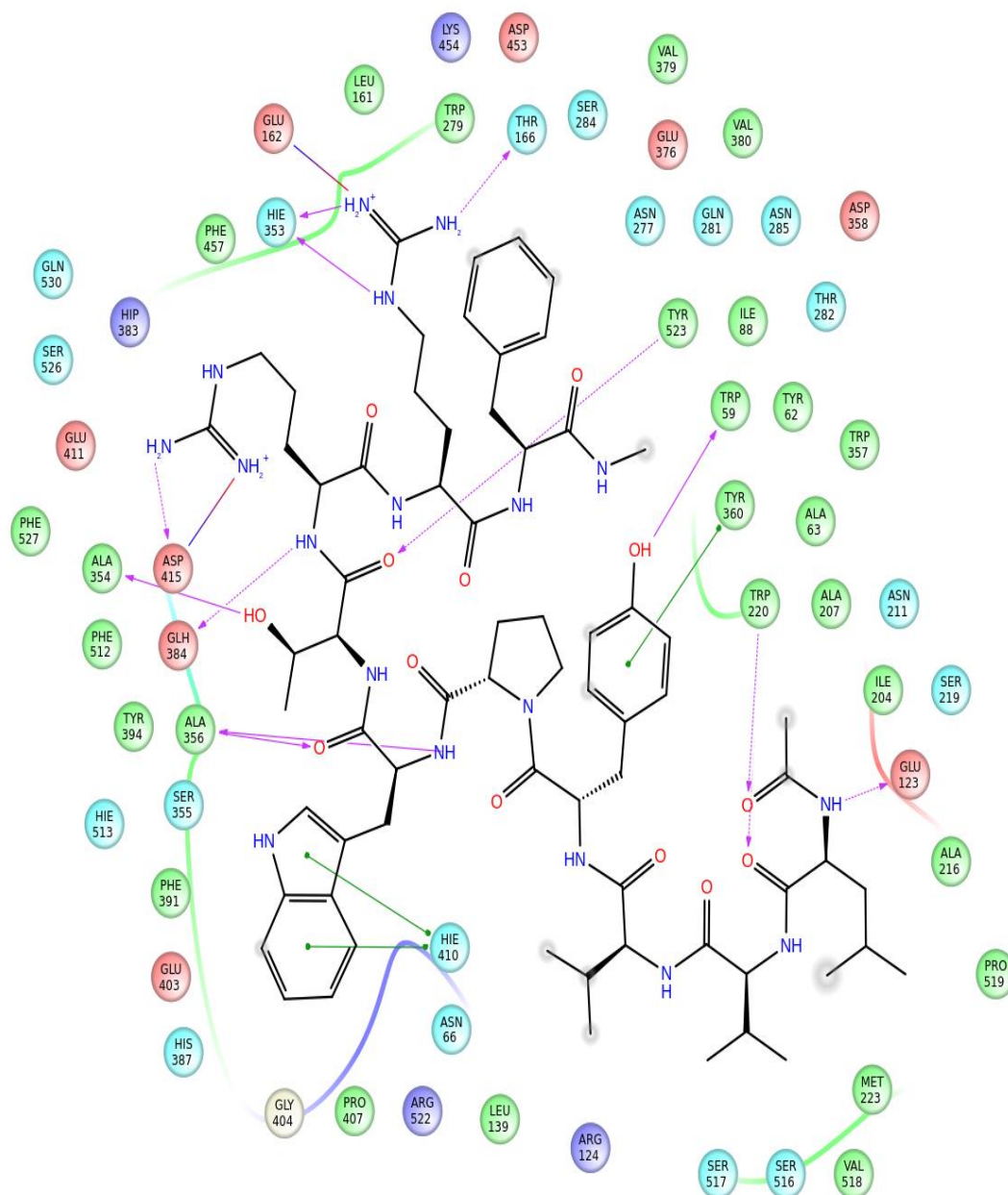


Figure 27: Interactions of camel hemorphin (LVVYPWTRRF) with ACE. Colored circles represent amino acids that form interaction with bound ligand. Red circles indicate negatively charged amino acids, dark blue colors indicate positively charged amino acids, light blue circles indicate polar amino acids, and green circles indicate hydrophobic amino acids. Hydrogen bonds are shown with purple arrows – dashed arrows for hydrogen bonds involving amino acid side chain and regular arrows for hydrogen bonds involving amino acid backbone.  $\pi$ - $\pi$  interactions are represented with green lines.



The binding mode of LVVYPWTRRF peptide was observed to be slightly different from that of LVVYPWTQRF. Precisely, the C-terminus residues binding and positioning in the S1 and S2 subsites of the active site along with the orientation of the N-terminus residues were different. The GScore and an MM-GBSA binding energy calculated for the top binding pose was  $-18.824$  kcal/mol and  $-147.566$  kcal/mol (Table 4). The C-terminal residue Phe10 exhibited polar interactions with S2 subsite residues such as Asn277, Gln281, Thr282, and Asn285. Phe10 also formed two electrostatic interactions with Glu376 and Asp453, and two hydrophobic interactions with Val379 and Val380. LVVYPWTRRF residues Thr7, Arg8, and Arg9 engrossed the S1, S2, and S1' subsites. The backbone functional groups of Arg9 such as amino groups formed hydrogen bonds with S1' subsite residue Glu162 and with S2 subsite residue His353, whereas its sidechain amino group showed a hydrogen bond with Thr166. Additionally, Arg9 also produced two hydrophobic interactions with Leu161 and Trp279. The backbone and sidechain amino groups of Arg8 exhibited hydrogen bonds with S1 subsite residue Glu384 and Asp415. Arg8 also interacted electrostatically with His383 and Glu411, and hydrophobically with Phe457 and Phe527. LVVYPWTRRF residue Thr7 showed two hydrogen bonds with the S1 subsite residues Ala354 and Tyr523. However, Trp6 exhibited a hydrogen bond and a cation- $\pi$  interaction with Ala356 and His410, respectively. Trp6 also formed two polar interactions with His387 and His513. Moreover, LVVYPWTRRF residues Pro5 and Trp6 interacted electrostatically with Trp357, Asp358, Tyr394, Glu403, and Pro407. Tyr4 formed a hydrogen bond with Trp59 and a  $\pi$ - $\pi$  stacking with Tyr360. The backbone of N-terminal residues Leu1 and Val2 produced hydrogen bonds with Glu123 and Trp220, respectively. Additionally, Leu1, Val2, and Val3 of LVVYPWTRRF peptide also interacted hydrophobically with

Leu139, Ile204, Ala207, Met223, Val518, and Pro519, and electrostatically with Arg124 (Figures 25 and 27).

#### **4.1.3 Docking of non-camel and camel hemorphin-7 to ACE**

The GScore and MM-GBSA binding energy calculated for the top binding pose of YPWTQRF peptide with ACE were  $-15.955$  kcal/mol and  $M -112.525$  kcal/mol, respectively (Table 4). The first residue of YPWTQRF, Tyr1 showed a hydrogen bond and  $\pi$ - $\pi$  stacking with Glu123 and Trp59 of ACE, respectively. The N-terminal residues of YPWTQRF, Tyr1 and Pro2 interacted hydrophobically with Tyr62, Ala63, Trp357, Tyr360, and Val380. The backbone functional groups of Trp3 such as amino and carboxyl groups, exhibited hydrogen bonds with Ala356, while the sidechain of Trp3 produced a cation- $\pi$  interaction with His410. Moreover, YPWTQRF peptide residues Thr4 and Gln5 occupied the S1 and S2 subsites. The backbone and sidechain functional groups of Thr4 produced hydrogen bonds with two ACE residues Ala354 and Tyr523. Gln5 exhibited a hydrogen bond with Glu384. Additionally, Thr4 and Gln5 residues also interacted hydrophobically with Phe359, Tyr394, Phe457, Phe512, and Tyr520. The C-terminal residues Arg6 and Phe7 exhibited hydrogen bonds with S1' subsite residue Glu162, and Asn277. A hydrogen bond was also formed between Arg6 and Asn377. Additionally, Arg6 produced three polar interactions with Gln369, Thr371, and Thr372, and also interacted hydrophobically with Cys352 and Cys370. Phe7 residue of YPWTQRF peptide formed four polar interactions with Thr166, Gln281, Thr282, and Asn285, and also interacted electrostatically with Glu376, His383, Asp415, and Lys511 (Figures 28 and 30).

On the other hand, YPWTRRF peptide produced a slightly different binding pose, specifically the N-terminus residues (Tyr1 and Pro2) and the C-terminus residues (Arg5 and Phe7). The C-terminus residue Phe7 produced a hydrogen bond with S2 subsite residue Gln281. Phe7 also exhibited interactions with Thr282, Glu376, Asp453, Lys454, and Phe457. Arg6 showed hydrogen bonds with Asn377, and the S1' subsite residue Glu162. Arg6 also formed five polar interactions with Thr166, Asn285, Gln369, Thr371, and Thr372 residues of ACE. The substituted residue of YPWTRRF peptide, Arg5 formed a hydrogen bond with S1 subsite residue Glu384 and Asp415. Arg5 showed a polar interaction with S2 subsite residue His353 and also interacted hydrophobically with Phe527. However, the Trp3 and Thr4 residues of both YPWTRRF and YPWTQRF peptides produced similar interactions with ACE. Moreover, Pro2 produced interactions with Trp357, Val518, and Asn66. Hydrogen bonds were formed between the backbone amino and sidechain hydroxyl groups of Tyr1 and with Lys118, Tyr360, and Arg402. Tyr1 also interacted electrostatically with Glu403 and hydrophobically with Tyr62, Ala63, Val399, and Phe512. Additionally, the first residue of YPWTRRF also exhibited  $\pi$ - $\pi$  stacking with Trp59 (Figures 29 and 31). Finally, a GScore and a MM-GBSA binding energy calculated for the top binding pose of YPWTRRF peptide with ACE was -17.202 kcal/mol and -130.392 kcal/mol, respectively (Table 4).

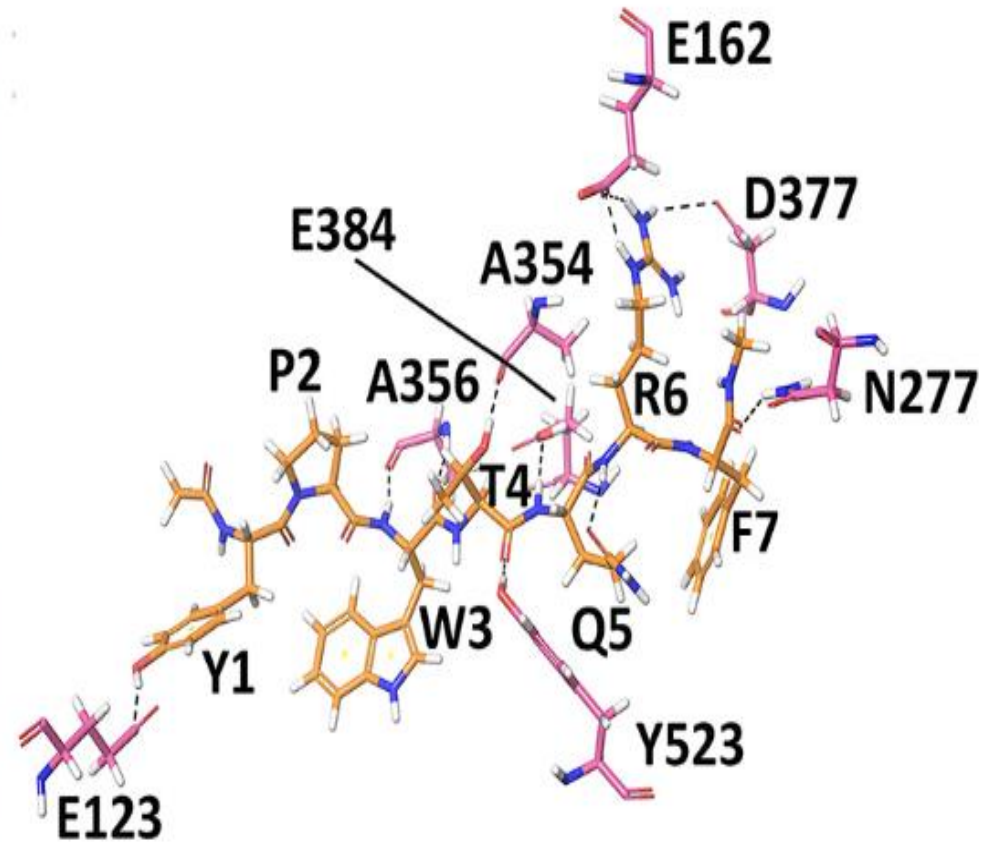
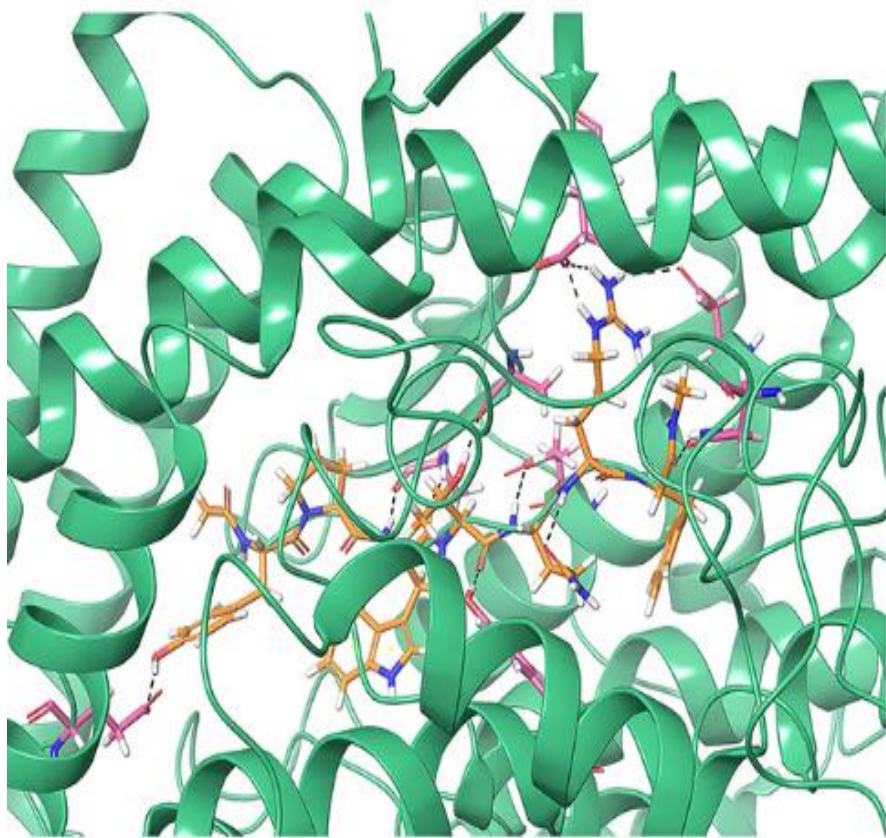


Figure 28: Closer view of the docked pose of YPWTQRF peptide and the hydrogen bond interactions it forms with ACE shown as black dashed lines. The ACE protein is shown with a green cartoon representation and its interacting residues are highlighted in pink stick representation; the docked ligand is shown as orange sticks, and hydrogen bonds are represented as black dashed lines.

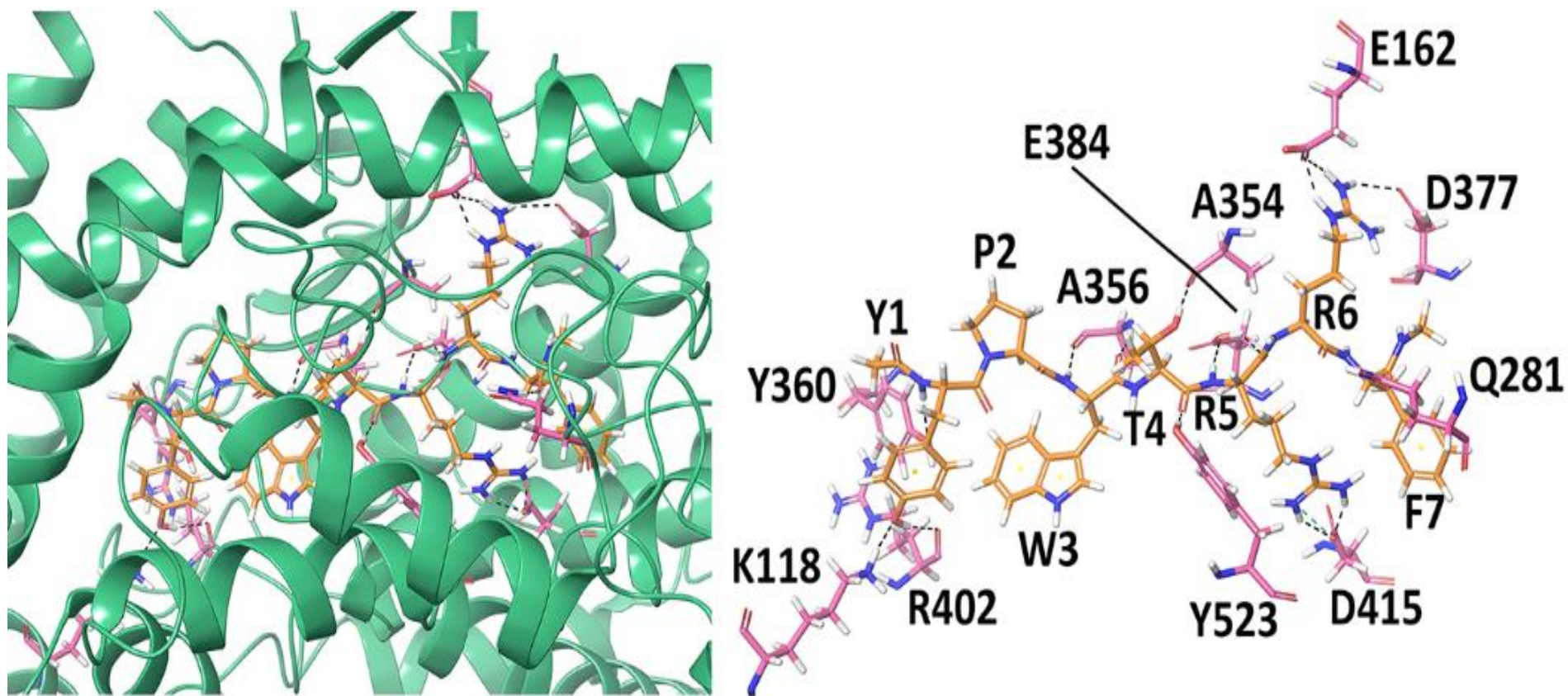


Figure 29: Closer view of the docked pose of YPWTRRF peptide and the hydrogen bond interactions it forms with ACE shown as black dashed lines. The ACE protein is shown with a green cartoon representation and its interacting residues are highlighted in pink stick representation; the docked ligand is shown as orange sticks, and hydrogen bonds are represented as black dashed lines.



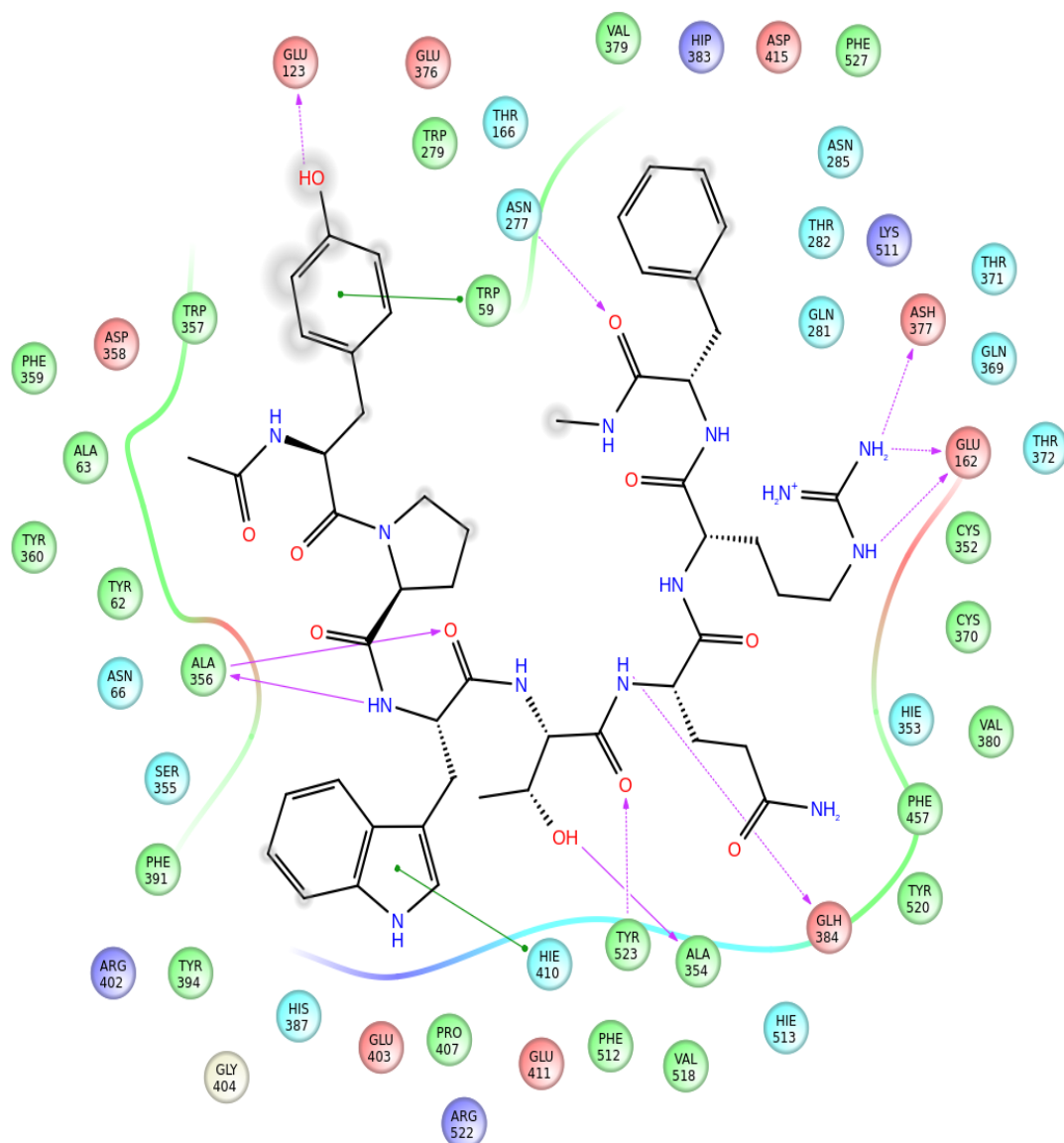


Figure 30: Interactions of human hemorphin (YPWTQRF) with ACE. Colored circles represent amino acids that form interaction with bound ligand. Red circles indicate negatively charged amino acids, dark blue colors indicate positively charged amino acids, light blue circles indicate polar amino acids, and green circles indicate hydrophobic amino acids. Hydrogen bonds are shown with purple arrows – dashed arrows for hydrogen bonds involving amino acid side chain and regular arrows for hydrogen bonds involving amino acid backbone.  $\pi$ - $\pi$  interactions are represented with green lines.

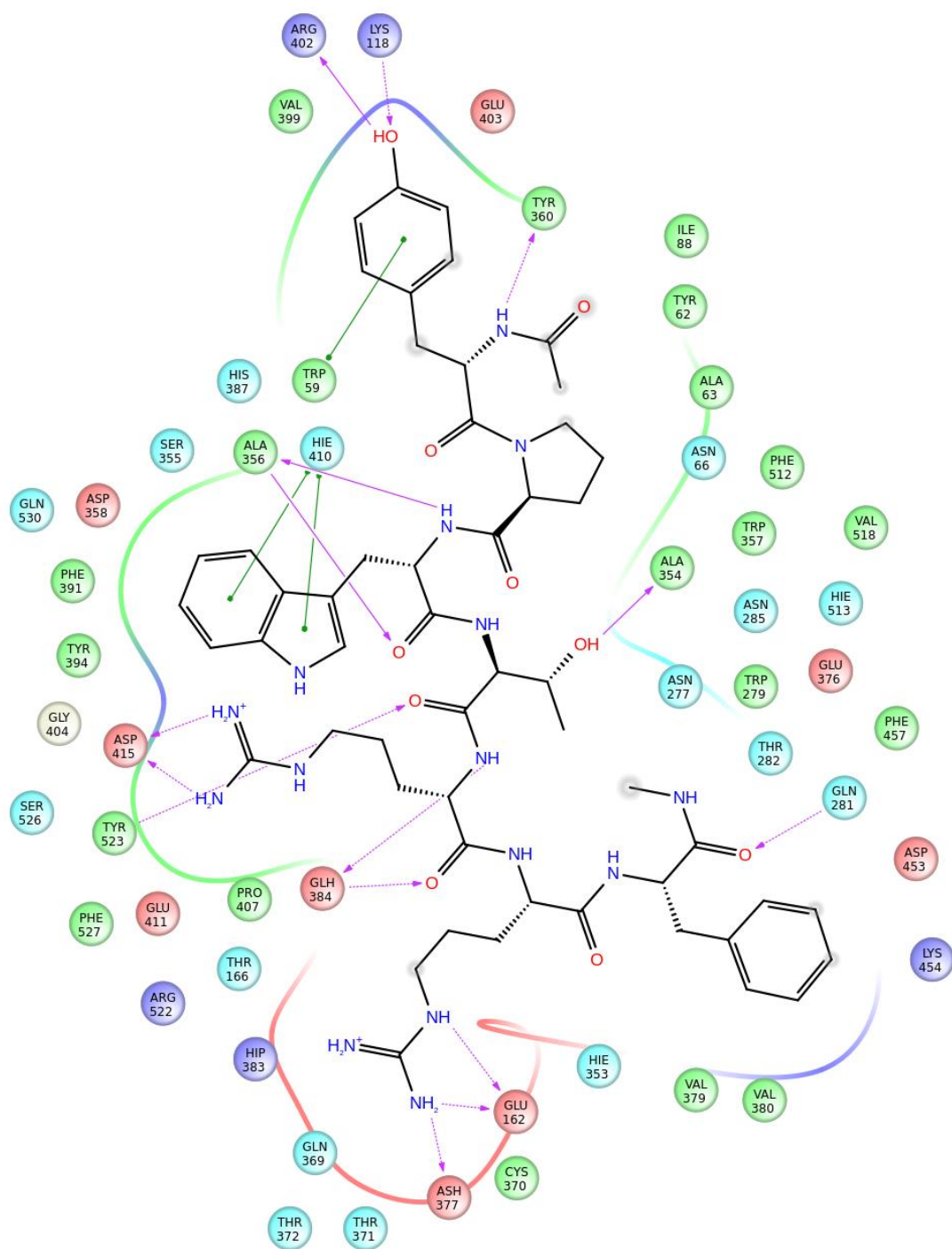


Figure 31: Interactions of camel hemorphin (YPWTRRF) with ACE. Colored circles represent amino acids that form interaction with bound ligand. Red circles indicate negatively charged amino acids, dark blue colors indicate positively charged amino acids, light blue circles indicate polar amino acids, and green circles indicate hydrophobic amino acids. Hydrogen bonds are shown with purple arrows – dashed arrows for hydrogen bonds involving amino acid side chain and regular arrows for hydrogen bonds involving amino acid backbone.  $\pi$ - $\pi$  interactions are represented with green lines.

#### **4.1.4 Molecular dynamics simulations**

In order to determine the stability and dynamics of the interactions between ACE and hemorphin peptides, all-atom MD simulations were run in triplicate using Desmond (Bowers et al., 2006).

#### **4.1.5 Simulations of different peptides of non-camel and camel hemorphins bound to ACE**

The results of MD simulations showed that both LVVYPWTQRF-ACE and LVVYPWTRRF-ACE complex systems remained stable for the full duration of 200 ns simulations. The RMSD of ACE was stabilized at approximately 2.0 Å for both LVVYPWTQRF and LVVYPWTRRF peptide bound structures (Figures 32A and 32B). Both LVVYPWTQRF and LVVYPWTRRF peptide bound simulations demonstrated that most protein residues exhibited lower fluctuations, but for loop regions (Figures 33A and 33B), and the secondary structures were maintained throughout the simulations. Gln8, Arg9, and Phe10 residues of the C-terminal of LVVYPWTQRF peptide were bound stably in S1, S2, and S1' subsites by forming hydrophobic and hydrogen interactions. Precisely, Glu162, Gln281, Glu384, Asp453, Lys511, His513, and Tyr523 residues of ACE retained interactions with Gln8, Arg9, and Phe10 residues during simulations. The analysis of the MD trajectory showed that Arg9 formed stable interaction with S1' subsite residue Glu162, and S2 subsite residue Gln281. Thr7 and Gln8 residues were situated in the S1 and S2 subsites and formed consistent interactions with Ala354, Glu384, Lys511, His513, and Tyr523. The first three residues of LVVYPWTQRF peptide interacted with Glu123, Arg124, and Tyr360 (Figure 34).



Additionally, LVVYPWTQRF peptide maintained interactions with Trp59, Glu143, His353, Glu411, Arg522, and Phe527. Similar to LVVYPWTQRF peptide, the last three residues of LVVYPWTRRF peptide occupied subsites of ACE active site (S1, S2, and S1') and showed consistent interactions with the essential residues of these subsites. Arg9 residue maintained sustained interaction with S1' subsite residue Glu162. Phe10 residue exhibited sustained interactions with Asn277, Gln281, and Phe457. Notably, the mutated Arg8 residue of LVVYPWTRRF demonstrated consistent interactions with Glu384, Glu411, Asp415, and Ser526, which were not observed in the LVVYPWTQRF-bound simulations (Figure 35). Pro5, Trp6 and Thr7 residues of LVVYPWTRRF interacted consistently with His353, Ala354, Ala356, His410, His513, and Tyr523. Moreover, the first three residues of LVVYPWTRRF peptide interacted with Lys118, Trp220, Glu123, Arg124, Glu403, Ser517, and Arg522 during the simulation time. Figures 34 and 35 demonstrate the average (from three runs) percentage of the equilibrated simulation time during which several residues of the LVVYPWTQRF and LVVYPWTRRF interacted with different amino acids of ACE.

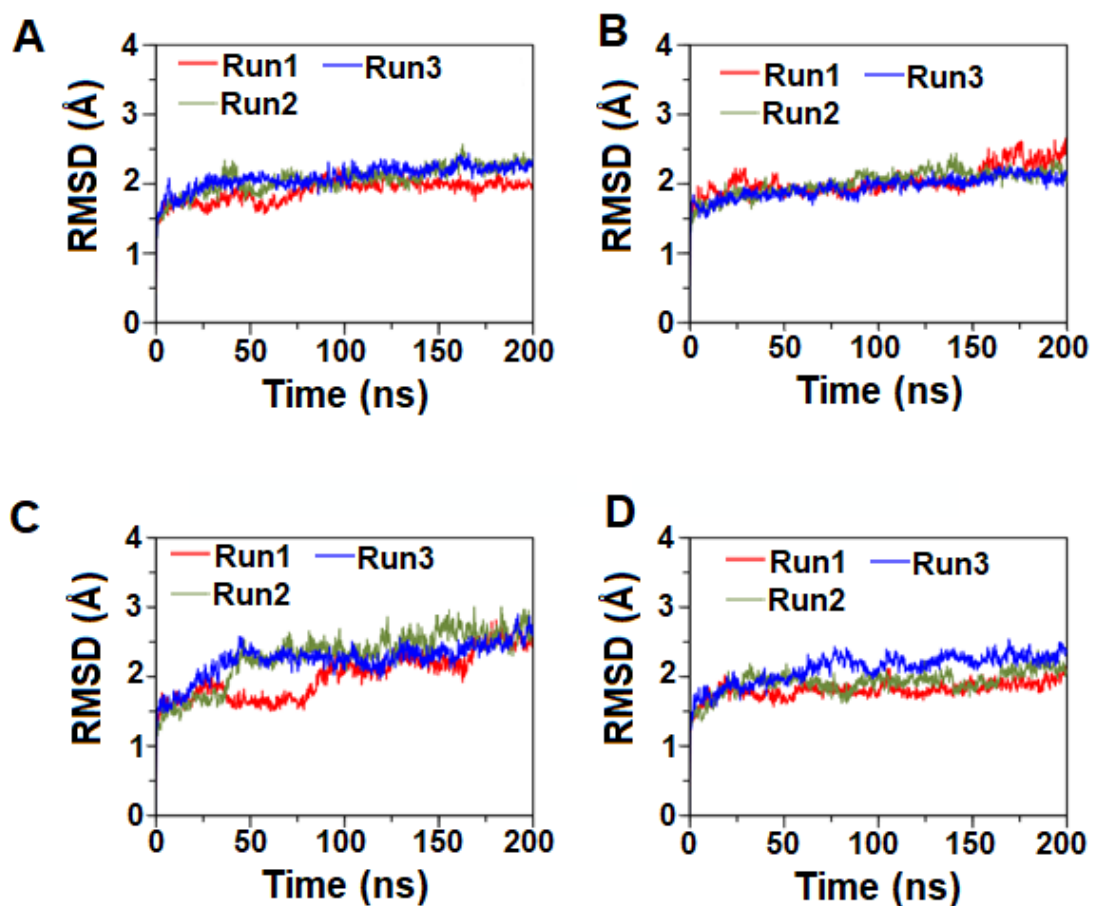


Figure 32: RMSD plots of C $\alpha$  atoms of ACE protein extracted from triplicate 200 ns simulations of hemorphin-ACE complex. Data extracted from three independent runs are shown with red, green, and blue. A) Simulation results of LVVYPWTQRF peptide bound to ACE; B) Simulation results of LVVYPWTRRF peptide bound to ACE; C) Simulation results of YPWTQRF peptide bound to ACE; D) Simulation results of YPWTRRF peptide bound to ACE.

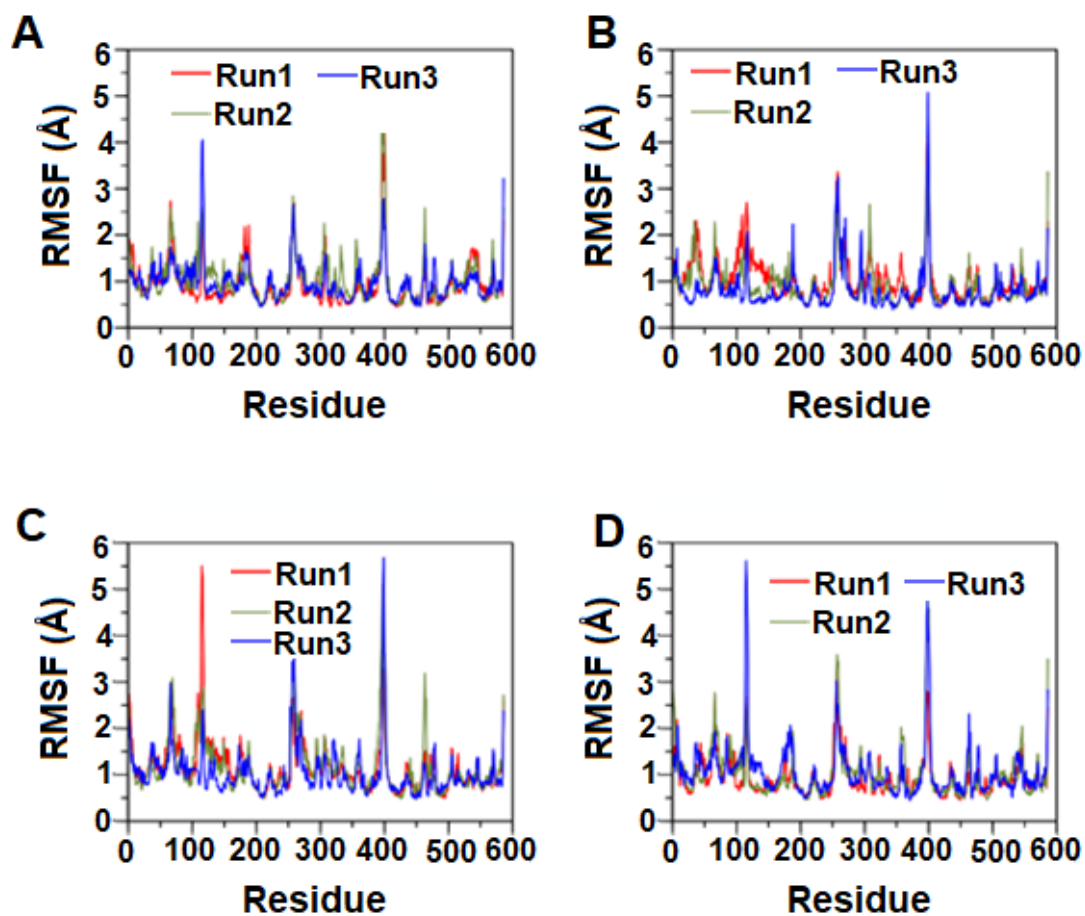


Figure 33: RMSF plots of  $C\alpha$  atoms of ACE protein extracted from triplicate 200 ns simulations of hemorphin-ACE complex. Data extracted from three independent runs are shown with red, green, and blue. A) Simulation results of LVVYPWTQRF peptide bound to ACE; B) Simulation results of LVVYPWTRRF peptide bound to ACE; C) Simulation results of YPWTQRF peptide bound to ACE; D) Simulation results of YPWTRRF peptide bound to ACE.



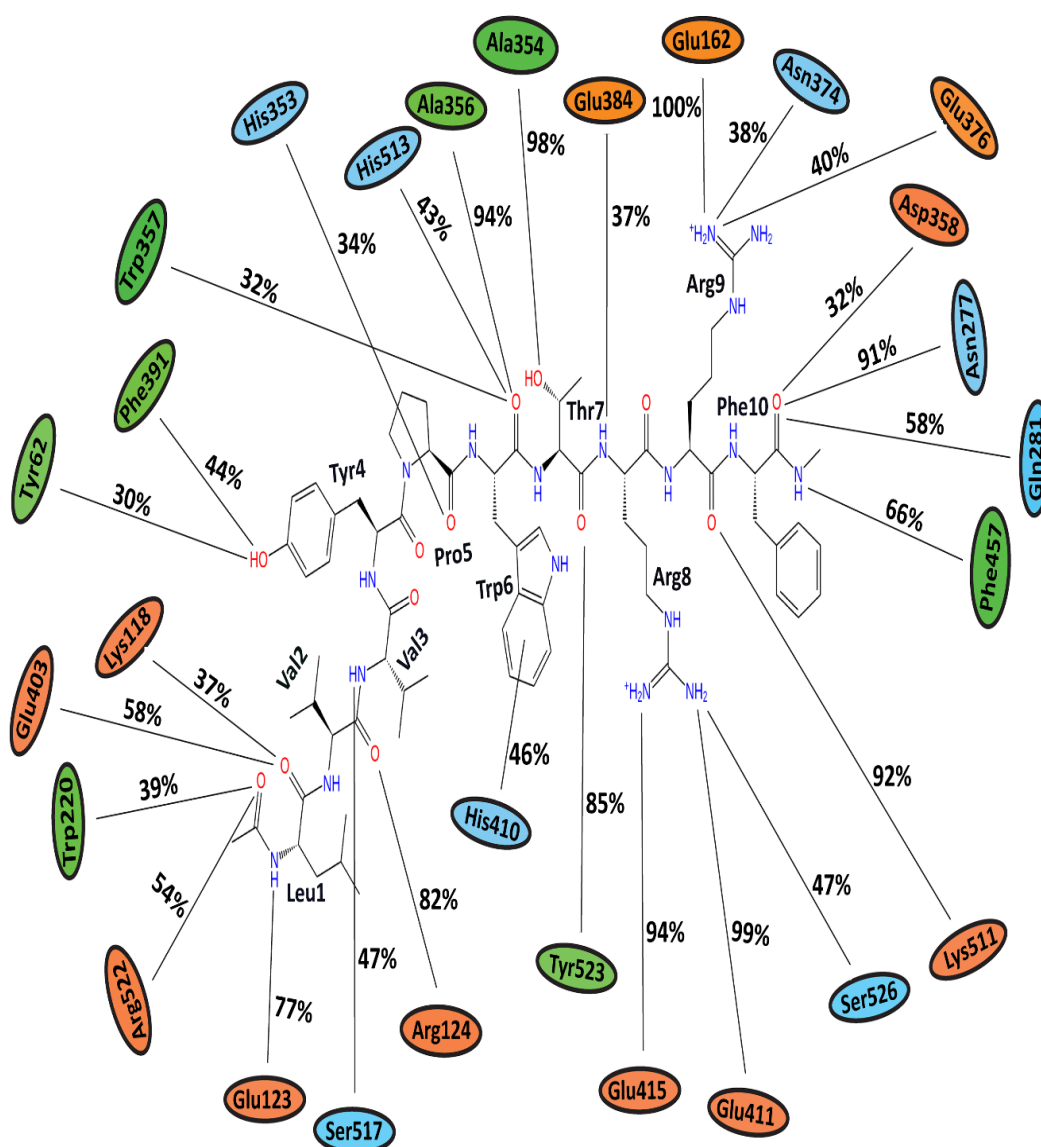


Figure 35: The average percentage of equilibrium simulation time during which ACE residues retain interaction with camel hemorphin (LVVYPWTRRF) peptides from triplicate 200 ns simulations. To extract the equilibrium simulation data, the initial 30 ns of each of the 3 simulations were removed. Charged, hydrophobic, and polar amino acids are shown with orange, green and blue color respectively.

The best docked complexes of YPWTQRF and YPWTRRF bound to ACE were also simulated for 200 ns in triplicates. The protein RMSD stabilized at approximately 2.5 Å in YPWTQRF-bound simulations (Figure 32C). The secondary structure composition was preserved during the simulations and protein residues

exhibited lower fluctuations, except loop regions (Figure 33C). Arg6 and Phe7 were bound stably in the S1' and S2 subsites, respectively, by producing consistent interactions with ACE residues Glu162, Gln281, His353, Lys511, and Tyr523. Gln5 formed sustained interactions with Glu384 and Asp415 during the simulation runs. Thr4 formed interaction with Ala354 and Glu411 residues of the S1 subsite. Tyr1, Pro2, and Trp3 residues at the N-terminus interacted with Asn66, Ala356, Trp357, Tyr360, and Glu403 (Figure 36). Similar to YPWTQRF, Arg6 and Phe7 residues of YPWTRRF engrossed the S1' and S2 subsites, respectively, by exhibiting consistent interactions with Glu162, Gln281, and His513 (Figure 37). They also retained consistent interactions with Asn277, Asn374, Glu376, and Phe457. Glu162 residue of S1' pocket formed interaction with Arg6 for the full duration of simulations. Arg5 of YPWTRRF peptide exhibited consistent interactions with Glu411, Asp415, Lys51, and Ser526. It also produced sustained interactions with the S1 subsite residues Ala354 and Glu384. His353 and Tyr523 residues of ACE interacted with Thr4. Moreover, Tyr1, Pro2, and Trp3 residues at the N-terminus displayed consistent interactions with Ala356, Trp357, His387, Phe391, Glu403, and Ser516 (Figures 36 and 37).

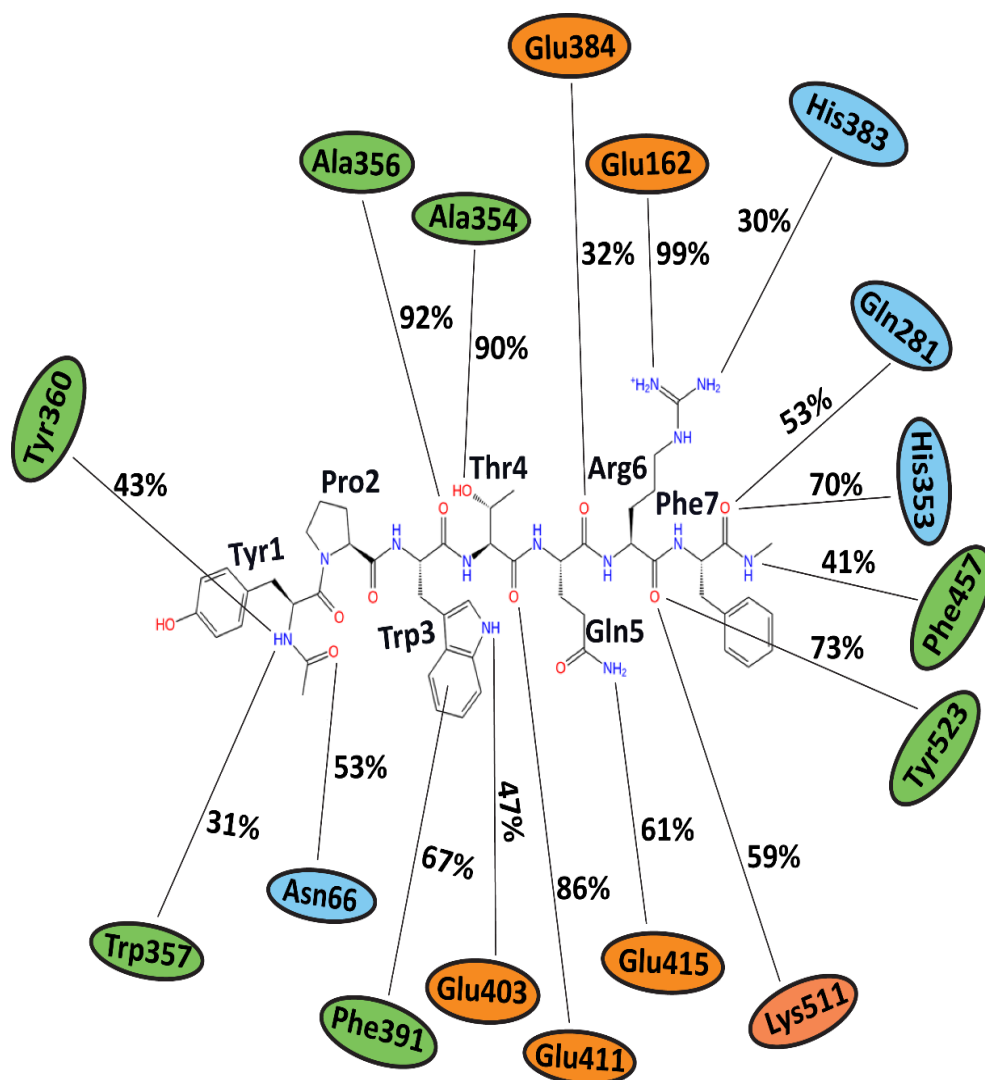


Figure 36: The average percentage of equilibrium simulation time during which ACE residues retain interaction with human hemorphin (YPWTQRF) peptides from triplicate 200 ns simulations. To extract the equilibrium simulation data, the initial 30 ns of each of the 3 simulations were removed. Charged, hydrophobic, and polar amino acids are shown with orange, green and blue color respectively.

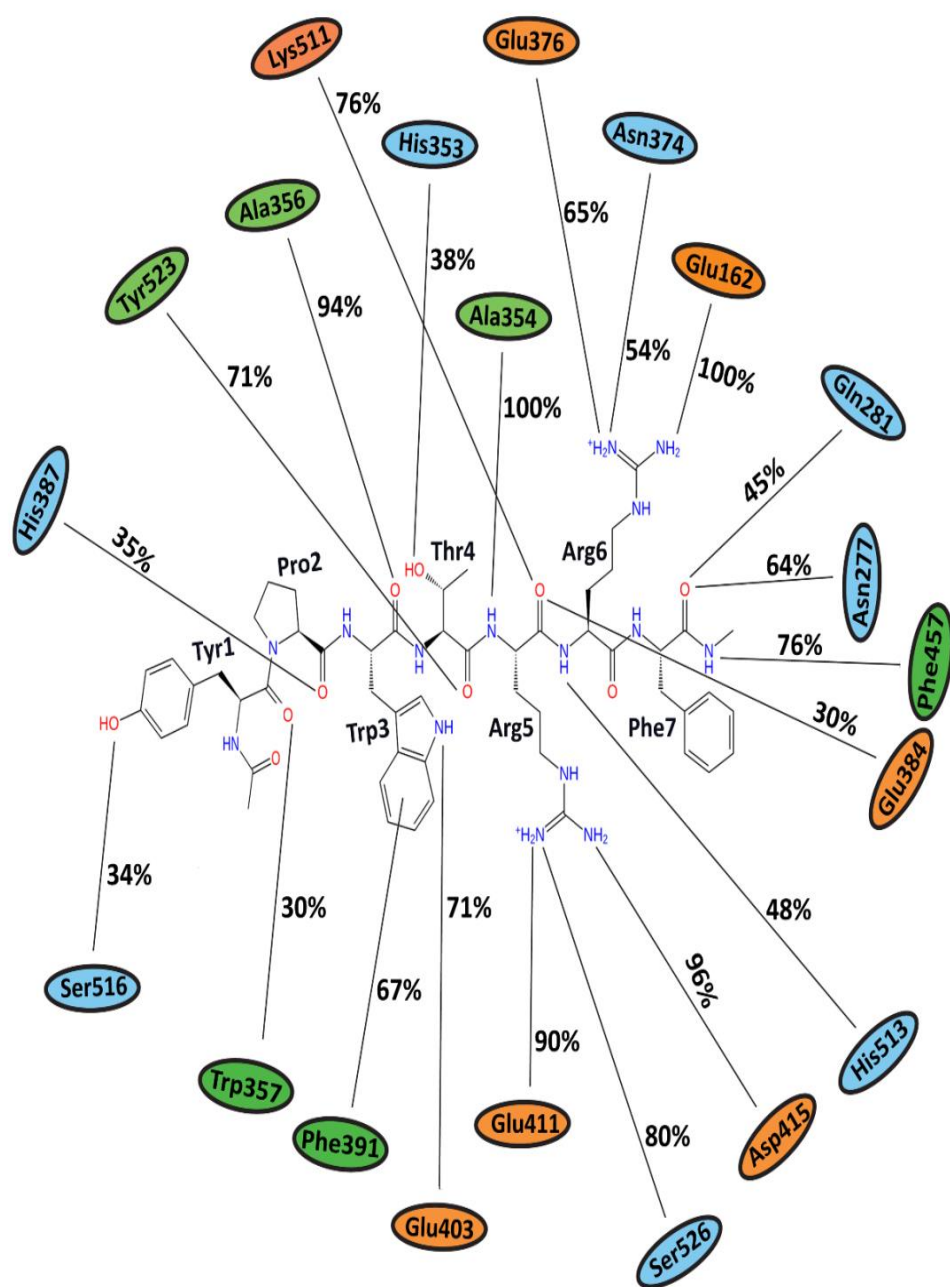


Figure 37: The average percentage of equilibrium simulation time during which ACE residues retain interaction with camel hemorphin (YPWTRRF) peptides from triplicate 200 ns simulations. To extract the equilibrium simulation data, the initial 30 ns of each of the 3 simulations were removed. Charged, hydrophobic, and polar amino acids are shown with orange, green and blue color respectively.



The RMSD of the protein C $\alpha$  atoms stabilized at approximately 2 Å in YPWTRRF-bound simulations, and the protein structure displayed structural stability for the full duration of simulations (Figure 32D). Overall, ACE residues exhibited fewer fluctuations except from loop regions and, the secondary structure remained preserved throughout the simulations (Figure 32D). Figures 33 and 34 demonstrate the average percentage of equilibrated simulation time during which several residues of ACE interacted with two peptides.

#### **4.1.6 In vitro ACE inhibition assay**

The data obtained from the molecular docking and MD simulation indicated that LVVYPWTRRF and YPWTRRF had more hydrogen bonds, electrostatic and hydrophobic interactions with critical amino acids in the active site that are essential for ACE inhibitory activity than LVVYPWTQRF and YPWTQRF, respectively. On the basis of this, it was hypothesized that camel LVVYPWTRRF and YPWTRRF peptides could demonstrate lower IC<sub>50</sub> than non-camel LVVYPWTQRF and YPWTQRF. To investigate this, the ACE inhibitory activity of all four peptides was studied with the help of an *in vitro* ACE inhibition assay.

#### **4.1.7 Determination of ACE inhibitory potential of non-camel and camel hemorphin peptides**

Firstly, longer hemorphin peptides (LVVYPWTQRF and LVVYPWTRRF) of both camel and human were investigated for their ACE inhibitory activity at different doses. ACE inhibitory activity was observed at all tested doses (Figure 38A). Both camel and human peptides demonstrated saturation at 200  $\mu$ M. Importantly, the experimental data exhibited a nice left shift in the dose-response

curve of camel LVVYPWTRRF peptide at all tested doses, relative to LVVYPWTQRF peptide (Figure 38A). Notably, this shift was statistically significant ( $p < 0.0001$ ,  $n = 3$ ) at 10  $\mu\text{M}$ , as demonstrated in Figure 38A. Additionally, dose-response experiments established the left shift of LVVYPWTRRF. This suggests that LVVYPWTRRF peptide exhibited a more potent *in vitro* inhibitory action on ACE. Both LVVYPWTQRF and LVVYPWTRRF peptides demonstrated a dose-dependent inhibitory activity on ACE and  $\text{IC}_{50}$  values were in the micromolar range (Figure 39).  $\text{IC}_{50}$  of LVVYPWTRRF peptide (6.601  $\mu\text{M}$ ) was significantly lower than LVVYPWTQRF peptide (12.649  $\mu\text{M}$ ) ( $p < 0.05$ ,  $n = 3$ ).

Moreover, the ACE inhibitory potential of both YPWTRRF and YPWTQRF was also determined at different doses. Similarly, dose-response data showed that YPWTRRF peptide exhibited a left shift at all tested doses, in comparison to YPWTQRF peptide (Figure 38B). Moreover, this left shift was especially significant at 10  $\mu\text{M}$ , 50  $\mu\text{M}$ , and 100  $\mu\text{M}$  concentrations ( $p < 0.05$ ,  $n = 3$ ). Interestingly, YPWTRRF exhibited significantly lower  $\text{IC}_{50}$  (9.310  $\mu\text{M}$ ) when compared to YPWTQRF (25.894  $\mu\text{M}$ ) ( $p < 0.001$ ,  $n = 3$ ), as demonstrated in the (Figure 39).

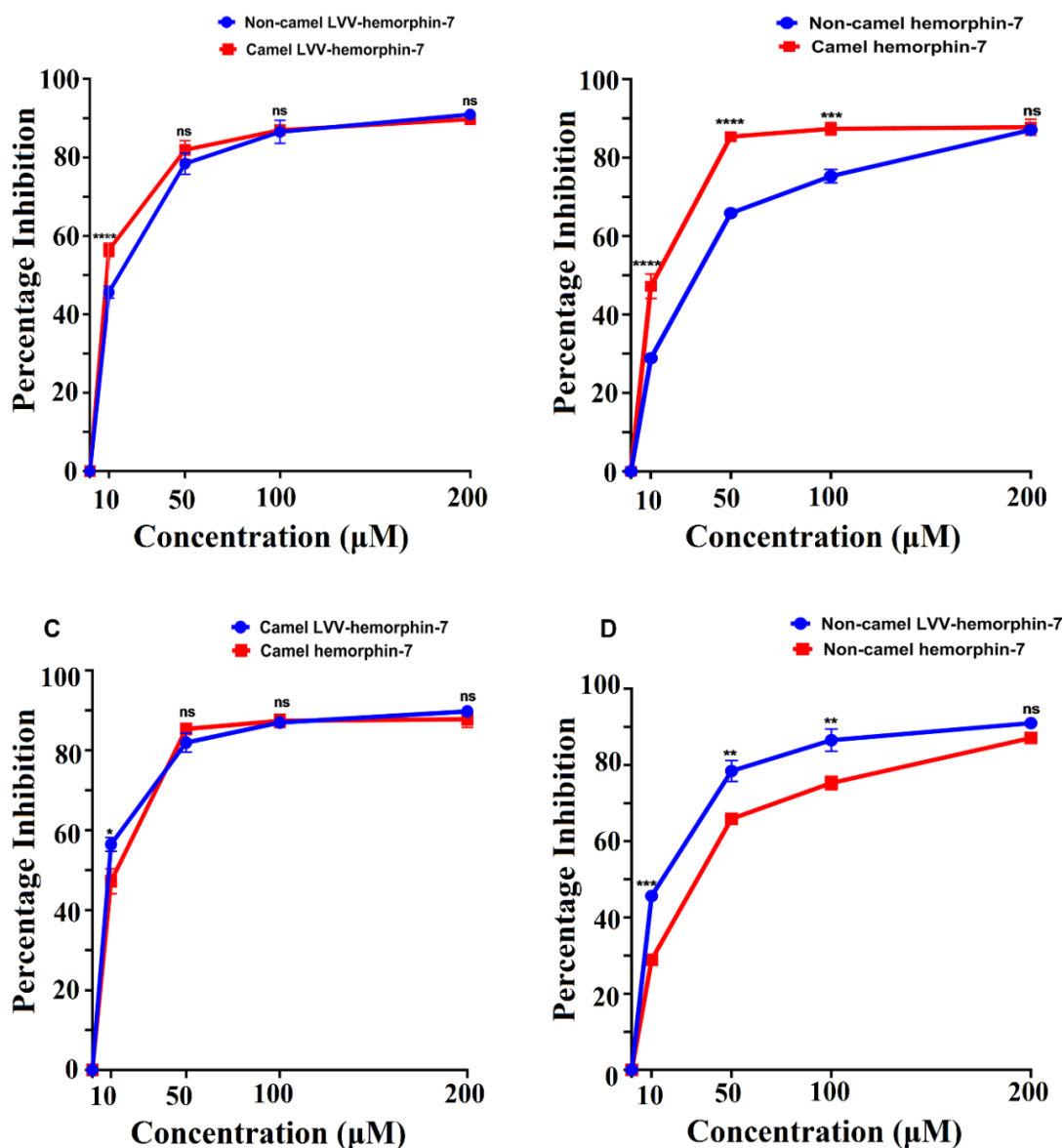


Figure 38: Dose-response curves of different hemorphin peptides. Per dose ACE inhibitory activity is demonstrated in percentage. (A) Comparison of ACE inhibitory activity of LVVYPWTRRF with LVVYPWTQRF at different doses; (B) Comparison of ACE inhibitory activity of YPWTRRF with YPWTQRF at different doses; (C) Comparison of ACE inhibitory activity of LVVYPWTRRF with YPWTRRF at different doses; (D) Comparison of ACE inhibitory activity of LVVYPWTQRF with YPWTQRF. The dose response comparisons were carried out using statistical analysis. For this, two-way ANOVA and Sidak's multiple-comparisons test was used to determine the degree of significance among different peptides. Data are shown as mean  $\pm$  SEM of three independent experiments.

\*\*\*\*  $p < 0.0001$ , \*\*\*  $p < 0.001$ , \*\*  $p < 0.01$ , \*  $p < 0.05$  and ns  $p > 0.05$ .

#### **4.1.8 Comparison of the ACE inhibitory activity of different hemorphin peptides**

Next, the ACE inhibitory role of the N-terminus residues (Leu1, Val2, and Val3) of both LVVYPWTQRF and LVVYPWTRRF peptides were assessed. For this, the ACE inhibition potential of LVVYPWTRRF with YPWTRRF and LVVYPWTQRF with YPWTQRF was evaluated (Figure 10C and 10D). The  $IC_{50}$  of LVVYPWTRRF (6.601  $\mu$ M) was observed to be lower when compared YPWTRRF (9.310  $\mu$ M) (Figure 39).

A comparison of the ACE inhibitory potential of LVVYPWTQRF and its shorter isoform YPWTQRF peptide showed that LVVYPWTQRF demonstrated substantially lower ACE inhibitory potential than YPWTQRF at 10  $\mu$ M, 50  $\mu$ M, and 100  $\mu$ M (Figure 38D). Interestingly, LVVYPWTQRF peptide exhibited significantly lower  $IC_{50}$  (12.649  $\mu$ M) than YPWTQRF (25.894  $\mu$ M) (Figure 39). This clearly indicated a positive role of the N-terminus residues (LVV-) of both LVVYPWTQRF and LVVYPWTRRF peptides in the binding and inhibition of ACE.

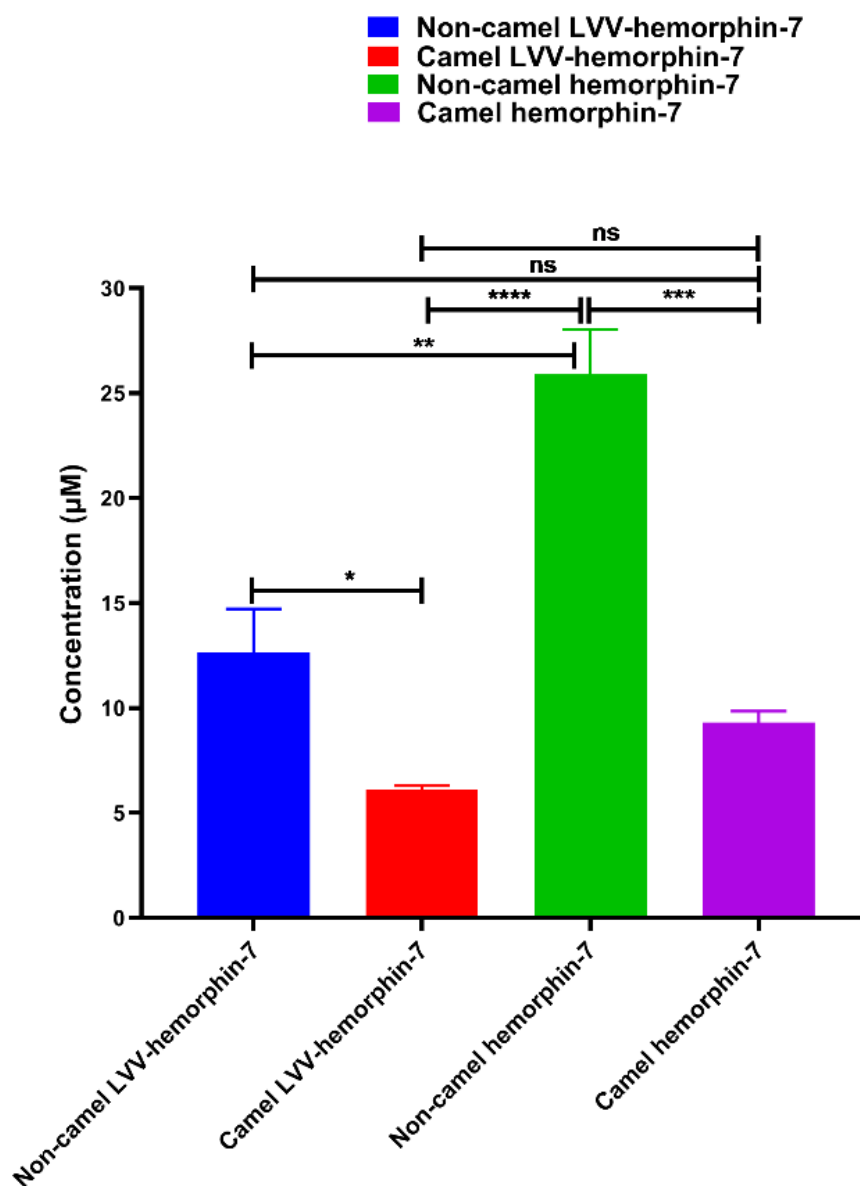


Figure 39: IC<sub>50</sub> of different hemorphin peptides. IC<sub>50</sub> values are shown in micro molar (μM) units, and comparisons of IC<sub>50</sub> was carried out using one-way ANOVA and Sidak's multiple-comparisons test to determine statistical significance between different peptides of hemorphin. Data are shown as mean ± SEM of three independent experiments. \*\*\*\* p < 0.0001, \*\*\* p < 0.001, \*\* p < 0.01, \* p < 0.05, and ns p > 0.05.

## 4.2 Discussion

Hemorphins are a class of bioactive opioid peptides released during proteolytic cleavage of hemoglobin. Their therapeutic potential has been highlighted in various studies (Cejka et al., 2004; Fruitier-Arnaudin et al., 2002; Lee et al., 2004). Molecular binding behavior and binding stability of both camel and non-camel LVV-hemorphin-7 on several targets have also been described in earlier work (Ali et al., 2019). Here, extensive *in silico* approaches and an *in vitro* ACE inhibition assay were employed to determine the precise binding and ACE inhibitory activity of four different human and camel hemorphin peptides. Results showed that LVVYPWTRRF and YPWTRRF peptides bind more stably to vital residues in the ACE active site, in comparison to LVVYPWTQRF and YPWTQRF, respectively. The *in vitro* ACE inhibition assay also supported this finding.

A vital role is played by ACE, which is a membrane-bound zinc metallopeptidase in the regulation of blood pressure by catalyzing the conversion of angiotensin I into angiotensin II, which is a well-known vasoconstrictor (Fleming, 2006). A zinc ion binding motif is present in ACE, coordinated by His383, His387, and Glu411, which is essential for the formation of the ACE-inhibitor complex. Moreover, the active site of ACE is comprised of three subsites, which are also essential for ACE inhibition, termed S1, S2, and S1'. These subsites contain residues that form interactions with potential inhibitors (Abdelhedi et al., 2018; Priyanto et al., 2015). Ala354, Glu384, and Tyr523 comprise the S1 subsite; Gln281, His353, Lys511, His513, and Tyr520 comprise the S2 subsite, and Glu162 constitutes the S1' subsite (Ma et al., 2018).

By using extensive molecular docking and simulations, the binding mode of each peptide with ACE was determined. Overall, all studied hemorphins stably interacted with the active site residues of ACE. The last three residues at the C-terminus of each peptide encompassed all three active subsites of ACE (Figures 24, 25, 28, and 29). Arg9 and Phe10 residues of LVVYPWTQRF anchored the peptide in the S2 and S1' pockets by producing hydrogen bonds with Glu162, Gln281, and Asp453. LVVYPWTQRF peptide residues Thr7 and Gln8 inhabited the S1 and S2 subsites by producing hydrogen bonds with Ala354, Lys511, His513, Tyr520, and Tyr523. They also exhibited consistent interactions with His383, and Glu411 (Figure 34). The positioning of LVVYPWTRRF peptide in the active site of ACE was observed to be slightly different. LVVYPWTRRF was observed to be deeply seated in the active site of ACE. LVVYPWTRRF was stabilized by Arg9 and Phe10 due to the formation of hydrogen bonds with Glu162, Asn277, Thr282, Asn374, and Glu376. Arg9 and Phe10 residues also exhibited polar interaction with Gln281 (Figures 25 and 27). LVVYPWTRRF residues Thr7 and Arg8 showed consistent interactions with vital S1 and S2 subsite residues during the simulation runs. In addition to this, Arg8 of LVVYPWTRRF also showed consistent interactions with Glu411, Asp415, and Ser526, compared to LVVYPWTQRF (Figures 34 and 35). YPWTQRF and YPWTRRF displayed dissimilar binding modes. Particularly, the positioning of Tyr1 and Pro2 residues of the N-terminus, and Arg5, and Phe7 residues of the C-terminus (Figures 28 and 29). Importantly, YPWTRRF showed strong interactions with all vital residues of ACE, such as Glu162, Ala354, Ala356, His387, Glu411, Glu415, Lys511, and Tyr523 during the simulations, in comparison to YPWTQRF (Figures 36 and 37).

FDA approved and widely prescribed ACE inhibitors such as captopril and lisinopril formed interaction with Glu162, His353, Ala354, Glu384, His387, Glu411, Lys511, His513, Tyr520, and Tyr523 of ACE (Natesh, Schwager, Evans, Sturrock, & Acharya, 2004; Wang, Wu, Xu, Xie, & Guo, 2011). However, clinically used ACE inhibitor enalaprilat, does not form any interaction with Glu162. This could be a reason for the lower affinity of enalaprilat when compared to lisinopril (Wang et al., 2011). These amino acids are important for designing prospective ACE inhibitors. Amongst all the hemorphins investigated in this study, only camel hemorphin-7 interacted with His387. Apart from His387 and Tyr520 residues, all the other hemorphins interacted with all of the essential residues, in the active site of ACE.

*In silico* data showed that LVVYPWTRRF and YPWTRRF possessed higher affinity in comparison to LVVYPWTQRF and YPWTQRF, respectively. For validating this, an ACE inhibition assay was carried out to determine the  $IC_{50}$  of these peptides. LVVYPWTRRF and YPWTRRF demonstrated  $IC_{50}$  values of 6.601  $\mu$ M and 9.310  $\mu$ M, respectively (Figure 39). Interestingly, the  $IC_{50}$  of LVVYPWTRRF and YPWTRRF peptides were considerably lower than LVVYPWTQRF (12.649  $\mu$ M) and YPWTQRF (25.894  $\mu$ M). This clearly showed that LVVYPWTRRF and YPWTRRF demonstrated more potent ACE inhibitory activity in comparison to LVVYPWTQRF and YPWTQRF. Nevertheless, the difference between camel hemorphins did not prove to be substantial (Figure 39). The results of non-camel hemorphin peptides were in agreement with the prior studies that were carried out to determine the ACE inhibition potential of hemorphins (Lantz et al., 1991; Zhao & Piot, 1997). Prior studies showed that LVVYPWTQRF has a significantly better ACE inhibitory activity when compared to shorter



hemorphins, such as YPWTQRF (Zhao & Piot, 1997). The results also demonstrated the significance of the hydrophobic N-terminus leucine-valine-valine residues for enhanced ACE inhibition. Moreover, the removal of leucine residue from the N-terminus of LVVYPWTQRF substantially decreased the ACE inhibitory potential of VVYPWTQRF when compared to LVVYPWTQRF. LVVYPWTQRF being a more potent inhibitor of ACE as compared to VVYPWTQRF has also been reported in another comparative study as well (Ali et al., 2019). These results indicate the importance of N-terminus in ACE inhibition.

From the perspective of structural activity, it has been demonstrated through various comparative studies that the ACE inhibition potential of a peptide is dependent on the presence of particular residues at N- and C-termini (Iwaniak et al., 2014). At the N-terminus of a peptide, the presence of hydrophobic residues, in particular leucine, valine, isoleucine and glycine, showed substantially higher ACE inhibitory activity, whereas at the C-terminus, aromatic amino acids, such as phenylalanine, proline, tryptophan, and tyrosine are important (Silvestre et al., 2012). In addition, the presence of charged residues, particularly arginine and lysine, near the C-terminus were also reported to be important to the peptide's inhibitory potential for ACE (Sun et al., 2017). Furthermore, a number of studies have already illustrated this phenomenon, which showed that by the elongation of the N-terminus, the ACE inhibitory potential of certain peptides could be enhanced (Kohmura et al., 1989; Liu et al., 2014). The results from *in silico* and *in vitro* techniques showed that both LVVYPWTRRF and LVVYPWTQRF formed more stable interactions with the active site residues of ACE and showed higher inhibition in comparison to shorter hemorphin-7 peptides. Residues from the N-terminus (leucine-valine-valine) were

found to bind to residues outside ACE's active site. This indicates that this part of the molecule does not appear to have any direct interactions with the active site residues, despite the ACE inhibitory effect. The peptide's substantially enhanced ACE inhibitory activity with the LVV- sequence may be attributed to the peptide's more stable binding in the presence of this sequence. Moreover, the comparative analysis of LVVYPWTRRF and LVVYPWTQRF revealed that LVVYPWTRRF to be a more potent ACE inhibitory peptide as compared to LVVYPWTQRF (Figure 38A). More importantly, the N-terminus residues of LVVYPWTRRF revealed more consistent interactions with Tyr62, Lys118, Glu123, Arg124, Trp220, Glu403, Arg522, and Ser517, whereas an arginine substitution at position 8 exhibited more consistent interactions with Glu411, Glu415, and Ser526 in comparison to LVVYPWTQRF (Figures 34 and 35). Such a binding mode of the mutated arginine residue demonstrated that residues from the N-terminus had been pulled deeper into the binding pocket. Hence, this could be one of the reasons for the higher ACE inhibition potential of camel LVVYPWTRRF. These results are in agreement with prior studies, that stated the significance of leucine and valine at the N-terminus and arginine near the C-terminus for enhanced inhibition of ACE (Sun et al., 2017; Zhao, Sannier, Garreau, Guillochon, & Piot, 1994). Furthermore, for the non-competitive inhibition of ACE, studies have shown that the binding of peptide residues outside the ACE active site, especially with Tyr62 and Asn70, also play an important role (Ni, Li, Liu, & Hu, 2012). Apart from that, a novel dual inhibitor inhabiting both the primary and secondary sites has also been described (Akif et al., 2011). The secondary binding site residues of ACE were found to be Lys118, Glu123, Arg124, Trp220, Glu403, and Arg522. This demonstrates the plasticity of ACE active site in accommodating different types of potent inhibitors (Akif et al., 2011). A similar

pattern was observed when LVVYPWTRRF was compared to the shorter camel hemorphin peptide (YPWTRRF) (Figures 36, and 37). MD simulations also showed that consistent interactions were produced by the N-terminus residues of LVVYPWTQRF with Glu123, Arg124, and Glu143 along with active site residues of ACE, compared to YPWTQRF (Figures 34 and 36). Likewise, comparative analysis of shorter camel (YPWTRRF) and non-camel (YPWTQRF) peptides showed that YPWTRRF exhibited substantially lower  $IC_{50}$  and more consistent interactions with ACE active site residues as compared to YPWTQRF (Figures 38B and 39). Moreover, interactions of the mutated arginine with Glu411, Asp415, and Ser526 placed the peptide more stably in the active site, compared to human hemorphin-7. Importantly, prior studies that investigated the ACE inhibitory activities of peptides have already positively linked the presence of arginine near the C-terminus with higher ACE inhibition (Sun et al., 2017).

## Chapter 5: Pharmacological Action of LVV-Hemorphin-7 on Angiotensin II Type 1 Receptor

### 5.1 Results

*In silico* and *in vitro* assays were performed to determine the pharmacological action and appropriate binding mode of LVV-hemorphin-7 on AT1R.

#### 5.1.1 Weak agonistic effect of LVV–Hemorphin-7 on AT1R

BRET technology in HEK293 cells was used to determine the pharmacological effects of camel and human LVV-hemorphin-7 on the functional AT1R-Gαq coupling and β-arrestin 2 recruitment to AT1R, in real time and live cells, as described in earlier studies (Ayoub et al., 2015). The activation of Gαq-mediated IP1 production, as an important AT1R downstream signaling pathway, was also examined. In this study, for the measurement of BRET assays in HEK293 cells, AT1R-Rluc was used as the BRET donor, co-expressed with either mini Gαq (mGsq) probe consisting of the GTPase domain of Gαq fused to Venus, as BRET acceptor (Wan et al., 2018), or yPET-β-arrestin 2. BRET experiments were carried out in the presence or absence of treatment of cells with different doses of AngII, camel LVV–hemorphin-7 or human LVV-hemorphin-7. The results indicated that AngII potentiated the BRET signals in a dose dependent manner between AT1R-Rluc and both Venus-Gαq and yPET-β-arrestin 2 (Figures 40A and 40B) (Table 5). Nevertheless, a partial effect on AT1R-Gαq coupling and β-arrestin 2 recruitment was observed only at high doses of camel and human LVV–hemorphin-7 (10–100 μM) (Figures 40A and 40B). This also suggested that both camel and human LVV–hemorphin-7 did not produce strong pharmacological effects on AT1R at reasonable

doses. Since, both camel and human LVV-hemorphin-7 produced similar potency, therefore human LVV-hemorphin-7 was used for further studies.

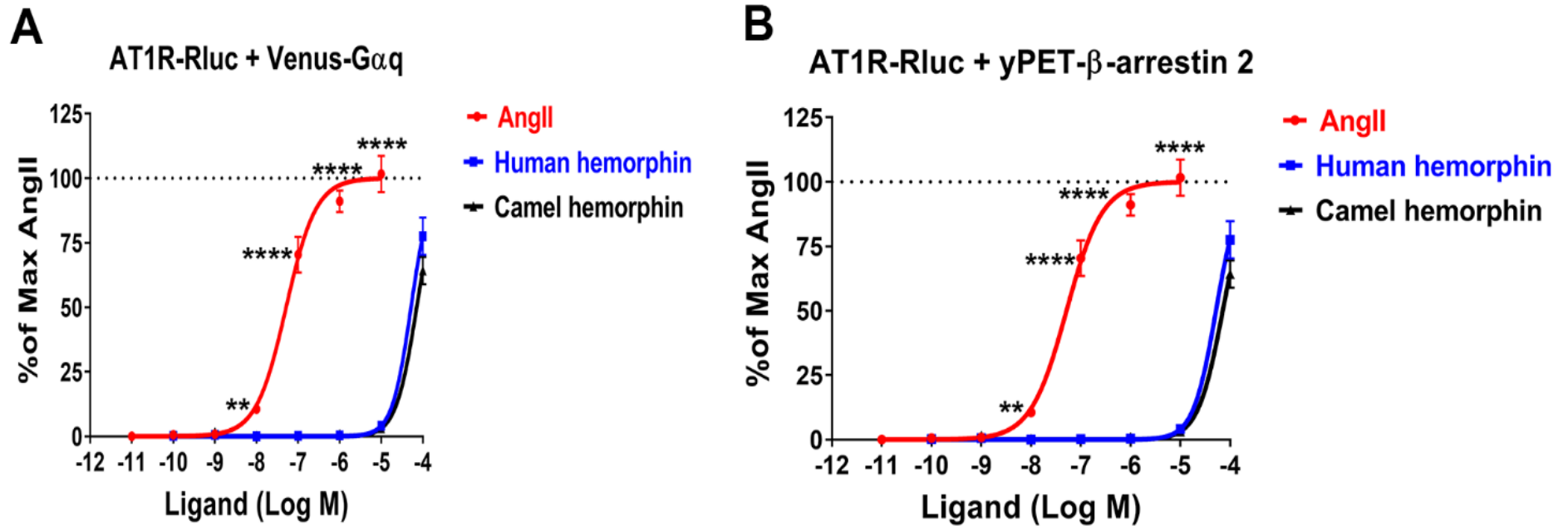


Figure 40: LVV-hemorphin-7's action on AT1R. BRET experiments were performed on human embryonic kidney (HEK293) cells briefly co-expressing AT1R-Rluc (as BRET donor) and either Venus-Gαq or yPET-β-arrestin 2 (as BRET acceptors) simulated or not with either AngII, LVV-hemorphin-7 or both. For the purpose of BRET measurements, HEK293 cells co-expressing AT1R-Rluc and either Venus-Gαq (A) or yPET-β-arrestin 2 (B) were simulated with different doses of AngII or LVV-hemorphin-7 at 37°C for 30 minutes and BRET measurements were determined. Data are represented as means ± SEM of 5 independent experiments carried out in triplicate.

Table 5: Log EC<sub>50</sub> values of LVV-hemorphin-7 and AngII. Two-way ANOVA and Tukey multiple-comparisons test was performed to measure the statistical significance between different treatment conditions.

<b>Transfections</b>	<b>Log EC<sub>50</sub> AngII (BRET)</b>		<b>Log EC<sub>50</sub> AngII (IPI)</b>		<b>Log EC<sub>50</sub> LVV-hemorphin-7 (BRET)</b>
AT1R-Rluc + Venus-Gαq	Control -7.68 ± 0.17	LVVhemorphin-7 -8.78 ± 0.14 ( <i>p</i> <0.001, n=6)	Control -7.57 ± 0.19	LVV-hemorphin-7 -8.93 ± 0.17 ( <i>p</i> <0.0001, n=7)	-5.41 ± 0.29 (n=5)
AT1R-Rluc + Ypet-β-arrestin 2	Control -7.75 ± 0.23	LVV-hemorphin-7 -8.91 ± 0.19 ( <i>p</i> <0.01, n=5)		ND	-5.48 ± 0.35 (n=5)
AT1R-WT		ND	Control -8.15 ± 0.03	LVV-hemorphin-7 -9.55 ± 0.03 ( <i>p</i> <0.0001, n=3)	ND

### 5.1.2 Positive allosteric effects of LVV-hemorphin-7 on AT1R

Multiple dose-response and real-time kinetic BRET assays were performed to determine the possible pharmacological action of LVV-hemorphin-7 on AngII-mediated AT1R activation. In order to measure the effects of dose-response experiments, cells were initially incubated with different doses of LVV-hemorphin-7 for 15 min, after that BRET reading were calculated upon stimulation of AT1R with different doses of AngII. Curves plotted from AngII BRET results between AT1R-Rluc and Venus-Gαq or yPET-β-arrestin demonstrated a substantial left shift (more than one log,  $p < 0.001$ ,  $n = 3$ ), 2 in cells incubated with either 10 or 100 μM of LVV-hemorphin-7 in comparison to control cells (Figures 41A and 41B). Moreover, to obtain statistically significant data, these dose-response experiments were repeated both in the presence of LVV-hemorphin-7 (10 μM) and absence (control). The additional dataset supported the previous experiment results, and a left shift of the AngII dose curves for BRET was observed between AT1R-Rluc and Venus-Gαq ( $p < 0.001$  for the whole dose curve,  $n = 6$ ) or yPET-β-arrestin 2 ( $p < 0.001$  for the whole dose curve,  $n = 5$ ) in cells pretreated with 10 μM of LVV-hemorphin-7 in comparison to control cells (Figures 41C and 41D) (Table 5). These results for the first time showed a positive pharmacological action of LVV-hemorphin-7 on AT1R activation briefly expressed in HEK293 cells. On the basis of these results, where a combination of 10 μM of LVV-hemorphin-7 and 10 nM of AngII, produced approximately 25% of AT1R-mediated response was selected and used for further BRET kinetics and functional assays.

In order to further confirm the positive pharmacological action of LVV-hemorphin-7 on AT1R, dose-response experiments were carried out the other way



around by either prior incubation of cells for 15 min or not in the presence of different doses of LVV-hemorphin-7 and then cells were activated with 10 nM of AngII for 20 min. The results clearly indicated that AngII-mediated BRET signals between AT1R-Rluc and Venus-Gαq or yPET-β-arrestin 2 were substantially increased by LVV-hemorphin-7 in a dose-dependent manner with EC<sub>50</sub> in the micromolar range (Table 5) (Figures 42A and 42B).

In this study, the thrombin receptor or protease-activated receptor 1 (PAR1) was used as a negative control, and the pharmacological action of LVV-hemorphin-7 were also investigated on this GPCR. The results indicated that LVV-hemorphin-7 did not produce any noteworthy changes in the dose-response curves of thrombin-mediated BRET increase between PAR1-Rluc and either Venus-Gαq or yPET-β-arrestin2 (Figures 42C and 42D).

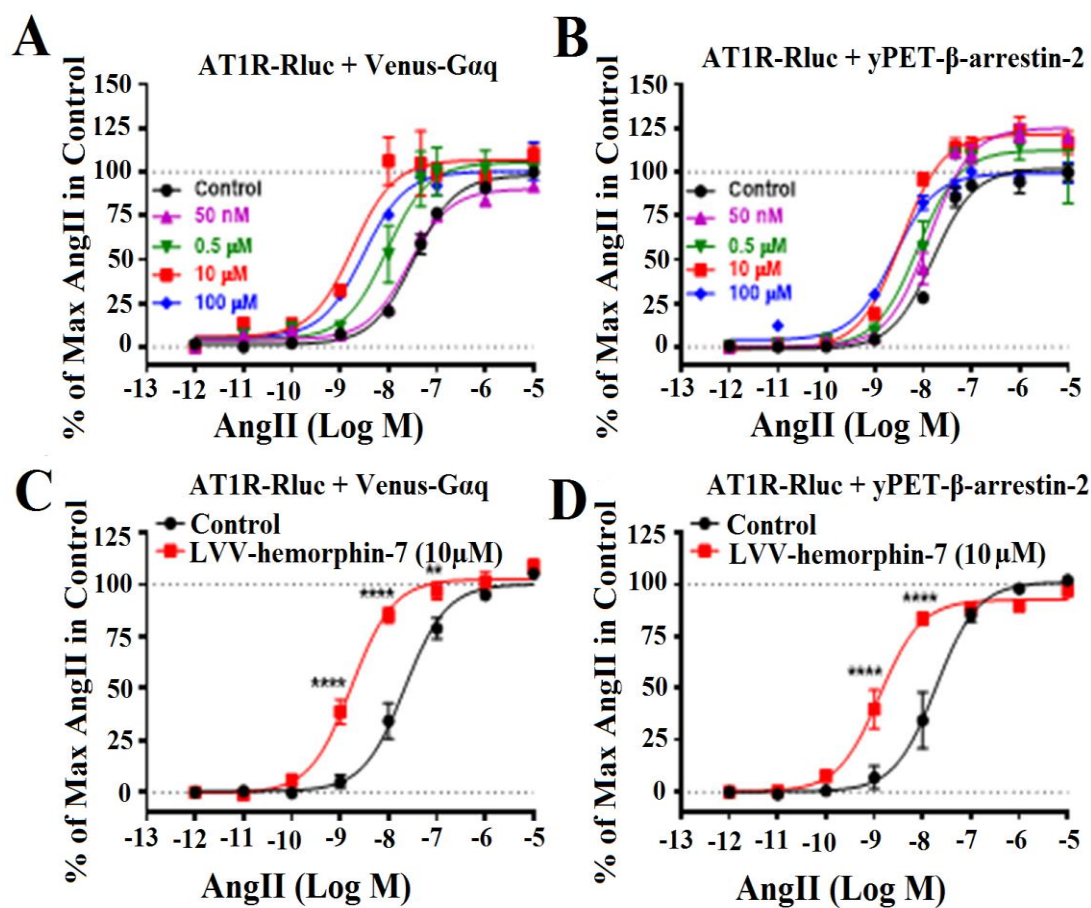


Figure 41: Positive allosteric modulation of LVV-hemorphin-7 on AT1R activation demonstrated by dose-response BRET technique. For dose-response BRET analysis, human embryonic kidney (HEK293) cells briefly co-expressing AT1R-Rluc and either Venus-Gαq (A, and C) or yPET-β-arrestin 2 (B, and D) were used. In A and B, HEK293 cells were initially incubated or not (control) with different doses of LVV-hemorphin-7 for 15 minutes and then challenged with different doses of AngII for 30 minutes. In C and D, HEK293 cells were initially incubated or not (Control) with 10 μM of LVV-hemorphin-7 for 15 minutes and then cells were treated with different doses of AngII for 30 minutes. Data are represented as means  $\pm$  SEM of 5-6 independent experiments carried out in triplicate.

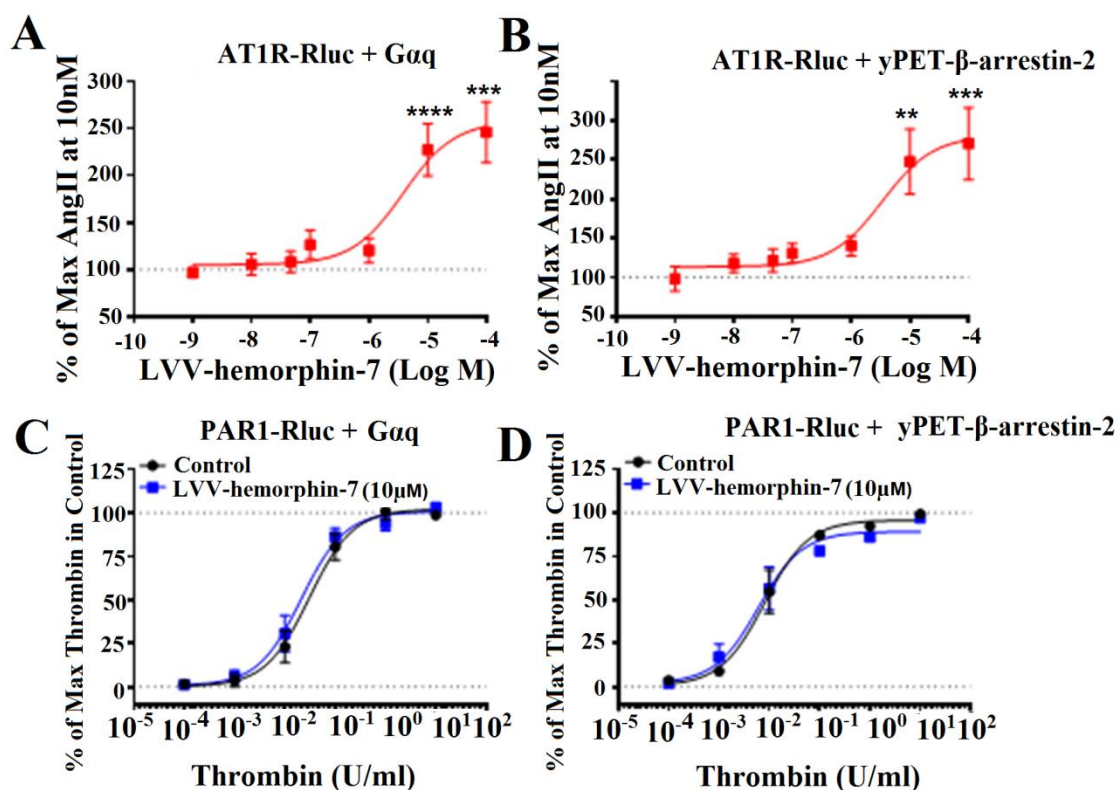


Figure 42: Positive allosteric modulation of LVV-hemorphin-7 on AT1R activation demonstrated by dose-response BRET technique. For dose-response BRET analysis, human embryonic kidney (HEK293) cells briefly co-expressing AT1R-Rluc and either Venus-Gαq (A) or yPET-β-arrestin 2 (B) were used. In A and B, HEK293 cells were initially incubated with different doses of LVV-hemorphin-7 for 15 minutes and then challenged with 10 nM of AngII for 30 minutes. Next, HEK293 cells briefly co-expressing PAR1-Rluc and either Venus-Gαq (C) or yPET-β-arrestin 2 (D) were initially incubated or not (control) with 10 μM of LVV-hemorphin-7 for 15 minutes and then challenged with different doses of thrombin, as a negative control for 30 minutes. Data are represented as means ± SEM of 3 (C and D) or 5-6 independent experiments carried out in triplicate.

### 5.1.3 Confirmation of the positive allosteric effects of LVV-hemorphin-7 on AT1R

Several real-time BRET kinetics were performed to further observe the PAM effects of LVV-hemorphin-7 on AT1R activation. For this, HEK293 cells briefly co-expressing AT1R-Rluc with either Venus-Gαq or yPET-β-arrestin 2 were used and stimulated with different combinations of AngII and LVV-hemorphin-7 in different protocols (Figures 43A, B, C, D, and F). Initially, BRET readings were measured in

real time immediately after cells were stimulated or not with either LVV-hemorphin-7 (10  $\mu$ M), AngII (10 nM), or both. The results of real time kinetics experiments demonstrated that the combination of LVV-hemorphin-7 and AngII substantially increased the BRET signals within AT1R-Rluc/Venus-G $\alpha$ q and AT1R-Rluc/yPET- $\beta$ -arrestin 2 pairs, in comparison to a single treatment of cells with AngII (Figure 39A and 39B) (Table 6). Additionally, LVV-hemorphin-7 also produced a partial agonistic effect on BRET between AT1R-Rluc and yPET- $\beta$ -arrestin 2 (Figure 43B). However, this effect was observed to be very weak between AT1R-Rluc and Venus-G $\alpha$ q (Figure 43A).

Next, sequential real-time kinetics experiments were carried out where BRET readings were determined before the treatment of cells for 5 min, which formed the baseline level. After 5 min, cells were treated with or not LVV-hemorphin-7 (10  $\mu$ M) (treatment 1 or T1) for 10 min, and lastly cells were challenged or not with AngII (10 nM) (treatment 2 or T2) for 25 min. The results of these kinetics experiments demonstrated a very weak, approximately 10% potentiation of BRET signals specifically in cells treated with LVV-hemorphin-7 only after 35 min of measurements. Nevertheless, AT1R-Rluc/Venus-G $\alpha$ q and AT1R-Rluc/yPET- $\beta$ -arrestin 2 pairs exhibited significantly higher AngII-induced BRET signals in cells which were initially stimulated with LVV-hemorphin-7, in comparison to those treated with vehicle (Figures 43C, and 43D) (Table 6). Moreover, BRET kinetics experiments were also carried out in such a way that cells were initially challenged with 10 nM of AngII for approximately 15 to 20 min to initiate BRET potentiation between AT1R-Rluc/Venus-G $\alpha$ q and AT1R-Rluc/yPET- $\beta$ -arrestin 2 pairs before treating the cells with 10  $\mu$ M of LVV-hemorphin-7 (Figures 43E and 43F). The

results of these experiments demonstrated a substantial BRET increase beyond the AngII-induced level in both cases signifying the positive allosteric effect of LVV-hemorphin-7. This indicates that LVV-hemorphin-7 can also produce PAM effect even after AngII binding to AT1R. Overall, these kinetic results were in agreement with the dose-response tests as demonstrated in Figure 38 showing the PAM effect of LVV-hemorphin-7 on AT1R activation.

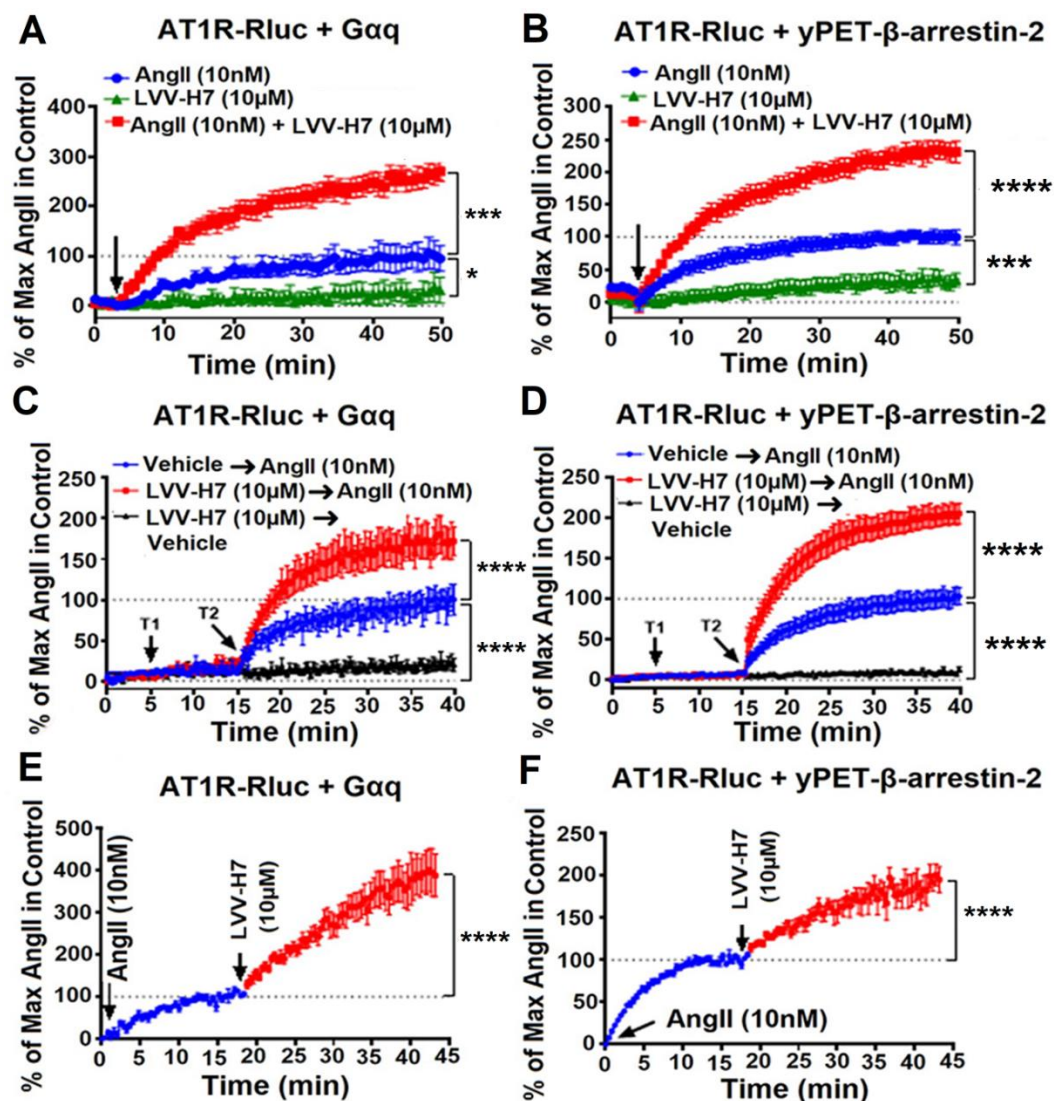


Figure 43: Positive allosteric modulation of LVV-hemorphin-7 on AT1R activation demonstrated by real-time BRET kinetic analysis. For this, HEK293 cells briefly co-expressing AT1R-Rluc and either Venus-Gaq or yPET-β-arrestin 2 were used. In A and B, BRET measurements were determined before (baseline) and upon cell treatment (arrow) with either 10 nM AngII, 10 μM LVV-hemorphin-7, or both for 50 minutes. However, in C and D, BRET measurements were determined without any treatment (baseline) for 5 minutes and then HEK293 cells were challenged or not (vehicle) with 10 μM of LVV-hemorphin-7 (T1) for 10 minutes and then further simulation or not (vehicle) with 10 nM of AngII (T2) for 25 minutes. While, in E and F, HEK293 cells were initially treated with 10 nM of AngII and BRET readings were calculated for approximately 20 minutes without any further treatment with 10 μM of LVV-hemorphin-7 and additional BRET readings were determined for 25 minutes. Data are represented as means ± SEM of 5-8 independent experiments carried out in duplicate or triplicate.

Table 6: Percentage  $E_{\max}$  values of AngII in the various BRET assays. An appropriate statistical analysis was performed to determine the degree of significance. Kinetics 1 and 2 correspond to the data in Figure 39A/B and Figure 39C/D, respectively.

<b>Transfections</b>	<b><math>E_{\max}</math></b> <i>(BRET dose-response)</i>	<b><math>E_{\max}</math></b> <i>(BRET kinetics 1)</i>	<b><math>E_{\max}</math></b> <i>(BRET kinetics 2)</i>
AT1R-Rluc + Venus-Gαq	109 ± 2  <i>(p&gt;0.05, n=9)</i>	263 ± 6  <i>(p&lt;0.0001, n=6)</i>	171 ± 3  <i>(p&lt;0.0001, n=8)</i>
AT1R-Rluc + yPET-β-arrestin 2	104 ± 4  <i>(p&gt;0.05, n=8)</i>	240 ± 5  <i>(p&lt;0.0001, n=5)</i>	200 ± 0.2  <i>(p&lt;0.0001, n=5)</i>

#### 5.1.4 Activation of AT1R by LVV-hemorphin-7

In order to observe the effect of AT1R inhibition on both AngII and LVV-hemorphin-7-mediated BRET potentiation, irbesartan was used as a selective AT1R antagonist on cells briefly co-expressing AT1R-Rluc with either Venus-Gαq or yPET-β-arrestin 2 (Figures 44A and 44B) challenged or not with either 10 μM of LVV-hemorphin-7, or 10 nM of AngII, or both. These experiments results initially established the substantial positive allosteric effects of LVV-hemorphin-7 on AngII-induced BRET potentiation in both BRET case scenarios with AT1R-Rluc and either Venus-Gαq or yPET-β-arrestin 2 (Figures 44A and 44B). Interestingly, a complete inhibition of AngII-induced BRET signal was detected and their increase by LVV-hemorphin-7 immediately after treatment with 10 μM dose of irbesartan (Figures 44A, and 44B). Indeed, these results clearly indicate that the PAM action of LVV-hemorphin-7 encompasses the active conformation of AT1R.



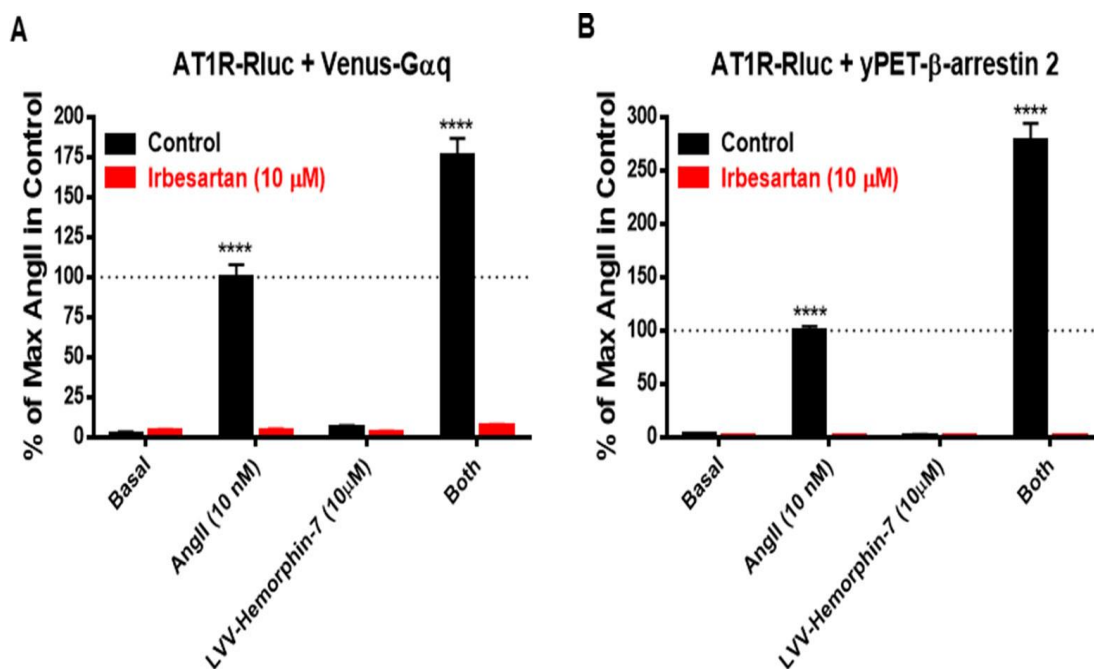


Figure 44: AT1R-selective antagonist (irbesartan) inhibited both AngII- and LVV-hemorphin-7-mediated BRET potentiation. Before measuring BRET signals, HEK293 cells briefly co-expressing AT1R-Rluc and either Venus-Gαq (A) or yPET-β-arrestin 2 (B) were initially stimulated or not (control using DMSO) with 10 μM of irbesartan at 37°C for 15 minutes. Next, cells were treated or not (basal) with either 10 nM of AngII, 10 μM of LVV-hemorphin-7, or both, at 37°C for 30 minutes were carried out. Data are represented as means ± SEM of 3 independent experiments performed in duplicate.

### 5.1.5 Effects of LVV-hemorphin-7 on AT1R-mediated downstream signaling

In order to associate the BRET results with downstream signaling pathways of AT1R, the pharmacological action of LVV-hemorphin-7 on AT1R-mediated IP1 production was determined as an indicator for Gαq/phospholipase C activation. To measure this, experimental conditions similar to BRET experiments were used. For this, initially HEK293 cells were used, briefly co-expressing Venus-Gαq and AT1R-Rluc. Initially, the assumed agonistic effect of LVV-hemorphin-7 was determined on AT1R-mediated IP1 production in cells challenged with different doses of either LVV-hemorphin-7 or AngII as control. As expected, LVV-hemorphin-7 did not exhibit any notable effect on IP1 production even at 100 μM, while AngII nicely

induced IP1 production in a dose-dependent manner and with the expected potency (Figure 45A) (Table 6). Additionally, the positive allosteric effect of LVV-hemorphin-7 was determined on AngII-mediated IP1 response by treating cells with the different doses of AngII with or no pretreatment of cells for 15 min with 10  $\mu$ M of LVV-hemorphin-7. Similar to BRET experiments, LVV-hemorphin-7 potentiated a noteworthy left shift of the AngII dose-dependent curve with a profound effect, approximately 18.6-fold increase in AngII, EC50, relative to BRET data (Table 6)

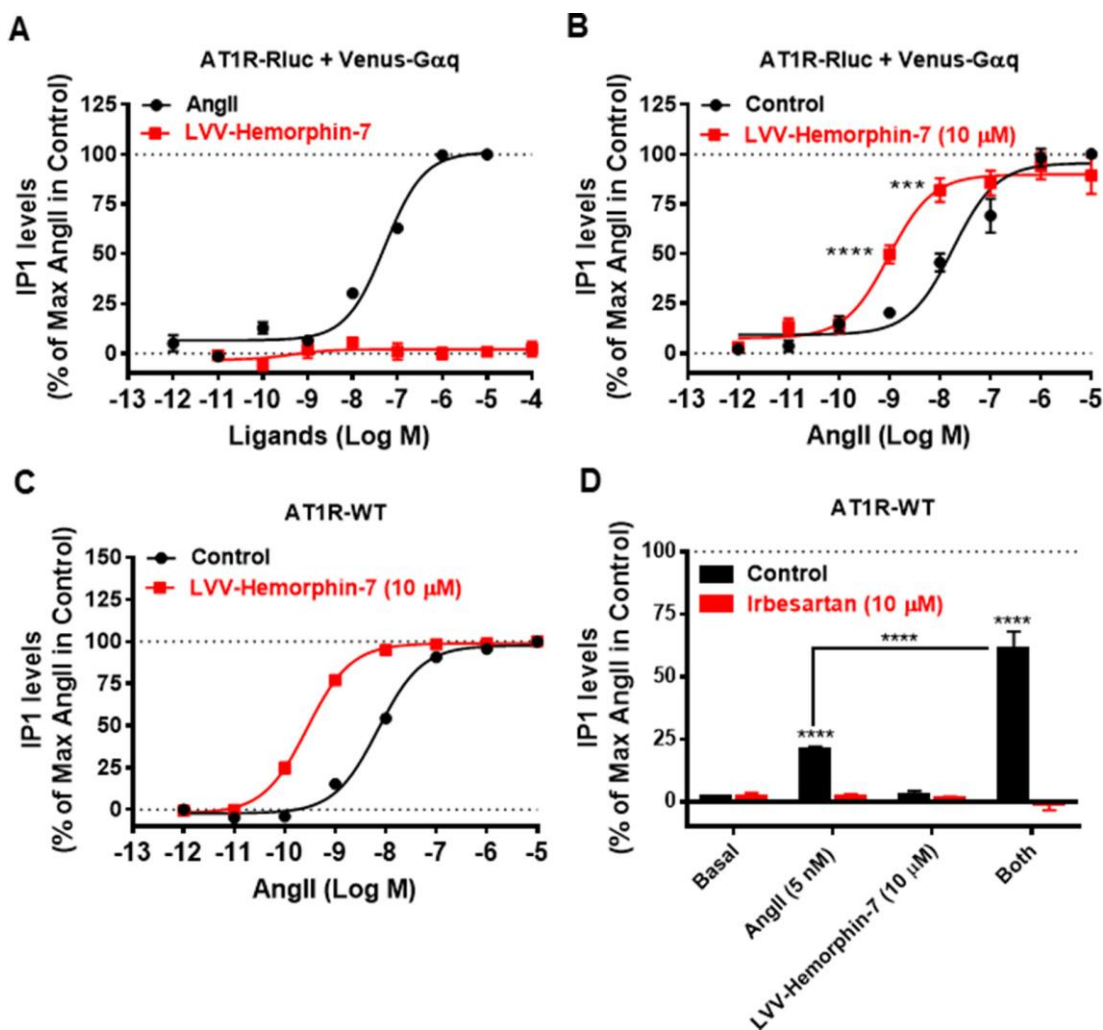


Figure 45: Positive allosteric modulation of LVV-hemorphin-7 on AT1R-mediated IP1 production. For IP1 assays, HEK293 cells briefly co-expressing AT1R-Rluc with Venus-Gαq or AT1R-WT was used (Figure A-D). For IP1 measurements in dose-response experiments, cells were challenged or not with the different doses of either AngII or LVV-hemorphin-7 or first pre-treated or not (Control) with 10 μM of LVV-hemorphin-7 for 15 minutes and then stimulated for 30 minutes with different doses of AngII (A-C). HEK293 cells expressing AT1R-WT were initially pre-treated or untreated (control using DMSO) with 10 μM of AT1R antagonist (Irbesartan) at 37°C for 15 minutes (D). After that, cells were treated or untreated (basal) with either 5 nM of AngII, 10 μM of LVV-hemorphin-7, or both, at 37°C for 30 minutes, before IP1 assays were carried out. IP1 data are represented as means ± SEM of 3-7 independent experiments carried out in duplicate or triplicate.

In order to rule out the possibility of any artifact in these experiments since only AT1R-Rluc co-expressed with Venus-Gαq similar to BRET experiments. Therefore, IP1 experiments were also carried out in HEK293 cells briefly expressing the untagged AT1R (AT1R-WT). The results of these experiments indicated that

AngII nicely promoted IP1 production in a dose–response manner, and combined treatment of cells with LVV–hemorphin-7 (10  $\mu$ M) substantially left shifted the AngII dose-dependent curve with approximately 25-fold potentiation in AngII EC<sub>50</sub> (Table 6). This also indicates the positive pharmacological effect of LVV–hemorphin-7 on AT1R-mediated IP1 response.

Moreover, irbesartan, a selective antagonist of AT1R was used to investigate its effect of AT1R inhibition, by using the same conditions and protocols as were used for BRET assays. In these experiments, AT1R-WT expressed on HEK293 cells was used treated or untreated with 10  $\mu$ M dose of irbesartan, after that cells were treated or not with LVV–hemorphin-7 dose of 10  $\mu$ M, either individually or together with a non-saturating dose of AngII (5 nM). Results clearly indicated that both AngII-mediated IP1 formation and its substantial increase by LVV–hemorphin-7 were fully blocked by the treatment of irbesartan. These results are in agreement with the BRET data as demonstrated in Figure 45.

Overall, the results of IP1 experiments in both AT1R-WT and AT1R-Rluc validated the positive allosteric effect of LVV–hemorphin-7 on the activation of AT1R and its downstream signaling pathways.

#### **5.1.6 Molecular docking and molecular dynamics studies**

In order to determine the stability and dynamics of the nteractions between ACE and hemorphin peptides, all-atom MD simulations were run in triplicate using Desmond (Bowers et al., 2006).

### 5.1.7 LVV-hemorphin-7 binds to an intracellular site of AT1R

SiteMap analysis identified three potential binding sites in AT1R – two were intracellular and the third was the extracellular orthosteric site. Since the *in vitro* data indicated positive allosteric effects of LVV-hemorphin-7, two potential binding cavities outside the orthosteric site were explored. LVV-hemorphin-7 was docked to intracellular sites of AT1R identified by SiteMap. However, one of the intracellular sites produced extremely poor docking results and was therefore excluded from further studies. The best-docked pose of LVV-hemorphin-7-AT1R complex in the other site produced a GScore of -11.05 kcal/mol. MM-GBSA based binding free was estimated as -125.05 kcal/mol (Table 7). The docked conformation of LVV-hemorphin-7 in this site interacted with intracellular loops 2 and 3, and the cytoplasmic end of transmembrane helices 3 and 6 (TM3 and TM6) of AT1R. The first three residues of the decapeptide formed hydrogen bonds with His132 and Lys135, hydrophobic interaction with Tyr127, and an electrostatic interaction with Arg137 (Figures 46 and 47). The side chain of LVV-hemorphin-7 Tyr4 formed a hydrogen bond with Val131 (Figures 4C and 46D). Pro5, Trp6 and Thr7 of LVV-hemorphin-7 formed hydrophobic interactions with Ile130, Pro133, Met134 and Ala221 of AT1R. Trp6 also formed an electrostatic interaction with Arg234. C-terminus residues Gln8, Arg9, and Phe10 of LVV-hemorphin-7 formed hydrogen bonds with Lys60 and Arg126. They also exhibited hydrophobic interactions with Val62, Ala129, Leu138, Met142, Ala225, Pro233 and Ile238, electrostatic interactions with Lys230 and Lys232, and polar interactions with Thr61 and Asn235 (Table 7 and Figure 47).

Five hundred nanosecond all-atom MD simulations of the docked system embedded in a DPPC membrane were performed in triplicate to investigate the binding dynamics and stability of the AT1R-LVV-H7 complex using Desmond (Bowers et al., 2006). Protein structure in the simulated systems remained stable with a protein C $\alpha$  root mean square deviation (RMSD) under 3.5 Å (Figure 48A). Per residue level root mean square fluctuation (RMSF) highlighted that intracellular loops (ICL) ICL1, ICL2 and ICL3 and extracellular loop (ECL) ECL2 were more flexible while membrane-embedded regions exhibited limited fluctuations (Figure 48D). The decapeptide interacted consistently with ICL2, and ICL3, while its interactions with TM3 and TM6 were considerably weak. The N-terminus residues (Val2 and Val3) formed intermittent interactions with His132 and Ala221 of ICL2 and ICL3, respectively (Figure 52). Tyr4 formed intermittent interactions with Val131 and Lys135 of ICL2. Pro5 showed an intermittent hydrogen bond with Met134 of ICL2. Trp6 of the peptide formed an intermittent hydrophobic interaction with Arg126 and a consistent hydrophobic interaction with Pro133 and Arg234 of ICL2 and ICL3. Gln8 exhibited sustained hydrophobic interactions with Ile130 and Pro233. Arg9 also intermittently interacted with Ala129 of ICL2. These ICL2 residues have been reported to form an allosteric site in other GPCRs (Luderman et al., 2018; P. Zhang et al., 2015).

Table 7: AT1R residues that interacted with the best docked pose of LVV-H7 and AngII.

Peptide	AT1R PBD ID	Glide docking score (kcal/mol)	MM-GBSA binding free energy (kcal/mol)	Residues forming hydrogen bonds	Residues forming hydrophobic interactions	Residues forming $\pi$ - $\pi$ stacking or cation- $\pi$ interactions
LVV-H7 (IC)	4ZUD	-11.05	-125.05	Lys60, Arg126, Val131, His132, Lys135	Val62, Tyr127, Ile130, Pro133, Met134, Leu138, Met142, Ala221, Ala225, Pro233, Ile238	Arg234
AngII	4ZUD	-12.01	-129.31	Arg167, Tyr184, Glu185, Ser186, Thr260, Asp263, Asp281	Leu13, Cys18, Ala21, Ile31, Tyr35, Trp84, Tyr87, Tyr92, Val108, Leu112, Pro162, Ala163, Phe182, Ile172, Val179, Ala181, Trp253, Ile266, Ala277, Val280, Met284, Pro285	
AngII together with LVV-H7	4ZUD	-13.51	-160.71	Ser15, Lys20, Tyr87, Arg167, Lys199, Asp263, Gln267, Asp281	Leu13, Pro19, Ala21, Tyr35, Phe77, Trp84, Val108, Leu112, Tyr113, Ala159, Pro162, Ala163, Ile172, Cys180, Ala181, Phe182, Tyr184, Leu195, Phe204, Ile266, Met284, Pro285, Ile288, Tyr292	Tyr9, Tyr87

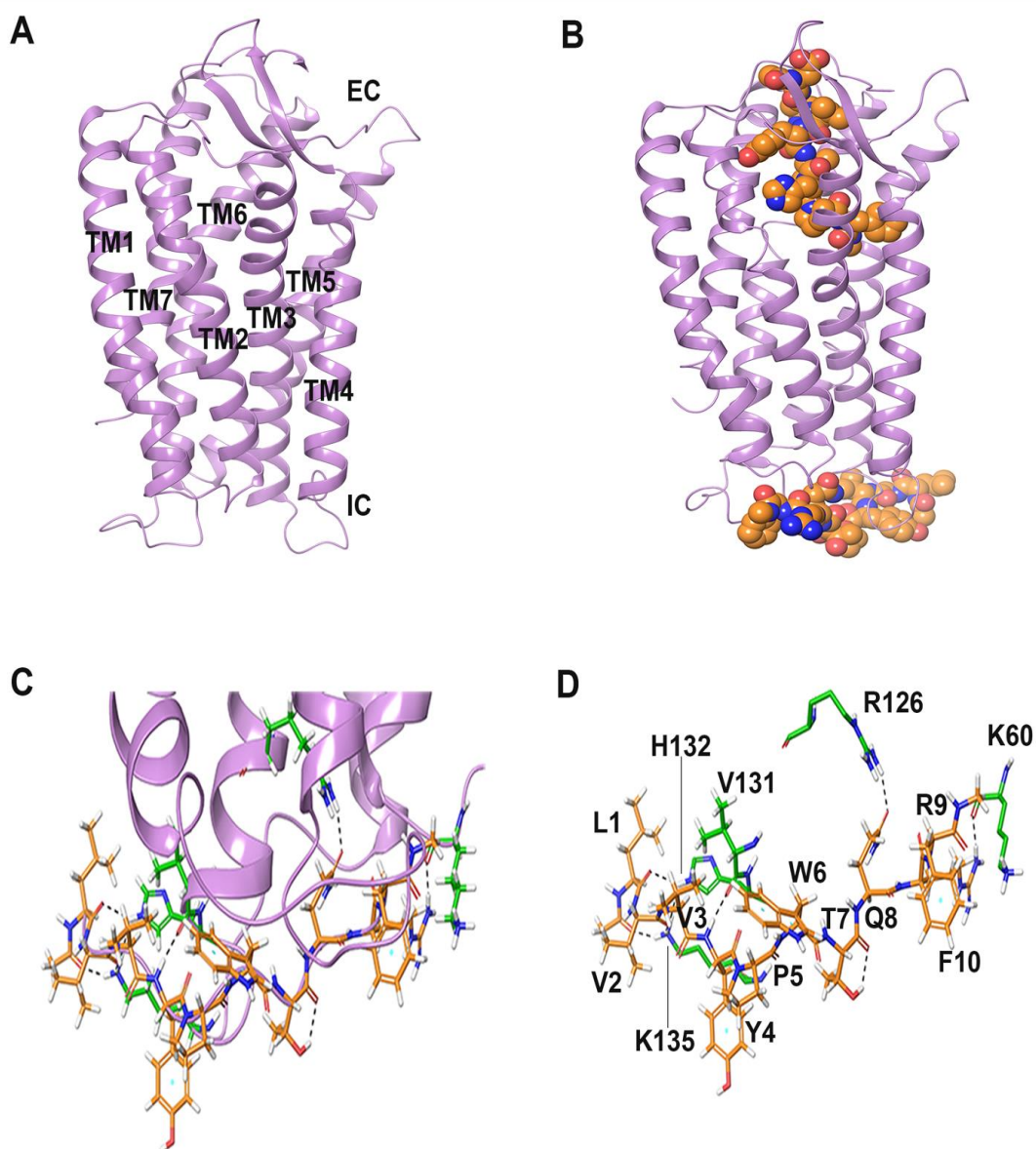


Figure 46: Structure of AT1R with the docked peptide. AT1R structure is shown in purple cartoon representation while its interacting residues are shown in green stick representation. Docked peptide is shown in orange stick representation. Black dotted lines represent hydrogen bonds and blue lines represent  $\pi$ - $\pi$  interactions. (A) Structure of AT1R. (B) AT1R with AngII docked in the orthosteric site and LVV-H7 docked to the intracellular site shown in space-filling representation. (C) Closer view of the docked pose of LVV-H7 and the hydrogen bond it forms with AT1R shown as black dashed lines. (D) Image in (C) shown with interacting residues labelled.



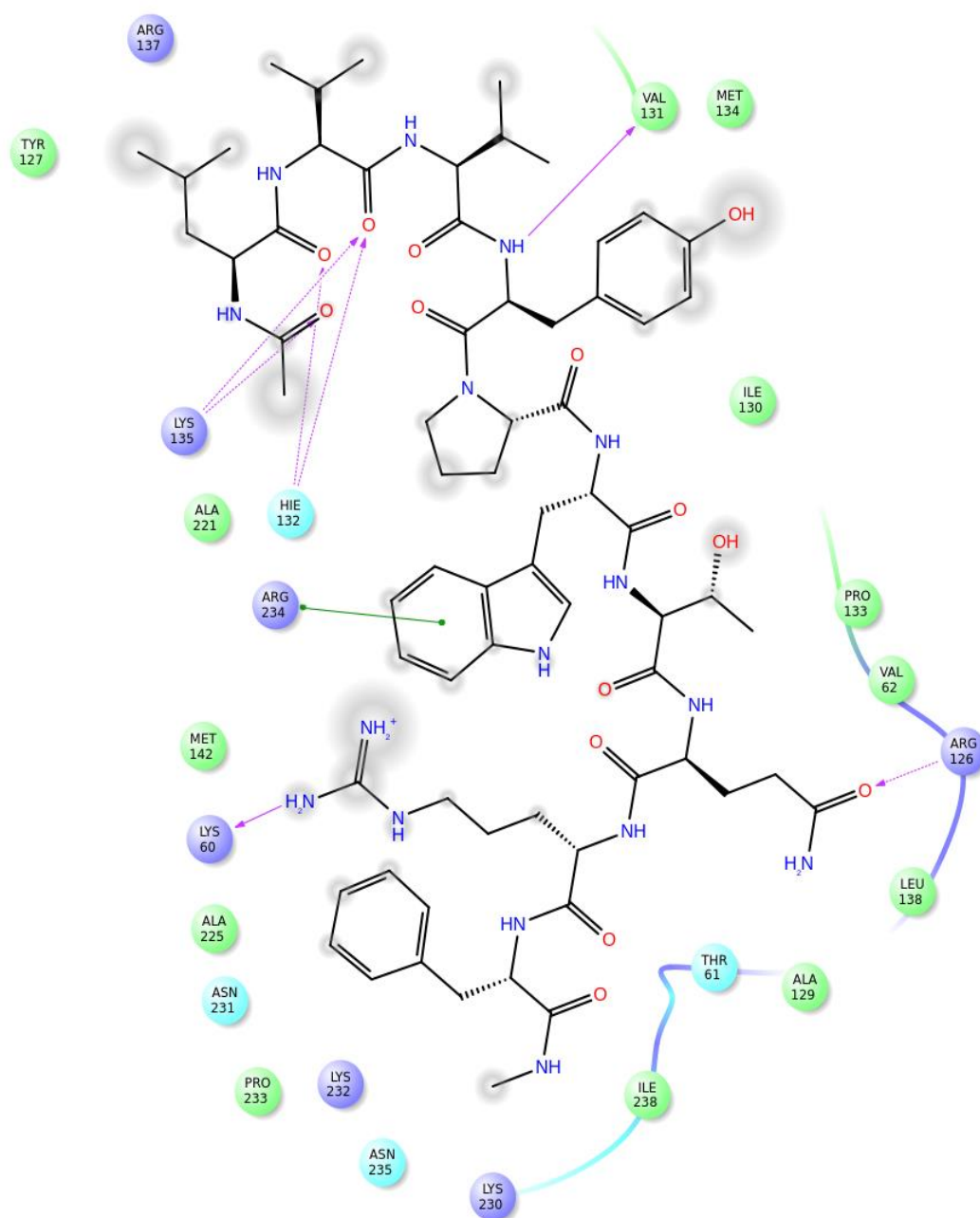


Figure 47: 2D ligand interaction diagram of LVV-hemorphin-7 with AT1R. LVV-hemorphin-7 interacting residues with intracellular binding pocket of AT1R (PDB: 4ZUD). Colored circles represent amino acids that form interaction with bound ligand. Red circles indicate negatively charged amino acids, dark blue colors indicate positively charged amino acids, light blue circles indicate polar amino acids, and green circles indicate hydrophobic amino acids. Hydrogen bonds are shown with purple arrows—dashed arrows for hydrogen bonds involving amino acid side chain and regular arrows for hydrogen bonds involving amino acid backbone.  $\pi$ - $\pi$  interactions are represented with green lines.

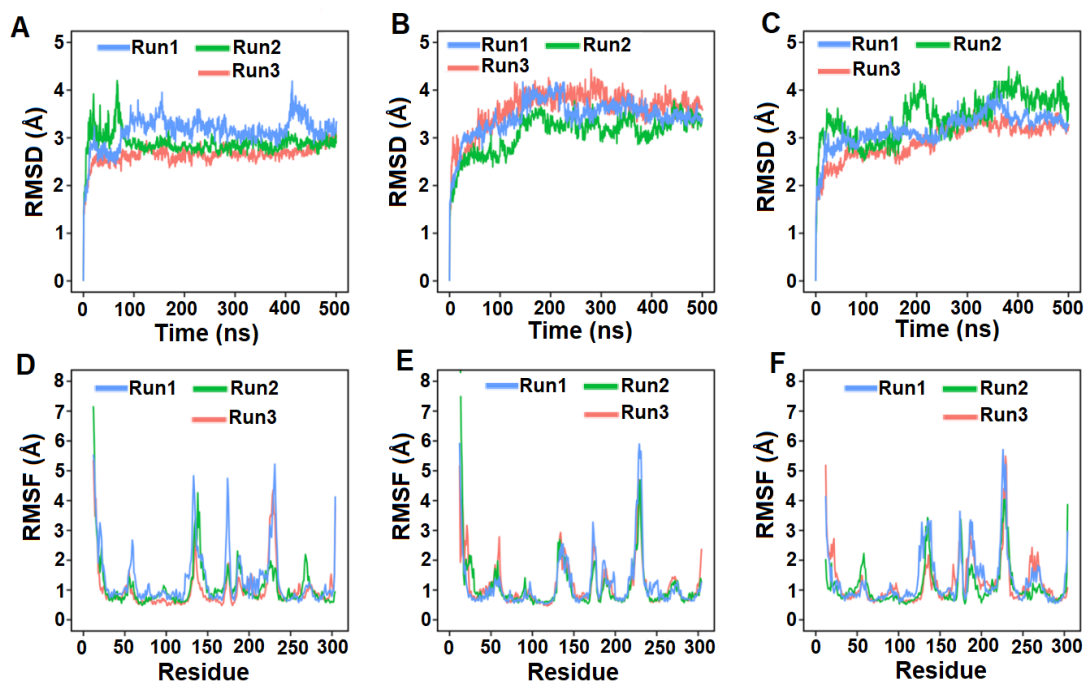


Figure 48: Plots of RMSD and RMSF of protein Ca atoms extracted from three independent 500 ns simulations of AT1R complexes. Data of three independent runs are plotted with blue, green and red colors. (A) RMSD of AT1R-LVV-H7 complex; (B) RMSD of AT1R-AngII complex; (C) RMSD of AT1R-LVV-H7-AngII complex; (D) RMSF of AT1R-LVV-H7 complex; (E) RMSF of AT1R-AngII complex; (F) RMSF of AT1R-LVV-H7-AngII complex.

### 5.1.8 Binding of LVV-H7 to AT1R potentiated the binding of AngII

The effect of intracellular binding of LVV-H7 on AngII binding affinity was evaluated. AngII was first docked in the orthosteric site of AT1R. In the docked pose, the C-terminus of AngII was embedded deep in the active site and the N-terminus was extended towards the lid (Figure 49A). The best binding pose of Ang II had a GScore of -12.01 kcal/mol. The calculated MM-GBSA binding energy for this pose was -129.31 kcal/mol (Table 7). AngII formed multiple hydrogen bonds, hydrophobic, electrostatic and polar interactions that was consistent with previous studies (Fillion et al., 2013; Singh, Unal, Desnoyer, & Karnik, 2019) (Figure 50). Interactions between AngII and AT1R are provided in Table 7.

Next, the last frame from a 500 ns simulation of LVV-H7 docked to AT1R intracellularly was taken and AngII was docked to the orthosteric binding site in this complex. Interestingly, the binding of AngII was improved. The best binding pose of AngII produced a GScore of -13.51 kcal/mol and MM-GBSA binding free energy of -160.71 kcal/mol (Table 7). This suggested that intracellular binding of LVV-H7 allosterically enhanced the binding affinity of AngII in extracellular orthosteric binding site. This observation is consistent with the BRET data obtained in HEK293 cells (Figure 41, 42 and 43). Notably, Asp1, Tyr4 and Phe8 residues of AngII were positioned differently when LVV-H7 was bound to AT1R (Figure 49). The C-terminus of AngII bound slightly deeper inside the binding pocket in the presence of LVV-H7 (Figure 49B). This allowed Phe8 of AngII to form a hydrogen bond with Lys199. Pro7 of AngII showed hydrogen bond with Arg167 both in the presence and absence of LVV-H7 (Figure 49). Tyr4 of AngII, without LVV-H7 formed a  $\pi$ - $\pi$  stacking with Tyr184 (Figure 49A). The sidechains amino groups of Arg2 of AngII formed hydrogen bonds with Asp263 and Asp281 of AT1R with and without LVV-H7 bound. Lastly, Asp1 of AngII, in the presence of LVV-H7, formed a hydrogen bond with Gln267 (Figures 49A and 49B). In the absence of LVV-H7, Asp1 was observed to form hydrogen bonds with Ser16, and Asp17 (Figure 37A and 37B). Overall, AngII was able to form more hydrogen, hydrophobic and polar interactions with AT1R when bound to LVV-H7 (Figures 50 and 51).

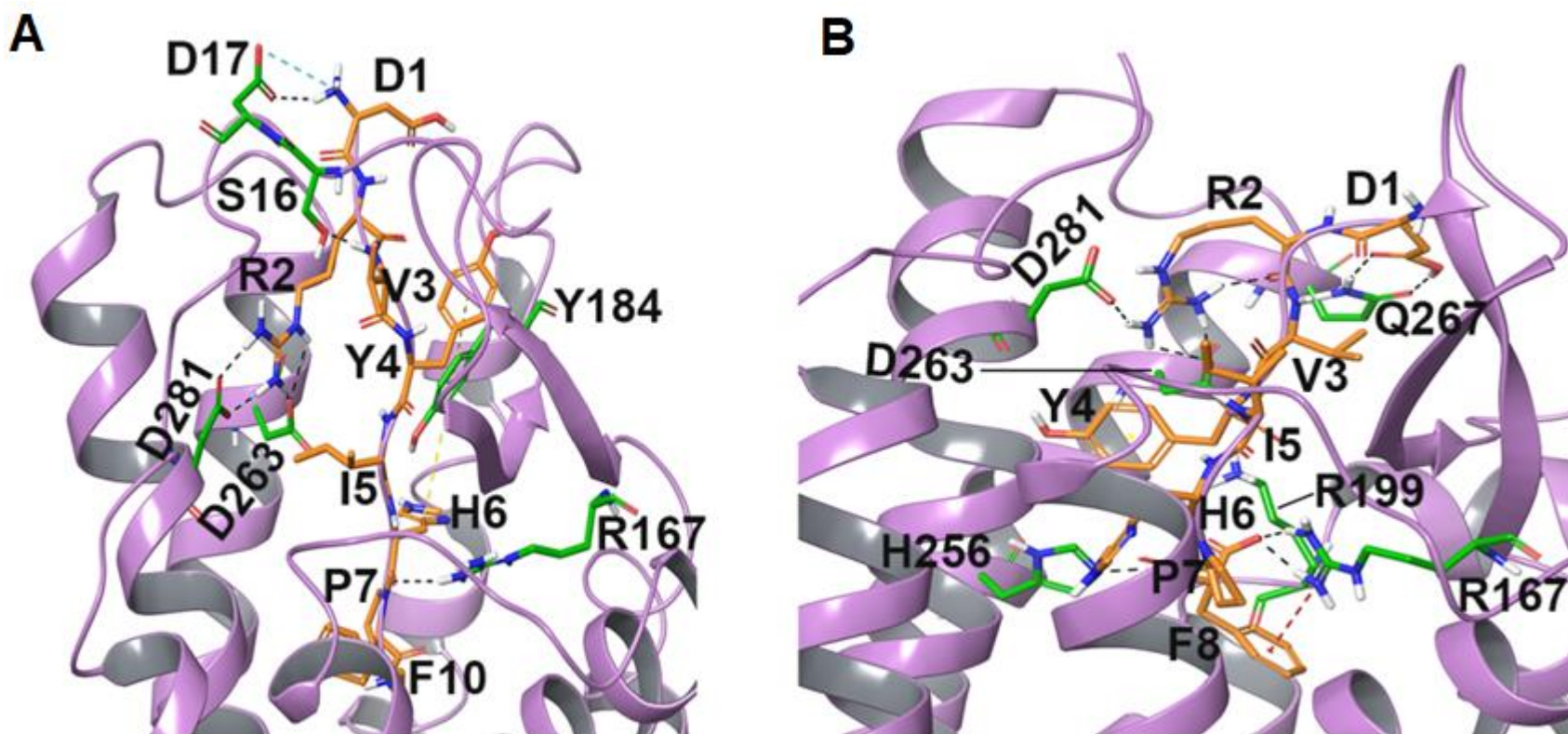


Figure 49: Binding pose of AngII with AT1R in the presence and absence of LVV-H7. AT1R structure is shown in purple cartoon representation while its interacting residues are shown in green stick representation. Docked peptide is shown in orange stick representation. Black dotted lines represent hydrogen bonds and blue lines represent  $\pi$ - $\pi$  interactions. (A) Interaction of the docked pose of AngII in the absence of LVV-H7 and hydrogen bonds it forms with AT1R shown as black dashed lines. (B) Interaction of the docked pose of AngII in the presence of LVV-H7 and hydrogen bonds (black dashed lines) and  $\pi$ - $\pi$  interactions (green dashed lines) it forms with the AT1R.

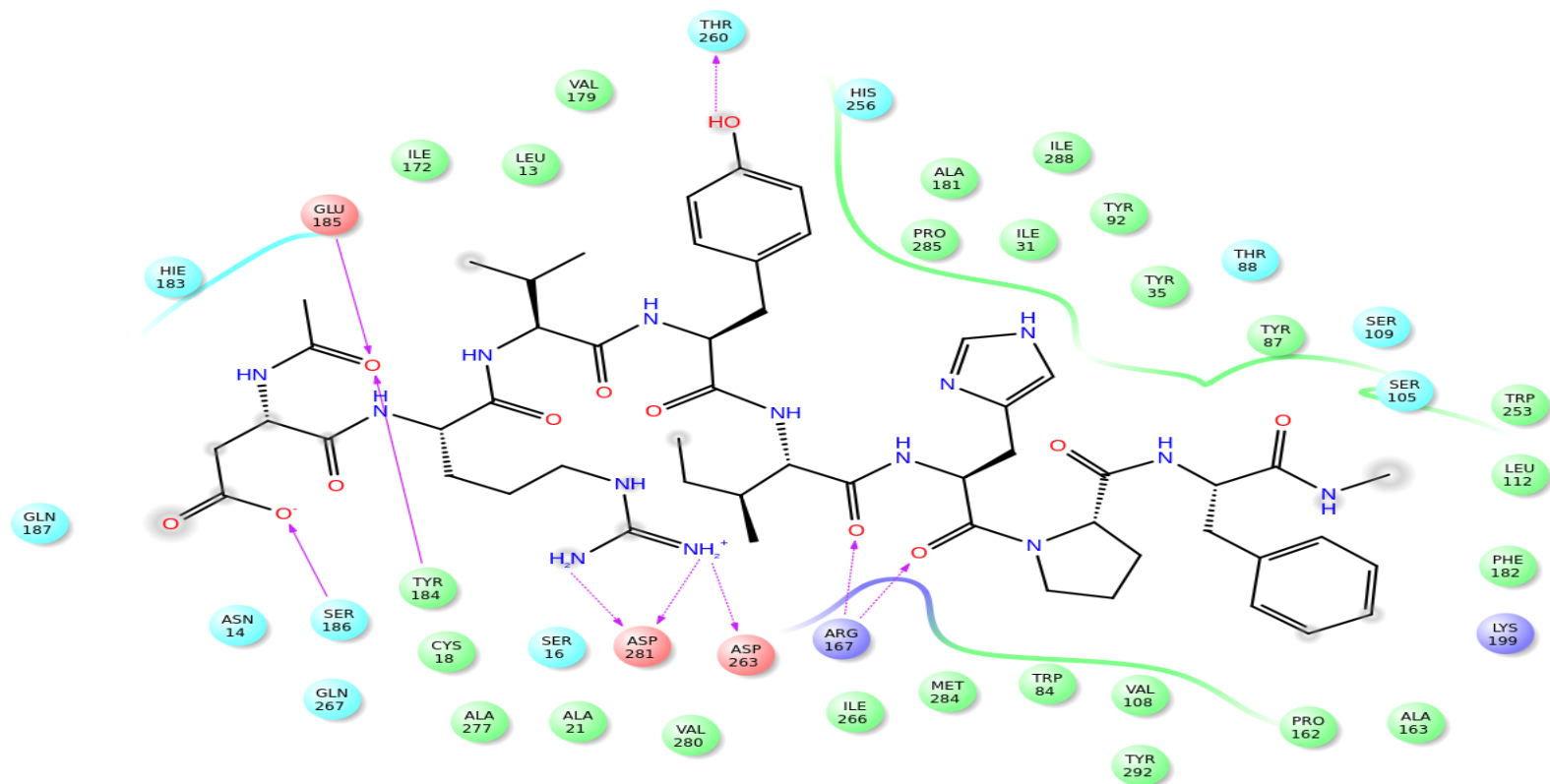


Figure 50: 2D ligand interaction diagram of AngII with AT1R. A) AngII interacting residues with orthosteric binding site of AT1R (PDB: 4ZUD). Colored circles represent amino acids that form interaction with bound ligand. Red circles indicate negatively charged amino acids, dark blue colors indicate positively charged amino acids, light blue circles indicate polar amino acids, and green circles indicate hydrophobic amino acids. Hydrogen bonds are shown with purple arrows—dashed arrows for hydrogen bonds involving amino acid side chain and regular arrows for hydrogen bonds involving amino acid backbone.  $\pi$ - $\pi$  interactions are represented with green lines.

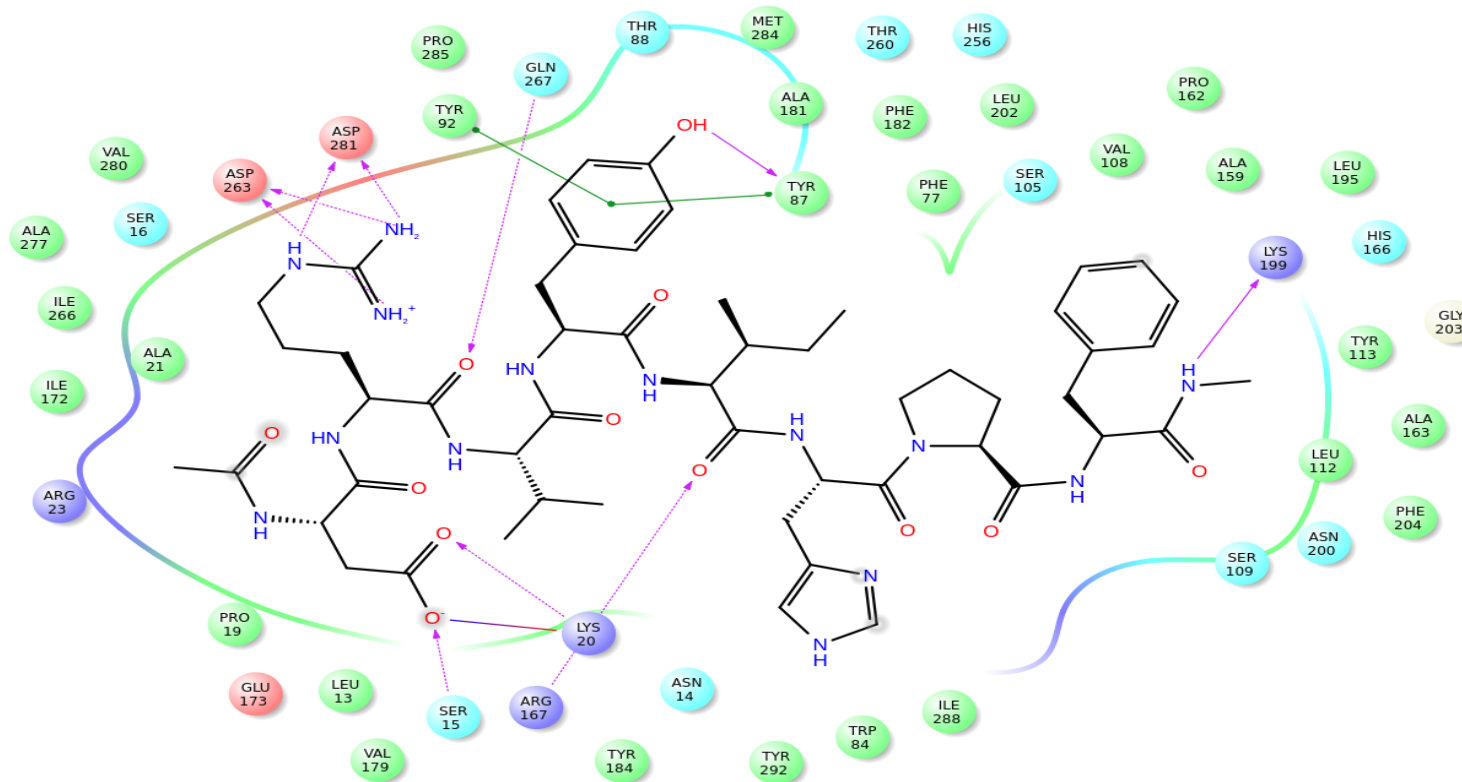


Figure 51: 2D ligand interaction diagram of AngII with AT1R-LVV-hemorphin-7. AngII interacting residues with orthosteric binding site of AT1R docked with LVV-H7. Colored circles represent amino acids that form interaction with bound ligand. Red circles indicate negatively charged amino acids, dark blue colors indicate positively charged amino acids, light blue circles indicate polar amino acids, and green circles indicate hydrophobic amino acids. Hydrogen bonds are shown with purple arrows—dashed arrows for hydrogen bonds involving amino acid side chain and regular arrows for hydrogen bonds involving amino acid backbone.  $\pi$ – $\pi$  interactions are represented with green line.

The best binding pose of AT1R-Ang II and AT1R-LVV-H7-Ang II complexes were extracted, and the complexes were simulated for 500 ns in triplicates to assess the binding stability and dynamics of AngII with AT1R in the presence and absence of LVV-H7. The membrane embedded AT1R structures remained stable when AngII and LVV-H7 were bound with a  $C\alpha$  RMSD that was under 4 Å (Figures 48B and 48C). RMSF of AT1R, where both LVV-H7 and Ang II were bound, showed that ICL2 (residues 131-137) and ECL2 (residues 180-191) fluctuated more compared to AT1R bound to AngII only (Figures 48E and 48F).

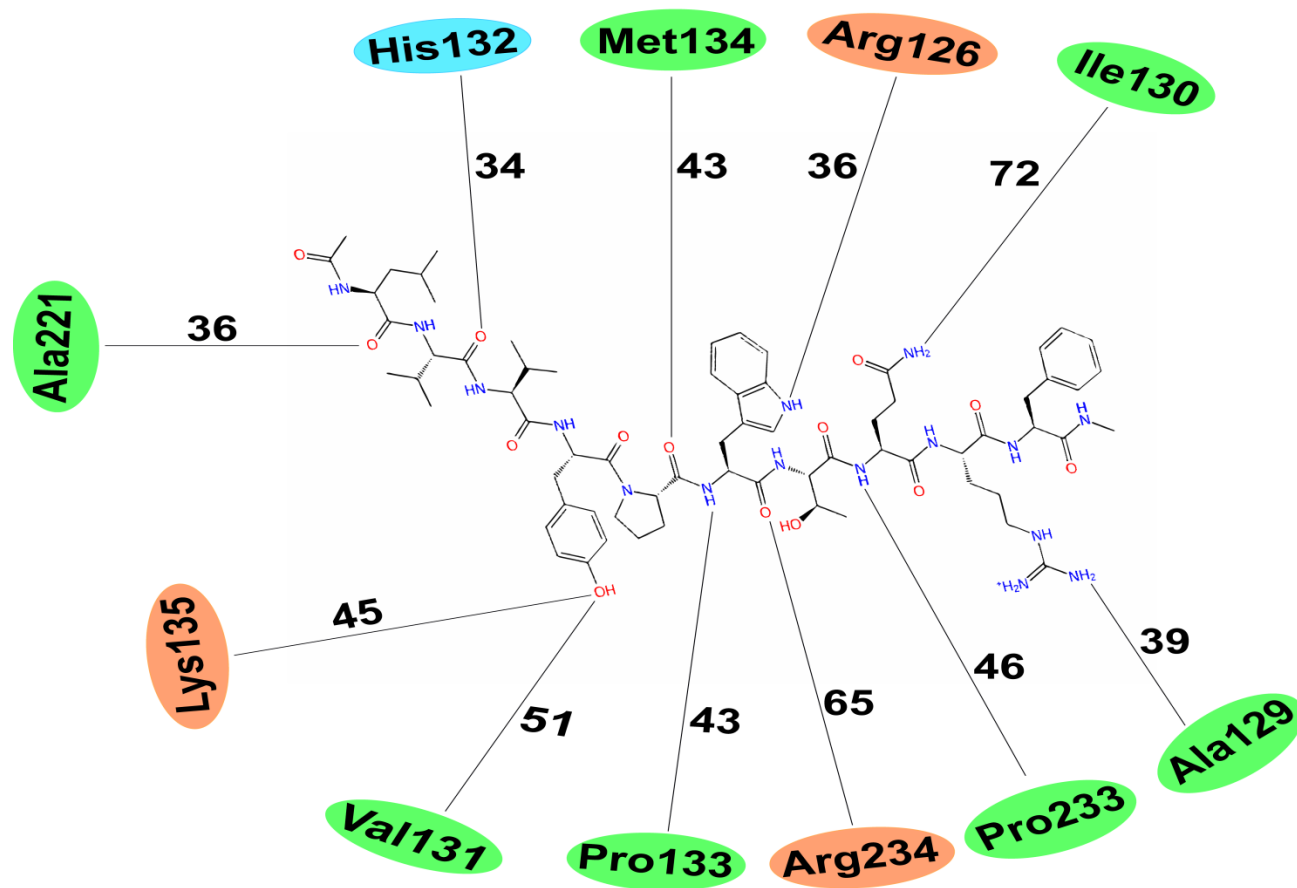


Figure 52: Average percentage of simulation time from three 500 ns runs during which AT1R residues maintain contact with LVV-H7. The average percentage of simulation time is shown next to the dotted line. Charged, hydrophobic, and polar residues are represented with orange, green and blue color respectively.



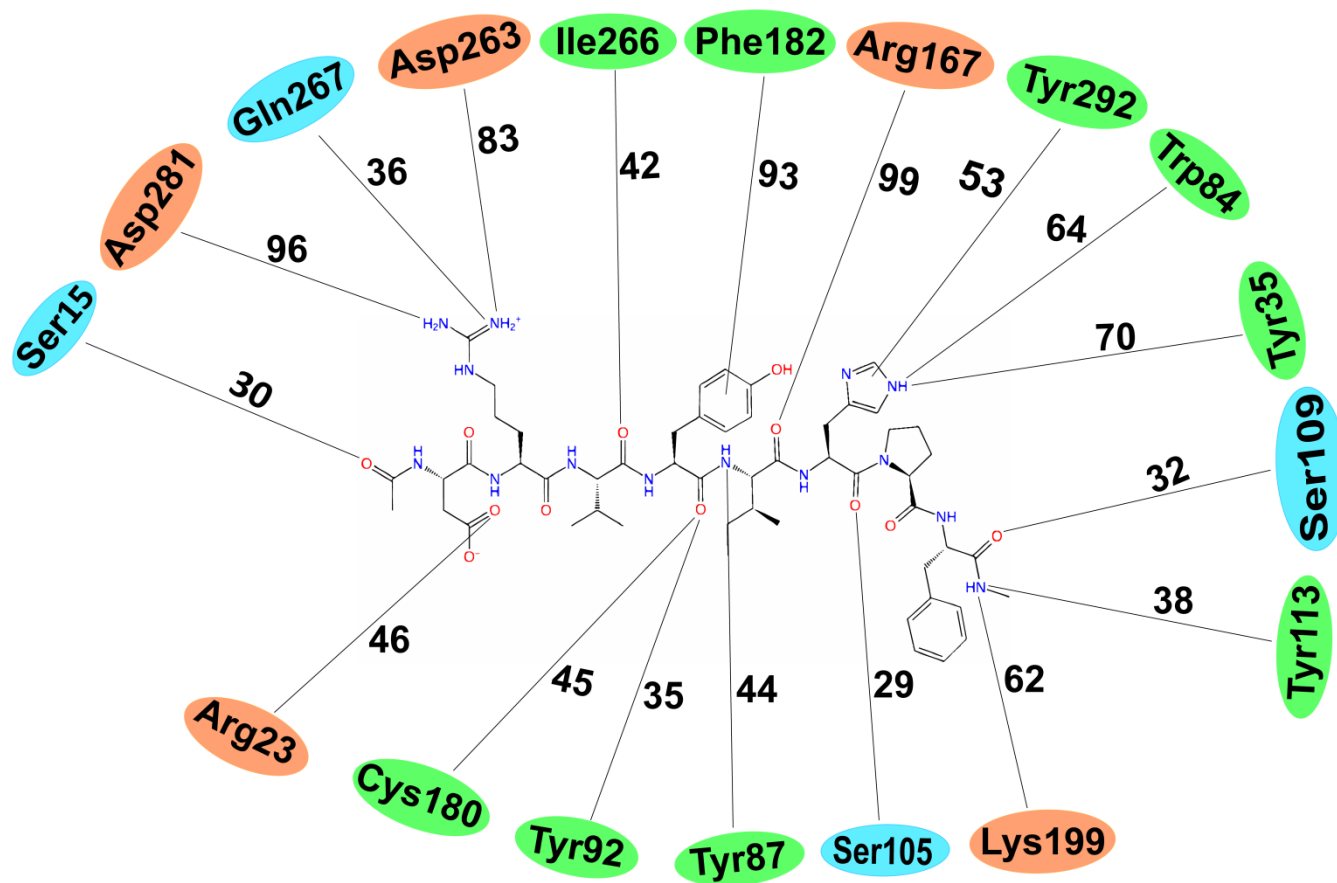


Figure 53: Average percentage of simulation time from three 500 ns runs during which AT1R residues maintain contact with AngII in the absence of LVV-H7. The average percentage of simulation time is shown next to the dotted line. Charged, hydrophobic, and polar residues are represented with orange, green and blue color respectively.

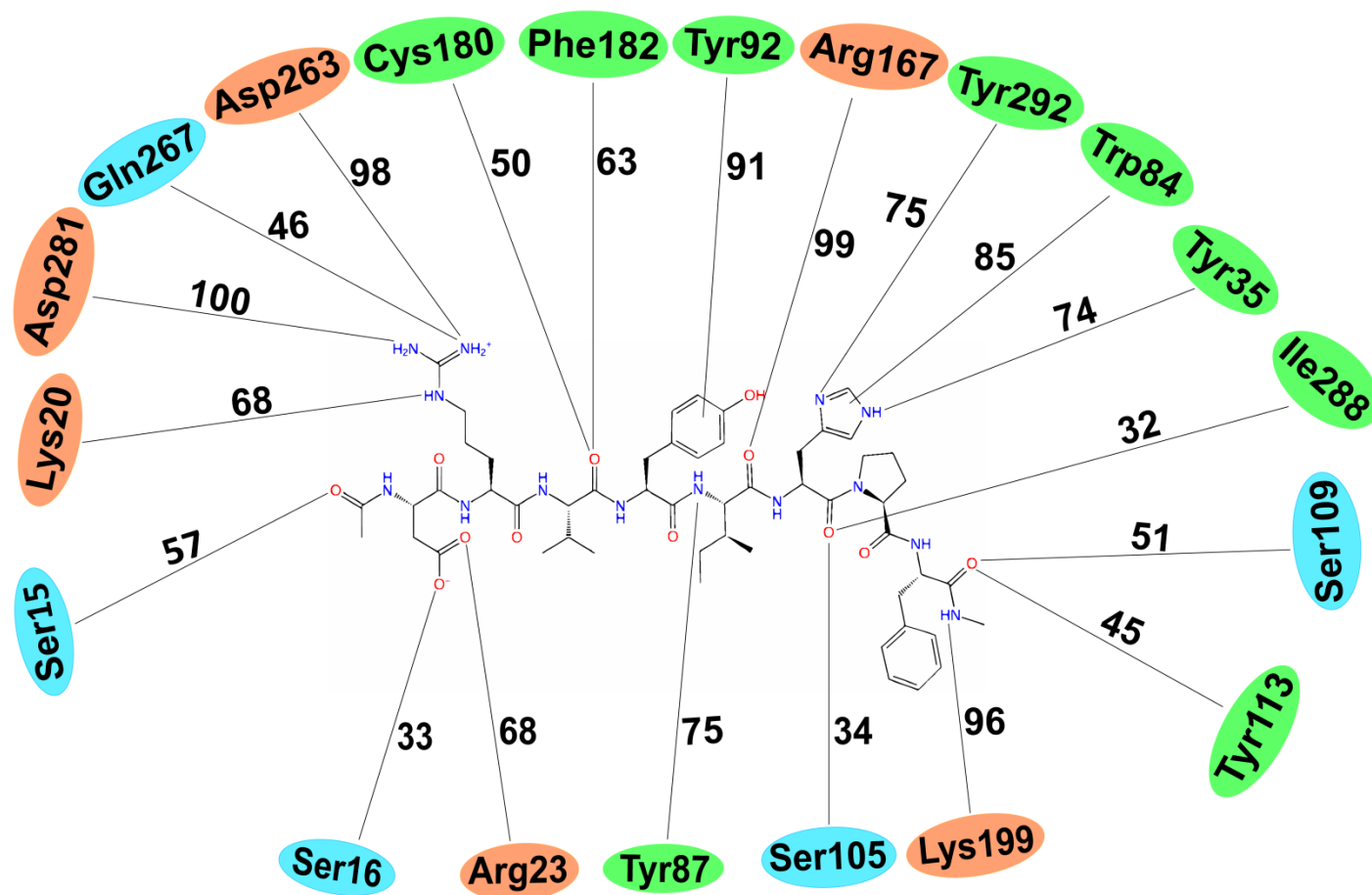


Figure 54: Average percentage of simulation time from three 500 ns runs during which AT1R residues maintain contact with AngII in the presence of LVV-H7. The average percentage of simulation time is shown next to the dotted line. Charged, hydrophobic, and polar residues are represented with orange, green and blue color respectively.

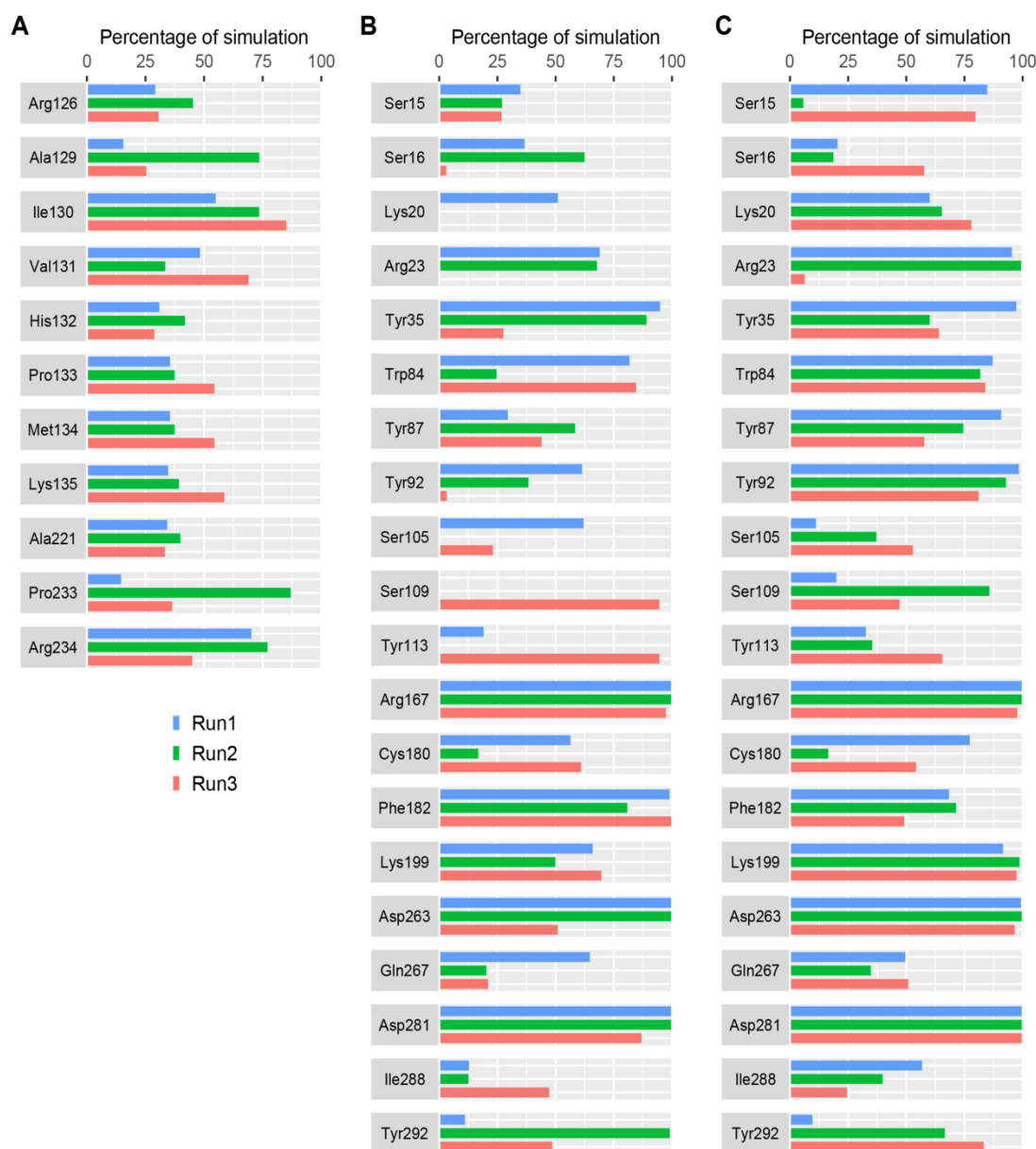


Figure 55: Histograms of the percentage of simulation time where an AT1R residue maintained contact with a peptide. (A) AT1R-LVV-H7; (B) AT1R-AngII; (C) AT1R-LVV-H7-AngII.

The stability of interactions between AT1R and the peptides were assessed from the simulations of AT1R-AngII complex in the presence and absence of LVV-H7 (Figures 53 and 54). AT1R residues Trp84, Val108, Leu112, Arg199 and Ile288, located at the bottom of the orthosteric binding site, interacted with Pro7 and Phe8 of AngII (Figures 49). Arg199 was observed to be close to Phe8 of AngII in the AT1R-

LVV-H7-AngII complex, and this inward movement was linked to a more sustained interaction of Arg199 with Phe8 during simulations when compared to the AT1R-Ang II complex (Figures 53 and 54). The interaction of Phe8 with Arg199 has been demonstrated to be an essential contact associated with AT1R activation (Fillion et al., 2013). Phe8 also formed consistent hydrophobic interactions with Ser109 and intermittent interactions with Tyr113 when LVV-H7 was bound. This interaction was observed in only one of the simulations when LVV-H7 was not bound to AT1R (Figures 53 and 54). His6 showed consistent interactions with Trp84 of AT1R bound with LVV-H7 in all runs of simulation, while the same interaction was formed in only two runs in the absence of LVV-H7. Pro7 of AngII formed limited interactions with Ser105 and Ile288 residues and which were better when LVV-H7 was bound to AT1R. Ile5 maintained sustained interactions with Arg167 in both cases for the full duration of the simulations. Arg167 is an important to AT1R when compared to other structurally similar GPCRs and play a vital role in defining ligand binding affinity. Tyr4 of AngII exhibited sustained interactions with Tyr92 of AT1R only when LVV-H7 was bound (Figure 54). However, Tyr4 interacted with Tyr35 in both cases. AngII residues Arg2 interacted with Asp263 and Asp281 of AT1R with and without LVV-H7 throughout the simulations. Such an interaction between AT1R and AngII has been reported previously (Feng et al., 1995; Wingler, McMahon, Staus, Lefkowitz, & Kruse, 2019). The interactions of Asp263 and Asp281 of AT1R with Arg2 of AngII were slightly weaker in the absence of LVV-H7. Val3 formed consistent interactions with Cys180 and Phe182 in the presence of LVV-H7. While, without LVV-H7, these residues of AT1R interacted with Tyr4 of AngII (Figures 53 and 54). Asp1 of AngII formed sustained interaction with Ser15, Lys20 and Arg23 of AT1R in the presence of LVV-H7. Overall, the docking and simulation data

indicates that the N-terminus of AngII was firmly held by hydrogen bonds as well as hydrophobic and polar interactions with Ile12, Leu13, Ser15, Lys20, Arg23, Asp263 and Asp281 residues of AT1R when LVV-H7 was bound. This permitted the C-terminus of AngII to bind stably deep inside the orthosteric site. However, in the absence of LVV-H7, the N-terminus of AngII formed less stable interactions with Ile12, Leu13, Ser15, Lys20 and Arg23 of AT1R (Figures 53 and 54). Such subtle changes support the higher binding affinity of AngII in the presence of LVV-H7.

MM-GBSA based free energy of binding ( $\Delta G_{\text{bind}}$ ) was estimated using frames extracted every 50 ns from the MD simulations. AT1R-AngII simulations in the presence of LVV-H7 exhibited  $\Delta G_{\text{bind}}$  ( $-224.8 \pm 7.6$  kcal/mol,  $-206.1 \pm 10.9$  kcal/mol and  $-228.4 \pm 8.1$  kcal/mol) that were higher than AT1R-AngII simulations without LVV-H7 ( $-193.0 \pm 14.9$  kcal/mol,  $-161.3 \pm 25.2$  kcal/mol and  $-189.9 \pm 24.7$  kcal/mol). There is a notable improvement in  $\Delta G_{\text{bind}}$  compared to the initially docked structure indicating that AngII remained stably bound in the simulations. Furthermore, this also indicates higher binding affinity of AngII in the presence of LVV-H7.

## 5.2 Discussion

Here, the pharmacological action of LVV-hemorphin-7 on HEK293 cells transiently expressing AT1R was observed. Interesting, a positive allosteric action on AT1R activation and signaling was observed for the first time. This effect was determined using multiple *in vitro* assays such as real-time BRET for AngII-mediated AT1R-G $\alpha$ q coupling and  $\beta$ -arrestin 2 recruitment. Their related downstream signaling pathway was also determined via the estimation of IP1

production. Additionally, extensive *in silico* studies indicate the allosteric potentiation of AngII binding affinity by LVV-H7 through binding to intracellular regions of AT1R. Results clearly showed that LVV-hemorphin-7 produced a positive allosteric effects on the activation of AT1R and also enhanced the functional coupling with Gαq and its interaction with β-arrestin 2. LVV-hemorphin-7 produced substantial potentiation of AngII-induced BRET signals as indicated by both dose–response and real-time kinetics experiments. The positive allosteric action of LVV-hemorphin-7 was also found on AngII-mediated Gαq/IP1 generation. Therefore, the findings reveal that LVV-hemorphin-7 produces a differential action on AT1R-mediated signaling. Furthermore, LVV-hemorphin-7 produce positive allosteric modulation (PAM)-like effect on Gαq activation and β-arrestin 2 recruitment (assessed by BRET).

Molecular docking and long (MD) simulations were performed to determine the most suitable binding pose of LVV-H7 and its effect on AngII binding to AT1R. Extensive molecular docking runs identified an intracellular location, previously linked to allosteric modulation in other GPCRs, to be the most suitable binding site of LVV-H7 (Wang et al., 2018) . Long MD simulations revealed that LVV-H7 binding in this IC site induced conformational changes in the orthosteric binding pocket associated with AngII binding. Interestingly, the C-terminus of AngII was embedded deeper in its binding site and formed sustained interaction with Trp84, Ser105, Ser109, Lys199 and Ile288 of AT1R when compared to the structure without LVV-H7 (Figures 49, 53 and 54).

These findings are of prime importance to pharmacology of GPCRs and hemorphins and their involvement in human physiology. This body of work reports

another member of the GPCR family - AT1R - that is a target of hemorphins with the possible involvement in the pathophysiology and physiology of renal and vascular systems, besides hemorphin's direct effect on opioid receptors (Brantl et al., 1986; Cheng et al., 2012; Davis et al., 1989; Glamsta et al., 1992). Additionally, the effect of LVV-hemorphin-7 on AT1R is in agreement with the earlier studies indicating LVV-hemorphin-7 acting on opioid receptors encompassing the fields of action of hemorphins on GPCRs. A partial to full radioligand binding have been confirmed in opioid receptors, with a competition with some opioids peptides such as endogenous dynorphins and enkephalins but not nonpeptide ligands (Garreau, Zhao, Pejoan, Cupo, & Piot, 1995; Zhao & Piot, 1997). Furthermore, an agonist like action of LVV-hemorphin-6 has been reported in guinea-pig ileum and GTP $\gamma$ S binding assays, respectively (Yukhananov et al., 1994). These studies clearly showed the precise binding of hemorphins on the opioid receptors that elucidate the palliative potentials of hemorphin found *in vivo* (Albiston et al., 2001; Cheng et al., 2012; Hughes et al., 1975). Indeed, *in vitro* experiments reported here clearly demonstrated the substantial PAM effects of LVV-hemorphin-7 on AT1R, as indicated by different BRET and in IP1 assays, and to less extent BRET (100  $\mu$ M), indicate such an interaction between AT1R and LVV-hemorphin-7. Importantly, results of BRET and IP1 dose-response curves are characteristic of PAM of LVV-hemorphin-7 on AT1R with no noteworthy effects of LVV-hemorphin-7 were observed when used alone. However, a left shift of the AngII dose curves were clearly observed in the presence of different doses of LVV-hemorphin-7. Indeed, this suggests that AT1R could exhibit an allosteric modulation in the presence of LVV-hemorphin-7 and may harbor an allosteric binding site as indicated in several earlier studies.

Positive allosteric binding sites of GPCRs have been identified in the past (Bruns & Fergus, 1990; Nemeth et al., 1998). However, recent studies have fully characterized the potential of PAM in multiple GPCRs using *in silico* and *in vitro* approaches (Congreve, Oswald, & Marshall, 2017; Kruse et al., 2013). Allosteric binding sites located near the EC face and IC face in different GPCRs have been documented (Bock et al., 2012; Kruse et al., 2013). Allosteric sites near the orthosteric site in GPCRs often block the entry of other ligands (Proska & Tucek, 1994; Wang et al., 2018). However, this would not be a problem for allosteric ligands that target the IC region. DETQ, an allosteric modulator of dopamine 1 receptor binds preferentially to ICL2 and significantly enhanced the potency of dopamine (Wang et al., 2018). Interestingly, LVV-H7 binds to the IC face of AT1R and predominantly targets the ICL2 (Figure 46). LVV-H7 targets ICL2 residues that are not conserved in dopamine 1 receptor at AT1R such as Lys135 and Ser136 as well as the conserved residues Arg126, Ile130 and Pro133 (Figures 46, and 47). These residues are located near the binding site of DETQ on ICL2 of dopamine 1 receptor (Wang et al., 2018). Moreover, recent studies have shown that AT1R stabilizing nanobodies target the intracellular side of AT1R, especially ICL2 residues and enhanced the binding affinity of AngII for AT1R (Wingler et al., 2019). This phenomenon shows complementary cooperativity anticipated for an allosteric interaction. Interestingly, here, LVV-H7 binds to these ICL2 residues of AT1R and could potentiate the binding affinity and potency of AngII. Moreover, the allosteric binding of LVV-H7 in the intracellular regions of AT1R is consistent with the allosteric modulation of GPCRs through the targeting of their intracellular surfaces which has been well documented with the lipidated peptides known as pepducins and



even small molecules (Covic, Gresser, Talavera, Swift, & Kuliopulos, 2002; P. Zhang et al., 2015).

Evaluating the binding mode of AngII in the presence and absence of LVV-H7 revealed that AngII bound deeper in the orthosteric binding pocket in the presence of LVV-H7 (Figure 49). The interaction between Phe8 of AngII with Lys199, located at the base of the orthosteric pocket of AT1R was improved in the presence of LVV-H7 (Figures 53 and 54). Lys199 has been identified as a residue critical for AT1R activation (H. Zhang et al., 2015a). Tyr35 and Trp84 are conserved in other GPCRs such as angiotensin, chemokine and opioid receptors and mutating these residues would abolish the binding of both peptide and synthetic ligands of AT1R (H. Zhang et al., 2015b). In simulations, Tyr35 and Trp84 were observed to form more sustained interactions with AngII in the presence of LVV-H7 (Figures 53 and 54). AT1R activation cascade has also been shown to be initiated by the van der Waals interaction between Phe8 and Ile288 (Singh et al., 2019). Interestingly, intracellular binding of LVV-H7 enhanced stability of the interaction between Phe8 with Ile288 (Figures 53 and 54). This could likely lead to a more robust disruption of the Asn111-Asn295 interaction, and better AngII binding affinity and potency (Singh et al., 2019). The existence of a stable hydrogen bond between Asn111 and Asn295 is characteristic of the inactive state of AT1R and its disruption is vital for AT1R activation (H. Zhang et al., 2015a; H. Zhang et al., 2015b). Mutagenesis studies have also reported that Tyr87, Arg167 and Tyr292 are important for AngII binding (Singh et al., 2019). Interestingly, these residues formed more sustained interactions with AngII in the presence of LVV-H7 (Figures 53 and 54).

DRY, Yx7K, NPxxY, and helix-8 motifs are highly conserved among GPCRs and are located in the cytoplasmic region. These motifs, initially reported in rhodopsin, act as microswitches (Elgeti et al., 2011). Functional studies of AT1R have illustrated the stability of these motifs in the inactive state (Elgeti et al., 2011; Lin, Han, & Sakmar, 2000). ICL2 residues of AT1R, where LVV-H7 bound, are associated with structural changes that induce a transition from an inactive to an active conformation in GPCRs (Wang et al., 2018). Trajectory analysis of AT1R-LVV-H7 complex indicated that the binding of LVV-H7 to ICL2 and ICL3 of AT1R induced conformational changes in the DRY motif present at the cytoplasmic end of TM3 that are important for GPCR activation (Singh et al., 2019; Wang et al., 2018). GPCR activation involves the breakage of a stable interaction that exists between Asp125 and Arg126 of the DRF motif in the inactive state (Matsoukas et al., 2013; Singh et al., 2019). Interestingly, LVV-H7 binds to the DRF motif and forms an intermittent interaction with Arg126 residue of AT1R throughout the simulations (Figure 52). Additionally, the side chain of Arg126 was observed to slightly orient itself towards TM6 in the presence of LVV-H7. These changes have been associated with the opening of the groove where G-protein binds and could, therefore, enhance the coupling of G-protein to AT1R (Rasmussen et al., 2011; Singh et al., 2019).

In the physiological context, the positive allosteric modulator effects of LVV-hemorphin-7 on AT1R captivantly indicate a hypertensive action. Such an effect is somehow is not in agreement with the previous antihypertensive effects of hemorphins demonstrated in several *in vivo* and *in vitro* studies (Ali et al., 2020; Fruitier-Arnaudin, Cohen, Coitoux, & Piot, 2003; Lantz et al., 1991; Zhao & Piot, 1997). Previous study has shown that hemorphins produce hypotensive activities

through the direct inhibition of ACE (Zhao & Piot, 1997). Additionally, hemorphins have been reported to enhance the hypotensive and vasodilatory effect of bradykinin (Ianzer et al., 2006). Lastly, studies have shown that serum hemorphin-7 levels after long distance running were determined to be very high (Glamsta et al., 1992), while they were observed quite low in diabetic and obese patients, which are associated to high blood pressure and cardiovascular risks (Maraninchi et al., 2013). Thus, conflicting activities of hemorphins on ACE (inhibition) and AT1R (activation) and their physiological outcomes, hypotensive and hypertensive, respectively, demonstrate the intricacy of hemorphin's action on RAS. One possibility of explaining these opposing effects is by assuming that the blockage of ACE which results in a reduction of AngII levels can be compensated by the positive effect of hemorphins on AT1R. This would suggest that low doses of AngII could be sufficient to activate RAS in this condition. In addition, it is possible that hemorphins regulate water reabsorption and blood pressure under different conditions by biasing RAS towards activation via their positive modulatory activities on AT1R or inhibition of ACE effect and AngII levels. The data presented here can be viewed and interpreted in both physiological and pathophysiological circumstances. Certainly, it is not established yet if hemorphins release from the hemoglobin is a normal or a pathogenic mechanism with an effect on blood pressure and water balance. Additionally, it is also unknown that which part of hemorphin's action ACE, or AT1R is actually the determinant of the system and how it interacts under physiological and pathophysiological conditions. In the physiological context, the two contradictory action of hemorphins could be components of the precise control of the blood pressure (and maybe even water balance) via the stimulatory and the inhibitory effects on AT1R and ACE, respectively, to maintain the blood pressure

in the normal range. For example, if elevated blood pressure occurs for some reason and this could be correlated with high ACE expression and/or activity, in such circumstances hemorphins could be released to counterbalance this condition so as to prevent any risk of consistent or chronic hypertension. Similarly, if there is a hypotensive/vasodilatation condition due to lower expression/activity of AT1R, hemorphins could then be produced and released to raise blood pressure by stimulating AT1R-dependent vasoconstriction. However, in pathological conditions, the increased expression/activity of AT1R correlated with possible decrease in the expression/activity of ACE and the enhanced release of hemorphins could be indicative of the pathophysiology of hypertension and of RAS. In such a scenario, hypertension may be either the cause or the outcomes of the action of hemorphins. Therefore, it could be speculated that in different physiological and pathophysiological conditions, the biological system including all these components (hemorphins, AT1R, or ACE) could rely on the circulating concentrations of hemorphins along with the comparative expression levels of the two RAS targets, ACE and AT1R. Until now, there is no reliable data available on the possible relationship between the quantity of hemorphins released in blood and the expression profiles of AT1R and ACE and their effects on the regulation of blood pressure and hypertension. This indicates that the stoichiometry of hemorphins/AT1R versus hemorphins/ACE in hypotensive and hypertensive situations remain elusive. A previous study has revealed that the blood of long-distance running subjects contained a higher concentration of hemorphins (Glamsta, Morkrid, Lantz, & Nyberg, 1993). This could be true with either a positive modulator effect of hemorphins (hypertensive) via action on AT1R due to exercise or their negative regulatory action (hypotensive) via the binding and inhibition of ACE to prevent any

unnecessary hypertension. Moreover, very low hemorphin levels have recently been documented in diabetic and obese patients that are associated to hypertension and cardiovascular risks indicating therapeutically beneficial effects of hemorphins on ACE inhibition (Maraninchi et al., 2013). Thus, it would be important to explore the possible effects of hemorphins on other primary RAS and kidney actor such as bradykinin, adrenergic, and vasopressin receptors, identified to have functional interactions with AT1R (Tóth, Turu, Hunyady, & Balla, 2018).

## Chapter 6: Structural and Genetic Changes of Camel Hemoglobin

### 6.1 Results

Genetic and *in silico* approaches were used to investigate the structural and genetic changes of camel hemoglobin and were compared with human hemoglobin.

#### 6.1.1 Hemoglobin $\alpha$ and $\beta$ genes sequences

Hemoglobin  $\alpha$  and  $\beta$  genes of 170 camel samples from different breeds were amplified to determine the variation near the heme, ATP and 2,3-BPG binding sites. PCR was first used to amplify hemoglobin  $\alpha$  and  $\beta$  genes of all samples. These samples were then purified and sent for DNA sequencing using the primers used for PCR. Chromatograms obtained from sequencing were inspected using Finch TV Viewer and the sequences were aligned using BioEdit Sequence Alignment Editor to identify locations that harbor variations. One synonymous variation (Ser82) was observed in hemoglobin  $\alpha$  gene in all camel breeds. The frequency of this variation in each breed is given in Table 8. The chromatogram showing the variation is given in Figure 56. The coding regions of both genes were devoid of any other variation. However, several non-coding variations were observed in both genes (Table 8).

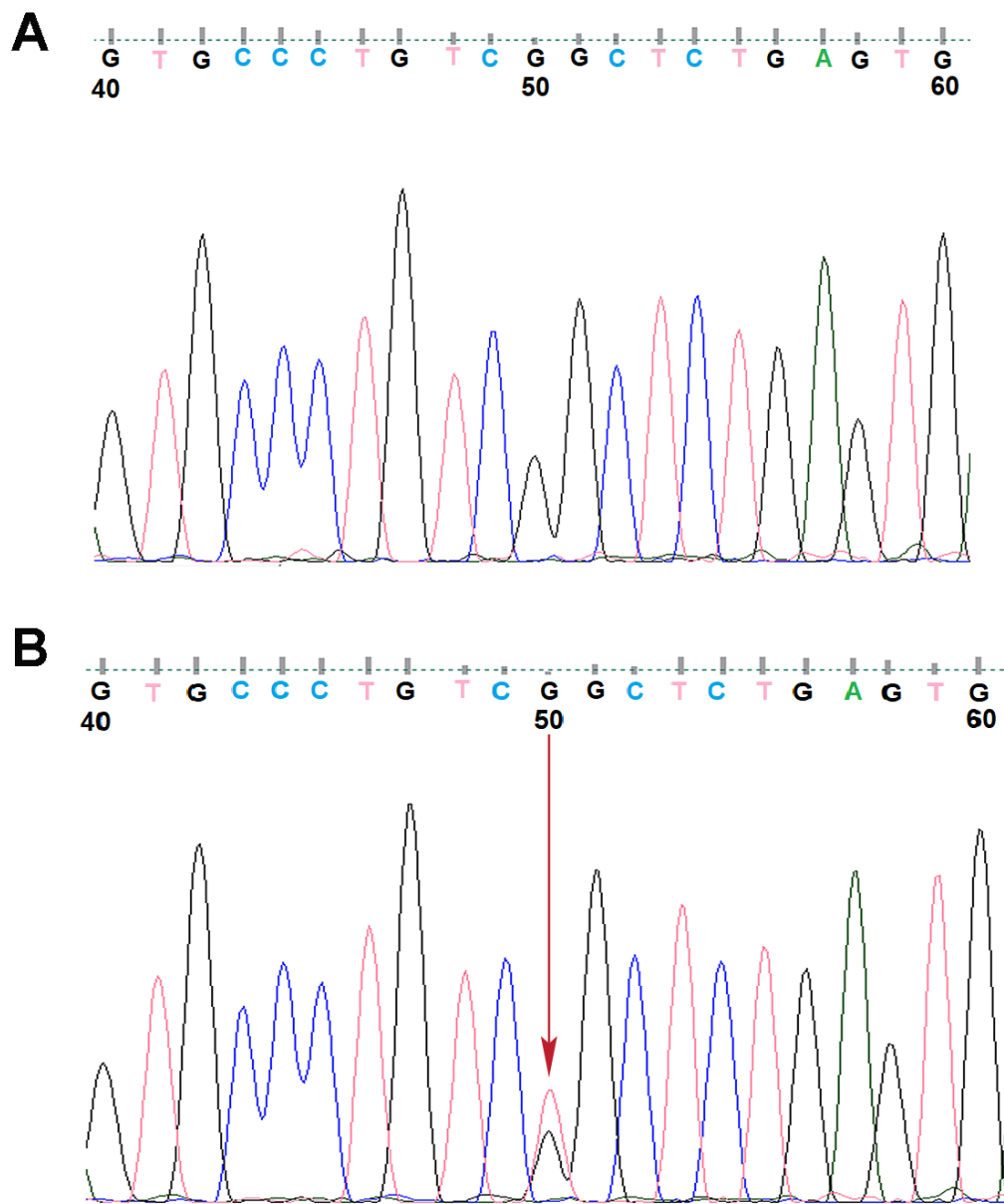


Figure 56: Chromatograms of camel samples. (A) Chromatogram of a wild camel; (B) Chromatogram of a camel with synonymous variation. Arrow in red color shows the position of variation.

Table 8: List of coding and non-coding variations observed in hemoglobin genes of different breeds of camel.

Gene Name	Bread Name	Variation	Exonic function	Frequency	
Hemoglobin $\alpha$	Local	g.384G>T	Synonymous p.S82=	5/50	
		g.454G>A	NA	26/50	
	Mixed	g.384G>T	Synonymous p.S82=	2/50	
		g.454G>A	NA	19/50	
	Sudani	g.384G>T	Synonymous p.S82=	6/50	
		g.454G>A	NA	16/50	
	Dairy	g.384G>T	Synonymous p.S82=	3/20	
	Hemoglobin $\beta$	Local	g.563C>T	NA	34/50
			g.608C>T	NA	2/50
			g.644C>T	NA	17/50
g.655A>C			NA	3/50	
g.677C>T			NA	24/50	
g.684C>T			NA	26/50	
g.694C>T			NA	11/50	
g.704C>T			NA	5/50	
g.707C>T			NA	2/50	
g.715C>T			NA	30/50	
g.1033T>C			NA	44/50	
g.1251T>C			NA	50/50	



Table 8: List of coding and non-coding variations observed in hemoglobin genes of different breeds of camel (Continued).

Gene Name	Breed Name	Variation	Exonic function	Frequency
Hemoglobin $\beta$	Mixed	g.563C>T	NA	25/50
		g.608C>T	NA	0/50
		g.644C>T	NA	5/50
		g.655A>C	NA	0/50
		g.677C>T	NA	15/50
		g.684C>T	NA	17/50
		g.694C>T	NA	9/50
		g.704C>T	NA	0/50
		g.707C>T	NA	8/50
		g.715C>T	NA	18/50
		g.1033T>C	NA	48/50
		g.1251T>C	NA	47/50
		Hemoglobin $\beta$	Sudani	g.563C>T
g.608C>T	NA			Nil
g.644C>T	NA			12/50
g.655A>C	NA			Nil
g.677C>T	NA			11/50
g.684C>T	NA			14/50
g.694C>T	NA			4/50
g.704C>T	NA			Nil
g.707C>T	NA			9/50
g.715C>T	NA			17/50
g.1033T>C	NA			46/50
g.1251T>C	NA			50/50

Table 8: List of coding and non-coding variations observed in hemoglobin genes of different breeds of camel (Continued).

Gene Name	Bread Name	Variation	Exonic function	Frequency
Hemoglobin $\beta$	Dairy	g.563C>T	NA	7/20
		g.608C>T	NA	1/20
		g.644C>T	NA	3/20
		g.655A>C	NA	0/20
		g.677C>T	NA	5/20
		g.684C>T	NA	8/20
		g.694C>T	NA	6/20
		g.704C>T	NA	1/20
		g.707C>T	NA	3/20
		g.715C>T	NA	5/20
		g.1033T>C	NA	16/20

### 6.1.2 Molecular dynamics (MD) simulation of camel and human hemoglobin

MD simulations were performed on camel and human hemoglobin at different temperatures (27°C, 30°C, 34°C, and 41°C) and salt concentration (0 mM, 150 mM, 300 mM, and 600 mM) to investigate the structural stability and flexibility of hemoglobin residues. The salt concentration of 150 mM was maintained in each simulation when the effects of different temperature conditions were measured. While, a temperature of 27°C was used in each simulation to assess the overall impact of different salts concentrations on hemoglobin stability. Sixteen different complex systems were prepared. The information of each prepared complex system is given in Table 9. One microsecond MD simulations were performed for each complex system to determine the dynamical features of the camel and human

hemoglobin structure under different salt concentrations and temperature conditions.

The dynamical features were investigated by evaluating RMSD and RMSF.

Table 9: MD simulation conditions used for simulating complex systems of camel and human hemoglobin.

<b>PDB ID</b>	<b>Temperature (°C)</b>	<b>Salt concentrations (mM)</b>	<b>Run time (ns)</b>
3GDJ	27	0	1000
3GDJ	27	150	1000
3GDJ	27	300	1000
3GDJ	27	600	1000
3GDJ	27	150	1000
3GDJ	30	150	1000
3GDJ	34	150	1000
3GDJ	41	150	1000
2HHB	27	0	1000
2HHB	27	150	1000
2HHB	27	300	1000
2HHB	27	600	1000
2HHB	27	150	1000
2HHB	30	150	1000
2HHB	34	150	1000
2HHB	41	150	1000

### 6.1.2.1 RMSD and RMSF of camel and human hemoglobin at different salt concentration

RMSD of camel and human hemoglobin was measured at different salt concentration (0 mM, 150 mM, 300 mM and 600 mM). Each simulation was performed at a constant temperature of 27°C. RMSD of Hb from each simulation system was computed and plotted to determine the dynamic features of camel and human Hb throughout the simulation runs (Figure 57). The backbone C $\alpha$  atoms of camel Hb showed the RMSD of approximately 2 Å at all salt concentration except 600mM where the complex system stabilized under 3 Å. All systems reached equilibrium after few nanoseconds of simulation except the complex system of 600 mM (Figure 57A). This system attained equilibrium after 500ns (Figure 57A). The average calculated RMSD values were 1.97 Å, 1.82 Å, 1.83 Å and 2.42 Å for the salt concentration of 0 mM, 150 mM, 300 mM and 600 mM respectively. Human Hb showed higher RMSD values at all salt concentration (Figure 57B). The average estimated RMSD values of human Hb were 3.56 Å, 4.07 Å, 3.23 Å, and 3.24 Å for the salt concentrations of 0 mM, 150 mM, 300 mM and 600 mM, respectively. Moreover, all human Hb complex systems required more time to reach equilibrium. This indicates that camel hemoglobin structure showed more stability at different salt concentrations, compared to human hemoglobin. The structural integrity of all simulations of camel and human Hb were retained as indicated by their RMSD.

To evaluate the flexibility of camel hemoglobin at constant temperature, T=27°C, with various salt concentrations (NaCl), the RMSF of C $\alpha$  atoms on a residue from the average structure obtained from the MD frames was calculated. The RMSF of the hemoglobin structure exhibited similar pattern of fluctuations at

different salt concentrations and high peaks were observed in some residues in the loop or turn region (Figure 57C). The residue numbering used in RMSF plots of hemoglobin shows the sequential combination of residues from the four chains ( $\alpha 1$ ,  $\beta 1$ ,  $\alpha 2$ , and  $\beta 2$ ) in the structure. Importantly, camel hemoglobin residues  $\alpha 2:46-55$  (represented by residues 330-342 in Figure 57C) showed more fluctuations at 600 mM NaCl concentration.  $\alpha 1:46-50$  showed high fluctuations at 0 mM and 600 mM salt concentrations (Figure 57C).  $\beta 1:47-53$  exhibited more fluctuations at only 0 mM. However, the same region remained stable in all other simulations.  $\beta 2:5-11$  exhibited higher fluctuations at 150 mM and 300 mM salt concentrations. However, the same region in  $\beta 1$  showed more fluctuations at 0 mM only (Figure 57C). The residue His87 of  $\alpha 1$  subunit and His92 of  $\beta 1$  and  $\beta 2$  subunits showed more fluctuations at higher salt concentrations. However, His87 of  $\alpha 2$  showed more fluctuation at 0 mM salt concentration. At 150 mM and 300 mM, Ser70-Phe71-Gly72 in the  $\beta 1$  and  $\beta 2$  subunits showed more fluctuations.

Residues of human hemoglobin compared to camel hemoglobin showed more fluctuations at all salt concentrations (Figure 57D). Loop region residues 42-51, and 70-77 of  $\alpha 1$  subunit exhibited more fluctuations particularly at 300 mM and 600 mM. Helical residues 78-91 of  $\alpha 1$  subunit also showed higher fluctuations at higher salt concentrations. Interestingly, the same helical residues of camel  $\alpha 1$  subunit demonstrated extremely low fluctuations at all salt concentrations (Figure 57D). However, such fluctuations were not observed in the same residues of both camel and human  $\alpha 2$  subunits. Moreover, residues 111-140 of  $\alpha 1$  subunit of human Hb showed higher fluctuations at higher salt concentrations especially at 300 mM. However, the same residues in camel Hb demonstrated very limited variations at all

salt concentrations. However, such a pattern was not observed in  $\alpha 2$  subunits of both camel and human Hb. Val2 of  $\beta 1$  and  $\beta 2$  subunits of human Hb showed more fluctuations particularly at higher salt concentrations, compared to camel Hb (Figure 57D). Helical residues 11-15 of camel Hb showed slightly higher fluctuations at all salt concentrations, particularly at 0 mM. However, the same residues in human  $\beta 2$  subunit showed slightly more fluctuations compared to camel Hb (Figure 57D). Loop residues 39-59 of  $\beta 1$  subunit of human Hb exhibited higher variations at all salt concentrations compared to camel  $\beta 1$  subunit. However, such a trend was observed in only 39-45 residues of  $\beta 2$  subunits of both human and camel Hb (Figure 57D). Residues 80-98, 84-98 which formed loops in  $\beta 1$  and  $\beta 2$  subunits showed higher fluctuations in human Hb compared to camel Hb at all salt concentrations, respectively (Figure 54D). Lys82 of both  $\beta 1$  and  $\beta 2$  chains is considered an essential residue for the binding of 2,3-BPG and ATP (Chen et al., 2017). However, His92 is an important residue of  $\beta 1$  and  $\beta 2$  subunits which form the binding sites for oxygen. Interestingly, these residues fluctuated more in human Hb at all salt concentrations. Residues 141-147 of  $\beta 1$  and  $\beta 2$  chain of human Hb exhibited higher fluctuations particularly at higher salt concentrations. However, camel Hb demonstrated limited variations at all salt concentrations (Figure 57). His143 and His146 of  $\beta 1$  and  $\beta 2$  chains are also important for the binding of 2,3-BPG and ATP (Berg et al., 2002). Overall, human Hb showed higher fluctuations at all salt concentrations, compared to camel hemoglobin (Figure 57).

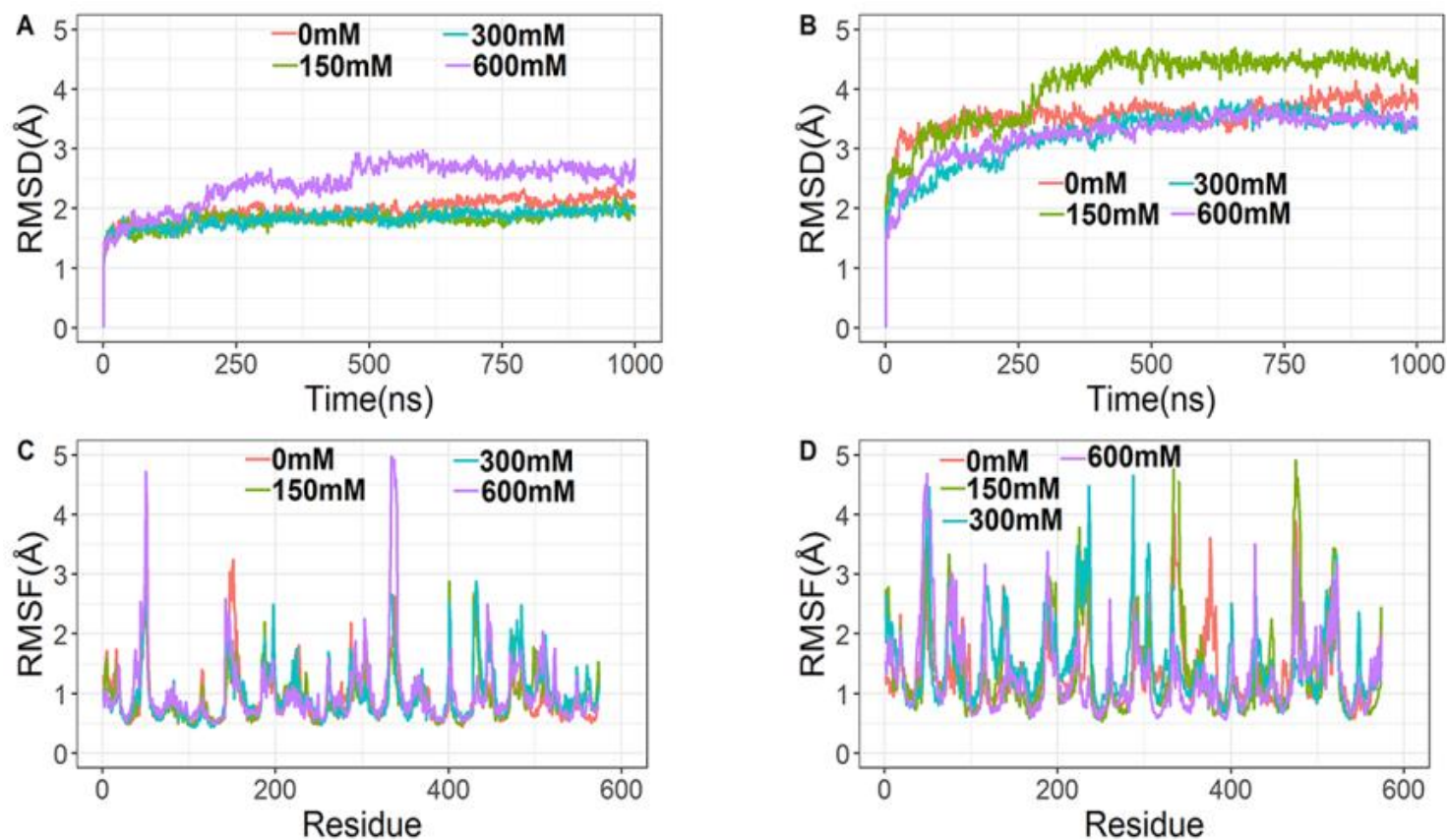


Figure 57: Root mean square standard deviation (RMSD) and root mean square fluctuation (RMSF) of protein C $\alpha$  atoms obtained from a 1000 ns run of camel and human hemoglobin simulation at different salt conditions. Data from different salt conditions are shown in red, green, blue and purple. (A) RMSD of camel hemoglobin; (B) RMSD of human hemoglobin; (C) RMSF of camel hemoglobin and, (D) RMSF of human hemoglobin. Note that the residue number used in the RMSF plots uses a sequential combination of the  $\alpha$ 1,  $\beta$ 1,  $\alpha$ 2, and  $\beta$ 2 in the PDB structure.

### 6.1.2.2 RMSD and RMSF of camel and human hemoglobin at different temperature conditions

The camel and human hemoglobin protein was simulated separately for one microsecond at four different temperature conditions (27°C, 30°C, 34°C, and 41°C). The final salt concentration was kept constant (150 mM) for these simulations. RMSD of main-chain atoms for the entire Hb was plotted to investigate the structural changes of camel and human Hb (Figure 58). RMSD of the C $\alpha$  atoms of camel Hb with respect to the initial structure stabilized under 2 Å in all the simulations except the one at 34°C. At 34°C the complex system of camel hemoglobin stabilized at approximately 2.5 Å. This indicates that the structure of hemoglobin exhibited a stable conformation from low to high temperature conditions. The average RMSD values were 2.04 Å, 2.17 Å, 2.76 Å and 2.34 Å for the temperature, 27°C, 30°C, 34°C and 41°C respectively. In the case of 27°C and 30°C, the hemoglobin structure reached equilibrium during the initial nanoseconds of the simulation, but the structure required more time in the case of high temperature (34°C and 41°C). In comparison to camel Hb, human Hb needed more time to reach equilibrium at all temperature conditions. The RMSD of backbone C $\alpha$  atoms of human Hb with respect to the initial structure stabilized under 4.5 Å in all the simulations which were higher compared to RMSD of camel Hb (Figure 58). The average RMSD values were 3.86 Å, 3.31 Å, 2.76 Å and 3.91 Å for the temperature, 27°C, 30°C, 34°C and 41°C respectively.

In order to evaluate and compare flexibility in camel Hb at various temperature conditions, the RMSF of C $\alpha$  atoms on a residue, from the average structure obtained from merged MD frames, was calculated. The camel Hb structure



exhibited more fluctuations at higher temperature conditions especially in loop regions (Figure 58C). The loop region residues 41-52 of  $\alpha 1$ , and  $\alpha 2$  subunit showed higher fluctuations compared to other residues particularly at higher temperature conditions. The  $\beta 1$  helical residues 1-7 demonstrated higher fluctuations at lower temperature conditions. However, the same residues of  $\beta 2$  subunits showed more fluctuations at 34°C. Val2 and His3 of both  $\beta 1$  and  $\beta 2$  subunits are considered important for the binding of 2,3-BPG and ATP (Chen et al., 2017). Higher fluctuations were observed for residues near to the heme binding sites in each subunit. The residues in these regions exhibited high RMSF values than the other residues. The loop residues 44-55 of  $\beta 1$  and  $\beta 2$  showed higher fluctuations at 41°C. Loop residues 72-82 of  $\beta 1$  exhibited higher fluctuations at only 34°C. The same residues of  $\beta 2$  exhibited more fluctuations at higher temperature conditions (30°C, 34°C, and 41°C) (Figure 58C). The helical residues 2-7 and loop residues 15-19 of  $\alpha 2$  showed higher fluctuations 34°C and 41°C, respectively. However, the same residues of  $\alpha 1$  subunit exhibited limited fluctuations at all temperature conditions. His87 of  $\alpha$  subunits and His92 of  $\beta 1$  subunits demonstrated more fluctuations at higher temperature conditions. These residues are essential for the binding of four heme groups and served as oxygen binding sites. Importantly, conserved residues  $\alpha 1$ -Phe43 and  $\alpha 1$ -Phe46 showed more fluctuations at higher temperature conditions (Figure 58). These functional residues are present in the heme pocket distal to heme where oxygen binds (Laberge et al., 2008). Moreover,  $\alpha 1$  conserved residues Leu86 and Leu91 also exhibited higher fluctuations when the temperature was increased (Figure 58C). These residues are part of the proximal heme pocket residues (Laberge et al., 2008).

The helical residues 1-10 and loop residues 11-17 of  $\alpha 1$  of human Hb showed higher fluctuations at higher temperature conditions when compared to camel Hb (Figure 58D). The loop region residues 41-52 of  $\alpha 1$  and  $\alpha 2$  subunits showed higher fluctuations at lower temperature conditions compared to camel Hb (Figure 58). Moreover, the loop residues 44-55 of  $\beta 1$  of human Hb showed higher fluctuations at higher temperature conditions compared to camel Hb. Loop residues 72-82 of human  $\beta 1$  and  $\beta 2$  exhibited higher fluctuations at lower temperature conditions compared to camel Hb. Interestingly, at higher temperature conditions these residues showed limited fluctuations in both camel and human Hb. Overall, in comparison to camel Hb, human hemoglobin showed more fluctuations at different temperature conditions.

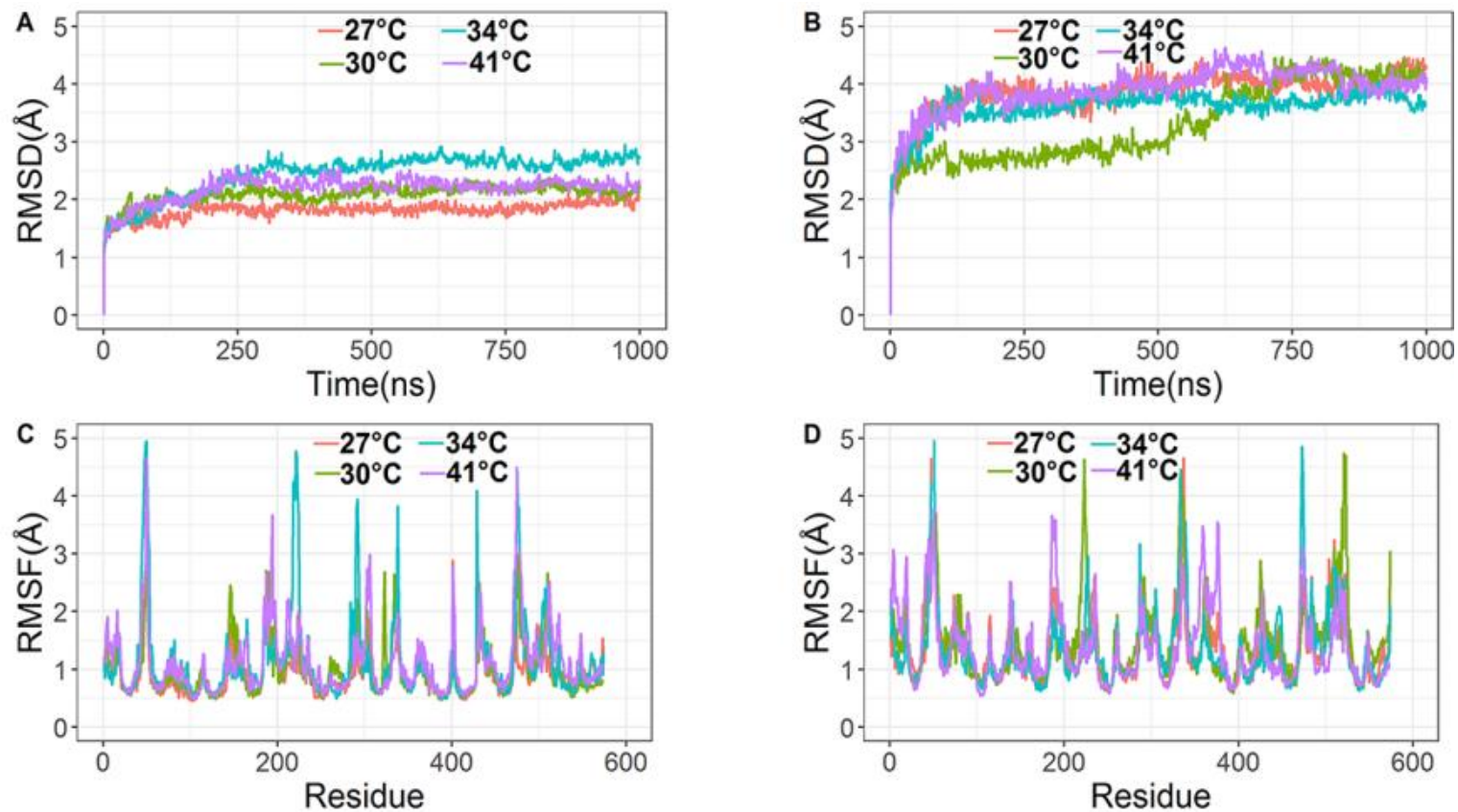


Figure 58: Root mean square standard deviation (RMSD) and root mean square fluctuation (RMSF) of protein  $\alpha$  atoms obtained from a 1000 ns run of camel and human hemoglobin simulation at different temperature conditions. Data from different temperature conditions are shown in red, green, blue and purple. (A) RMSD of camel hemoglobin; (B) RMSD of human hemoglobin; (C) RMSF of camel hemoglobin and, (D) RMSF of human hemoglobin. Note that the residue number used in the RMSF plots uses a sequential combination of the  $\alpha 1$ ,  $\beta 1$ ,  $\alpha 2$ , and  $\beta 2$  in the PDB structure.

### 6.1.3 Molecular docking of 2,3-BPG and ATP with camel hemoglobin

The binding pose and binding affinity of 2,3-BPG and ATP was investigated with camel deoxyhemoglobin structure (PDB ID: 3GDJ). 2,3-BPG and ATP preferentially bind to deoxyhemoglobin and target the same binding site which is located in the central cavity of hemoglobin molecule. The best binding pose of 2,3-BPG had a GScore of -5.165 kcal/mol. The carbonyl and phosphate groups of 2,3-BPG formed hydrogen bonds and salt bridges with Lys82 of  $\beta$ 2 chain (Figure 59A). Lys82 of  $\beta$ 1 showed hydrogen bonds and salt bridge formation with carbonyl and phosphate groups of 2,3-BPG. His146 residue of  $\beta$ 2 formed hydrogen bond with phosphate group. 2,3-BPG showed polar interactions with His143 of both  $\beta$ 1 and  $\beta$ 2 chains. Additionally,  $\beta$ 1 chain formed hydrophobic interactions with Leu81 and Ala140, electrostatic interaction with Asp79, and polar interactions with Asn80 and Asn139 (Figure 59A).

GScore of the best binding pose of ATP with camel hemoglobin was -7.44 kcal/mol. Phosphate groups formed hydrogen bonds and a salt bridge with Lys82 residue of both  $\beta$ 1 and  $\beta$ 2 chains (Figure 59C). They also formed hydrogen bond and polar interaction with His146 and His143 of  $\beta$ 2 respectively. Additionally, Leu81 and Asp79 of  $\beta$ 1 exhibited hydrophobic and electrostatic interactions with phosphate groups of ATP. Hydroxyl group present on the ribose sugar of ATP formed hydrogen bonds with Asp79 of  $\beta$ 2 (Figure 59C). The  $\beta$ 1 residues His143 and His146 were involved in the formation of polar interactions with adenine group. Residues Arg144 and Tyr145 of  $\beta$ 1 formed electrostatic and hydrophobic interactions with adenine. Val2 and His3 of  $\beta$ 2 showed hydrophobic and polar interactions with adenine (Figure

59C). Overall, camel hemoglobin formed more interactions with ATP, compared to human hemoglobin.

#### **6.1.4 Molecular docking of 2,3-BPG and ATP with human hemoglobin**

The binding pose and binding affinity of 2,3-BPG and ATP of camel hemoglobin was compared with human deoxyhemoglobin structure (2HHB). The best binding pose of 2,3-BPG showed GScore of -4.925 kcal/mol. These findings were in agreement with previous studies performed to determine the binding affinity of 2,3-BPG with hemoglobin (Chen et al., 2017). 2,3-BPG formed interactions with critical residues of only  $\beta$ 1 chain of hemoglobin as reported by previous studies. Both phosphate groups of 2,3-BPG formed hydrogen bonds and salt formation with Lys82 of  $\beta$ 1 chain of hemoglobin (Figure 59B). The phosphate group of 2,3-BPG showed electrostatic interaction with His143 of  $\beta$ 1 chain. Additionally, phosphate group also formed hydrogen bond with Val2, hydrophobic interaction with Leu81 and electrostatic interaction with Asn80 (Figure 59B). However, carbonyl group of 2,3-BPG showed hydrogen bond formation with Asn139.

The best binding pose of ATP exhibited GScore of -7.205 kcal/mol. All three phosphate groups of ATP formed hydrogen bonds and salt formation with Lys82 of  $\beta$ 2 chain (Figure 59D). The third phosphate group also showed hydrogen bond and hydrophobic interaction with Val2 and Leu81 of  $\beta$ 2 chain respectively. The phosphate groups also formed polar interactions with Asn79 and His143 of  $\beta$ 1 and  $\beta$ 2 chains respectively (Figure 59D). The hydroxyl group of ribose sugar of ATP formed hydrogen bonds with Asn79 of  $\beta$ 1 subunit. The adenine group of ATP formed a hydrogen bond and  $\pi$ -cation interaction with Asp79 and Lys82 of  $\beta$ 1 chain

respectively. Adenine also formed hydrophobic and polar interactions with Val2 and Asn80 of  $\beta$ 1 (Figure 59D).

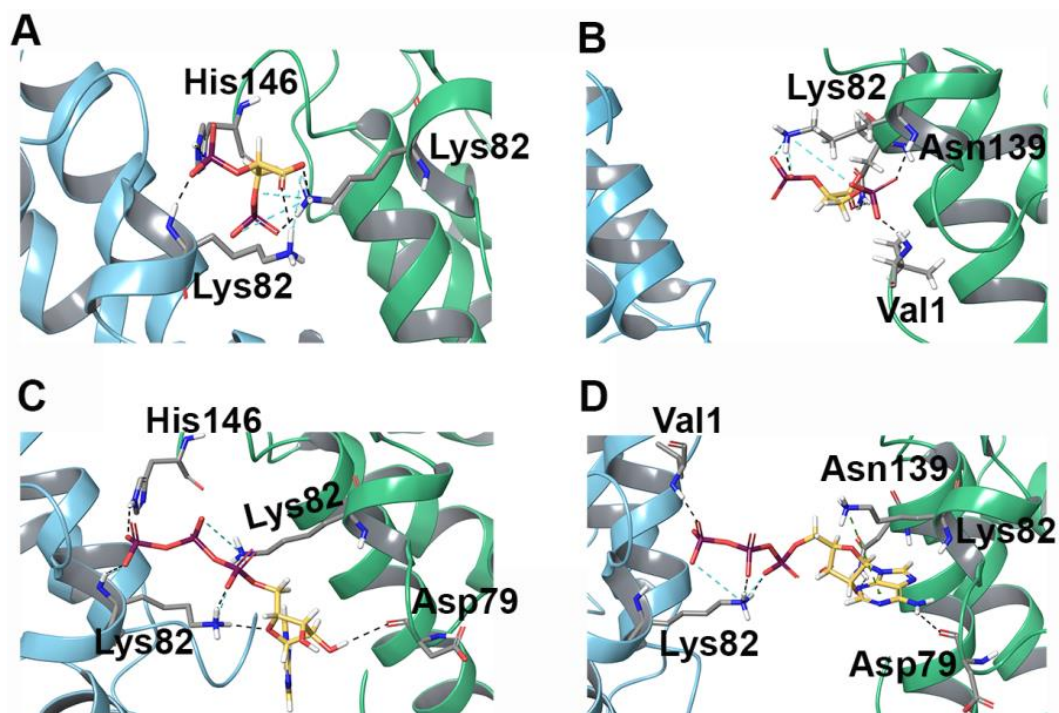


Figure 59: Docked pose of 2,3-BPG and ATP with camel and human hemoglobin. B) Docked pose of 2,3-BPG with human hemoglobin. C) Docked pose of ATP with camel hemoglobin. D) Docked pose of ATP with human hemoglobin.  $\beta$ 1 and  $\beta$ 2 subunits of camel and human hemoglobin are represented with blue and green cartoons respectively. Interacting residues are shown in gray stick representation, the docked ligands are represented as yellow stick, hydrogen bonds and salt bridges are shown as black and blue dashed lines, respectively.

Table 10: Interacting residues of camel and human hemoglobin with 2,3-BPG and ATP.

<b>Ligand</b>	<b>Hemoglobin PDB ID</b>	<b>Glide docking Gscore  (kcal/mol)</b>	<b>Residues forming hydrogen bonds</b>	<b>Residues forming hydrophobic and polar interactions</b>	<b>Residues forming <math>\pi</math>-<math>\pi</math> stacking or cation-<math>\pi</math> interactions</b>
2,3-BPG	3GDJ	-5.165	$\beta$ 1:Lys82, $\beta$ 2:Lys82, $\beta$ 2:His146	$\beta$ 1:Leu81, $\beta$ 1:Ala140 $\beta$ 1:Asn139, $\beta$ 1:His143, $\beta$ 2:His143	$\beta$ 1:Lys82, $\beta$ 2:Lys82
2,3-BPG	2HHB	-4.925	$\beta$ 1:Lys82, $\beta$ 1:Val2	$\beta$ 1:Asn80, $\beta$ 1:Leu81, $\beta$ 1:Asn139, $\beta$ 1:Ala140, $\beta$ 1:His143	$\beta$ 1:Lys82
ATP	3GDJ	-7.44	$\beta$ 2:Asp79, $\beta$ 1:Lys82, $\beta$ 2:Lys82, $\beta$ 2:His146	$\beta$ 2:Val2, $\beta$ 2:His2, $\beta$ 1:Leu81, $\beta$ 1:Asn80, $\beta$ 1:His143, $\beta$ 2:His143, $\beta$ 1:Tyr145, $\beta$ 1:His146	$\beta$ 1:Lys82, $\beta$ 2:Lys82
ATP	2HHB	-7.205	$\beta$ 1:Val2, $\beta$ 2:Asp79, $\beta$ 2:Lys82, $\beta$ 1:Asn139	$\beta$ 1:Val2, $\beta$ 2:Val2, $\beta$ 1:Asn80, $\beta$ 1:Leu81, $\beta$ 2:Leu81, $\beta$ 2:Asn139, $\beta$ 1:Ala140, $\beta$ 1:His143	$\beta$ 1:Lys82, $\beta$ 2:Lys82

### 6.1.5 Molecular dynamics (MD) simulations of 2,3-BPG and ATP bound to camel and human hemoglobin

MD simulations were performed to determine the binding stability of 2,3-BPG and ATP with camel and human hemoglobin in the presence of different salt concentrations (0 mM, 150 mM, 300 mM, and 600 mM) and different temperature conditions (27°C, 30°C, 34°C, 41°C). For measuring the impact of different temperatures on the binding stability of 2,3-BPG-Hb and ATP-Hb complexes, a single salt concentration of 150 mM was used for all simulations, whereas for determining the effect of different salt concentrations, a single temperature of 27°C was used for all simulations. Thirty two different complex systems were prepared. The information of each prepared complex system is given in Table 11. For each complex, two hundred nanosecond MD simulations were performed to determine the binding stability of 2,3-BPG and ATP bound to camel and human hemoglobin.

Table 11: MD simulation conditions used for simulating complex systems of 2,3-BPG and ATP with camel and human hemoglobin.

<b>PDB ID</b>	<b>Ligand</b>	<b>Temperature (°C)</b>	<b>Salt concentrations (mM)</b>	<b>Run time (ns)</b>
3GDJ	2,3-BPG	27	0	200
3GDJ	2,3-BPG	27	150	200
3GDJ	2,3-BPG	27	300	200
3GDJ	2,3-BPG	27	600	200
3GDJ	2,3-BPG	27	150	200
3GDJ	2,3-BPG	30	150	200
3GDJ	2,3-BPG	34	150	200
3GDJ	2,3-BPG	41	150	200
3GDJ	ATP	27	0	200
3GD	ATP	27	150	200
3GDJ	ATP	27	300	200



Table 11: MD simulation conditions used for simulating complex systems of 2,3-BPG and ATP with camel and human hemoglobin (Continued).

<b>PDB ID</b>	<b>Ligand</b>	<b>Temperature (°C)</b>	<b>Salt concentrations (mM)</b>	<b>Run time (ns)</b>
3GDJ	ATP	27	600	200
3GDJ	ATP	27	150	200
3GDJ	ATP	30	150	200
3GDJ	ATP	34	150	200
3GDJ	ATP	41	150	200
2HHB	2,3-BPG	27	0	200
2HHB	2,3-BPG	27	150	200
2HHB	2,3-BPG	27	300	200
2HHB	2,3-BPG	27	600	200
2HHB	2,3-BPG	27	150	200
2HHB	2,3-BPG	30	150	200
2HHB	2,3-BPG	34	150	200
2HHB	2,3-BPG	41	150	200
2HHB	ATP	27	0	200
2HHB	ATP	27	150	200
2HHB	ATP	27	300	200
2HHB	ATP	27	600	200
2HHB	ATP	27	150	200
2HHB	ATP	30	150	200
2HHB	ATP	34	150	200
2HHB	ATP	41	150	200

#### **6.1.6 MD simulations of camel and human hemoglobin bound to 2,3-BPG at different salt concentrations**

2,3-BPG is an important co-factor present abundantly in erythrocytes and is involved in binding with deoxyhemoglobin. Different salt concentrations were used

to determine the effect of osmotic pressure on the structural stability, residual flexibility and the binding stability of 2,3-BPG with camel and human hemoglobin. The RMSD of both camel and human hemoglobin-2,3-BPG complexes at different salt concentration remained stable throughout the simulation time. RMSD of the C $\alpha$  atoms of camel and Hb bound to 2,3-BPG with respect to the initial structure were stabilized under 3.5Å in all the simulations (Figures 60A and 60B). However, human hemoglobin bound to 2,3-BPG demonstrated higher RMSD at 600 mM. To determine the effect of 2,3-BPG on the backbone stability and residual flexibility of camel and human hemoglobin, the RMSF of backbone C $\alpha$  atoms of both camel and human hemoglobin were investigated (Figures 60C and 60D). Overall, camel hemoglobin showed limited fluctuations compared to human hemoglobin. The loop residues 44-52 and 45-52 of  $\alpha$ 1 and  $\alpha$ 2 subunits showed similar fluctuations at all salt concentrations, in both camel and human hemoglobin bound to 2,3-BPG, except 150 mM, where camel Hb-2,3-BPG complex showed lower fluctuations (Figures 60C and 60D). The loop residues 78-93 of  $\alpha$ 1 subunit exhibited higher fluctuations at higher salt concentrations in both camel and human Hb-2,3-BPG complexes. However, the fluctuations of the same residues of  $\alpha$ 1 subunit were observed higher in human Hb-2,3-BPG complex at 600 mM, compared to camel. The loop residues 111-120, and the helical residues 120-132 of  $\alpha$ 1 exhibited higher fluctuations at higher salt concentrations in human Hb-2,3-BPG complex, compared to camel complex system. The helical residues 2-13 and loop residues 14-20 of  $\beta$ 1 and  $\beta$ 2 subunits of camel Hb showed higher fluctuations at 300 mM. However, residues 1-32 of  $\beta$ 1 and  $\beta$ 2 subunits of human Hb, composed of loops and helical regions exhibited higher fluctuations at 600 mM, compared to camel. The loop residues 44-55 of  $\beta$ 1 showed higher fluctuations at lower salt concentrations (0 mM and 150 mM), while the same

residues of  $\beta 2$  showed higher fluctuations at higher salt concentrations (300 mM and 600 mM) in camel Hb-2,3-BPG complex. However, the same residues showed higher fluctuations at all salt concentrations in human Hb. Loop residues 80-100 of  $\beta 1$  and  $\beta 2$  showed higher fluctuations at only 0 mM and 600 mM, (Figures 60C and 60D). While the same residues in human demonstrated higher fluctuations at higher salt concentrations (300 mM and 600 mM). Importantly, residues 79 and 82 of  $\beta 1$  of camel Hb showed higher fluctuations at higher salt concentrations, while the same residues of  $\beta 2$  subunit showed higher fluctuations at only 300 mM. However, the same residues in human Hb showed higher fluctuations at higher salt concentrations (300 mM and 600 mM). Additionally, residues 139, 143 and 146 of both  $\beta 1$  and  $\beta 2$  subunits exhibited lower fluctuations at higher salt concentrations, compared to human Hb. Overall, the fluctuations of these important residues of  $\beta 1$  and  $\beta 2$  subunits were observed higher in human compared to camel at all salt concentrations, especially at 300 mM and 600 mM.

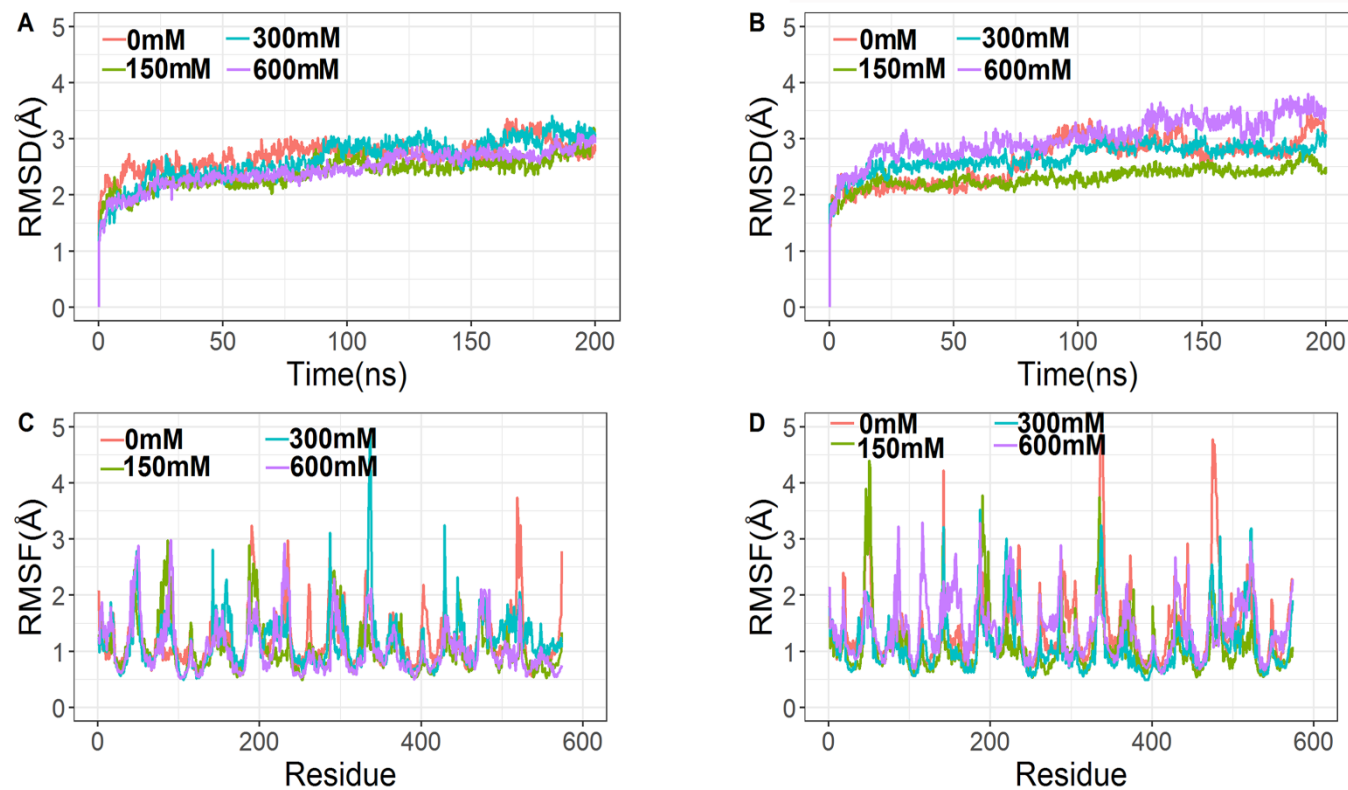


Figure 60: Root mean square standard deviation (RMSD) and root mean square fluctuation (RMSF) of protein C $\alpha$  atoms obtained from a 200 ns run of 2,3-BPG bound camel and human hemoglobin simulations at different salt conditions. Data from different salt conditions are shown in red, green, blue, and purple. (A) RMSD of camel Hb-2,3-BPG complex simulations; (B) RMSD of human Hb-2,3-BPG complex simulations; (C) RMSF of camel Hb-2,3-BPG complex simulations and, (D) RMSF of human Hb-2,3-BPG complex simulations. Note that the residue number used in the RMSF plots uses a sequential combination of the  $\alpha 1$ ,  $\beta 1$ ,  $\alpha 2$ , and  $\beta 2$  in the PDB structure.

The contact duration of critically important residues of hemoglobin  $\beta$  subunits with 2,3-BPG were observed during the simulations. Several hydrogen bonds, hydrophobic interactions, salt bridges, cation- $\pi$ , and  $\pi$ - $\pi$  interactions were observed to form, break, and reform throughout the simulation runs. Asp79 of both  $\beta 1$  of  $\beta 2$  subunits of camel Hb exhibited consistent interactions at all salt concentrations. While the same residue of  $\beta 1$  chain of human Hb formed intermittent interaction at lower salt concentrations only. Lys82 of both  $\beta$  chains of human and camel Hb formed sustained interactions for the full duration of the simulations at all salt concentrations. Moreover, Asn139 of  $\beta 1$  chain of camel Hb exhibited sustained interactions with 2,3-BPG at higher salt concentration. However, Asn139 of both  $\beta$  chains of human Hb formed interactions with 2,3-BPG at lower salt concentrations only. The residue His143 of  $\beta 1$  and  $\beta 2$  of camel hemoglobin formed more sustained interactions with 2,3-BPG at higher salt concentrations, compared to human hemoglobin. Similarly, His146 of camel  $\beta$  subunits formed more sustained interactions with 2,3-BPG at higher salt concentrations (300 mM and 600 mM). However, such interactions were not observed in human Hb. Additionally, Asn80 of camel  $\beta 2$  subunit showed more sustained interactions at 300 mM, and 600 mM, while, the same residue of  $\beta 1$  of human Hb showed interactions with 2,3-BPG at 0 mM and 150 mM only (Figures 61 and 62).

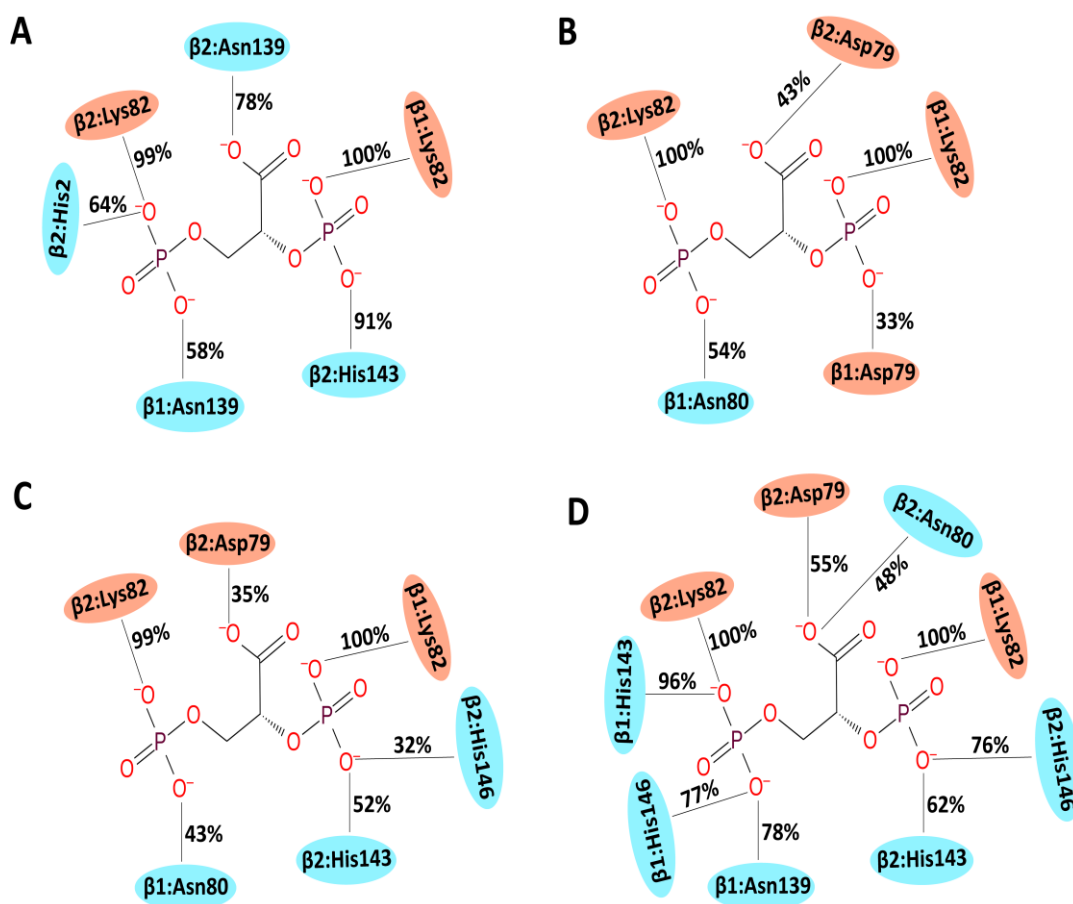


Figure 61: The percentage of simulation time during which different residues of camel hemoglobin interacted with 2,3-BPG. Orange, green, and blue colors represent charged, hydrophobic and polar amino acids, respectively. (A) Simulations of camel hemoglobin-2,3-BPG complex at 0mM; (B) Simulations of camel hemoglobin-2,3-BPG complex at 150 mM; (C) Simulations of camel hemoglobin-2,3-BPG complex at 300 mM; and, (D) Simulations of camel hemoglobin-2,3-BPG complex at 600 mM.

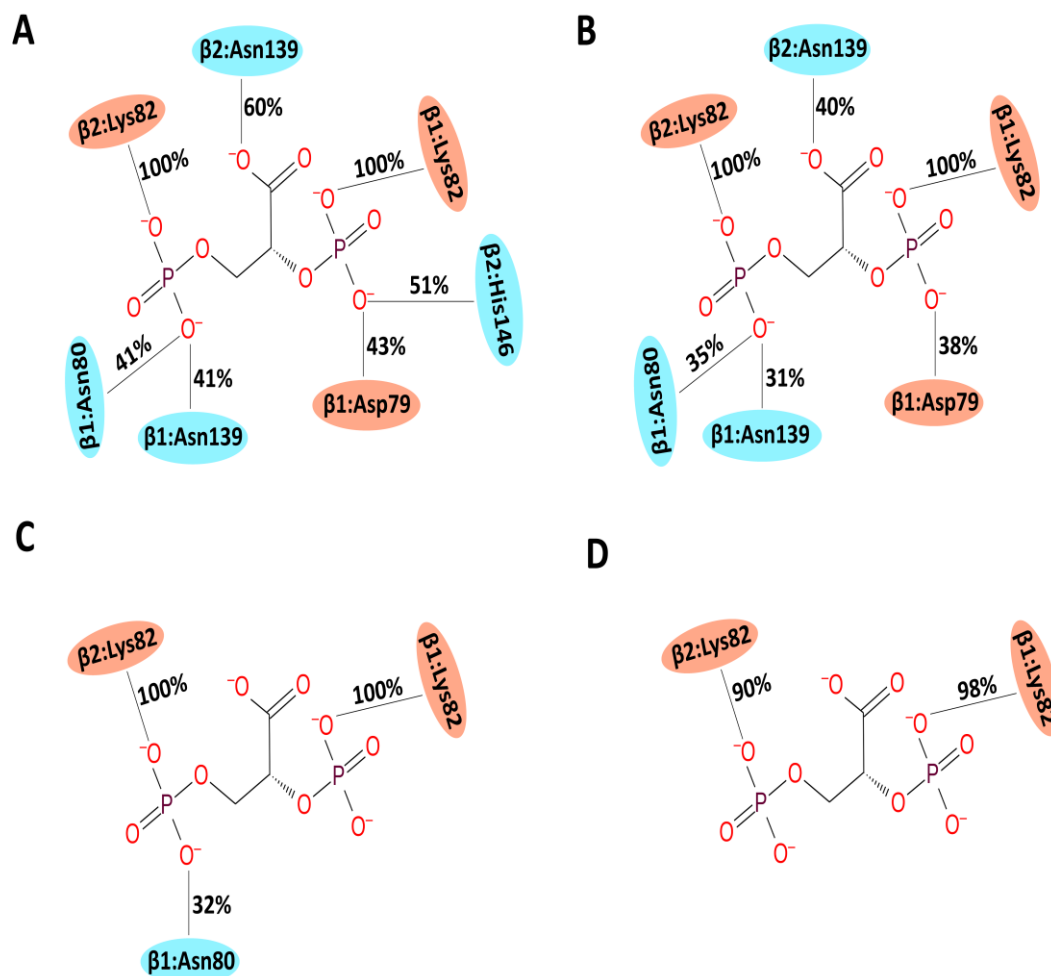


Figure 62: The percentage of simulation time during which different residues of human hemoglobin interacted with 2,3-BPG. Orange, green, and blue colors represent charged, hydrophobic and polar amino acids, respectively. (A) Simulations of human hemoglobin-2,3-BPG complex at 0mM; (B) Simulations of human hemoglobin-2,3-BPG complex at 150 mM; (C) Simulations of human hemoglobin-2,3-BPG complex at 300 mM; and, (D) Simulations of human hemoglobin-2,3-BPG complex at 600 mM.

### 6.1.7 MD simulations of camel and human hemoglobin bound to 2,3-BPG at different temperature conditions

Next, the RMSD of both camel and human hemoglobin-2,3 BPG complexes at different temperature conditions were determined. The structures of both camel and human Hb remained stable during simulation runs. The RMSD of the  $C\alpha$  atoms of camel and human Hb bound to 2,3-BPG with respect to the initial structure

stabilized under 3.5 Å and 4 Å in all the simulations, respectively (Figures 63A and 63B). However, human hemoglobin bound to 2,3-BPG demonstrated higher RMSD at 34°C. In order to measure the effect of 2,3-BPG on the backbone stability and residual flexibility of camel and human hemoglobin, the RMSF of backbone C $\alpha$  atoms of both camel and human hemoglobin were investigated (Figures 63C and 63D). Overall, camel hemoglobin showed limited fluctuations compared to human hemoglobin. The loop residues 41-52 of  $\alpha$ 1 of camel Hb showed limited fluctuation at all temperature conditions, compared to human Hb when bound to 2,3-BPG. Whereas, loop residues 46-52 of  $\alpha$ 2 subunit of both camel and human showed similar fluctuations at all conditions, especially at 41°C. Additionally, fluctuations in human Hb were observed to be higher at 34°C and 41°C, compared to camel Hb (Figures 63C and 63D). The loop residues 78-87 of  $\alpha$ 1 subunit in camel Hb showed higher fluctuations at lower temperature condition (27°C). However such an effect was not observed in human Hb. The loop residues 44-55 of  $\beta$ 1 demonstrated similar fluctuations in both camel and human hemoglobin. However, these residues of  $\beta$ 2 chain showed higher fluctuations at higher temperature conditions (34°C and 41°C) in human Hb, compared to camel Hb (Figures 63C and 63D). The loop residues 81-97 of  $\beta$ 1 chain of camel Hb demonstrated more fluctuations at only 34°C, while the same residues of human Hb showed higher fluctuations at all temperature conditions. Additionally, the same residues of  $\beta$ 2 chain of human Hb exhibited higher fluctuations at higher temperature conditions when compared to camel Hb. More importantly, residues 79, 82, 139, 143, and 146 of  $\beta$ 1 and  $\beta$ 2 subunits of camel Hb showed limited fluctuations at higher temperature conditions, compared to human Hb.



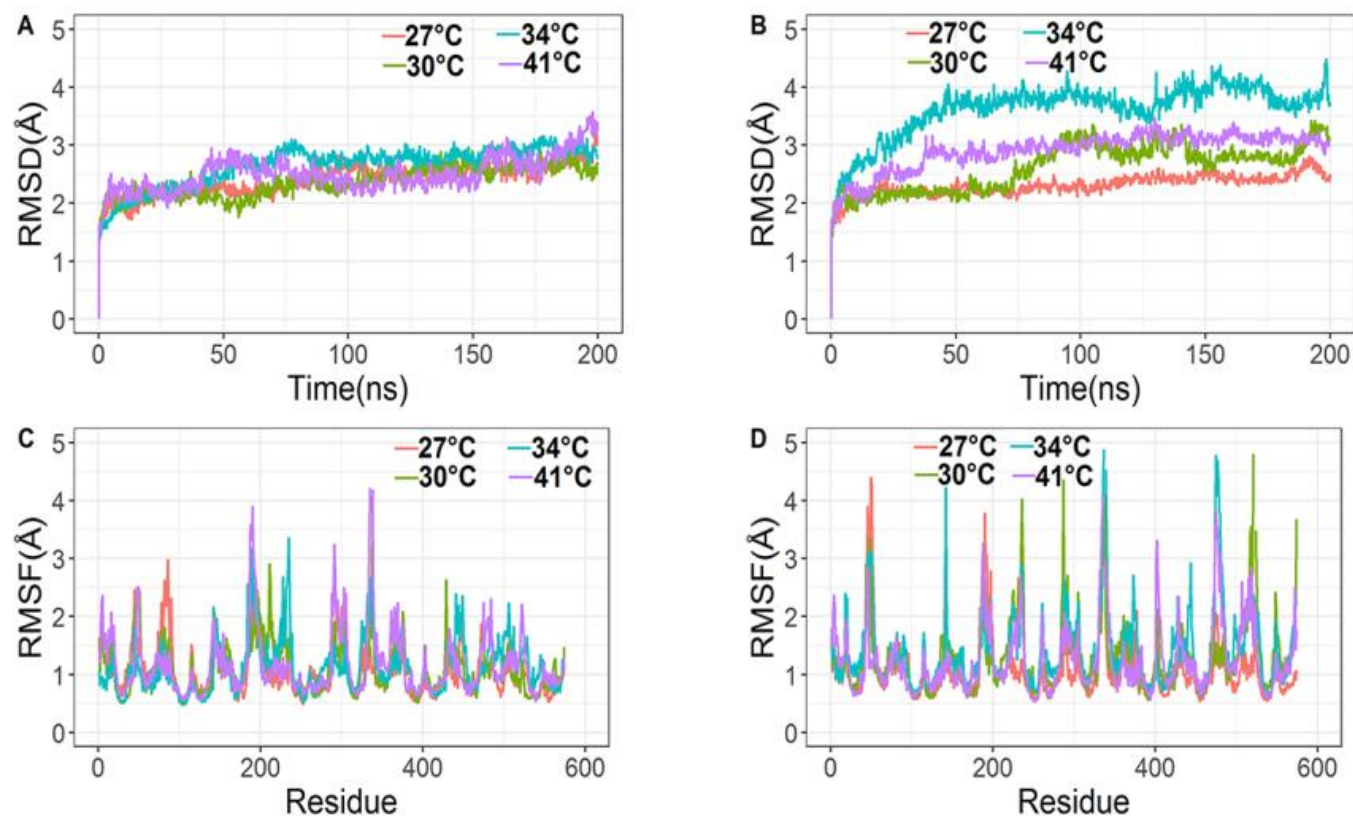


Figure 63: Root mean square standard deviation (RMSD) and root mean square fluctuation (RMSF) of protein C $\alpha$  atoms obtained from a 200 ns run of 2,3-BPG bound camel and human hemoglobin simulations at different temperature conditions. Data from different temperature conditions are shown in red, green, blue, and purple. (A) RMSD of camel Hb-2,3-BPG complex simulations; (B) RMSD of human Hb-2,3-BPG complex simulations; (C) RMSF of camel Hb-2,3-BPG complex simulations and, (D) RMSF of human Hb-2,3-BPG complex simulations. Note that the residue number used in the RMSF plots uses a sequential combination of the  $\alpha$ 1,  $\beta$ 1,  $\alpha$ 2, and  $\beta$ 2 in the PDB structure.

The contact duration of important interacting residues of camel and human Hb with 2,3-BPG at different temperature conditions were also determined. Asp79 of both  $\beta 1$  of  $\beta 2$  subunits of camel Hb exhibited intermittent interactions at different temperature conditions (Figure 64). However, such interactions were not observed in human Hb. Lys82 of both  $\beta$  chains of human and camel Hb formed sustained interactions for the full duration of the simulations at all temperature conditions (Figures 64 and 65). Moreover, Asn139 of both  $\beta$  chains of human Hb exhibited intermittent interactions with 2,3-BPG, especially at lower temperature conditions. However, camel hemoglobin did not produce such interactions in any simulation run. The residues His143, His146 of  $\beta 1$  and  $\beta 2$  of camel hemoglobin formed more sustained interactions with 2,3-BPG at higher salt concentrations, compared to human hemoglobin. However, such interactions were not observed in human Hb. Additionally, Asn80 of camel  $\beta 2$  subunit showed more sustained interactions at 300 mM, and 600 mM, while, the same residue of  $\beta 1$  of human Hb showed interactions with 2,3-BPG at 0 mM and 150 mM only. The contact duration of important interacting residues of camel and human Hb with 2,3-BPG at different temperature conditions were also determined. Asp79 of both  $\beta 1$  of  $\beta 2$  subunits of camel Hb exhibited intermittent interactions at different temperature conditions. However, such interactions were not observed in human Hb. Lys82 of both  $\beta$  chains of human and camel Hb formed sustained interactions for the full duration of the simulations at all temperature conditions. Moreover, Asn139 of both  $\beta$  chains of human Hb exhibited intermittent interactions with 2,3-BPG, especially at lower temperature conditions. However, camel hemoglobin did not produce such interactions in any simulation run. The residues His143, His146 of  $\beta 1$  and  $\beta 2$  of camel hemoglobin formed more sustained interactions with 2,3-BPG at higher salt concentrations, compared to

human hemoglobin. However, such interactions were not observed in human Hb. Additionally, Asn80 of camel  $\beta 2$  subunit showed more sustained interactions at 300 mM, and 600 mM, while, the same residue of  $\beta 1$  of human Hb showed interactions with 2,3-BPG at 0 mM and 150 mM only (Figures 64 and 65).

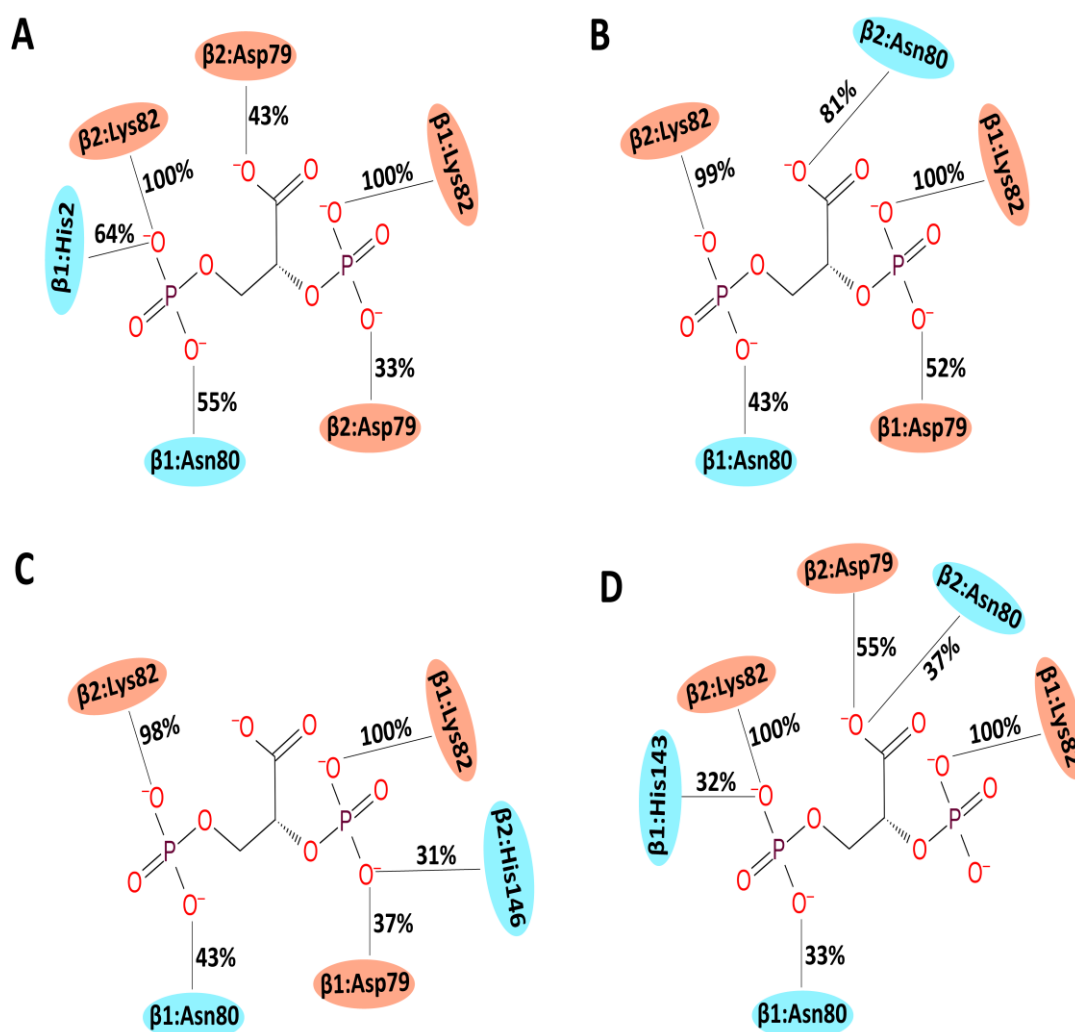


Figure 64: The percentage of simulation time during which different residues of camel hemoglobin interacted with 2,3-BPG. Orange, green, and blue colors represent charged, hydrophobic and polar amino acids, respectively. (A) Simulations of camel hemoglobin-2,3-BPG complex at 27°C; (B) Simulations of camel hemoglobin-2,3-BPG complex at 30°C ; (C) Simulations of camel hemoglobin-2,3-BPG complex at 34°C; and, (D) Simulations of camel hemoglobin-2,3-BPG complex at 41°C.

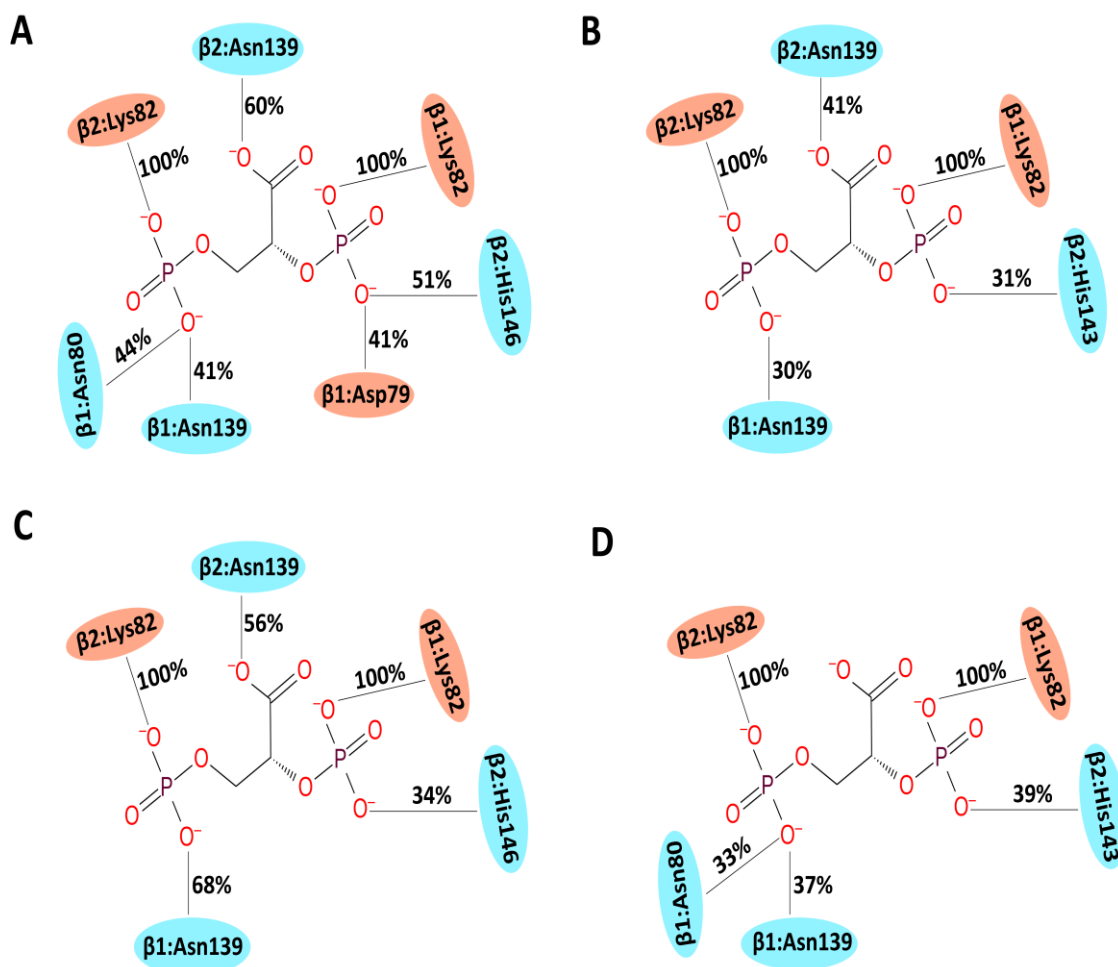


Figure 65: The percentage of simulation time during which different residues of human hemoglobin interacted with 2,3-BPG. Orange, green, and blue colors represent charged, hydrophobic and polar amino acids, respectively. Orange, green, and blue colors represent charged, hydrophobic and polar amino acids, respectively. (A) Simulations of human hemoglobin-2,3-BPG complex at 27°C; (B) Simulations of human hemoglobin-2,3-BPG complex at 30°C ; (C) Simulations of human hemoglobin-2,3-BPG complex at 34°C; and, (D) Simulations of human hemoglobin-2,3-BPG complex at 41°C.

### 6.1.8 MD simulations of ATP bound to camel and human hemoglobin at different salt conditions

ATP is another important co-factor present in erythrocytes and is also involved in binding with deoxyhemoglobin. However, its levels in erythrocytes are significantly lower compared to 2,3-BPG. Camel and human hemoglobin bound to ATP were simulated at different salt concentration. RMSD of C $\alpha$  atoms of camel

hemoglobin with respect to initial structure showed stability at 2.5 Å in all salt concentrations except 150 mM (Figure 66A). Camel Hb-ATP complex systems were observed more stabilized with lower RMSD at higher salt concentrations (300 mM and 600 mM) compared to lower salt concentrations (Figure 66A). However, the structural integrity of human Hb-ATP complex systems at different salt concentrations were retained with a RMSD of C $\alpha$  atoms from the initial structure that was under 3.5 Å (Figure 66B). Moreover, to determine and compare backbone stability and residual fluctuations of the camel and human Hb-ATP complex at different salt concentrations, RMSF of backbone C $\alpha$  atoms were measured and plotted (Figures 66A and 66B). Overall, camel Hb showed lower fluctuations, compared to human hemoglobin. Loop residues 45-51 of  $\alpha$ 1 subunit showed more variations only at 150 mM, while the same region in human hemoglobin fluctuated more at 150 mM and 300 mM. The similar residues of  $\alpha$ 2 subunits of both camel and human Hb exhibited higher fluctuations at 300 mM and 600 mM (Figure 66). These residues fluctuated more in camel Hb compared to human Hb. The Loops residues 1-5, and 16-20 of camel  $\beta$ 1 chain exhibited more fluctuations at higher salt concentrations (300 mM and 600 mM), compared to human Hb. Loop residues 44-55 and 80-100 residues of  $\beta$ 1 of human Hb showed higher fluctuations at higher salt concentrations, while the same residues of camel Hb exhibited more fluctuations at lower salt concentrations. However, the same residues of  $\beta$ 2 of camel and human Hb showed higher fluctuations at higher and lower salt concentrations, respectively (Figures 66C and 66D). Interestingly, these regions fluctuated more in human Hb, compared to camel hemoglobin. Importantly, residues 79, 82, 139, 143, and 146 of  $\beta$ 1 and  $\beta$ 2 subunits of camel Hb showed lower fluctuations at higher salt concentrations, compared to human Hb.

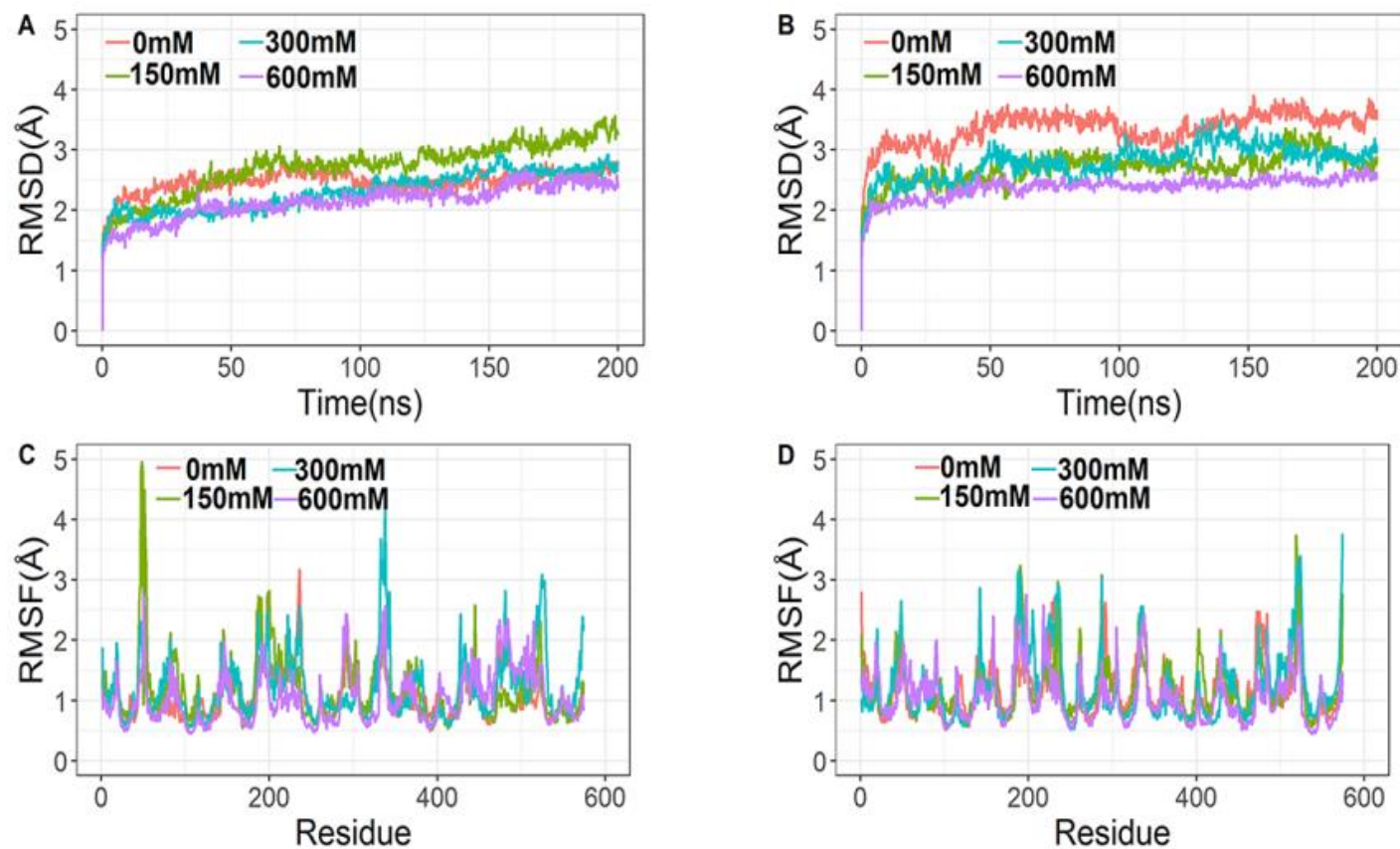


Figure 66: Root mean square standard deviation (RMSD) and root mean square fluctuation (RMSF) of protein C $\alpha$  atoms obtained from a 200 ns run of ATP bound camel and human hemoglobin simulations at salt conditions. Data from different salt conditions are shown in red, green and blue. (A) RMSD of camel Hb-ATP complex; (B) RMSD of human Hb-ATP complex simulations (C) RMSF of camel Hb-ATP complex simulations and, (D) RMSF of human Hb-ATP complex simulations. Note that the residue number used in the RMSF plots uses a sequential combination of the  $\alpha$ 1,  $\beta$ 1,  $\alpha$ 2, and  $\beta$ 2 in the PDB structure.

The contact duration of important interacting residues of camel and human Hb with ATP were determined. Asp79 of both  $\beta 1$  of  $\beta 2$  subunits of camel Hb exhibited intermittent interactions at lower salt concentrations (Figure 67). While the same residue of  $\beta 1$  chain of human Hb formed intermittent interaction at 600 mM only (Figure 67). Lys82 of both  $\beta$  chains of human and camel Hb formed sustained interactions for the full duration of the simulations at all salt concentrations. Moreover, Asn139 of both  $\beta$  chains of human Hb exhibited intermittent interactions with ATP in all simulation runs. However, such interactions were not observed in camel Hb. The residue His143 and His146 of  $\beta 1$  and  $\beta 2$  of camel hemoglobin formed more sustained interactions at 300 mM, with ATP, respectively. However, His143 of  $\beta 1$  chain in human hemoglobin produced consistent interaction at all salt concentrations. His146 of camel  $\beta 1$  chain formed more sustained interactions with ATP at 0 mM and 300 mM. However, such an interaction was not observed in human Hb. Moreover, Arg144, a substituted residue in camel Hb  $\beta 1$  subunit formed interactions with ATP at higher salt concentrations. Human Hb did not produce such an interaction. Additionally, Asn80, and Leu81 of camel  $\beta 2$  subunit showed more sustained interactions at 300 mM, compared to other salt concentrations. However, Asn80 residue of  $\beta 1$  of human Hb showed interactions with ATP at 600 mM only (Figures 67 and 68).

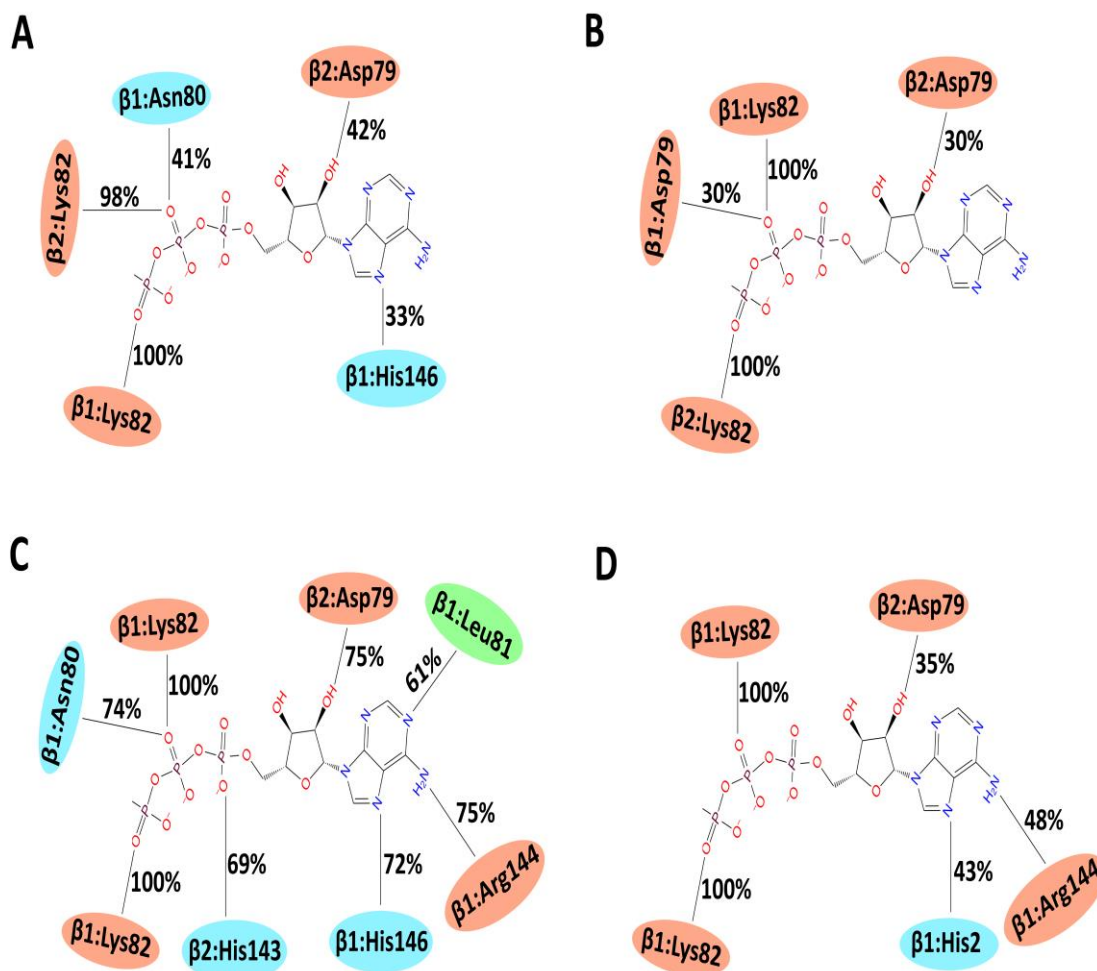


Figure 67: The percentage of simulation time during which different residues of camel hemoglobin interacted with ATP. Orange, green, and blue colors represent charged, hydrophobic and polar amino acids, respectively. (A) Simulations of camel hemoglobin-ATP complex at 0 mM; (B) Simulations of camel hemoglobin-ATP complex at 150 mM; (C) Simulations of camel hemoglobin-ATP complex at 300 mM; and, (D) Simulations of camel hemoglobin-ATP complex at 600 mM.



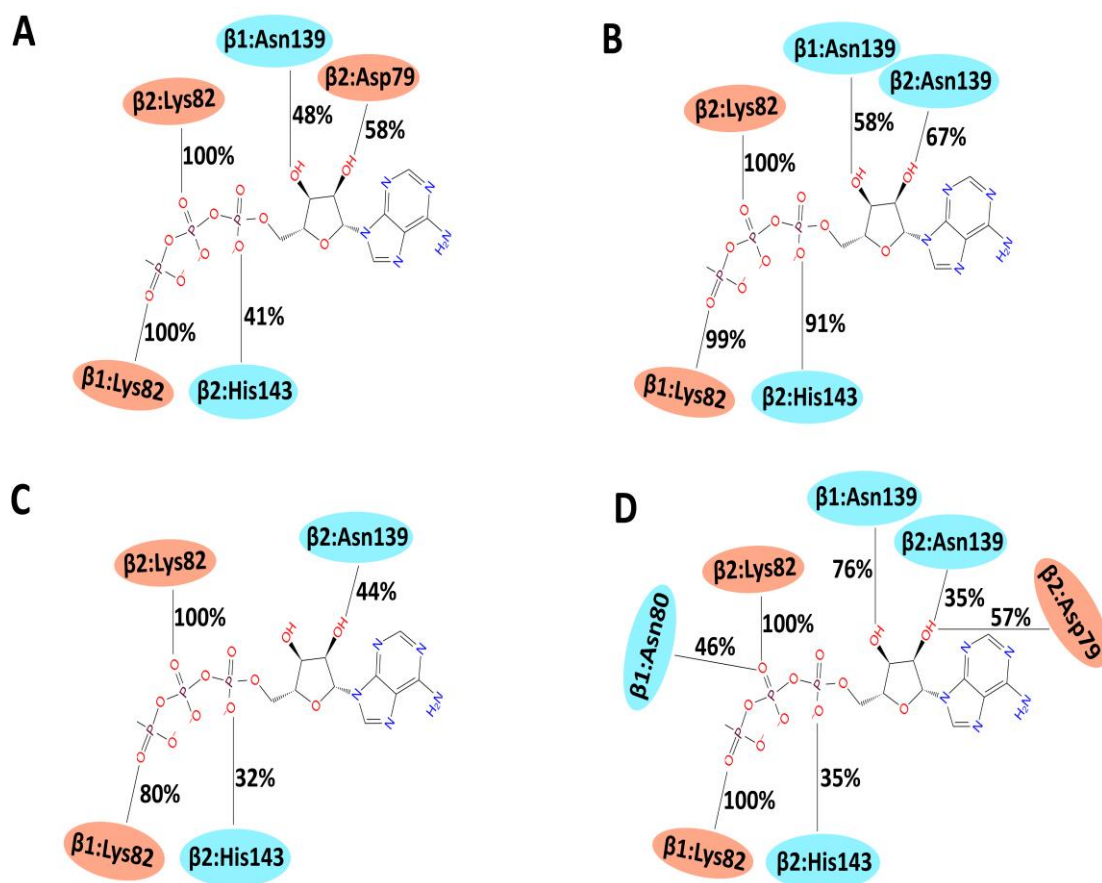


Figure 68: The percentage of simulation time during which different residues of human hemoglobin interacted with ATP. Orange, green, and blue colors represent charged, hydrophobic and polar amino acids, respectively. (A) Simulations of human hemoglobin-ATP complex at 0 mM; (B) Simulations of human hemoglobin-ATP complex at 150 mM; (C) Simulations of human hemoglobin-ATP complex at 300 mM; and, (D) Simulations of human hemoglobin-ATP complex at 600 mM.

### 6.1.9 MD simulations of ATP bound to camel and human hemoglobin at different temperature conditions

Camel and human hemoglobin bound to ATP were simulated at different temperature conditions. Camel and human Hb structures remained stable during simulation runs. The RMSD of  $C\alpha$  atoms of both camel and human hemoglobin with respect to initial structures showed stability under 3.5 Å in all simulations (Figures 69A, 69B). In order to determine and compare the backbone stability and residual fluctuations of both camel and human Hb-ATP complexes at different temperature

conditions, RMSF of backbone C $\alpha$  atoms were measured and plotted (Figures 69C and 69D). Loop residues 12-18 of  $\alpha$ 1 exhibited more fluctuations in human Hb only, especially at 30°C and 34°C. Loop residues 48-51 of  $\alpha$ 1 subunit of camel Hb showed higher fluctuations at lower temperature condition (27°C), while  $\alpha$ 1 subunit residues 44-54 of human Hb showed higher fluctuations at higher temperature conditions (34°C and 41°C). However, similar residues of  $\alpha$ 2 subunits of both camel and human Hb exhibited higher fluctuations at higher temperature conditions (Figures 69C and 69D). These residues fluctuated more in camel Hb compared to human Hb. The loop residues 74-94 of both  $\alpha$ 1 and  $\alpha$ 2 subunits of human Hb exhibited more fluctuations at higher temperature conditions when compared to camel Hb. The loop residues 113-118 of  $\alpha$ 1 chain of human Hb also demonstrated higher fluctuations at 30°C and 41°C, compared to camel Hb. The loop residue 1-5 and helical residues 6-13 of  $\beta$ 1 chain of camel Hb showed higher fluctuations at 41°C, compared to human Hb. While the loop residues of 1-5 of  $\beta$ 2 subunit of only human Hb exhibited higher fluctuations at 34°C. Loop residues 44-54 and 82-100 of  $\beta$ 1 and  $\beta$ 2 of camel Hb showed higher fluctuations at higher temperature conditions (34°C and 41°C). While in human Hb, the residues 44-54  $\beta$ 1 exhibited more fluctuations at lower temperature conditions, and 87-100 residues of both  $\beta$ 1 and  $\beta$ 2 showed higher fluctuations at higher temperature conditions. Moreover, the residues 82-100 of  $\beta$ 1 and  $\beta$ 2 of camel Hb showed limited fluctuations at higher temperature conditions, compared to human Hb (Figure 69). Importantly, residues 79, and 82 of  $\beta$ 1 and  $\beta$ 2 subunits of camel Hb showed lower fluctuations, compared to human Hb. However, 139, 143, and 146 of  $\beta$ 1 and  $\beta$ 2 subunits demonstrated higher fluctuations in both camel and human Hb (Figures 69C and 69D).

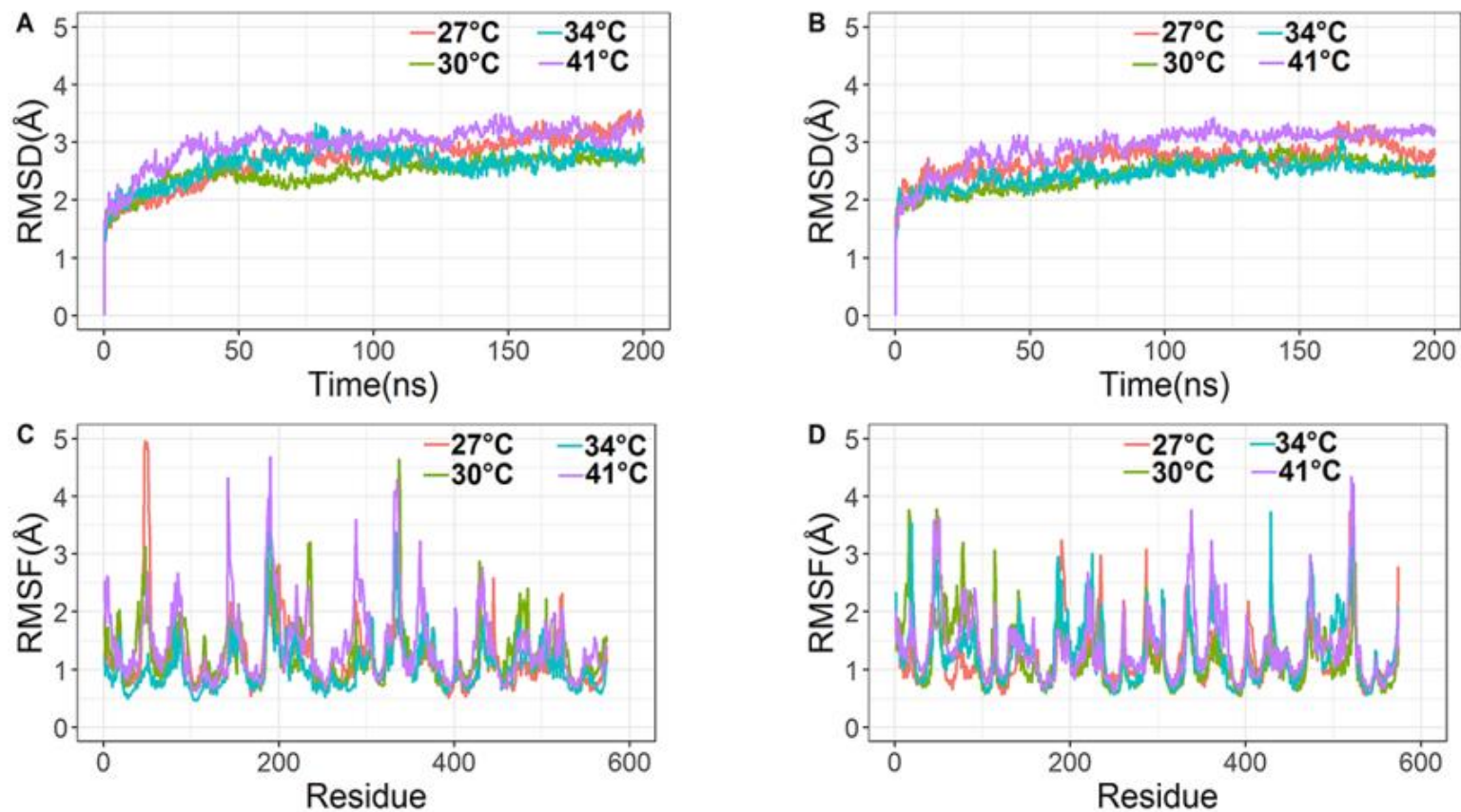


Figure 69: Root mean square standard deviation (RMSD) and root mean square fluctuation (RMSF) of protein C $\alpha$  atoms obtained from a 200 ns run of ATP bound camel and human hemoglobin simulations at different temperature conditions. Data from different temperature conditions are shown in red, green, blue, and purple. (A) RMSD of camel Hb-ATP complex simulations; (B) RMSD of human Hb-ATP complex simulations; (C) RMSF of camel Hb-ATP complex simulations and, (D) RMSF of human Hb-ATP complex simulations. Note that the residue number used in the RMSF plots uses a sequential combination of the  $\alpha 1$ ,  $\beta 1$ ,  $\alpha 2$ , and  $\beta 2$  in the PDB structure.

The contact duration of important interacting residues of camel and human Hb with ATP were determined. Asp79 of both  $\beta 1$  of  $\beta 2$  subunits of camel Hb exhibited consistent interactions at all temperature conditions (Figure 70). However, such interactions were not formed in human Hb (Figure 71). Lys82 of both  $\beta$  chains of human and camel Hb formed sustained interactions throughout the simulations at all temperature conditions. Asn139 of both  $\beta$  chains of human Hb exhibited consistent interactions with ATP in all simulation runs. However, Asn139 of camel Hb showed extremely weak interactions with ATP. The residue His143 of  $\beta 1$  of human hemoglobin formed more sustained interactions with ATP at 34°C, and the same residue  $\beta 2$  exhibited intermittent interactions at all temperature conditions, except at 30°C. However, in camel only  $\beta 1$  chain produced intermittent interaction at only 34°C and 41°C. His146 of human  $\beta$  chains also formed intermittent interactions with ATP at only lower temperature conditions. However, such an interaction was not observed in camel Hb. Moreover, Arg144, a substituted residue in camel Hb  $\beta 1$  subunit formed interactions with ATP at 34°C. Human Hb did not produce such an interaction (Figures 70 and 71).

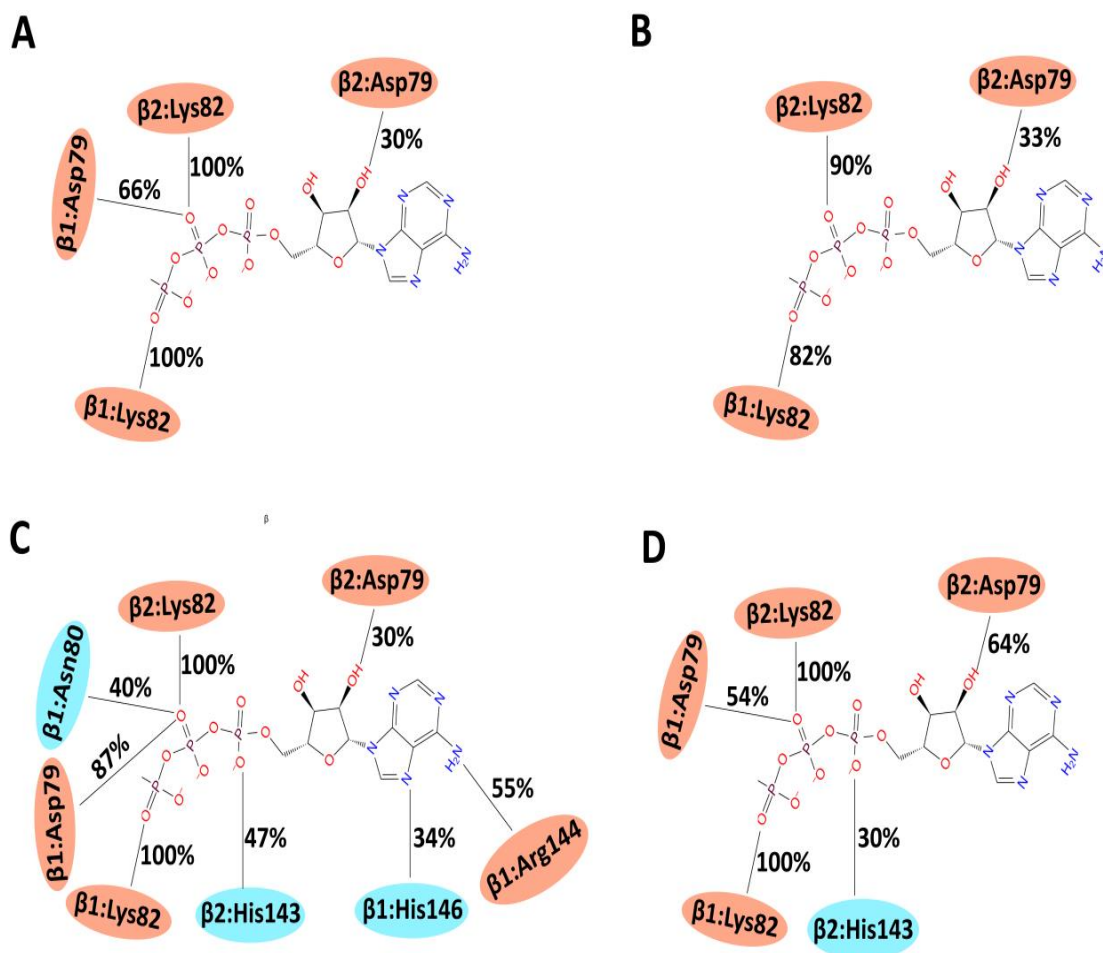


Figure 70: The percentage of simulation time during which different residues of camel hemoglobin interacted with ATP. Orange, green, and blue colors represent charged, hydrophobic and polar amino acids, respectively. (A) Simulations of camel hemoglobin-ATP complex at 27°C; (B) Simulations of camel hemoglobin-ATP complex at 30°C; (C) Simulations of camel hemoglobin-ATP complex at 34°C; and, (D) Simulations of camel hemoglobin-ATP complex at 41°C.

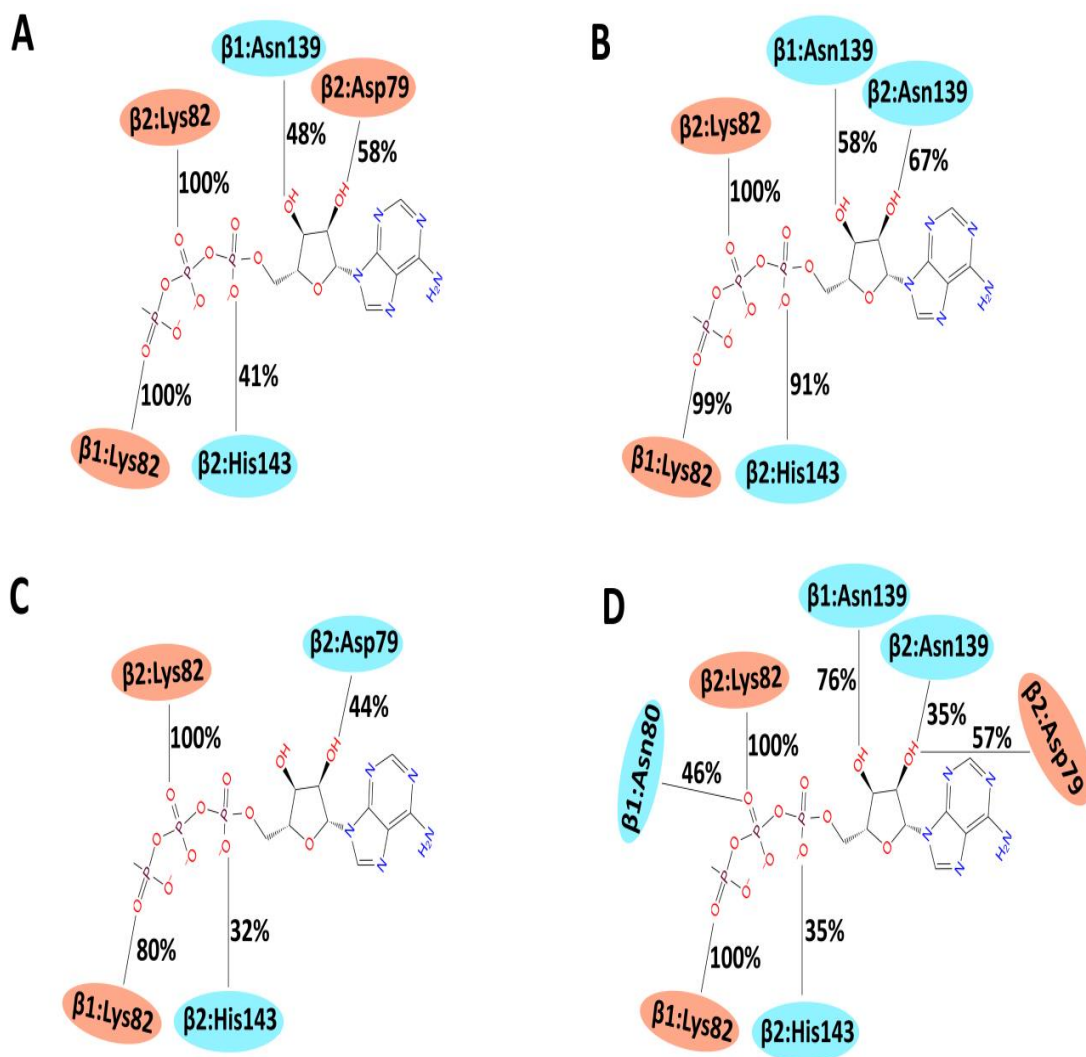


Figure 71: The percentage of simulation time during which different residues of human hemoglobin interacted with ATP. Orange, green, and blue colors represent charged, hydrophobic and polar amino acids, respectively. (A) Simulations of human hemoglobin-ATP complex at 27°C; (B) Simulations of human hemoglobin-ATP complex at 30°C ; (C) Simulations of human hemoglobin-ATP complex at 34°C; and, (D) Simulations of human hemoglobin-ATP complex at 41°C.

## 6.2 Discussion

This study provide insights into the stability of camel and human hemoglobin under various dehydrated conditions, as well as the stability of interaction of 2,3-BPG and ATP, which are essential for the unloading of oxygen from hemoglobin, with camel and human hemoglobin using several long MD simulations. Overall, interestingly, extended MD simulations at different salt and temperature conditions

revealed that camel hemoglobin structures showed more stability when compared to human hemoglobin. Additionally, in camel hemoglobin, critical regions important for the binding of heme, 2,3-BPG, and ATP molecules demonstrated limited fluctuations in the studied conditions. Molecular docking and MD simulations indicated that 2,3-BPG, and ATP molecules, which are abundantly present in erythrocytes, formed more stable interactions with essential residues with camel hemoglobin when compared to human hemoglobin.

Generally, mammalian erythrocytes are highly sensitive to osmotic fragility except camels (Bogner et al., 2005; Schmidt-Nielsen et al., 1956). Importantly, camels RBCs are extremely resistant to osmotic fragility and are inherently adapted to endure the sudden fluctuations in blood osmolarity without affecting its function (Oyewale et al., 2011). In order to measure the changes resulting from different salt concentrations, MD simulations were performed, since no prior attempt has been made to look at the residue level fluctuations of this macromolecule. Indeed, simulations are clearly representative of fluctuations being affected by different salt concentrations (Figure 57). The natural capability of protein function is highly dependent on the extent of the innate fluctuations of a macromolecule (Frauenfelder, Parak, & Young, 1988; Steinbach et al., 1991). Here, simulations in the presence of different salt concentrations demonstrated fluctuations of the important regions essential for the oxygen binding (Figure 57). Interestingly, the high fluctuations were observed in residues near to the heme binding sites in each subunit. The residues in these regions exhibited high RMSF values than the other residues. Importantly, His87 of  $\alpha$  subunits and His92 of  $\beta$  subunits demonstrated more fluctuations at higher salt concentrations. These residues are essential for the binding of four heme

groups and served as oxygen binding sites. Importantly, conserved residues  $\alpha 1$ :Phe43 and  $\alpha 1$ :Phe46 showed more fluctuations at higher salt conditions (Figure 57). These functional residues are present in the heme pocket distal to heme where oxygen binds (Laberge & Yonetani, 2008). Moreover,  $\alpha 1$  conserved residues Leu86 and Leu91 also exhibited higher fluctuations when salt concentration was increased. These residues are part of proximal heme pocket residues (Laberge & Yonetani, 2008). Interestingly, in comparison to human hemoglobin, camel hemoglobin demonstrated lower fluctuations at all salt concentrations. Similarly, when different temperature conditions were used camel hemoglobin showed lower fluctuations at higher temperature conditions especially in the regions important for the binding of heme groups and thus considered as oxygen binding sites, compared to human hemoglobin (Figure 58). Therefore, these changes could affect the affinity of oxygen molecule with camel hemoglobin.

2,3-BPG and ATP are two important co-factors present abundantly in the erythrocytes that bind to hemoglobin (Castilho, Glass, & Manco, 2003). Prior studies have demonstrated that both these co-factors preferentially bind to deoxyhemoglobin (Chen et al., 2017; Chu et al., 2008). Additionally, their binding with deoxyhemoglobin is responsible for stabilizing the deoxyhemoglobin or tense (T) state of the hemoglobin. Generally, oxygen is unloaded from hemoglobin to tissue cells during the deoxyhemoglobin state. Therefore, these two co-factors have significant role in the unloading of oxygen molecules and also in the regulation of transition from oxyhemoglobin (relaxed state) to deoxyhemoglobin (tensed state). During the transition from deoxyhemoglobin to oxyhemoglobin, the binding pocket present in the center of hemoglobin or more precisely at the entrance of the  $\beta 1/\beta 2$



cavity, is disrupted and therefore not available for these co-factors to bind in oxyhemoglobin state (Berg et al., 2002). Thus, only deoxyhemoglobin or tensed state of Hb was selected for the molecular docking and MD simulations of 2,3-BPG and ATP with camel and human Hb. The molecular docking of 2,3-BPG and ATP identified the active site residues of Hb and were situated at the entrance of  $\beta 1/\beta 2$  cavity. These findings are in agreement with previous studies (Arnone, 1972; Chen et al., 2017). Importantly, both 2,3-BPG and ATP share the same binding site on Hb. In comparison to ATP, 2,3-BPG is the more abundant co-factor present in erythrocytes of most mammals present at a concentration 4-13 mmol/l. While, observed ATP concentration in the mammal's RBCs is 1.3 mmol/l. Additionally, ATP is mostly present as  $\text{ATP-Mg}^{2+}$  in the erythrocytes, which binds weakly to hemoglobin. Thus, this suggests that ATP has minimal effect on oxygen affinity, while 2,3-BPG predominantly binds with deoxyhemoglobin and play a major role in the regulation of oxygen affinity and unloading of oxygen to tissue cells. Importantly, the levels and precise functions of these co-factors in the erythrocytes of camel have not been reported so far. Therefore, extensive computational modeling approaches were used to determine the binding mode, and stability of critical interactions between camel deoxyhemoglobin and 2,3-BPG or ATP. Several stresses such as different salt concentrations and different temperature conditions were used to determine the impact of these conditions on the binding stability of 2,3-BPG and ATP with camel Hb. Additionally, these results were compared with human Hb. Previous studies have reported that Lys82 and His143 residues of both  $\beta$  subunits are highly essential for the binding of 2,3-BPG and ATP with deoxyhemoglobin subunit. However, Asp79, Asn139 and His146 residues are also considered vital for the binding of these co-factors. However, 2,3-BPG produced interactions with only  $\beta 1$  chain residues of

human Hb and were in agreement with prior studies (Chen et al., 2017). Additionally, ATP formed similar interactions with human Hb, except His143 of  $\beta_2$ , and His146 of both  $\beta$  subunits. MD simulations indicated that 2,3-BPG formed more sustained interactions with essential residues Lys82, His143, and His146 of camel hemoglobin at higher salt concentrations (Figure 61). However, 2,3-BPG only maintained interactions with His143 at lower salt concentrations and with Lys82 of human Hb at all salt concentrations (Figure 62). This indicates that at higher osmotic pressure induced by increased concentrations of NaCl, camel Hb formed stronger interactions with 2,3-BPG and support the release of oxygen to tissue cells. The effect of different temperature conditions on the binding stability of 2,3-BPG with camel and human Hb indicated that 2,3-BPG maintained intermittent interactions with critical residues of both camel and human Hb at lower temperatures (Figures 64 and 65). These findings are in agreement with previous studies which mentioned that lower temperature favored the binding of 2,3-BPG with Hb (Benesch, Benesch, & Yu, 1969). Human Hb residues (Asn139, His143) also showed more consistent interactions at lower temperature conditions, compared to camel. However, Lys82 formed sustained interactions with both camel and human Hb at all temperature conditions. Importantly, Asp79, Asn80 residues of camel Hb exhibited more consistent interactions with 2,3-BPG even at higher temperature conditions, compared to human Hb (Figures 64 and 65).

The binding stability of ATP with camel and human Hb residues at different temperature and salt conditions exhibited similar results. ATP formed more sustained interactions with Asp79, Asn80, His143, and His146 residues of camel Hb at higher salt concentrations, compared to human Hb (Figures 70 and 71). Lys82 of both camel

and human Hb exhibited consistent interactions throughout the simulations at all salt concentrations (Figure 70). However, the binding stability of camel residues His143, and His146 with ATP were weaker when compared to 2,3-BPG at higher salt concentrations. However, at different temperature conditions, human Hb residues His143, and His146 produced more consistent interactions with ATP, especially at lower temperature conditions, compared to camel Hb (Figures 70 and 71). While, Asp79, Asn80, and Arg144 of camel Hb showed more consistent interactions with ATP at higher temperature conditions, compared to human Hb (Figures 70 and 71). Hb Lys82 residue formed interactions with ATP for the full duration of simulation time at all temperature conditions in both camel and human.

The findings of this study are of significant importance in understanding the behaviour of camel hemoglobin under different dehydrated conditions, particularly the involvement of erythrocytes co-factors during dehydrated conditions. Indeed, hemoglobin is the most well studied protein both genetically, and biochemically (Oyewale et al., 2011). However, from structural prospective, the behavior of hemoglobin under different stresses have not been greatly explored. This study provided useful insights into the interactions of 2,3-BPG and ATP with camel and human Hb with implications in the physiology of these mammals under dehydrated conditions. Interestingly, camels can fluctuate their body temperature from approximately 34°C to 40°C during daytime (Oyewale et al., 2011; Schmidt-Nielsen et al., 1956). Moreover, camels have an exceptional ability to live without drinking water for longer period of time. These two conditions in combination produces a severe dehydrated environment in camels. Other mammals cannot withstand such drastic conditions any significant period of time. More importantly, severe

dehydration and high temperature conditions are significantly associated with increased respiratory rate in mammals (Barcroft & Izquierdo, 1931; Gaalaas, 1945; Rubini & Bosco, 2013). Higher temperature conditions decrease the overall binding affinity of oxygen molecules with hemoglobin and is also involved in an increased production of 2,3-BPG as a result of hyperventilation. These phenomena support more unloading of oxygen into tissues to meet their oxygen demand during high temperature and hyperventilation. It is also important to mention that these effects are due to Bohr effect (Yonetani *et al.*, 2002). It states that hemoglobin's lower affinity for oxygen is associated with an increase in partial pressure of carbon dioxide and a decrease in blood pH. For instance, higher temperature, and hyperventilation enhances the metabolic activities within tissues lead in the generation of more carbon dioxide. As a result of high CO<sub>2</sub>, more hydrogen ion (H<sup>+</sup>) will be produced which ultimately lead to lower pH and the production of more 2,3-BPG. These effects ultimately reduce the affinity of hemoglobin for oxygen. However, hyperventilation for longer period of time or chronic hyperventilation blocks the potential of Bohr effects and increases the hemoglobin binding affinity for oxygen with lesser release to peripheral tissues, including important organs such as brain, liver, kidney, and heart (Benner, Patel, Singh, & Dua, 2020). Importantly, more stable interactions of 2,3-BPG especially with camel hemoglobin at higher dehydrated conditions support these arguments and are vital to fulfill the oxygen demands of the peripheral tissues. This could be the reason why a camel's vital organs and peripheral tissues remain functional for longer period of time during severe environmental conditions.

## Chapter 7: Conclusion

This study looked at a number of aspects related to structural, genetic and pharmacological properties of camel hemoglobin and hemoglobin-derived peptides. First, the work presented here provides structural insights into the binding of camel and human hemorphins with MOR, IRAP and ACE. Importantly, camel hemorphins demonstrated more stable interactions with these drug targets and also produced more potent ACE inhibitory activity, compared to human hemorphins. This study also identified, for the first time, a G protein-coupled receptor, angiotensin II type 1 receptor (AT1R) that is a target of hemorphins. *In silico* and *in vitro* data indicated that LVV-hemorphin-7 binds to the intracellular side of AT1R and allosterically potentiated the potency of AngII as well as its downstream signaling. Additionally, this study explored the genetic and structural variations of camel hemoglobin and how these variations could contribute to the overall stability and residue-level flexibility in camel hemoglobin in response to dehydrated conditions when compared to human hemoglobin. The study helped in determining the stability of crucial residues important for the binding of co-factors like heme, 2,3-BPG and ATP. Several critical residues of camel hemoglobin  $\alpha$  and  $\beta$  subunits exhibited fluctuations that were notably different when compared to humans. This study also showed that camel hemoglobin exhibited more stability in severe dehydrated conditions when compared to human hemoglobin. Additionally, *in silico* data indicated a more stable binding of 2,3-BPG and ATP with  $\beta$  subunits of camel hemoglobin when compared to human hemoglobin when severe dehydrated conditions were used. These results illustrate that under extreme dehydrated conditions, especially with high salt concentrations, 2,3-BPG could bind more strongly to camel hemoglobin and help with the unloading of oxygen in peripheral tissues.

## Chapter 8: Future Prospects

The synthesis, metabolism and therapeutic potential of hemoglobin-derived peptides (hemorphins) continue to be both fascinating and challenging. The tissue-specific release and its ability to bind diverse targets are yet to be clearly elucidated. Hemorphins have been studied for the last three or four decades. Even though hemorphins are endogenous peptides with several therapeutic and pharmacological activities, astonishingly, these peptides have not been actively explored in the last decade. Moreover, a huge gap still exists between *in vitro* and *in vivo* data using human subjects and animal models and mechanistic basis at the cellular and molecular level. Indeed, different aspects of hemoglobin-derived peptides discussed in this study clearly demonstrate the direct pharmacological and biological action of hemorphins on key receptors and enzymes. However, a big gap still exists in our understanding of the precise mode of action and the specific binding sites on the targets. Future studies should aim specifically toward dissecting the cellular and molecular pathways and to investigate the critical residues of hemorphins that interact with a target. Additionally, in depth structure activity relationship and binding assays involving hemorphins and putative targets should be considered using both *in vitro* and *in silico* studies. A lot is known about hemorphins. However, the story is still enormously incomplete and further studies are needed to understand and to unlock the true potential of hemoglobin derived peptides for therapeutic and diagnostic purposes.

## References

- Abdelhedi, O., Nasri, R., Mora, L., Jridi, M., Toldra, F., & Nasri, M. (2018). In silico analysis and molecular docking study of angiotensin I-converting enzyme inhibitory peptides from smooth-hound viscera protein hydrolysates fractionated by ultrafiltration. *Food Chemistry*, 239, 453-463.
- Agrawal, R. P., Jain, S., Shah, S., Chopra, A., & Agarwal, V. (2011). Effect of camel milk on glycemic control and insulin requirement in patients with type 1 diabetes: 2-years randomized controlled trial. *European Journal of Clinical Nutrition*, 65(9), 1048-1052.
- Akif, M., Schwager, S. L., Anthony, C. S., Czarny, B., Beau, F., Dive, V., . . . Acharya, K. R. (2011). Novel mechanism of inhibition of human angiotensin-I-converting enzyme (ACE) by a highly specific phosphinic tripeptide. *Biochemical Journal*, 436(1), 53-59.
- Al-Ali, A. K., Husayni, H. A., & Power, D. M. (1988). A comprehensive biochemical analysis of the blood of the camel (*Camelus dromedarius*). *Comparative Biochemistry and Physiology*, 89(1), 35-37.
- Al-Swailem, A. M., Shehata, M. M., Abu-Duhier, F. M., Al-Yamani, E. J., Al-Busadah, K. A., Al-Arawi, M. S., . . . Otu, H. H. (2010). Sequencing, analysis, and annotation of expressed sequence tags for *Camelus dromedarius*. *PLoS One*, 5(5), 1371-1389.
- Albiston, A. L., McDowall, S. G., Matsacos, D., Sim, P., Clune, E., Mustafa, T., . . . Connolly, L. M. (2001). Evidence that the angiotensin IV (AT4) receptor is the enzyme insulin-regulated aminopeptidase. *Journal of Biological Chemistry*, 276(52), 48623-48626.
- Albiston, A. L., Pederson, E. S., Burns, P., Purcell, B., Wright, J. W., Harding, J. W., . . . Chai, S. Y. (2004). Attenuation of scopolamine-induced learning deficits by LVV-hemorphin-7 in rats in the passive avoidance and water maze paradigms. *Behavioural Brain Research*, 154(1), 239-243.
- Albiston, A. L., Pham, V., Ye, S., Ng, L., Lew, R. A., Thompson, P. E., . . . Chai, S. Y. (2010). Phenylalanine-544 plays a key role in substrate and inhibitor binding by providing a hydrophobic packing point at the active site of insulin-regulated aminopeptidase. *Molecular Pharmacology*, 78(4), 600-607.
- Ali, A., Alzeyoudi, S. A. R., Almutawa, S. A., Alnajjar, A. N., Al Dhaheri, Y., & Vijayan, R. (2020). Camel Hemorphins Exhibit a More Potent Angiotensin-I Converting Enzyme Inhibitory Activity than Other Mammalian Hemorphins: An In Silico and In Vitro Study. *Biomolecules*, 10(3), 486-505.
- Ali, A., Baby, B., Soman, S. S., & Vijayan, R. (2019). Molecular insights into the interaction of hemorphin and its targets. *Scientific Reports*, 9(1), 1-16.

- Almathen, F., Charruau, P., Mohandesan, E., Mwacharo, J. M., Orozco-terWengel, P., Pitt, D., . . . Burger, P. A. (2016). Ancient and modern DNA reveal dynamics of domestication and cross-continental dispersal of the dromedary. *Proceedings of the National Academy of Sciences*, 113(24), 6707-6712.
- Andersson, B., Olsson, K., & Rundgren, M. (1980). ADH in regulation of blood osmolality and extracellular fluid volume. *Journal of Parenteral and Enteral Nutrition*, 4(2), 88-96.
- Andersson, L., & Georges, M. (2004). Domestic-animal genomics: deciphering the genetics of complex traits. *Nature Reviews Genetics*, 5(3), 202-212.
- Antczak, D. (2013). Major histocompatibility complex genes of the dromedary camel. Paper presented at the *Qatar Foundation Annual Research Conference*.
- Arnone, A. (1972). X-ray diffraction study of binding of 2, 3-diphosphoglycerate to human deoxyhaemoglobin. *Nature*, 237(5351), 146-149.
- Ayoub, M. A., Landomiel, F., Gallay, N., Jegot, G., Poupon, A., Crepieux, P., & Reiter, E. (2015). Assessing Gonadotropin Receptor Function by Resonance Energy Transfer-Based Assays. *Frontiers in Endocrinology*, 6, 3389-3403.
- Azwai, S. M., Abdouislam, O. E., Al-Bassam, L. S., Al Dawek, A. M., & Al-Izzi, S. A. L. (2007). Morphological characteristics of blood cells in clinically normal adult llamas (*Lama glama*). *Veterinarski Arhiv*, 77(1), 69-79.
- Balasubramanian, M., Moorthy, P. S., Neelagandan, K., & Ponnuswamy, M. N. (2009). Purification, crystallization and preliminary crystallographic study of haemoglobin from camel (*Camelus dromedarius*): a high oxygen-affinity lowland species. *Acta Crystallographica Section F: Structural Biology Communications*, 65(8), 773-775.
- Barcroft, J., & Izquierdo, J. J. (1931). The effect of temperature on the frequency of heart and respiration in the guinea-pig and cat. *Journal of Physiology*, 71(4), 364-372.
- Benesch, R. E., Benesch, R., & Yu, C. I. (1969). The oxygenation of hemoglobin in the presence of 2,3-diphosphoglycerate. Effect of temperature, pH, ionic strength, and hemoglobin concentration. *Biochemistry*, 8(6), 2567-2571.
- Benner, A., Patel, A. K., Singh, K., & Dua, A. (2020). Physiology, Bohr Effect. In *StatPearls*. Treasure Island (FL).
- Berg, J., Tymoczko, J., & Stryer, L. (2002). Section 10.2: Hemoglobin transports oxygen efficiently by binding oxygen cooperatively. *Biochemistry*. 5<sup>th</sup> edition, New York, USA.
- Beuzen, N., Stear, M., & Chang, K. (2000). Molecular markers and their use in animal breeding. *The Veterinary Journal*, 160(1), 42-52.



- Blishchenko, E. Y., Sazonova, O. V., Kalinina, O. A., Moiseeva, E. V., Vass, A. A., Karelin, A. A., & Ivanov, V. T. (2005). Antitumor effect of valorphin in vitro and in vivo: combined action with cytostatic drugs. *Cancer Biology and Therapy*, 4(1), 125-131.
- Bock, A., Merten, N., Schrage, R., Dallanoce, C., Batz, J., Klockner, J., . . . Mohr, K. (2012). The allosteric vestibule of a seven transmembrane helical receptor controls G-protein coupling. *Nature Communication*, 3, 1-11.
- Bogner, P., Csutora, P., Cameron, I. L., Wheatley, D. N., & Miseta, A. (1998). Augmented water binding and low cellular water content in erythrocytes of camel and camelids. *Biophysical Journal*, 75(6), 3085-3091.
- Bogner, P., Miseta, A., Berente, Z., Schwarcz, A., Kotek, G., & Repa, I. (2005). Osmotic and diffusive properties of intracellular water in camel erythrocytes: effect of hemoglobin crowdedness. *Cell Biology International*, 29(9), 731-736.
- Bowers, K. J., Chow, D. E., Xu, H., Dror, R. O., Eastwood, M. P., Gregersen, B. A., . . . Sacerdoti, F. D. (2006). *Scalable algorithms for molecular dynamics simulations on commodity clusters*. Paper presented at the SC 2006 conference, proceedings of the ACM/IEEE.
- Brantl, V., Gramsch, C., Lottspeich, F., Henschen, A., Jaeger, K. H., & Herz, A. (1985). Novel opioid peptides derived from mitochondrial cytochrome b: cytochromophins. *Journal of Pharmacology*, 111(2), 293-294.
- Brantl, V., Gramsch, C., Lottspeich, F., Mertz, R., Jaeger, K. H., & Herz, A. (1986). Novel opioid peptides derived from hemoglobin: hemorphins. *European Journal of Pharmacology*, 125(2), 309-310.
- Bruns, R. F., & Fergus, J. H. (1990). Allosteric enhancement of adenosine A1 receptor binding and function by 2-amino-3-benzoylthiophenes. *Molecular Pharmacology*, 38(6), 939-949.
- Burger, P. A. (2016). The history of Old World camelids in the light of molecular genetics. *Tropical Animal Health and Production*, 48(5), 905-913.
- Carroll, M. A., Balazy, M., Margiotta, P., Huang, D., Falck, J., & McGiff, J. (1996). Cytochrome P-450-dependent HETEs: profile of biological activity and stimulation by vasoactive peptides. *American Journal of Physiology-Regulatory, Integrative and Comparative Physiology*, 271(4), 863-869.
- Castilho, E. M., Glass, M. L., & Manco, J. C. (2003). The effects of 2,3-diphosphoglycerate, adenosine triphosphate, and glycosylated hemoglobin on the hemoglobin-oxygen affinity of diabetic patients. *Brazilian Journal of Medical and Biological Research*, 36(6), 731-737.
- Cejka, J., Zelezna, B., Velek, J., Zicha, J., & Kunes, J. (2004). LVV-hemorphin-7 lowers blood pressure in spontaneously hypertensive rats: radiotelemetry study. *Physiological Research*, 53(6), 603-607.

- Chen, W.-R., Yu, Y., Zulfajri, M., Lin, P.-C., & Wang, C. C. (2017). Phthalide derivatives from *Angelica Sinensis* decrease hemoglobin oxygen affinity: a new allosteric-modulating mechanism and potential use as 2, 3-BPG functional substitutes. *Scientific Reports*, 7(1), 1-15.
- Cheng, B. C., Tao, P. L., Cheng, Y. Y., & Huang, E. Y. (2012). LVV-hemorphin 7 and angiotensin IV in correlation with antinociception and anti-thermal hyperalgesia in rats. *Peptides*, 36(1), 9-16.
- Chow, L.-H., Chen, Y.-H., Lai, C.-F., Lin, T.-Y., Chen, Y.-J., Kao, J.-H., & Huang, E. Y.-K. (2018). Sex Difference of Angiotensin IV-, LVV-Hemorphin 7-, and Oxytocin-Induced Antiallodynia at the Spinal Level in Mice With Neuropathic Pain. *Anesthesia & Analgesia*, 126(6), 2093-2101.
- Chu, H., Breite, A., Ciraolo, P., Franco, R. S., & Low, P. S. (2008). Characterization of the deoxyhemoglobin binding site on human erythrocyte band 3: implications for O<sub>2</sub> regulation of erythrocyte properties. *Blood*, 111(2), 932-938.
- Clustal, W., Thompson, J., Higgins, D., & Gibson, T. (1994). Improving the sensitivity of progressive multiple sequence alignment through sequence weighting, position-specific gap penalties and weight matrix choice. *Nucleic Acids Research*, 22(22), 4673-4680.
- Congreve, M., Oswald, C., & Marshall, F. H. (2017). Applying Structure-Based Drug Design Approaches to Allosteric Modulators of GPCRs. *Trends in Pharmacological Sciences*, 38(9), 837-847.
- Covic, L., Gresser, A. L., Talavera, J., Swift, S., & Kuliopulos, A. (2002). Activation and inhibition of G protein-coupled receptors by cell-penetrating membrane-tethered peptides. *Proceedings of the National Academy of Sciences of the United States of America*, 99(2), 643-648.
- Cui, X., Yeliseev, A., & Liu, R. (2013). Ligand interaction, binding site and G protein activation of the mu opioid receptor. *European Journal of Pharmacology*, 702(1-3), 309-315.
- Da Cruz, K. R., Turones, L. C., Camargo-Silva, G., Gomes, K. P., Mendonca, M. M., Galdino, P., . . . Xavier, C. H. (2017). The hemoglobin derived peptide LVV-hemorphin-7 evokes behavioral effects mediated by oxytocin receptors. *Neuropeptides*, 66, 59-68.
- Dagouassat, N., Garreau, I., Sannier, F., Zhao, Q., & Piot, J. M. (1996). Generation of VV-hemorphin-7 from globin by peritoneal macrophages. *FEBS Letters*, 382(1-2), 37-42.
- Davidson, A. (2014). *The Oxford companion to food*: OUP Oxford.
- Davis, T. P., Gillespie, T. J., & Porreca, F. (1989). Peptide fragments derived from the beta-chain of hemoglobin (hemorphins) are centrally active in vivo. *Peptides*, 10(4), 747-751.

- De Bundel, D., Smolders, I., Yang, R., Albiston, A. L., Michotte, Y., & Chai, S. Y. (2009). Angiotensin IV and LVV-haemorphin 7 enhance spatial working memory in rats: effects on hippocampal glucose levels and blood flow. *Neurobiology of Learning and Memory*, *92*(1), 19-26.
- Eguchi, M. (2004). Recent advances in selective opioid receptor agonists and antagonists. *Medicinal Research Reviews*, *24*(2), 182-212.
- Eitan, A., Aloni, B., & Livne, A. (1976). Unique properties of the camel erythrocyte membrane, II. Organization of membrane proteins. *Biochimical Biophysics Acta*, *426*(4), 647-658.
- Elgeti, M., Kazmin, R., Heck, M., Morizumi, T., Ritter, E., Scheerer, P., . . . Bartl, F. J. (2011). Conserved Tyr223(5.58) plays different roles in the activation and G-protein interaction of rhodopsin. *Journal of the American Chemical Society*, *133*(18), 7159-7165.
- Elmahdi, B., Sallmann, H. P., Fuhrmann, H., von Engelhardt, W., & Kaske, M. (1997). Comparative aspects of glucose tolerance in camels, sheep, and ponies. *Comparative Biochemistry and Physiology Part A: Physiology*, *118*(1), 147-151.
- Emmanuel, B., & Nahapetian, A. (1980). Fatty acid composition of depot fats, and rumen wall of the camel (*Camelus dromedarius*). *Comparative Biochemistry and Physiology, B*, *67*(4), 701-704.
- Engelmann, M., T Wotjak, C., Neumann, I., Ludwig, M., & Landgraf, R. (1996). Behavioral consequences of intracerebral vasopressin and oxytocin: focus on learning and memory. *Neuroscience & Biobehavioral Reviews*, *20*(3), 341-358.
- Essmann, U., Perera, L., Berkowitz, M. L., Darden, T., Lee, H., & Pedersen, L. G. (1995). A smooth particle mesh Ewald method. *The Journal of Chemical Physics*, *103*(19), 8577-8593.
- Feng, Y.-H., Noda, K., Saad, Y., Liu, X.-p., Husain, A., & Karnik, S. S. (1995). The docking of Arg2 of angiotensin II with Asp281 of AT1 receptor is essential for full agonism. *Journal of Biological Chemistry*, *270*(21), 12846-12850.
- Fermi, G., Perutz, M. F., Shaanan, B., & Fourme, R. (1984). The crystal structure of human deoxyhaemoglobin at 1.74 Å resolution. *Journal of Molecular Biology*, *175*(2), 159-174.
- Fesenko, I., Azarkina, R., Kirov, I., Kniazev, A., Filippova, A., Grafaskaia, E., . . . Govorun, V. (2019). Phytohormone treatment induces generation of cryptic peptides with antimicrobial activity in the Moss *Physcomitrella patens*. *BMC Plant Biology*, *19*(1), 1-16.

- Fillion, D., Cabana, J., Guillemette, G., Leduc, R., Lavigne, P., & Escher, E. (2013). Structure of the human angiotensin II type 1 (AT1) receptor bound to angiotensin II from multiple chemoselective photoprobe contacts reveals a unique peptide binding mode. *Journal of Biological Chemistry*, 288(12), 8187-8197.
- Finberg, J., Yagil, R., & Berlyne, G. (1978). Response of the renin-aldosterone system in the camel to acute dehydration. *Journal of Applied Physiology*, 44(6), 926-930.
- Fitak, R. R., Mohandesan, E., Corander, J., & Burger, P. A. (2016). The de novo genome assembly and annotation of a female domestic dromedary of North African origin. *Molecular Ecology Resources*, 16(1), 314-324.
- Fleming, I. (2006). Signaling by the angiotensin-converting enzyme. *Circulatory Research*, 98(7), 887-896.
- Frauenfelder, H., Parak, F., & Young, R. D. (1988). Conformational substates in proteins. *Annual Review of Biophysics and Biophysical Chemistry*, 17, 451-479.
- Friesner, R. A., Murphy, R. B., Repasky, M. P., Frye, L. L., Greenwood, J. R., Halgren, T. A., . . . Mainz, D. T. (2006). Extra precision glide: docking and scoring incorporating a model of hydrophobic enclosure for protein-ligand complexes. *Journal of Medicinal Chemistry*, 49(21), 6177-6196.
- Fruitier-Arnaudin, I., Cohen, M., Bordenave, S., Sannier, F., & Piot, J. M. (2002). Comparative effects of angiotensin IV and two hemorphins on angiotensin-converting enzyme activity. *Peptides*, 23(8), 1465-1470.
- Fruitier-Arnaudin, I., Cohen, M., Coitoux, C., & Piot, J. M. (2003). In vitro metabolism of LVV-Hemorphin-7 by renal cytosol and purified prolyl endopeptidase. *Peptides*, 24(8), 1201-1206.
- Gaalaas, R. (1945). Effect of atmospheric temperature on body temperature and respiration rate of Jersey cattle. *Journal of Dairy Science*, 28, 555-563.
- Gaglione, R., Cesaro, A., Dell'Olmo, E., Della Ventura, B., Casillo, A., Di Girolamo, R., . . . Arciello, A. (2019). Effects of human antimicrobial cryptides identified in apolipoprotein B depend on specific features of bacterial strains. *Scientific Reports*, 9(1), 6728-6741.
- Garby, L., Gerber, G., & De Verdier, C. H. (1969). Binding of 2,3-diphosphoglycerate and adenosine triphosphate to human haemoglobin A. *European Journal of Biochemistry*, 10(1), 110-115.
- Garreau, I., Zhao, Q., Pejoan, C., Cupo, A., & Piot, J. M. (1995). VV-hemorphin-7 and LVV-hemorphin-7 released during in vitro peptic hemoglobin hydrolysis are morphinomimetic peptides. *Neuropeptides*, 28(4), 243-250.

- Gerber, G., Berger, H., Jänig, G. R., & Rapoport, S. M. (1973). Interaction of haemoglobin with ions: quantitative description of the state of magnesium, adenosine 5'-triphosphate, 2, 3-bisphosphoglycerate, and human haemoglobin under simulated intracellular conditions. *European Journal of Biochemistry*, 38(3), 563-571.
- Glamsta, E. L., Marklund, A., Hellman, U., Wernstedt, C., Terenius, L., & Nyberg, F. (1991). Isolation and characterization of a hemoglobin-derived opioid peptide from the human pituitary gland. *Regulatory Peptides*, 34(3), 169-179.
- Glamsta, E. L., Meyerson, B., Silberring, J., Terenius, L., & Nyberg, F. (1992). Isolation of a hemoglobin-derived opioid peptide from cerebrospinal fluid of patients with cerebrovascular bleedings. *Biochemical Biophysical Research Communication*, 184(2), 1060-1066.
- Glamsta, E. L., Morkrid, L., Lantz, I., & Nyberg, F. (1993). Concomitant increase in blood plasma levels of immunoreactive hemorphin-7 and beta-endorphin following long distance running. *Regulatory Peptides*, 49(1), 9-18.
- Goldstein, A., Tachibana, S., Lowney, L. I., Hunkapiller, M., & Hood, L. (1979). Dynorphin-(1-13), an extraordinarily potent opioid peptide. *Proceedings of the National Academy of Sciences of the United States of America*, 76(12), 6666-6670.
- Goniakowska-Witalinska, L., & Witalinski, W. (1976). Evidence for a correlation between the number of marginal band microtubules and the size of vertebrate erythrocytes. *Journal of Cell Science*, 22(2), 397-401.
- Haines, S. R., McCann, M. J., Grosvenor, A. J., Thomas, A., Noble, A., & Clerens, S. (2019). ACE inhibitory peptides in standard and fermented deer velvet: an in silico and in vitro investigation. *BMC Complementary Alternative Medicine*, 19(1), 350-362.
- Hamers-Casterman, C., Atarhouch, T., Muyldermans, S., Robinson, G., Hamers, C., Songa, E. B., . . . Hamers, R. (1993). Naturally occurring antibodies devoid of light chains. *Nature*, 363(6428), 446-448.
- Hothersall, J. D., Torella, R., Humphreys, S., Hooley, M., Brown, A., McMurray, G., & Nickolls, S. A. (2017). Residues W320 and Y328 within the binding site of the  $\mu$ -opioid receptor influence opiate ligand bias. *Neuropharmacology*, 118, 46-58.
- Huang, W., Manglik, A., Venkatakrishnan, A., Laeremans, T., Feinberg, E. N., Sanborn, A. L., . . . Kling, R. C. (2015). Structural insights into  $\mu$ -opioid receptor activation. *Nature*, 524(7565), 315-321.
- Hughes, J., Smith, T. W., Kosterlitz, H. W., Fothergill, L. A., Morgan, B. A., & Morris, H. R. (1975). Identification of two related pentapeptides from the brain with potent opiate agonist activity. *Nature*, 258(5536), 577-580.

- Ianzer, D., Konno, K., Xavier, C. H., Stöcklin, R., Santos, R. A. S., de Camargo, A. C. M., & Pimenta, D. C. (2006). Hemorphin and hemorphin-like peptides isolated from dog pancreas and sheep brain are able to potentiate bradykinin activity in vivo. *Peptides*, 27(11), 2957-2966.
- Ivanov, V. T., Karelin, A. A., Philippova, M. M., Nazimov, I. V., & Pletnev, V. Z. (1997). Hemoglobin as a source of endogenous bioactive peptides: The concept of tissue-specific peptide pool. *Peptide Science*, 43(2), 171-188.
- Iwaniak, A., Minkiewicz, P., & Darewicz, M. (2014). Food-originating ACE inhibitors, including antihypertensive peptides, as preventive food components in blood pressure reduction. *Comprehensive Reviews in Food Science and Food Safety*, 13(2), 114-134.
- Janeway, C. A., Travers, P., Walport, M., & Shlomchik, M. (2001). The immune system in health and disease. Immunobiology. *Gerald Publishing, New York*
- Jerne NK (1955) The natural selection theory of antibody formation. *Proceedings of the National Academy of Sciences of the United States of America*, 41, 849-857.
- Jinsmaa, Y., & Yoshikawa, M. (2002). Release of hemorphin-5 from human hemoglobin by pancreatic elastase. *Bioscience, Biotechnology, and Biochemistry*, 66(5), 1130-1132.
- Jirimutu, Wang, Z., Ding, G., Chen, G., Sun, Y., Sun, Z., . . . Meng, H. (2012). Genome sequences of wild and domestic bactrian camels. *Nature Communication*, 3, 1202-1221.
- John, H., Schulz, S., & Forssmann, W. G. (2007). Comparative in vitro degradation of the human hemorphin LVV-H7 in mammalian plasma analysed by capillary zone electrophoresis and mass spectrometry. *Biopharmaceutics and Drug Disposition*, 28(2), 73-85.
- Kakidani, H., Furutani, Y., Takahashi, H., Noda, M., Morimoto, Y., Hirose, T., . . . Numa, S. (1982). Cloning and sequence analysis of cDNA for porcine beta-neo-endorphin/dynorphin precursor. *Nature*, 298(5871), 245-249.
- Karelin, A. A., Philippova, M. M., Karelina, E. V., & Ivanov, V. T. (1994). Isolation of endogenous hemorphin-related hemoglobin fragments from bovine brain. *Biochemical Biophysical Research Communication*, 202(1), 410-415.
- Kasahara, M., Naruse, K., Sasaki, S., Nakatani, Y., Qu, W., Ahsan, B., . . . & Kasai, Y. (2007). The medaka draft genome and insights into vertebrate genome evolution. *Nature*, 447(7145), 714-719.
- Kaske, M., Elmahdi, B., Engelhardt, W. v., & Sallmann, H.-P. (2001). Insulin responsiveness of sheep, ponies, miniature pigs and camels: results of hyperinsulinemic clamps using porcine insulin. *Journal of Comparative Physiology B*, 171(7), 549-556.

- Kearney, P. M., Whelton, M., Reynolds, K., Muntner, P., Whelton, P. K., & He, J. (2005). Global burden of hypertension: analysis of worldwide data. *Lancet*, 365(9455), 217-223.
- Kohmura, M., Nio, N., Kubo, K., Minoshima, Y., Munekata, E., & Ariyoshi, Y. (1989). Inhibition of angiotensin-converting enzyme by synthetic peptides of human  $\beta$ -casein. *Agricultural and Biological Chemistry*, 53(8), 2107-2114.
- Kruse, A. C., Ring, A. M., Manglik, A., Hu, J., Hu, K., Eitel, K., . . . Kobilka, B. K. (2013). Activation and allosteric modulation of a muscarinic acetylcholine receptor. *Nature*, 504(7478), 101-106.
- Laberge, M., & Yonetani, T. (2008). Molecular dynamics simulations of hemoglobin A in different states and bound to DPG: effector-linked perturbation of tertiary conformations and HbA concerted dynamics. *Biophysical Journal*, 94(7), 2737-2751.
- Lantz, I., Glämsta, E.-L., Talbäck, L., & Nyberg, F. (1991). Hemorphins derived from hemoglobin have an inhibitory action on angiotensin converting enzyme activity. *FEBS Letters*, 287(1-2), 39-41.
- Lau, J. L., & Dunn, M. K. (2018). Therapeutic peptides: Historical perspectives, current development trends, and future directions. *Bioorganic and Medicinal Chemistry*, 26(10), 2700-2707.
- Lawes, C. M., Vander Hoorn, S., & Rodgers, A. (2008). Global burden of blood-pressure-related disease, 2001. *Lancet*, 371(9623), 1513-1518.
- Lee, J., Albiston, A., Allen, A., Mendelsohn, F., Ping, S., Barrett, G., . . . Chai, S. (2004). Effect of ICV injection of AT4 receptor ligands, NLE1-angiotensin IV and LVV-hemorphin 7, on spatial learning in rats. *Neuroscience*, 124(2), 341-349.
- Lee, J., Mustafa, T., McDowall, S. G., Mendelsohn, F. A., Brennan, M., Lew, R. A., . . . Chai, S. Y. (2003). Structure-activity study of LVV-hemorphin-7: angiotensin AT4 receptor ligand and inhibitor of insulin-regulated aminopeptidase. *Journal of Pharmacology and Experimental Therapeutics*, 305(1), 205-211.
- Lennon, A. J., Scott, N. R., Chapman, B. E., & Kuchel, P. W. (1994). Hemoglobin affinity for 2, 3-bisphosphoglycerate in solutions and intact erythrocytes: studies using pulsed-field gradient nuclear magnetic resonance and Monte Carlo simulations. *Biophysical Journal*, 67(5), 2096-2109.
- Li, J., Abel, R., Zhu, K., Cao, Y., Zhao, S., & Friesner, R. A. (2011). The VSGB 2.0 model: a next generation energy model for high resolution protein structure modeling. *Proteins*, 79(10), 2794-2812.
- Li, J. G., Chen, C., Yin, J., Rice, K., Zhang, Y., Matecka, D., . . . Liu-Chen, L. Y. (1999). ASP147 in the third transmembrane helix of the rat mu opioid receptor forms ion-pairing with morphine and naltrexone. *Life Sciences*, 65(2), 175-185.

- Lin, S. W., Han, M., & Sakmar, T. P. (2000). Analysis of functional microdomains of rhodopsin. *Methods in Enzymology*, *315*, 116-130.
- Liu, R., Zhu, Y., Chen, J., Wu, H., Shi, L., Wang, X., & Wang, L. (2014). Characterization of ACE inhibitory peptides from *Macraa veneriformis* hydrolysate by nano-liquid chromatography electrospray ionization mass spectrometry (Nano-LC-ESI-MS) and molecular docking. *Marine Drugs*, *12*(7), 3917-3928.
- Luderman, K. D., Conroy, J. L., Free, R. B., Southall, N., Ferrer, M., Sanchez-Soto, M., . . . Jain, P. (2018). Identification of positive allosteric modulators of the D1 dopamine receptor that act at diverse binding sites. *Molecular Pharmacology*, *94*(4), 1197-1209.
- Ma, F. F., Wang, H., Wei, C. K., Thakur, K., Wei, Z. J., & Jiang, L. (2018). Three Novel ACE Inhibitory Peptides Isolated From Ginkgo biloba Seeds: Purification, Inhibitory Kinetic and Mechanism. *Frontiers in Pharmacology*, *9*, 1579-1590.
- Macdonald, R. (1977). Red cell 2, 3-diphosphoglycerate and oxygen affinity. *Anaesthesia*, *32*(6), 544-553.
- Macfarlane, W., Morris, R., & Howard, B. (1963). Turn-over and distribution of water in desert camels, sheep, cattle and kangaroos. *Nature*, *197*, 270-271.
- Maraninchi, M., Feron, D., Fruitier-Arnaudin, I., Bégu-Le Corroller, A., Nogueira, J. P., Mancini, J., . . . Vialettes, B. (2013). Serum hemorphin-7 levels are decreased in obesity. *Obesity*, *21*(2), 378-381.
- Martyna, G. J., Klein, M. L., & Tuckerman, M. (1992). Nosé–Hoover chains: the canonical ensemble via continuous dynamics. *The Journal of Chemical Physics*, *97*(4), 2635-2643.
- Martyna, G. J., Tobias, D. J., & Klein, M. L. (1994). Constant pressure molecular dynamics algorithms. *The Journal of Chemical Physics*, *101*(5), 4177-4189.
- Matsoukas, M.-T., Potamitis, C., Plotas, P., Androutsou, M.-E., Agelis, G., Matsoukas, J., & Zoumpoulakis, P. (2013). Insights into AT1 receptor activation through AngII binding studies. *Journal of Chemical Information and Modeling*, *53*(11), 2798-2811.
- McKinley, M. J., McBurnie, M. I., & Mathai, M. L. (2001). Neural mechanisms subserving central angiotensinergic influences on plasma renin in sheep. *Hypertension*, *37*(6), 1375-1381.
- Ming, L., Yi, L., Sa, R., Wang, Z., Wang, Z., & Ji, R. (2017). Genetic diversity and phylogeographic structure of Bactrian camels shown by mitochondrial sequence variations. *Animal Genetics*, *48*(2), 217-220.
- Moeller, I., Lew, R. A., Mendelsohn, F. A., Smith, A. I., Brennan, M. E., Tetaz, T. J., & Chai, S. Y. (1997). The globin fragment LVV-hemorphin-7 is an endogenous ligand for the AT4 receptor in the brain. *Journal of Neurochemistry*, *68*(6), 2530-2537.



- Moisan, S., Harvey, N., Beaudry, G., Forzani, P., Burhop, K. E., Drapeau, G., & Rioux, F. (1998). Structural requirements and mechanism of the pressor activity of Leu-Val-Val-hemorphin-7, a fragment of hemoglobin beta-chain in rats. *Peptides*, *19*(1), 119-131.
- Mousa, H. M., Ali, K. E., & Hume, I. D. (1983). Effects of water deprivation on urea metabolism in camels, desert sheep and desert goats fed dry desert grass. *Comparative Biochemistry and Physiology Part A: Molecular & Integrative Physiology*, *74*(3), 715-720.
- Muyldermans, S. (2001). Single domain camel antibodies: current status. *J Biotechnology*, *74*(4), 277-302.
- Muyldermans, S., Baral, T., Retamozzo, V. C., De Baetselier, P., De Genst, E., Kinne, J., . . . Revets, H. (2009). Camelid immunoglobulins and nanobody technology. *Veterinary Immunology Immunopathology*, *128*(1-3), 178-183.
- Natesh, R., Schwager, S. L., Evans, H. R., Sturrock, E. D., & Acharya, K. R. (2004). Structural details on the binding of antihypertensive drugs captopril and enalaprilat to human testicular angiotensin I-converting enzyme. *Biochemistry*, *43*(27), 8718-8724. doi:10.1021/bi049480n
- Nemeth, E. F., Steffey, M. E., Hammerland, L. G., Hung, B. C., Van Wagenen, B. C., DelMar, E. G., & Balandrin, M. F. (1998). Calcimimetics with potent and selective activity on the parathyroid calcium receptor. *Proceedings of the National Academy of Sciences of the United States of America*, *95*(7), 4040-4045.
- Ni, H., Li, L., Liu, G., & Hu, S. Q. (2012). Inhibition mechanism and model of an angiotensin I-converting enzyme (ACE)-inhibitory hexapeptide from yeast (*Saccharomyces cerevisiae*). *PLoS One*, *7*(5), 37077-37084.
- Noori, H. R., Mucksch, C., & Urbassek, H. M. (2014). A structural feature of the non-peptide ligand interactions with mice mu-opioid receptors. *Current Computer Aided Drug Design*, *10*(4), 354-360.
- Nyberg, F., Sanderson, K., & Glamsta, E. L. (1997). The hemorphins: a new class of opioid peptides derived from the blood protein hemoglobin. *Biopolymers*, *43*(2), 147-156.
- Nydahl, K. S., Pierson, J., Nyberg, F., Caprioli, R. M., & Andren, P. E. (2003). In vivo processing of LVV-hemorphin-7 in rat brain and blood utilizing microdialysis combined with electrospray mass spectrometry. *Rapid Communication in Mass Spectrometry*, *17*(8), 838-844.
- Ondetti, M. A., Rubin, B., & Cushman, D. W. (1977). Design of specific inhibitors of angiotensin-converting enzyme: new class of orally active antihypertensive agents. *Science*, *196*(4288), 441-444.

- Oyewale, J., Dzenda, T., Yaqub, L., Akanbi, D., Ayo, J., Owoyele, O., . . . Dare, T. (2011). Alterations in the osmotic fragility of camel and donkey erythrocytes caused by temperature, pH and blood storage. *Veterinarski Arhiv*, 81(4), 459-470.
- Perk, K. (1963). The Camel's Erythrocyte. *Nature*, 200, 272-273.
- Pimenta, D. C., & Lebrun, I. (2007). Cryptides: buried secrets in proteins. *Peptides*, 28(12), 2403-2410.
- Priyanto, A. D., Doerksen, R. J., Chang, C. I., Sung, W. C., Widjanarko, S. B., Kusnadi, J., . . . Hsu, J. L. (2015). Screening, discovery, and characterization of angiotensin-I converting enzyme inhibitory peptides derived from proteolytic hydrolysate of bitter melon seed proteins. *Journal of Proteomics*, 128, 424-435.
- Proska, J., & Tucek, S. (1994). Mechanisms of steric and cooperative actions of alcuronium on cardiac muscarinic acetylcholine receptors. *Molecular Pharmacology*, 45(4), 709-717.
- Ralston, G. B. (1975). Proteins of the camel erythrocyte membrane. *Biochimical Biophysics Acta*, 401(1), 83-94.
- Rasmussen, S. G., DeVree, B. T., Zou, Y., Kruse, A. C., Chung, K. Y., Kobilka, T. S., . . . Calinski, D. (2011). Crystal structure of the  $\beta$  2 adrenergic receptor–Gs protein complex. *Nature*, 477(7366), 549-555.
- Reed, C. A. (1972). The Origin of the Domestic Animals of Africa. *Science*, 176(4035), 656-657.
- Rubini, A., & Bosco, G. (2013). The effect of body temperature on the dynamic respiratory system compliance–breathing frequency relationship in the rat. *Journal of Biological Physics*, 39(3), 411-418.
- Sanderson, K., Andren, P. E., Caprioli, R. M., & Nyberg, F. (1996). In vitro metabolism of LVV-hemorphin-7 in human plasma studied by reversed-phase high-performance liquid chromatography and micro-electrospray mass spectrometry. *Journal of Chromatography A*, 743(1), 207-212
- Sanderson, K., Nyberg, F., & Khalil, Z. (1998). Modulation of peripheral inflammation by locally administered hemorphin-7. *Inflammation Research*, 47(2), 49-55.
- Sastry, G. M., Adzhigirey, M., Day, T., Annabhimoju, R., & Sherman, W. (2013). Protein and ligand preparation: parameters, protocols, and influence on virtual screening enrichments. *Journal of Comput Aided Molecular Design*, 27(3), 221-234.
- Sawicka, K., Szczyrek, M., Jastrzebska, I., Prasal, M., Zwolak, A., & Daniluk, J. (2011). Hypertension–The silent killer. *Journal of Pre-Clinical and Clinical Research*, 5(2), 43-46.

- Schmidt-Nielsen, K., Schmidt-Nielsen, B., Jarnum, S., & Houpt, T. (1956). Body temperature of the camel and its relation to water economy. *American Journal of Physiology*, 188(1), 103-112.
- Schütten, M. T., Houben, A. J., de Leeuw, P. W., & Stehouwer, C. D. (2017). The link between adipose tissue renin-angiotensin-aldosterone system signaling and obesity-associated hypertension. *Physiology*, 32(3), 197-209.
- Siebert, B., & Macfarlane, W. (1971). Water turnover and renal function of dromedaries in the desert. *Physiological Zoology*, 44(4), 225-240.
- Silvestre, M. P. C., Silva, M. R., Silva, V. D. M., Souza, M. W. S. d., Junior, L., de Oliveira, C., & Afonso, W. d. O. (2012). Analysis of whey protein hydrolysates: peptide profile and ACE inhibitory activity. *Brazilian Journal of Pharmaceutical Sciences*, 48(4), 747-757.
- Singh, K. D., Unal, H., Desnoyer, R., & Karnik, S. S. (2019). Mechanism of Hormone Peptide Activation of a GPCR: Angiotensin II Activated State of AT1R Initiated by van der Waals Attraction. *Journal of Chemical Information and Modeling*, 59(1), 373-385.
- Soman, S. S., & Tinson, A. (2016). Development and evaluation of a simple and effective real time PCR assay for mitochondrial quantification in racing camels. *Molecular Cell Probes*, 30(5), 326-330.
- Spivak, C. E., Beglan, C. L., Seidleck, B. K., Hirshbein, L. D., Blaschak, C. J., Uhl, G. R., & Surratt, C. K. (1997). Naloxone activation of  $\mu$ -opioid receptors mutated at a histidine residue lining the opioid binding cavity. *Molecular Pharmacology*, 52(6), 983-992.
- Stein, C., Schäfer, M., & Machelska, H. (2003). Attacking pain at its source: new perspectives on opioids. *Nature medicine*, 9(8), 1003-1008.
- Steinbach, P. J., Ansari, A., Berendzen, J., Braunstein, D., Chu, K., Cowen, B. R., . . . Johnson, J. B. (1991). Ligand binding to heme proteins: connection between dynamics and function. *Biochemistry*, 30(16), 3988-4001.
- Storz, J. F. (2016). Gene Duplication and Evolutionary Innovations in Hemoglobin-Oxygen Transport. *Physiology (Bethesda)*, 31(3), 223-232.
- Sun, L., Wu, S., Zhou, L., Wang, F., Lan, X., Sun, J., . . . Liao, D. (2017). Separation and Characterization of Angiotensin I Converting Enzyme (ACE) Inhibitory Peptides from *Saurida elongata* Proteins Hydrolysate by IMAC-Ni(2). *Marine Drugs*, 15(2), 3390-3400.
- Teschemacher, H. (1993). Atypical opioid peptides. In *Opioids* (pp. 499-528): Springer.
- Thompson, J. D., Higgins, D. G., & Gibson, T. J. (1994). CLUSTAL W: improving the sensitivity of progressive multiple sequence alignment through sequence weighting, position-specific gap penalties and weight matrix choice. *Nucleic Acids Research*, 22(22), 4673-4680.

- Tillib, S. V., Vyatchanin, A. S., & Muyldermans, S. (2014). Molecular analysis of heavy chain-only antibodies of *Camelus bactrianus*. *Biochemistry (Mosc)*, 79(12), 1382-1390.
- Tóth, A. D., Turu, G., Hunyady, L., & Balla, A. (2018). Novel mechanisms of G-protein-coupled receptors functions: AT1 angiotensin receptor acts as a signaling hub and focal point of receptor cross-talk. *Best Practice & Research Clinical Endocrinology & Metabolism*, 32(2), 69-82.
- Trinks, A., Burger, P., Beneke, N., & Burger, J. (2012). Simulations of populations ancestry of the two-humped camel (*Camelus bactrianus*). *Camels in Asia and North Africa. Interdisciplinary perspectives on their significance in past and present*, E. Knoll and P. Burger (Eds.), *Academy of Science Press, Vienna (Austria)*, 79-86.
- Tuckerman, M., Berne, B. J., & Martyna, G. J. (1992). Reversible multiple time scale molecular dynamics. *The Journal of chemical physics*, 97(3), 1990-2001.
- Venkatakrishnan, A. J., Deupi, X., Lebon, G., Tate, C. G., Schertler, G. F., & Babu, M. M. (2013). Molecular signatures of G-protein-coupled receptors. *Nature*, 494(7436), 185-194.
- Waldhoer, M., Bartlett, S. E., & Whistler, J. L. (2004). Opioid receptors. *Annual Review of Biochemistry*, 73, 953-990.
- Wan, Q., Okashah, N., Inoue, A., Nehme, R., Carpenter, B., Tate, C. G., & Lambert, N. A. (2018). Mini G protein probes for active G protein-coupled receptors (GPCRs) in live cells. *Journal of Biological Chemistry*, 293(19), 7466-7473.
- Wang, X., Chen, H., Fu, X., Li, S., & Wei, J. (2017). A novel antioxidant and ACE inhibitory peptide from rice bran protein: Biochemical characterization and molecular docking study. *LWT*, 75, 93-99.
- Wang, X., Heinz, B. A., Qian, Y. W., Carter, J. H., Gadski, R. A., Beavers, L. S., . . . Bruns, R. F. (2018). Intracellular Binding Site for a Positive Allosteric Modulator of the Dopamine D1 Receptor. *Molecular Pharmacology*, 94(4), 1232-1245.
- Wang, X., Wu, S., Xu, D., Xie, D., & Guo, H. (2011). Inhibitor and substrate binding by angiotensin-converting enzyme: quantum mechanical/molecular mechanical molecular dynamics studies. *Journal of Chemical Information and Modeling*, 51(5), 1074-1082.
- Wardeh, M. (2004). Classification of the dromedary camels. *Journal of Camelid Science*, 1, 1-7.
- Watts, K. S., Dalal, P., Murphy, R. B., Sherman, W., Friesner, R. A., & Shelley, J. C. (2010). ConfGen: a conformational search method for efficient generation of bioactive conformers. *Journal of Chemical Information and Modeling*, 50(4), 534-546.
- Wernery, U., & Kaaden, O. R. (2004). Foot-and-mouth disease in camelids: a review. *Veterinary Journal*, 168(2), 134-142.

- Wheatley, M., Wootten, D., Conner, M. T., Simms, J., Kendrick, R., Logan, R. T., . . . Barwell, J. (2012). Lifting the lid on GPCRs: the role of extracellular loops. *British Journal of Pharmacology*, *165*(6), 1688-1703.
- Wingler, L. M., McMahon, C., Staus, D. P., Lefkowitz, R. J., & Kruse, A. C. (2019). Distinctive Activation Mechanism for Angiotensin Receptor Revealed by a Synthetic Nanobody. *Cell*, *176*(3), 479-490.
- Wong, A. H., Zhou, D., & Rini, J. M. (2012). The X-ray crystal structure of human aminopeptidase N reveals a novel dimer and the basis for peptide processing. *Journal of Biological Chemistry*, *287*(44), 36804-36813.
- Wu, H., Guang, X., Al-Fageeh, M. B., Cao, J., Pan, S., Zhou, H., . . . Wang, J. (2014). Camelid genomes reveal evolution and adaptation to desert environments. *Nature Communication*, *5*, 5188-5213.
- Xu, H., Lu, Y. F., Partilla, J. S., Zheng, Q. X., Wang, J. B., Brine, G. A., . . . Rothman, R. B. (1999). Opioid peptide receptor studies, 11: involvement of Tyr148, Trp318 and His319 of the rat mu-opioid receptor in binding of mu-selective ligands. *Synapse*, *32*(1), 23-28.
- Ye, S., Chai, S. Y., Lew, R. A., & Albiston, A. L. (2007). Insulin-regulated aminopeptidase: analysis of peptide substrate and inhibitor binding to the catalytic domain. *Biological Chemistry*, *388*(4), 399-403.
- Yu, Z., Chen, Y., Zhao, W., Li, J., Liu, J., & Chen, F. (2018). Identification and molecular docking study of novel angiotensin-converting enzyme inhibitory peptides from *Salmo salar* using in silico methods. *Journal of the Science of Food and Agriculture*, *98*(10), 3907-3914.
- Yukhananov, R., Glämsta, E.-L., & Nyberg, F. (1994). Interaction of hemorphins with opioid receptors in the rat vas deferens and guinea-pig ileum. *Regulatory Peptides*, *53*, S239-S242.
- Yonetani, T., Park, S., Tsuneshige, A., Imai, K., & Kanaori, K. (2002). Global allosteric model of hemoglobin modulation of O<sub>2</sub> affinity, cooperativity, and Bohr effect by heterotropic allosteric effectors. *Journal of Biological Chemistry*, *277*(37), 34508-34520.
- Zadina, J. E., Kastin, A. J., Kersh, D., & Wyatt, A. (1992). Tyr-MIF-1 and hemorphin can act as opiate agonists as well as antagonists in the guinea pig ileum. *Life Sciences*, *51*(11), 869-885.
- Zhang, H., Unal, H., Desnoyer, R., Han, G. W., Patel, N., Katritch, V., . . . Stevens, R. C. (2015a). Structural basis for ligand recognition and functional selectivity at angiotensin receptor. *Journal of Biological Chemistry*, *290*(49), 29127-29139.
- Zhang, H., Unal, H., Gati, C., Han, G. W., Liu, W., Zatspein, N. A., . . . Cherezov, V. (2015b). Structure of the Angiotensin receptor revealed by serial femtosecond crystallography. *Cell*, *161*(4), 833-844.

- Zhang, P., Leger, A. J., Baleja, J. D., Rana, R., Corlin, T., Nguyen, N., . . . Kuliopulos, A. (2015). Allosteric Activation of a G Protein-coupled Receptor with Cell-penetrating Receptor Mimetics. *Journal of Biological Chemistry*, *290*(25), 15785-15798.
- Zhao, Q., & Piot, J. (1997). Investigation of inhibition angiotensin-converting enzyme (ACE) activity and opioid activity of two hemorphins, LVV-hemorphin-5 and VV-hemorphin-5, isolated from a defined peptic hydrolysate of bovine hemoglobin. *Neuropeptides*, *31*(2), 147-153.
- Zhao, Q., Sannier, F., Garreau, I., Guillochon, D., & Piot, J. M. (1994). Inhibition and inhibition kinetics of angiotensin converting enzyme activity by hemorphins, isolated from a peptic bovine hemoglobin hydrolysate. *Biochemical and Biophysical Research Communication*, *204*(1), 216-223.
- Zhao, X., Pollock, D. M., Inscho, E. W., Zeldin, D. C., & Imig, J. D. (2003). Decreased renal cytochrome P450 2C enzymes and impaired vasodilation are associated with angiotensin salt-sensitive hypertension. *Hypertension*, *41*(3), 709-714.

### List of Publications

1. Ali, A., & Vijayan, R. (2020). Dynamics of the ACE2–SARS-CoV-2/SARS-CoV spike protein interface reveal unique mechanisms. *Scientific reports*, 10(1), 1-12.
2. Ali, A., Alzeyoudi, S. A. R., Almutawa, S. A., Alnajjar, A. N., & Vijayan, R. (2020). Molecular basis of the therapeutic properties of hemorphins *Pharmacological Research*, 158, 104855-104866.
3. Ali, A., Alzeyoudi, S. A. R., Almutawa, S. A., Alnajjar, A. N., Al Dhaheri, Y., & Vijayan, R. (2020). Camel Hemorphins Exhibit a More Potent Angiotensin-I Converting Enzyme Inhibitory Activity than Other Mammalian Hemorphins: *An in silico* and *in vitro* study. *Biomolecules*, 10(3), 486-505.
4. Antony, P., Baby, B., Homedi, Z. A., Halabi, W. A., Ali, A., & Vijayan, R. (2020). Polypharmacological potential of natural compounds against prostate cancer explored using molecular docking and molecular dynamics simulations. *International Journal of Computational Biology and Drug Design*, 13(2), 181-199.
5. Ali, A., Baby, B., Soman, S. S., & Vijayan, R. (2019). Molecular insights into the interactions of hemorphin and its targets. *Scientific Reports*, 9(1), 1-16.
6. Ali, A., Palakkott, A., Ashraf, A., Al Zamel, I., Baby, B., Vijayan, R., & Ayoub, M. A. (2019). Positive Modulation of Angiotensin II Type 1 Receptor-mediated signaling by LVVhemorphin-7. *Frontiers in Pharmacology*, 10, 1258-1272.
7. Ali, A., Baby, B., & Vijayan, R. (2019). Camel genome - from desert to medicine: A review of camel genomics and therapeutic products. *Frontiers in Genetics*, 10, 3389-3409.
8. Jobe A., Baby B., Ali A., & Vijayan R. (2020). Identification of potential anti-obesity drug scaffolds using molecular modeling. *International Journal of Computational Biology and Drug Design*. (accepted for publishing).